

CHARGE-DENSITY ANALYSES OF
METAL COMPLEXES OF THE
BIS(BENZOAZOL-2-YL)METHANIDE LIGAND

DISSERTATION ZUR ERLANGUNG DES
MATHEMATISCH-NATURWISSENSCHAFTLICHEN DOKTORGRADES
„DOCTOR RERUM NATURALIUM“
DER GEORG-AUGUST UNIVERSITÄT GÖTTINGEN

IM PROMOTIONSPROGRAMM CHEMIE
DER GEORG-AUGUST UNIVERSITY SCHOOL OF SCIENCE (GAUSS)

VORGELEGT VON CHRISTIAN KÖHLER

AUS HANNOVER

GÖTTINGEN, 2022

Betreuungsausschuss:

Prof. Dr. Dietmar Stalke, Fakultät für Chemie, Institut für Anorganische Chemie, Georg-August-Universität Göttingen

Prof. Dr. Ricardo Mata, Fakultät für Chemie, Institut für Physikalische Chemie, Georg-August-Universität Göttingen

Mitglieder der Prüfungskommission:

Referent: Prof. Dr. Dietmar Stalke, Fakultät für Chemie, Institut für Anorganische Chemie, Georg-August-Universität Göttingen

Korreferent: Prof. Dr. Ricardo Mata, Fakultät für Chemie, Institut für Physikalische Chemie, Georg-August-Universität Göttingen

Weitere Mitglieder der Prüfungskommission:

Prof. Dr. Manuel Alcarazo, Fakultät für Chemie, Institut für Organische und Biomolekulare Chemie, Georg-August-Universität Göttingen

Jun.-Prof. Dr. Anna Krawczuk, Fakultät für Chemie, Institut für Anorganische Chemie, Georg-August-Universität Göttingen

Dr. Lisa Vondung, Fakultät für Chemie, Institut für Anorganische Chemie, Georg-August-Universität Göttingen

Dr. Alessandro Bismuto, Fakultät für Chemie, Institut für Organische und Biomolekulare Chemie, Georg-August-Universität Göttingen

Inhaltsverzeichnis

Abbreviations	vii
1 Introduction	1
1.1 BOX ligands as an alternative to the ubiquitous NacNac ligand family	1
1.2 Charge-Density investigations on single crystals	4
1.3 Scope of this thesis	5
2 Basic concepts of single crystal X-ray diffraction.....	6
2.1 Foundations of X-ray diffraction at periodic solids.....	6
2.2 Diffraction condition and Bragg equation.....	6
2.3 Data reduction and scaling	8
2.4 Observed and Calculated Structure Factors.....	9
2.5 Figures of merit and quality indicators.....	10
2.5.1 Data Quality indicators.....	11
2.5.2 Model Quality Indicators.....	12
2.6 The Independent Atom Model (IAM)	15
2.7 Hirshfeld Atom Refinement	16
3 Experimental charge-density investigations.....	17
3.1 The Hansen & Coppens Multiple Model (MM).....	17
3.1.1 Refinement of anharmonic motion.....	19
3.1.2 Anisotropic hydrogen atoms and the Hirshfeld test	20
3.2 Experimental requirements and specific challenges.....	21
3.2.1 Overfitting and cross-validation	22
3.2.2 Thermal Diffuse Scattering and other resolution-dependent errors	24
3.3 Quantum Theory of Atoms in Molecules (QTAIM)	25
3.3.1 Critical Points	27
3.3.2 Bond Characterisation	28
3.3.3 Source function investigations	29
4 Investigation of a disordered Aluminium dihydride-BOX complex: A new approach to modelling molecular disorder?	30
4.1 Disordered structures in charge-density analysis	30

4.2	Experimental	32
4.2.1	Data collection and processing.....	32
4.2.2	Theoretical study	33
4.2.3	Structure refinement	33
4.2.4	Additional model structures	34
4.3	Multipole model refinement.....	36
4.3.1	“2Part” approach	36
4.3.2	“1Part” approach	37
4.3.3	Disorder in the Methyl Groups and Final Model	38
4.4	Results and discussion: AlH ₂	39
4.4.1	Residual density analysis.....	40
4.4.2	Structural analysis	41
4.4.3	Molecular Graph and Critical Points.....	43
4.4.4	Bader charges and source function.....	48
4.5	Results and discussion: Additional model compounds	49
4.5.1	Residual density analysis.....	49
4.5.2	Impact on the deformation density and structural properties	50
4.6	Conclusion and outlook.....	55
5	Charge-Density Analysis of three d-metal BOX complexes with different magnetic properties..	56
5.1	Introduction to molecular magnetism.....	57
5.2	Experimental d-orbital populations from the multipole model	59
5.3	Experimental	60
5.3.1	Data collection and processing:.....	60
5.3.2	Temperature-dependent study of CoMeBOX.....	62
5.3.3	Theoretical study	63
5.4	Multipole model refinement.....	64
5.5	Results and Discussion of structural properties.....	71
5.5.1	Structural analysis	71
5.5.2	Molecular Graph and Critical points	72
5.5.3	Bader charges and Source function	76

5.5.4	Determination of d-Orbital populations	79
5.5.5	Impact of model decisions on structural properties.....	81
5.6	Conclusion and outlook.....	82
6	Comparison of different strategies for modelling hydrogen atoms in charge-density analyses....	84
6.1	Treatment of Hydrogen atoms in charge-density analyses.....	84
6.2	Methods for comparison of ADPs.....	86
6.3	Model compounds and MM refinement.....	87
6.4	Hydrogen atom ADPs from Hirshfeld atom refinement: Old and contemporary methods...	88
6.5	Results and discussion.....	89
6.5.1	Visual comparison of approximate ADPs using PEANUT	89
6.5.2	Comparison of X-H distances	93
6.5.3	Comparison of Interaction Energies.....	94
6.6	Conclusion and Outlook.....	95
7	Summary an Outlook.....	97
8	Other Projects.....	99
8.1	Attempted Data collection for other BOX ligands and their metal complexes	99
8.1.1	Free Ligands	99
8.1.2	Additional aluminium dihydride and group 13 complexes	102
8.2	Charge-density Investigation on Si-O bonds in two different structures	103
8.2.1	Data collection.....	103
8.2.2	Data reduction	103
8.2.3	Model refinement	104
8.2.4	Discussion and results	105
8.2.5	Conclusion and outlook.....	106
8.3	Development of a Crystallisation strategy for growing [2.2]paracyclophane crystals of sufficient size for neutron and benchmarking experiments.....	107
9	Crystal Structure Determination in Collaboration.....	109
9.1	Structures determined for Dr. Wenling Li.....	109
9.1.1	CK_WL2	109
9.1.2	CK_WL5	110

9.1.3	CK_WL8	111
9.1.4	CK_WL9	112
9.1.5	CK_WL10	114
9.2	Structures determined for Dr. Majahuddin Siddiqui	115
9.2.1	CK_MM268	115
9.2.2	CK_MM290	117
9.3	Structures determined for Dr. Chowan Ashok	119
9.3.1	CK_CAK_CiSiAlSiCl	119
9.3.2	CK_CAK67	120
9.4	Structures determined for Arghavan Abolghasempour	122
9.4.1	KR_CK_18	122
9.4.2	A18_twin	123
9.4.3	KR_CK_AFC	124
9.4.4	KR_CK_AFI	125
9.4.5	KR_CK_AI3	125
9.4.6	KR_CK_ANI	127
9.4.7	KR_CK_EC	128
9.4.8	KR_CK_EF1	129
9.4.9	EI2	130
10	Appendix	131
10.1	Additional details about the structure refinement of AlH ₂ MeBOX	131
10.1.1	Local coordinate systems, symmetry and chemical constraints	131
10.1.2	Test for overfitting and final refinement strategies	133
10.1.3	Treatment of hydrogen atoms	138
10.1.4	Iteration of occupancy factors in the 2Part approach	141
10.1.5	Attempted Refinement of Disordered Methyl Groups	141
10.1.6	Molecular Graphs for all molecular disorder approaches	142
10.2	Additional details about the structure Refinement of HCTD	144
10.2.1	Local coordinate systems, symmetry and chemical constraints	144
10.2.2	Final refinement strategy	145

10.3	Additional details about the structure Refinement of NPP.....	147
10.3.1	Local coordinate systems, symmetry and chemical constraints	147
10.3.2	Final refinement strategy	148
10.4	Additional details about the structure Refinement of MnMeBOX.....	150
10.4.1	Selected data quality indicators	150
10.4.2	Comparison of integration options	151
10.4.3	Local coordinate systems, symmetry and chemical constraints	152
10.4.4	Test for overfitting and final refinement strategies	154
10.4.5	DMSDA values of freely refined hydrogen ADPS	159
10.4.6	Additional model quality indicator plots	160
10.4.7	ORCA 5 input for CASSCF/NEVPT2 calculations	161
10.5	Additional details about the structure Refinement of FeMeBOX	162
10.5.1	Selected data quality indicators	162
10.5.2	Local coordinate systems, symmetry and chemical constraints	163
10.5.3	Test for overfitting and final refinement strategies	163
10.5.4	DMSDA values of freely refined hydrogen ADPS	168
10.5.5	Additional model quality indicator plots	169
10.5.6	Molecular Graph.....	170
10.5.7	ORCA 5 input for CASSCF/NEVPT2 calculations	171
10.6	Additional details about the structure Refinement of CoMeBOX.....	172
10.6.1	Selected data quality indicators by dataset.....	172
10.6.2	Local coordinate systems, symmetry and chemical constraints	174
10.6.3	Test for overfitting and final refinement strategies	175
10.6.4	DMSDA values of freely refined hydrogen ADPS	180
10.6.5	Additional model quality indicator plots	181
10.6.6	Molecular Graph.....	182
10.6.7	ORCA 5 input for CASSCF/NEVPT2 calculations	183
10.7	Additional details about the structure refinement of SPAnH	184
10.7.1	Local coordinate systems, symmetry and chemical constraints	184
10.7.2	Test for overfitting and final refinement strategies	187

10.7.3	Residuals after final refinement step against X-ray data with fixed C-H distances	191
10.7.4	List of evaluated BCPs between the toluene molecule and the anthracene moiety.....	192
10.7.5	Calculated interaction energies.....	193
10.8	Additional details about the structure Refinement of SPAnPS	194
10.8.1	Local coordinate systems, symmetry and chemical constraints	194
10.8.2	Test for overfitting and final refinement strategies	196
10.8.3	Residuals after final refinement step against X-ray data with fixed C-H distances	200
10.8.4	List of evaluated BCPs between the toluene molecule and the anthracene moiety.....	201
10.8.5	Calculated interaction energies.....	203
11	References	204
12	Lebenslauf.....	Fehler! Textmarke nicht definiert.
13	Danksagung.....	211

Abbreviations

BOX	bis(benzoxazol-2-yl)methanide ligands
NacNac	β -diketaminato
ED	electron density
MM	Hansen & Coppens multiple model
XD	The <i>XD2016</i> software suite
QTAIM	quantum theory of atoms in molecules
MeBOX	bis(4-CH ₃ -benzoxazol-2-yl)methanide ligand
SCXRD	single crystal X-ray diffraction
R value	residual value
GoF	Goodness of Fit
ADPs	anisotropic displacement parameters
IAM	independent atom model
HAR	Hirshfeld Atom Refinement
GCC	Gram-Charlier coefficients
DMSDA	difference of mean-square displacement amplitudes
X-H bond	bond between a hydrogen atom and a heavier atom
TDS	thermal diffuse scattering (and similar effects)
BCP	bond critical point
RCP	ring critical point
CCP	cage critical point
HP rule	Hopf-Poincaré rule
VSCDs	valence shell charge depletions
VSCCs	valence shell charge concentrations
SOF	site occupation factor
molecular disorder	disorder of a whole molecule
AlH ₂	[AlH ₂ {(4-CH ₃ -benzoxazol-2-yl)CH ₂ } ₂] complex
HCTD	NO ₃ -Heptacyclo[6.6.0.0 ^{2,6} .0 ^{3,13} .0 ^{4,11} .0 ^{5,9} .0 ^{10,14}]tetradecane
NPP	N-phenylpyrrole
theoMM	multipole model refinement against theoretical structure factors
SMM	single-molecule magnet
SIM	single-ion magnet
OAM	orbital angular momentum
ZFS	zero-field splitting
CASSCF	complete active space self-consistent field
NEVPT2	n-electron valence state perturbation theory

Aniso	anisotropic hydrogen refinement against X-ray data
10scale	multipole model refinement with 10 resolution dependent scale factors
SPAnH	9-diphenylethiophosphanylanthracene
SPAnPS	9,10-bis-diphenylethiophosphanylanthracene
Q0	bond-directed quadrupoles
PCP	[2.2]Paracyclophane

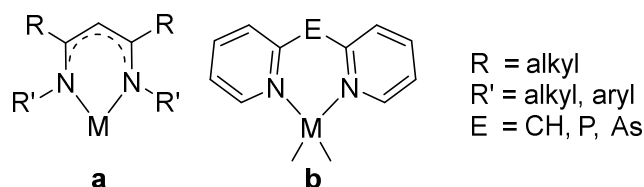
1 Introduction

For my PhD thesis, I used the method of charge-density analysis based on high-resolution single crystal X-ray diffraction experiments to investigate numerous complexes of bis(benzoxazole-2-yl)methanide (BOX) ligand family. In this chapter, a brief history of BOX ligands and their complexes, the focal structure family of this thesis, will be provided. This includes a short summary of their development and a list of previous structural investigations that inspired the current work. This is followed by a brief introduction of the used method. In the end, a list of all investigated structures as well as the scope of this thesis is provided.

1.1 BOX ligands as an alternative to the ubiquitous NacNac ligand family

Customized catalysts for specific reactions are invaluable to a large number of chemical processes in research and industry and are therefore a widely explored field.^[1] A large portion of commercially available catalysts are organometallic compounds, in which a metal centre in a relevant oxidation state is stabilised by a ligand optimised for high turnover rates and product selectivity in the targeted reaction.^[2] The constantly arising demand for newly adapted catalysts for newly emerging and improving industrial processes incentivises the design of multifunctional ligand platforms or “families” that can be easily attuned to new specifications. Ligand systems facilitating several catalytic compounds are often specifically designed for two main properties: Versatility of use and customisable shielding of the coordination site. On one hand, ligands of the respective family should be non-innocent and able of undergoing ligand–metal interactions, as these characteristics are useful for facilitating charge delocalisation within the formed complexes, increasing their stability. They should be capable of stabilizing both high and low oxidation state ions of variable sizes and should preferably have more than one possible coordination site, to increase the number of possible complexes. On the other hand, the ligands should provide sufficient and adjustable sterical shielding in order to prevent oligomerisation and unwanted side reactions like electrophilic attacks.^[3] Furthermore, the choice of substituents around the coordination site can have an impact on the solubility of the resulting complexes as well. A well-known example of a ligand family combining most of these desired features are the ubiquitous β -diketamine or “NacNac” ligands,^[4] deriving their name from their structural similarity to acetylacetonone (“AcAc”). Unsurprisingly, today a large number of NacNac-based catalysts are known.^[5] As the title suggests, this thesis will mainly deal with the family of Bis(benzoxazole-2-yl)methanide (BOX) ligands, which were designed and investigated in the Stalke group as a possible alternative to the NacNac system.

The investigation of BOX ligands from this work in the Stalke group started with the PhD of David Dauer, in which he synthesised and characterised several bisheterocyclic methanides and amides.^[6,7] Dauer started with his work based on earlier results published by Kottke in 1997^[8] and Gornitzka in 1998,^[9] who started with bipyridyl methane ligands not yet containing Group 16 elements.



Scheme 1: A usual NacNac ligand (**a**) and the ligand class previously investigated by Kottke and Gornitzka (**b**).^[8,9]

One area for improvement over the NacNac ligands is in the field of planarity and hetero-aromaticity: For substituted NacNac systems it is known that the resulting metal complex often deviates from a planar shape due to commonly used bulky, but flexible substituents such as 2,6-diisopropylphenyl (Dipp). While this bending of the ligand provides increased shielding to the coordinated centre, it also detracts from the hetero-aromatic delocalisation of electron density in the resulting complex, and therefore, the stability of the complex. The family of BOX ligands as worked on in my thesis grew from an attempt by Dauer to minimize the potential for twisting in the ligand by introducing more rigid benzoxazole groups in the known methanide framework, therefore, enhancing hetero-aromaticity.

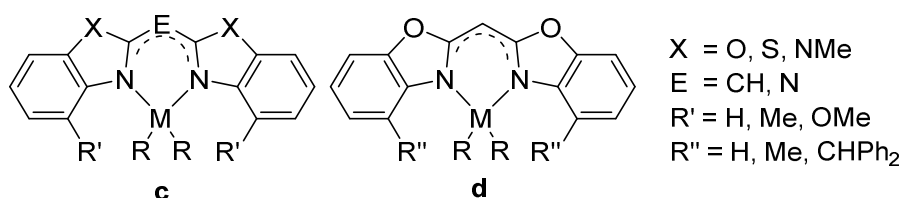


Figure 1-1: General formula of the ligands investigated by Dauer (**c**)^[6] and the class of BOX ligands investigated in this thesis (**d**).

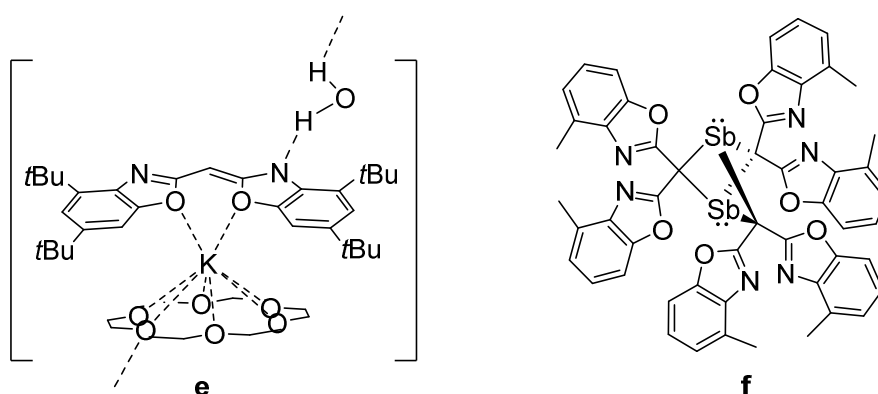


Figure 1-2: BOX complexes with more unusual geometries: The first reported organopotassium complex containing water (**e**)^[10] and the unusual BOX coordination motive of an antimony compound synthesized by Nico Graw (**f**).^[11]

Ligands as shown in Figure 1-1 have two possible coordination sites, allowing coordination at both the nitrogen and the oxygen atoms of the benzoxazole moiety and enabling the formation of Janus head compounds. On the other hand, a choice of different alkyl substituents close to the coordination site afford the ligand with highly customisable steric shielding of the coordinated metal. Over the last years,

BOX ligands were used mainly by Johannes Kretsch and Ingo Köhne to synthesize a variety of metal compounds with a wide range of intriguing chemical properties. This includes several alkali and alkaline earth metal BOX complexes,^[12] among them the first reported organopotassium compound in presence of water.^[10,13] Several Group 13 complexes have been reported,^[7] including the heavier elements of the group,^[14] as well as aluminium(III) halide complexes,^[15] and following them, a range of low valent alanes.^[16] Alanes are highly relevant in organometallic chemistry due to their possible applications as hydrogen storage materials.^[17] Furthermore, NacNac-based aluminium dihydride complexes have been reported to have catalytical applications in the hydroboration of terminal alkynes and the de-hydro-coupling of boranes,^[18,19] making the investigation of the analogue BOX complexes especially rewarding. Daniel Lüert and Christina Legendre, on the other hand, recently used BOX ligands in the synthesis of a row of d-metal complexes for benchmarking molecular magnetism^[20] and for precursor compounds to lanthanide-based molecular magnets.^[21] Most recently, in his PhD thesis, Nico Graw reported of the synthesis of a novel antimony BOX complex with a hitherto unreported coordination motive.^[11]

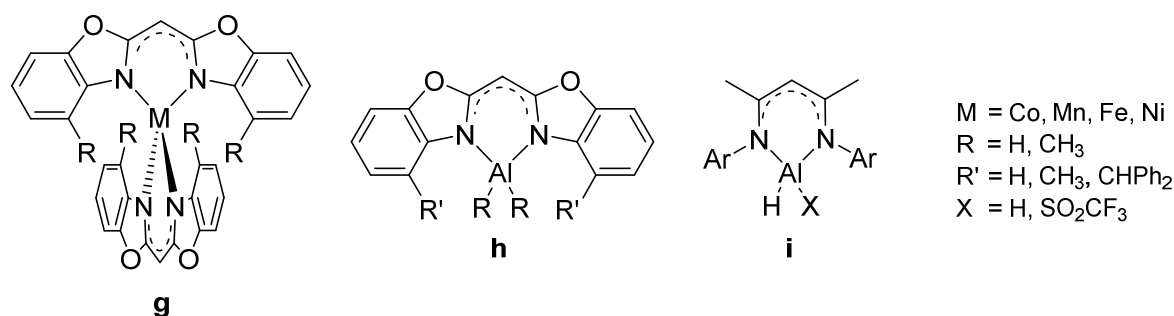


Figure 1-3: Left: BOX complexes synthesized by Lüert and Legendre *et al.* for benchmarking of magnetic properties (**g**). Middle and right: BOX alane complexes synthesized by Kretsch *et al.* (**h**), which are BOX-equivalents of NacNac complexes with reported catalytic applications for the hydroboration of terminal alkynes and the de-hydro-coupling of boranes, as reported on by Roesky *et al.* in 2015/16 (**i**).^[18,19]

Considering the reported results of BOX ligand complexes, the relatively new ligand family is well-suited to establish itself as future NacNac alternative. A number of computational studies comparing the capabilities of selected BOX complexes to their NacNac competitors have shown promising results so far.^[3,22] To assist future design of BOX ligands and their complexes, the method of charge-density analysis based on high-resolution diffraction data was chosen to gain additional insight into the inner workings of several of the aforementioned recently synthesised BOX complexes.

1.2 Charge-Density investigations on single crystals

Since their first study on interference of X-rays at a molecular lattice by Laue, Friedrich and Knipping in 1912,^[23] X-ray diffraction experiments at single crystals have developed to become one of the most relevant analytical methods. Today, it is routinely used for obtaining the three-dimensional structure of any substance that can be crystallized in sufficient quality. While such routine measurements only allow to determine distances and angles between atom positions, more demanding high-angle measurements with a maximum resolution of at least 0.50 Å allow for a much more thorough investigation of the electron density (ED) distribution within a crystal. Using the Multipole Model (MM) by Hansen and Coppens,^[24] the ED can even be described in interatomic regions, and topological analysis according to Bader's Quantum Theory of atoms in Molecules (QTAIM)^[25] in order to characterise chemical bonding, which is known provide useful insights for synthetic chemists for *de novo* ligand design and comparison of structural properties.^[26,27]

Besides the aforementioned analysis of critical points in the second derivative of the electron density function, a wider selection of more specialized evaluation options exist that are useful to obtain insights into more specific chemical topics. With the so-called *source function*, delocalization in π -systems can be analysed by calculating the impact of electron density across the structure on a chosen reference point.^[28] This method, besides supplementary quantum-chemical calculations, was used by Jacob Hey for his investigation of hetero-aromaticity in a BOX-like ligand (Figure 1-4).^[29] His approach in his doctoral thesis and specifically this project served as inspiration for my work on these compounds. As the spherical harmonics used for modelling of the ED in the MM are mathematically related to the shape of orbitals, experimental d-orbital populations can easily be determined from a final model.^[30] These populations, on the other hand, have recently been well established as experimental validation for theoretical calculations of d-orbital energies, which are highly relevant for the topic of d-metal single-ion magnets.^[31,32]

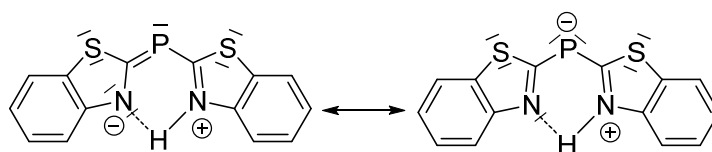


Figure 1-4: Mesomeric structures of the compound investigated by Hey via charge-density analysis and theoretical calculations.^[29]

Beyond the work of Jacob Hey, so far, no charge-density studies of BOX or similar ligands and their metal complexes have been reported.

1.3 Scope of this thesis

In my PhD, I set out to perform charge-density comparison studies between the BOX complexes depicted in Figure 1-3 and the respective three free ligands. However, process along this way was halted by several obstacles, because several complexes showing initially promising crystals did not fulfil the requirements for charge-density investigation.

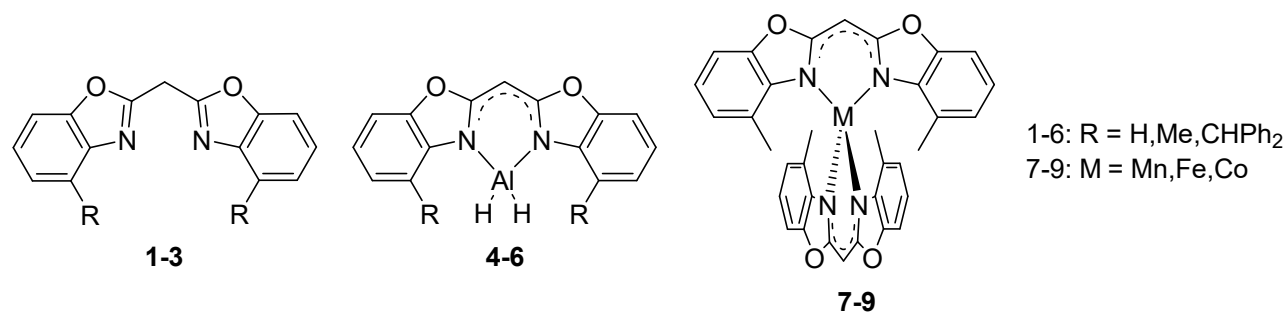


Figure 1-5: BOX ligands and complexes within the scope of this thesis. Compounds are enumerated following the list of varying alkyl rests and metals on the right.

While among the free ligands, only **3** was suitable for collection of high-resolution data, only the alane complex **4** of the “MeBOX” ligand (**2**) could be obtained, which showed, however, signs of a small molecular disorder. Disorder, as will be laid in more detail later in this thesis, is generally considered a deal breaker in terms of multipole model refinements. Among the complexes synthesised by Daniel Lüert and Christina Legendre, on the other hand, only those with the MeBOX ligand (**2**) were eligible as well, limiting results of this work to only complexes of this ligand. Nevertheless, several fruitful studies could be conducted with the available datasets, which will be presented in the following.

Theoretical concepts of single crystal X-ray diffraction experiments in general and the focal method of charge-density investigation based on high-resolution X-ray data will be presented in Chapters 2 and 3. Chapter 4 deals with the development and validation of a new approach for modelling disorder in the charge-density refinement of the alane BOX complex **4**. A comparison study between the d-metal complexes **7**, **8** and **9**, focussing on experimental d-orbital populations and their comparison with results from quantum chemical calculations can be found in Chapter 0. In Chapter 6, a comparison study of different approximation methods for hydrogen thermal vibration parameters in charge-density analyses is presented. This project started during my master thesis, but was only finalised in the first year of my PhD. The lessons learned from this study influenced all other projects during my thesis, making it relevant for this work. Furthermore, this chapter explores two new approximation methods that were not yet published at the time when the project was started. Final conclusion from this thesis will be drawn and summarised in Chapter 7.

2 Basic concepts of single crystal X-ray diffraction

In this chapter, all basic concepts of single crystal X-ray diffraction (SCXRD) will be introduced, including a description of routine structure refinement. While more advanced structure investigations based on high-angle data are the central focus of this work, a standard dataset of excellent quality is oftentimes the starting point for a successful charge-density analysis. Several graphics, as well as certain passages of text within this part, were reused or only slightly altered from the theoretical background chapter of my master thesis on the same scientific field.^[33]

2.1 Foundations of X-ray diffraction at periodic solids

The foundation of SCXRD lies in the diffraction of electromagnetic waves at a lattice with a grating constant in the same order of magnitude as the wavelength of incident waves. This is most easily demonstrated by the well-known double slit experiment. X-ray diffraction utilizes the fact that crystals consist of a molecular lattice, which can function as an optical lattice if a sufficiently short wavelength of radiation is chosen. A crystalline solid is characterized by periodic repetition of a three-dimensional structural motif in all three dimensions, which is called the *unit cell* of the crystal. As the rest of the crystal can be described by repetition of the unit cell, a satisfactory description of the whole molecular structure can be achieved by only inspecting a small portion with unit cell edges usually below 40 Å. Coordinates of any point with position vector \mathbf{r} within the unit cell can be described in *fractional coordinates* x, y, z , which are fractions of the length of the three vectors $\mathbf{a}, \mathbf{b}, \mathbf{c}$ spanning the cell, with angles α, β, γ between them.

$$\mathbf{r} = x\mathbf{a} + y\mathbf{b} + z\mathbf{c} \quad (\text{Eq. 1})$$

Molecular distances within a crystal are usually in the range of a few Angstroms. Therefore, diffraction in SCXRD experiments can be expected to occur with incident X-ray wavelengths between 0.5 Å and 5 Å. The most commonly used type of radiation used for small molecule structures today, which was mainly used for this work as well, is Molybdenum K_α radiation with a wavelength of approximately 0.71 Å.^[34,35]

2.2 Diffraction condition and Bragg equation

X-rays are scattered at the electrons within the crystal. If an atom is hit by an X-ray, this atom becomes the starting point of a new radial wave. This process is called *elastic scattering*. Given an incident angle of ν , an intensity maximum in the diffracted X-rays can be observed from an observation angle of μ when constructive interference occurs within the molecular lattice. For this to happen, the path difference Δ between two waves scattered at arbitrary scattering points $P1, P2$ within the crystal with a distance vector \mathbf{R} has to be an integer multiple of the used wavelength (Figure 2-1). This condition is fulfilled when the scalar product of the path difference and \mathbf{R} is an integer.^[34]

$$\mathbf{R} \cdot \Delta = n ; n \in \mathbb{Z} \quad (\text{Eq. 2})$$

$$\Delta = \Delta_1 + \Delta_2$$

If constructive interference occurs, the so-called *Laue equations* (Equation 3) are fulfilled, and $\Delta \mathbf{k}$ is a vector \mathbf{r}^* in the reciprocal lattice. In the following notation, the argument for the cosine function is the angle between the two given vectors.

$$\mathbf{a} \cdot \Delta \mathbf{k} = |\mathbf{a}| \cdot |\Delta \mathbf{k}| \cdot \cos(\Delta \mathbf{k}, \mathbf{a}) = h$$

$$\mathbf{b} \cdot \Delta \mathbf{k} = |\mathbf{b}| \cdot |\Delta \mathbf{k}| \cdot \cos(\Delta \mathbf{k}, \mathbf{b}) = k$$

$$\mathbf{c} \cdot \Delta \mathbf{k} = |\mathbf{c}| \cdot |\Delta \mathbf{k}| \cdot \cos(\Delta \mathbf{k}, \mathbf{c}) = l \quad (\text{Eq. 3})$$

$$\mathbf{r}^* = h\mathbf{a}^* + k\mathbf{b}^* + l\mathbf{c}^* = \Delta$$

$$h, k, l \in \mathbb{Z}$$

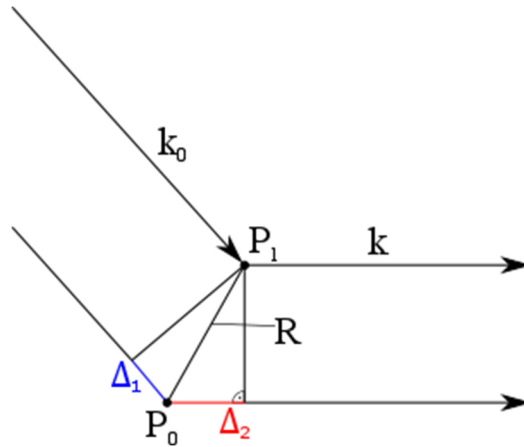


Figure 2-1: Schematic depiction of Laue scattering. \mathbf{k}_0 is the wave vector of the incident beam, \mathbf{k} is the wave vector of the scattered beam. \mathbf{R} is the difference vector between two arbitrarily chosen scattering points within the crystal. Image was reused from my master thesis.^[33]

If the Laue conditions are fulfilled, the observed diffraction is equivalent to the reflection of the X-rays at family of imaginary lattice planes within the crystal with distance d (Figure 2-2), which are characterised by the Miller indices $h, k, l \in \mathbb{Z}$. Each specific family of planes intersect the edges a, b, c of the unit cell at $1/h, 1/k, 1/l$, respectively.^[35,36] A observable reflection emanating from this given family of planes is then called hkl . Again, the diffraction condition is met if the path difference between waves diffracted at different lattice planes is an integer multiple of the wavelength, resulting in the Bragg equation:^[37]

$$2\Delta = 2d \cdot \sin(\theta) = n \cdot \lambda \quad n \in \mathbb{Z} \quad (\text{Eq. 4})$$

Herein, n denotes the order of the diffraction and d_{hkl} the distance between the lattice plane characterized by one respective set of Miller indices. θ is the angle between the incident beam and the lattice plane, and Δ the path difference between waves “reflected” at neighbouring lattice plane.

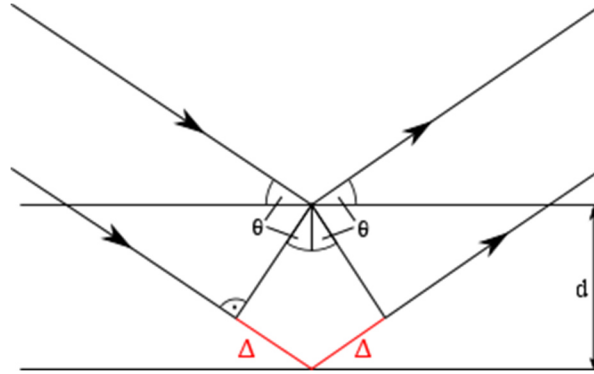


Figure 2-2: Schematic depiction of Bragg scattering. Image was reused from my master thesis.^[33]

2.3 Data reduction and scaling

Data reduction for this work was performed with the Bruker software SAINT.^[38] First, reflex positions are determined, from whom crystal system and cell symmetry are determined. Then, an integration routine determines the background, identifies reflections and integrates their intensities. Each reflection is assigned an integration box in which the integration is performed. The box size is usually refined during integration, but there are specific cases where using a fixed box size is advisable instead. The data is then scaled in the Bruker program SADABS,^[39] which performs scaling and absorption correction of the experimental intensities I_0 according to the formula

$$I_c = I_0 \cdot S(n) \cdot P(u, v, w) \cdot Q(\mu r, 2\theta) \quad (\text{Eq. 5})$$

Herein, $S(n)$ is the incident beam scale factor depending on the frame number n . $P(u, v, w)$ is the diffracted beam correction factor, u, v, w being the direction cosines of the diffracted beam relative to the crystal axes. $Q(\mu r)$ is the spherical absorption correction factor, μ being the linear absorption coefficient and r the radius of the crystal. Furthermore, an error model is created, where raw, experimental standard deviations σ_{raw} are adjusted to fit a χ^2 statistic.^[40]

$$\sigma_{\text{Corr.}}^2 = (K \cdot \sigma_{\text{raw}})^2 + (g \cdot \langle I \rangle)^2 \quad (\text{Eq. 6})$$

Depending on the used detector, it can be advisable to use the experimental errors instead ($K = 1, g = 0$). For this thesis, datasets were mainly collected used the older APEX II detector and the more contemporary PHOTON III detector. Both error models were compared for all datasets. The resulting

observations were that the use of experimental errors benefitted the APEX II datasets, while PHOTON III datasets provided better results when an error model was refined.

As shown by Macchi *et al.* in 2011,^[41] Mo-K α microsource X-ray sources with desired wavelength λ also emit the threefold wavelength, leading to a systematic overexposure of all reflection whose Miller indices are all multiples of three. If this problem was encountered during structure refinement, a so-called 3λ correction was performed, as proposed by Krause *et al.* in 2015.^[42] Here, a correction factor for said reflections is iteratively determined and then entered in *SADABS*, which generally leads to a model improvement if the correction is sound.

2.4 Observed and Calculated Structure Factors

The measurable Bragg intensities of reflections observed in a diffraction experiment do not only contain structural information about the crystal, but are also influenced by other effects, which have to be corrected for during data reduction.

$$I_{hkl} = P \cdot L \cdot A \cdot E \cdot K \cdot |F_{hkl}|^2 \quad (\text{Eq. 7})$$

P is the angle-dependent polarisation coefficient accounting for decreasing intensity caused by polarisation effects. The Lorentz coefficient L accounts for the fact that different lattice planes are in reflection position for varying amounts of time. The absorption coefficient A accounts for absorption of X-rays caused by changing energy levels of electrons within the crystal. The extinction coefficient E accounts for loss of intensity caused secondary diffraction effects. K is an overall scale factor. Besides these effects, the measured intensity of a reflection hkl is proportional to the square of the so-called complex *structure factor* F_{hkl} .^[36]

$$F_{hkl} = \int_V \rho(\mathbf{r}) \cdot \exp(2\pi i \mathbf{h}^T \mathbf{r}) d\mathbf{r}; \quad \mathbf{h} = \begin{pmatrix} h \\ k \\ l \end{pmatrix} \quad (\text{Eq. 8})$$

$$\rho(\mathbf{r}) = \frac{1}{V} \sum_{hkl} F_{hkl} \cdot \exp(-2\pi i \mathbf{h}^T \mathbf{r}) \quad (\text{Eq. 9})$$

As previously described in Chapter 2.2 above, every atom within a crystal is the origin of a new diffracted radial wave. Therefore, each reflection holds information about the entire crystal. If structure factors can be successfully determined from a diffraction experiment, Fourier transformations yields the electron density function $\rho(\mathbf{r})$ of the crystal, which attributes an ED value to each location vector \mathbf{r} and effectively allows to map the location of electrons throughout the entire crystal. However, as seen in Equation 7, the measured intensities are only proportional to the square of observed structure factors $F_{o,hkl}$. Therefore, the phase information, the imaginary part of the complex number F_{hkl} , is not experimentally obtainable and has to be reconstructed in another way. This is called the *crystallographic phase problem*, for which several mathematical solution procedures have been developed.^[43] Today, the

most commonly known approach called *direct methods* uses statistical relationships between phases of sufficiently strong reflections to generate a set of valid starting phases. Structure solution in the scope of this thesis was generally performed with the *SHELXT* program.^[44]

As the observed structure $F_{o,hkl}$ are usually affected by experimental errors, and the process of Fourier transformation itself as described in Equation 9 leads to additional truncation errors, experimental structure factors are not used directly to describe the investigated structure. Instead, a parameterized model of the structure is created, from which calculated structure factors $F_{c,hkl}$ are then derived. These structure factors can be described as sum of the atomic scattering amplitudes of all atoms in the modelled unit cell. As real crystals are not perfect lattices with point-shaped atoms, atoms can be expected to have a small volume with different diffraction properties in different regions. Furthermore, they are affected by thermal vibrations and small statistical disorder throughout the non-ideal, real crystal. X-rays are scattered at the electronic shells of atoms within the crystal, so different atom types with varying numbers of electrons should have different contributions to the scattered intensities, which decrease with increasing scattering angle 2θ . These angle-dependent scattering amplitudes, more commonly called *atomic form factors* $f_{hkl,a}$, are obtained from quantum theoretical calculations. While for the longest time, tabulated and spherical scattering factors were used, a more recently explored approach is the determination of aspherical form factors custom-made for the respective structure.^[45] To account for the aforementioned thermal vibration, atomic form factors are expanded by the so-called *Debye-Waller factor* $t_{a,hkl}$. Functions of varying complexity can be used to describe thermal motion. Generally, it is the Fourier transform of the probability density function used to describe the thermal displacement of atoms. More detailed information about the specific functions usually used is provided in the following chapters. As a whole, a calculated structure factor $F_{c,hkl}$ can then be written as

$$F_{c,hkl} = \sum_a f_{a,hkl} \cdot t_{a,hkl} \cdot \exp(2\pi i \mathbf{h}^T \mathbf{r}) \quad (\text{Eq. 10})$$

Through the process of least squares refinement of the various parameters of the structure model, the difference between observed and calculated structure factors is then minimised.

2.5 Figures of merit and quality indicators

In order to achieve a meaningful description of the investigated structural properties, a sufficient quality of the collected data *and* the parameterized model are required. Several figures of merit were designed as quality indicators for the accomplishment of successful SCXRD studies. Usually, these quality indicators are mathematical equations designed to equate to a specific target value (like unity or zero) in idealized conditions. Likewise, a range of plotted graphs of certain variables is examined, which should not stray too much from their expected shape (e.g. a parabola or a straight line). While unusual values on their own do not invalidate an entire dataset or model, they should give cause to a thorough investigation of the area evaluated by the respective quality indicator. A prime example are the so-called

residuals or *R values*, which decrease with an increase in agreement between two sets of compared structure factors. While any sensible improvement in data or model quality should lead to an improvement of the respective *R* values, not a decrease of *R* values has to be caused by a meaningful improvement. Therefore, all criteria presented in the following are meant to serve as guidelines in need of additional interpretation.

2.5.1 Data Quality indicators

For routine structure datasets, the most basic examined figures of merit are the multiplicity and the completeness of the dataset. Over the whole range of integrated data, all reflections should clearly stand out from background noise, the dataset should be complete and with redundancy of at least 3 for the outermost reflections. Specifically, the innermost resolution shell should be as complete as possible, which can sometimes prove challenging due to problems with overexposure and limitations of the instrument setup. While minor exceptions to these guidelines are tolerable, they should be upheld for the significantly more challenging charge-density investigations. Furthermore, the internal agreement factor R_{int} for internal agreement between symmetry related reflections and the residual factor R_{sigma} of the standard deviations should be well below 0.05 for the innermost data, while values up to 0.2 for the outermost data are considered acceptable. In edge cases, a value of 0.25 might still be tolerated.

$$R_{int} = \frac{\sum_h \sum_i |F_{o,i}^2(hkl) - \langle F_o^2(hkl) \rangle|}{\sum_h F_o^2(hkl)} \quad (\text{Eq. 11})$$

$$R_{sigma} = \frac{\sum_h \sigma(F_o^2(hkl))}{\sum_h F_o^2(hkl)}$$

However, both R_{int} and R_{sigma} can be expected to increase for large multiplicities, which are expected to be high for high-resolution datasets for charge-density analyses (see Chapter 3). While the more standard residual still provide some useful information in this case, examination of the multiplicity independent residuals $R_{r.i.m.}$ and $R_{p.i.m.}$ is advised instead.^[46]

$$R_{r.i.m.} = \frac{\sum_h \left(\frac{N}{N-1}\right)^{1/2} \sum_i |F_o^2(hkl) - \langle F_o^2(hkl) \rangle|}{\sum_h F_o^2(hkl)} \quad (\text{Eq. 12})$$

$$R_{p.i.m.} = \frac{\sum_h \left(\frac{1}{N-1}\right)^{1/2} \sum_i |F_o^2(hkl) - \langle F_o^2(hkl) \rangle|}{\sum_h F_o^2(hkl)}$$

All these quality indicators can be generated for different resolution shells with the programs XPREP^[47] or SADABS,^[39] which were used during data reduction for all datasets worked on for this thesis.

2.5.2 Model Quality Indicators

The most prominent residuals for model refinement are crystallographic agreement factors, or R factors, between calculated and observed structure factors (Equation 13). While in the earlier days of x-ray structure analysis refinements were usually performed against the unaltered structure factors themselves due to computational limitation, today, a refinement against squared structure factors is generally superior and preferred.^[35] For standard structure refinements the $R_1(F^2)$ factor is used. For charge-density investigations, the more responsive weighted residual $wR_2(F^2)$ factor is used. The weight of each reflection is usually inversely proportional its estimated standard deviation σ . As the compared structure factors in the wR_2 are squared, at comparable model qualities, the latter value can be expected to be two to three times higher than the former, which then accentuate small errors in the data. The “Goodness of Fit” or “GoF” value assesses the quality of data scaling and should be close to unity for good scaling and a well refined model.^[48,49]

$$\begin{aligned}
 R_1(F) &= \frac{\sum_h ||F_o(hkl)| - |F_c(hkl)||}{\sum |F_o(hkl)|} & R_1(F^2) &= \frac{\sum_h |F_o^2(hkl) - F_c^2(hkl)|}{\sum |F_o^2(hkl)|} \\
 wR_2(F^2) &= \sqrt{\frac{\sum_h w(F_o^2(hkl) - F_c^2(hkl))^2}{\sum_h wF_o^2(hkl)^2}} & GoF &= \sqrt{\frac{\sum_h w(F_o^2(hkl) - F_c^2(hkl))^2}{N_{reflections} - N_{parameters}}}
 \end{aligned}
 \tag{Eq. 13}$$

Besides these residual values measuring the agreement between model and data, another way to evaluate model quality is residual density analysis. To obtain the residual density map after structure refinement, a Fourier transformation of the difference between the experimental structure factors F_o and the structure factors F_c calculated from the model is performed. A “flat and featureless” residual density map is generally considered a hallmark of a successful structure refinement (Figure 2-3): A low overall level of the residual densities without any structural motifs like singular high residual density peaks or holes shows that no systematic phenomena ignored by and a good general agreement between data and model has been achieved.^[27]

Besides a visual inspection of residual density in a molecular viewer of choice, a number of additional tools for residual density were introduced by Meindl and Henn in 2008.^[50] After each refinement, the gross number of residual electrons, the so-called e_{gross} value can be determined from the gross residual density.

$$\rho_{\text{gross}} = \frac{1}{2V} \int_V |\Delta\rho(\mathbf{r})| d^3\mathbf{r}
 \tag{Eq. 14}$$

$$e_{\text{gross}} = \rho_{\text{gross}} \cdot V
 \tag{Eq. 15}$$

A factor of $\frac{1}{2}$ is included to account for the fact that one misplaced electron will cause both a residual density hole in the spot it is missing as well as a peak in its falsely assigned position. For a perfect

agreement of F_o and F_c , both parameters should amount to zero, regardless of cell volume. Consequently, any meaningful improvement should lead to a decrease in e_{gross} , which makes it a good guideline for comparing different integrations, datasets or refinement stages.

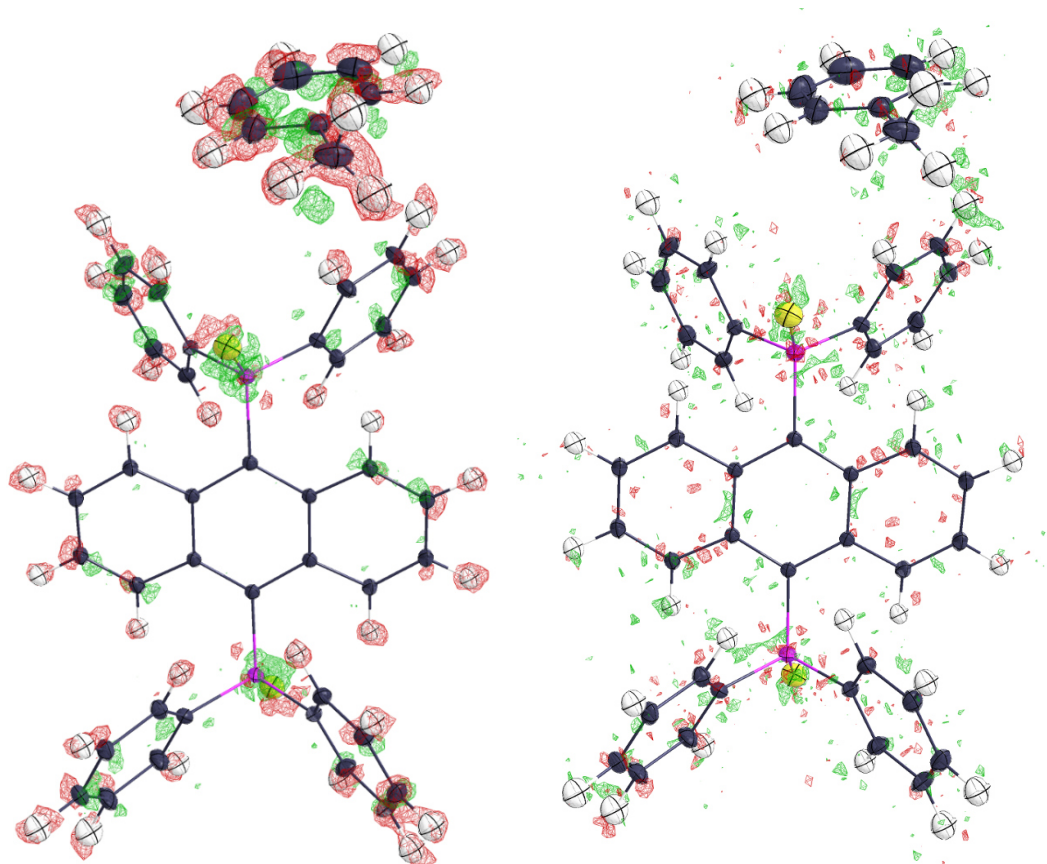


Figure 2-3: Examples for residual density maps. ADPs are depicted at 50 % probability level Left: Starting model multipole model refinement (see Chapter 3.1), directly obtained from a finished standard structure refinement. Several “features” are visible, such as residual ED concentrations around atomic positions. Isolevel for residual density: $\pm 1.1 \text{ \AA}^{-3}$. Right: Same structure after final refinement. Overall residual ED is greatly reduced, with remaining areas being randomly distributed: The residual density is now “flat and featureless”. Isolevel for residual density: $\pm 0.084 \text{ \AA}^{-3}$. Images are taken from the model structures used for Chapter 6^[51] and were originally created for my master thesis.^[33]

While the e_{gross} can be used to gauge the amount of residual density, it does not yield any information about residual density features. To gain this information, Henn and Meindl proposed plotting the residual against fractal dimension d^f ,^[52] which should result in a parabola-shaped graph with an intercept of around 3 for ideal data. In practice, even theoretical model never reached the optimal value, a value above 2.7 can be seen as indicator for excellent model quality. Contrary, a lower value of d^f or an asymmetrical shape is usually indicative of underlying problems in the model. A “shoulder” to the left or the right of the graph, in particular, is indicative of an excess of residual density holes or peaks, respectively.

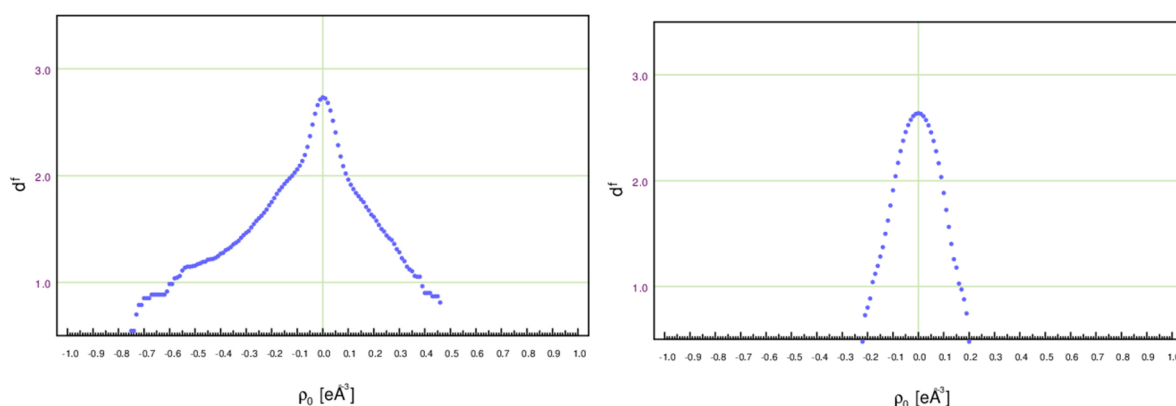


Figure 2-4: Examples for Henn-Meindl plots. Left: Poorly refined model, indicating a high amount of residual density, with an excess of negative residual density. Right: Well refined model. The parabola is symmetric and displays significantly less broadening for higher absolute values of ρ_0 . Images were reused from my master thesis.^[33]

A number of additional useful plots generally not inspected for standard measurements can be viewed in the program *DRKPlot* by Adam Stash.^[53] The resolution-dependent structure factor plot $\Sigma F_0^2 / \Sigma F_c^2$ should form a line for an ideal model.

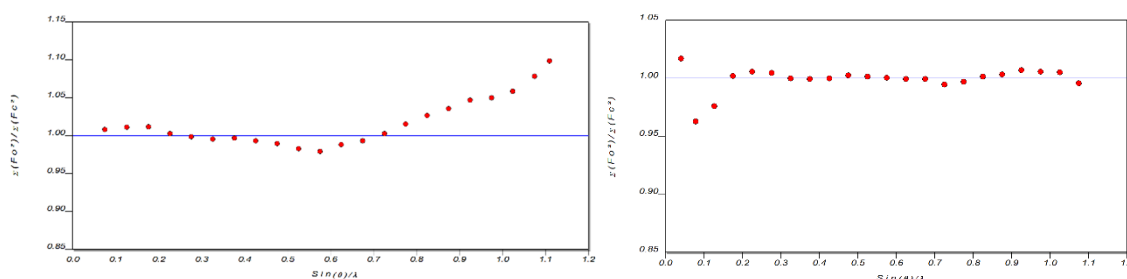


Figure 2-5: Examples for $\Sigma F_0^2 / \Sigma F_c^2$ plots generated with *DRKPlot*. Left: Steady increase of $\Sigma F_0^2 / \Sigma F_c^2$ for higher $\text{sin}(\theta)/\lambda$ indicates overestimation of the high order data. Right: No serious errors, all deviations from unity are within a ± 0.05 interval.

For good data, deviations from this optimal case should not surpass ± 0.02 , while deviations of more than ± 0.05 are considered a warning sign for resolution-dependent errors in the data.^[54] As the innermost shell contains only a small number of reflections, strong deviations in these regions of the structure factor plot can often be caused by limited number of outlier reflections, which were, for example, affected by the experimental setup. In this case, a strong deviation in the innermost resolution shell can be relatively easily resolved by omission of these erroneous reflections.

An additional tool for model evaluation, which is available in the *DRKPlot* program as well, is the Normal Probability Plot first proposed by Abrahams and Keve.^[55] An ordered statistic of the experimental $R(h)$ values (Equation 16) is plotted against the quantiles of the expected Gaussian distribution (Figure 2-6).

$$R(h) = \frac{F_o^2(h) - F_c^2(h)}{\sigma^2(h)} \quad (\text{Eq. 16})$$

For ideal data with well-determined standard deviations, the plot should be a straight line with a slope of one and an intercept of zero. A strong digression from this shape usually hints at problems in the data.

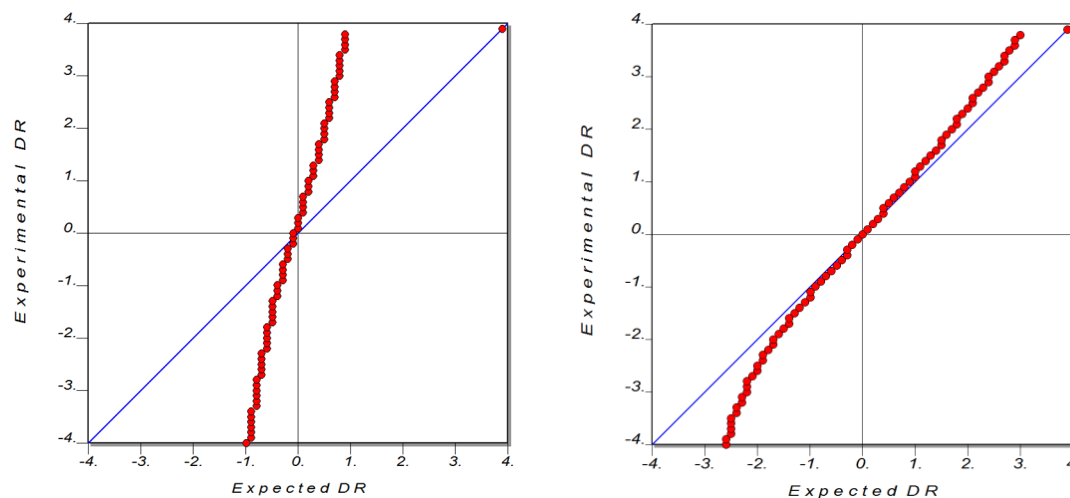


Figure 2-6: Examples of normal probability plots generated with *DRKplot*.^[53] Left: The slope of the plot severely higher than unity, indicating an underestimation of the standard deviation. Right: No serious errors in the standard deviation, indicating a well-adjusted error model.

2.6 The Independent Atom Model (IAM)

The *Independent Atom Model* (IAM) is the main way to describe structures during standard SCXRD investigations. Such routine experiments are usually interested in obtaining a three-dimensional model and the discussion of bond lengths and angles. In the IAM, atoms are assumed to be neutral, non-interactive and spherical, meaning electron density is only modelled as Gaussian distributed around the atomic positions, which coincide with maxima in the experimental $\rho(\mathbf{r})$ function. Each atom in the model is assigned three positional parameters x, y, z . Thermal vibrations are assumed to be harmonic and accounted for with

$$t_{0,hkl} = \exp(-2\pi^2 \mathbf{h}^T \mathbf{U} \mathbf{h}) \quad (\text{Eq. 17})$$

$$F_{hkl} = \sum_a f_{a,hkl} \cdot \exp(-2\pi^2 \mathbf{h}^T \mathbf{U} \mathbf{h}) \cdot \exp(2\pi i \mathbf{h}^T \mathbf{r})$$

wherein \mathbf{U} is a matrix that contains the six atomic mean square displacement parameters U_{ij} , $i, j \in \{1,2,3\}$ (also called Anisotropic Displacement Parameters, “ADPs”. Thus, every atom is assigned a total

of nine parameters. These parameters are then allowed to change in a least-squares refinement against $R_1(F^2)$ in order to reach the best possible agreement between observed and calculated structure factors. Today, IAM refinement for structure determination can generally be executed in a straightforward and streamlined manner. A structure without any complications can often be handled by modern crystallographic program tool without much need for user input. For the less complicated cases of the most common complications such as disorder or twinning, a set of helpful tools exists as well, like the DSR-Plugin by Daniel Kratzert^[56,57] or the automatic twin domain identification in the new APEX4 suite by Bruker. Even the trickier cases of these problem can, however, generally be described well enough by the skilled crystallographer to reach a valid final model with reasonably high precision of interatomic distances and a clear assignment of atom types, which is usually sufficient for routine structure investigations. As ED in interatomic space is generally not modelled in standard IAM refinements, a flawless final model should show residual density only in bonding regions.

2.7 Hirshfeld Atom Refinement

An alternative method for refining a starting model from X-ray data is Hirshfeld Atom Refinement (HAR).^[58] Unlike standard IAM refinement which relies on tabulated scattering factors, custom aspherical scattering factors are calculated specifically for the refined structure, using the assistance of quantum chemical calculations. The HAR process starts with a set of atomic coordinates taken from a standard IAM refinement, which is used to calculate a first electron density of the molecule from a quantum mechanical wave function. This ED is divided up into “stockholder” Hirshfeld atoms, meaning that the molecular ED at each point is distributed among the molecules. Like partners in a stockholders’ corporation, each atom partakes in local gain and loss of density in direct proportion to its “share” of the total molecule.^[59] The charges and moments of these atoms^[59] are used to create a simulated crystal field surrounding the molecule of interest. This “ED cycle” is repeated until convergence in the molecular energy is achieved. The Fourier transforms of the Hirshfeld atoms are then used as non-spherical scattering factors in a conventional least-squares refinement. The resulting model is then used as starting point for a new ED refinement cycle. The entire process is repeated until both the ED cycles and the least squares refinement have converged. The main advantage of HAR compared to conventional IAM refinement its ability to provide bonding distances including hydrogen atoms that are on par with those derived from “gold standard” neutron diffraction experiments.^[60,61] While refinement of anisotropic thermal displacement parameters was shown to improve the accuracy of said distances, it regularly lead to unreasonable ADP shapes for several hydrogen atoms.^[62,63] However, as the method is rapidly expanded and developed, more and more accurate H-ADP description have been reported.^[64–66] This improvement of H-ADPs from the latest HAR developments will be discussed in more detail in the H-ADP comparison study presented in Chapter 6. Furthermore, the aspherical scattering factors allow for the modelling of ED even in bonding regions, thereby eliminating the systematically remaining residual density there compared to IAM refinements. Thus, HAR might prove beneficial to the refinement of pathological disordered structures, using the additional information gained from the tailor-made

structure factors to better deconvolute ED contribution from different disordered components.^[67] In this work, the method was used in a similar fashion to better identify disorder in an aluminium dihydride BOX complex, which can be found in Chapter 4.

3 Experimental charge-density investigations

After the base principles of SCXRD were explained in Chapter 2, this chapter will focus on the theory behind the central method of this work: Experimental charge-density studies based on high-resolution SCXRD datasets. First off, the used ED model will be presented, as well as a number of procedures and challenges specific to this method. Then, the topological analysis of the final model and the determination of structural properties will be elucidated. Several graphics as well as certain passages of text within this part were reused or only slightly altered from the theoretical background chapter of my master thesis on the same scientific field.^[33]

3.1 The Hansen & Coppens Multiple Model (MM)

Experimental charge-density investigations strive to model and discuss ED even in interatomic regions in order to determine and discuss a range of structural properties unavailable from IAM models. To achieve this goal, a more sophisticated model of atomic ED is required. Several models for describing ED in intermolecular space have been developed, the most prominent one of which being the *Hansen and Coppens Multipole Model* (MM) published in 1978.^[24] In the MM, atoms are no longer by default assumed to be spherical and neutral. The total atomic ED $\rho_a(\mathbf{r})$ is divided into three components: the spherical core density $\rho_c(\mathbf{r})$, the spherical valence density $\rho_v(\kappa\mathbf{r})$ and the aspherical valence density $\rho_d(\kappa'\mathbf{r})$.^[68]

$$\rho_a(\mathbf{r}) = P_c\rho_c(\mathbf{r}) + P_v\kappa^3\rho_v(\kappa\mathbf{r}) + \rho_d(\kappa'\mathbf{r})$$

$$\text{with } \rho_d(\kappa'\mathbf{r}) = \sum_{l=0}^{l \max} \kappa'^3 R_l(\kappa'\mathbf{r}) \sum_{m=-l}^l P_{lm} d_{lm}(\theta, \Phi) \quad (\text{Eq. 18})$$

The parameters P_c , P_v and P_{lm} describe the population of the core and valence density respectively. The parameters κ and κ' are linear scale factors allowing for expansion or contraction of the valence shell. Core and valence densities are calculated from Hartree-Fock atomic wavefunctions expanded in terms of Slater-type basis functions. The radial functions of the aspherical part are usually single-zeta Slater-type functions, however other choices are possible (see below). The aspherical part of ρ_d is described with spherical harmonics d_{lm} , the so-called *multipoles*, which are the only parameters eventually used to calculate structural properties. Usually, multipole parameters are refined up to hexadecapole level, which would amount to up to 25 parameters per atom in the unit cell, plus two additional kappa parameters per atom type in the refinement. To reduce the number of refined parameters and increase refinement stability, only those parameters in agreement with local symmetry are refined for every atom.

Furthermore, chemical constraints are refined for atoms in similar chemical surroundings, meaning that these atoms are assigned identical multipole parameters. Both of these restrictions require the definition of a local atomic coordinate system and can be incrementally released over the course of a refinement. Multipole model refinements for this thesis were performed using the *XD2016* suite (in short: XD).^[69] Namely, the module *XDINI* was used for starting model generation from standard IAM refinements in *SHELXL*^[70] using the *ShelXle* GUI.^[71] *XDLSM* was used to perform MM refinements against F^2 . The standard starting MM refinement strategy for this work can be found in Table 3-1 below. If needed, this starting point was then expanded with additional steps to account for different phenomena that will be explained in the rest of this chapter. Finally, *XDPROP* was used to obtain various structural properties from a final MM model, as explained in more detail in Chapter 3.3. Various visual representation of *XDPROP* output like topological maps were generated with *XDGRAPH*.

Table 3-1: Starting refinement strategy for MM refinements in this work. At the start of the refinement process, only reflections with $I/\sigma > 3$ are taken into account for model refinement (“sigobs 3”). SCALE is an overall scaling factor refined in every step. In the first step, only SCALE is refined. Then, parameters are added in a stepwise process to ensure refinement stability. In case of a refinement against theoretical structure factors, atomic coordinates and M: Monopoles, D: Dipoles, Q: Quadrupoles, O: Octupoles, H: Hexadecapoles. Uij: Anisotropic displacement parameters of heavy atoms- xyz: Coordinates of heavy atoms, κ, κ' : Valence density expansion parameters. In step 7, an unconstrained refinement of only hydrogen atom positions is conducted against data with $\sin \theta/\lambda < 0.5$ is conducted. In step 11, the “sigobs 3” limitation is lifted and the model is refined against all data.

Step	Refined parameters (new)
1	SCALE
2	M
3	M DQOH
4	M DQOH Uij
5	M DQOH Uij xyz
6	M DQOH Uij xyz κ
7	Hxyz
8	M DQOH Uij xyz κ
9	κ'
10	M DQOH Uij xyz κ
14	Sigobs 0

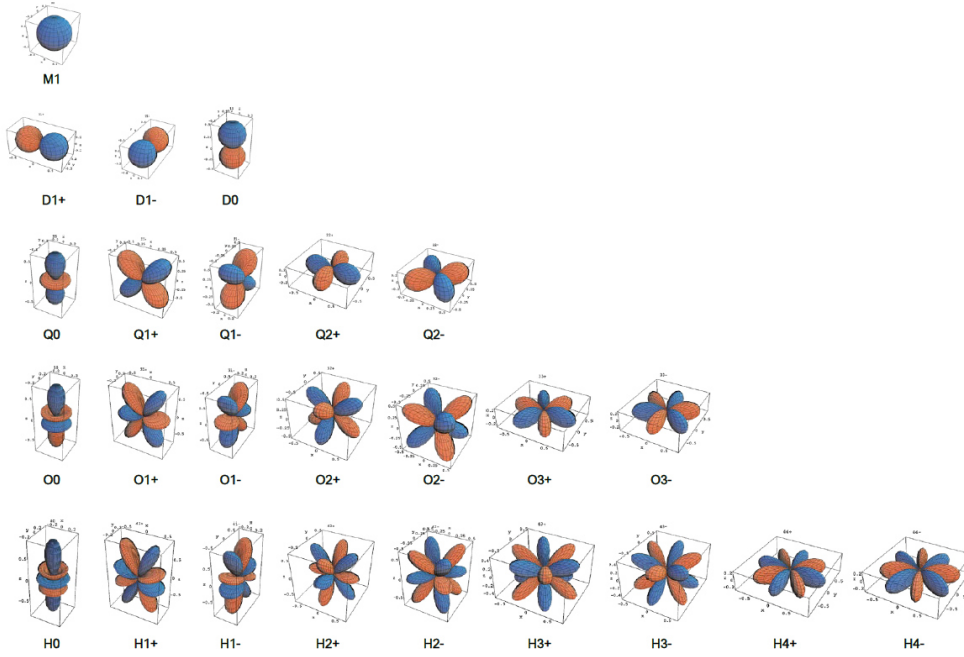


Figure 3-1: Multipole spherical harmonics of monopole (M), dipole (D), quadrupole (Q), octupole (O) and hexadecapole level (H).^[24] Positive areas are displayed in blue, while negative areas are displayed in red.

3.1.1 Refinement of anharmonic motion

With the more detailed ED description of the MM, previously negligible effects in the ED become visible. While the thermal vibrations of atoms in the IAM are assumed to be harmonic in nature, signs of anharmonic motion can be found in MM refinements in form of “shashlik shape” residual density around certain atoms (Figure 3-2).^[72] A common method to describe anharmonic vibration is the so-called *Gram-Charlier expansion* introduced by Johnson and Levy. Here, additional terms are used in the temperature factor to account for the anharmonicity beyond a harmonic part.^[73]

$$t_{hkl} = \left(1 - \frac{4}{3}\pi^3 i C_{jkl} h_j h_k h_l + \frac{2}{3}\pi^4 C_{jklm} h_j h_k h_l h_m + \dots \right) \cdot t_{0,hkl} \quad (\text{Eq. 19})$$

Here, $C_{jkl\dots}$ are the Gram-Charlier coefficients (GCCs) of order corresponding their number of indices. Gram-Charlier expansion introduces a relatively large number of parameters per atoms, which usually cannot be feasibly reduced with constraints. Furthermore, the prospective information gain of a newly introduced GCCs is dependent on the mean-square displacement ($\langle x^2 \rangle$) of the respective atoms and the resolution of the diffraction experiment. At a certain point, introducing new anharmonic motion parameters do not contribute any meaningful information not already provided existing ones. A general rule for estimating the required minimum data resolution Q_n for introduction of GCCs of n^{th} order was proposed by Kuhs in 1992, wherein ($\langle x^2 \rangle$) is the mean square displacement of the atom of interest:^[74]

$$Q_n = 2n^{1/2} (2\pi)^{-1/2} (2 \ln 2)^{1/2} \langle x^2 \rangle \quad (\text{Eq. 20})$$

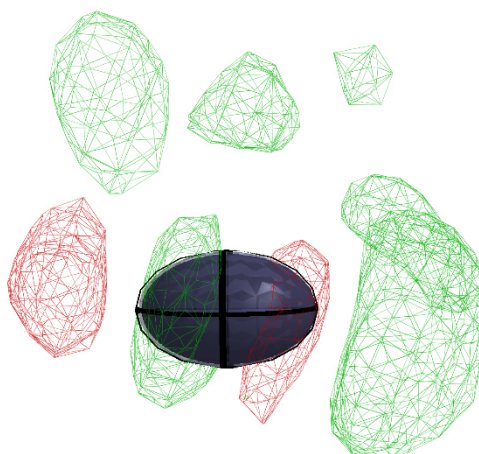


Figure 3-2: Alternating positive and negative residual density in a “shashlik-like” pattern near an atomic position is a sign for anharmonic motion.

Usually, Gram-Charlier expansion is not performed beyond the 4th order, introducing ten 3rd order GCCs (skewness coefficients) and fifteen 4th GCCs (kurtosis coefficients). It should be noted, that the GCCs by themselves carry no physical meaning. Instead, they can help to better deconvolute thermal vibration from aspherical ED and therefore provide more accurate multipole parameters. As such, they should be carefully investigated for consistency and validity: Refined GCCs should be largely significant with values larger than 3σ , not strongly correlated with multipole parameters and should not lead to atomic displacement probability functions with large negative regions, which is not only prohibited by their mathematical definition but also results in unphysical negative probabilities for certain displacements.

3.1.2 Anisotropic hydrogen atoms and the Hirshfeld test

In the IAM, hydrogen atoms are refined with positions based on a riding model and isotropic thermal vibration parameters amounting to 1.2 or 1.5 times the ADPs of the bonded heavier atom. In a baseline MM refinement, this is handled in a similar fashion. However, to enhance model quality, one can elect to employ ADPs for hydrogen atoms as well. This can, however, be challenging, as X-rays are diffracted at the electrons within a crystal. Therefore, hydrogen atoms which possess only one electron are “less visible” to SCXRD studies than the heavier atoms. To approach this problem, one can resort to neutron diffraction experiments in large scale facilities, a number of approximation methods based on tabulated data like the *SHADE* server^[75] or *APD-Toolkit*,^[76] or nevertheless perform a refinement of hydrogen ADPs against the collected high-resolution SCXRD data. This matter, and specifically, the viability of the various approximation methods is explained and discussed in great detail in Chapter 6. To investigate the quality of approximate ADPs, one useful criterion is the so-called *Hirshfeld* or *DMSDA test*, from “difference of mean-square displacement amplitudes”. According the concept of rigid bodies proposed by Hirshfeld in 1976,^[77] the mean-square displacement amplitudes of a pair of bonded atoms of similar weight should be equal in bond direction. Let $z_{A,B}^2$ be the mean-square displacement of an atom *A* in the direction of a bonded atom *B* and vice versa. In this case, the difference

$$\Delta_{A,B} = z_{A,B}^2 - z_{B,A}^2 \quad (\text{Eq. 21})$$

should be close to zero. However, even in the case of different molecular weights, like for a heavy atom bonded to a hydrogen atom (a “X-H bond”), DMSDA values for atoms in similar chemical surroundings should be similar, and the hydrogen atom should always be the one with stronger vibrations. Therefore, large differences between similar X-H bonds that should have similar DMSDAs or negative $\Delta_{H,X}$ values are a sign for problems with the used approximation.

3.2 Experimental requirements and specific challenges

As previously elaborated, MM refinements elaborate a vastly increased number of parameters compared to the IAM to describe more minute structural details like bond characters or orbital populations. Thus, requirements for data quality and completeness are substantially higher than for routine investigations, to enhance model convergence and avoid overfitting. Diffraction data has to be collected to a very high resolution of $\sin(\theta)/\lambda \approx 1.0 \text{ \AA}^{-1} / d \approx 0.50 \text{ \AA}$ to ensure a satisfactory data-to-parameter ratio. For comparison, a maximum resolution of $\sin(\theta)/\lambda \approx 0.6 \text{ \AA}^{-1} / d \approx 0.8 \text{ \AA}$ is regarded sufficient for standard IAM refinements. Both high order and low order data are equally important: High-order reflections (e.g. $\sin(\theta)/\lambda > 0.7 \text{ \AA}^{-1}$) allow for better deconvolution of core electrons, and therefore, of atomic positions and thermal motion. Only low-order data, on the other hand, contain information about density in bonding regions as diffuse bonding electrons only scatter at low angles. For the model refinement process, the number of parameters should be increased incrementally to improve convergence and avoid unphysical correlations between parameters. For the same reason, the aspherical ED expansion parameter κ' should not be refined simultaneously with the multipole parameters it directly affects. As another difference to IAM refinement, many systematic problems easily resolvable in IAM investigation prove more troublesome in charge-density analysis and are generally avoided wherever possible. Disordered structures come with a wide range of problems for charge-density investigations, first and foremost that many of the structural properties can often not be unambiguously determined for the disordered parts. A more in-depth discussion of the possibilities of disorder refinement on the basis of structures investigated by me will be provided in Chapter 4. Moreover, the treatment of hydrogen atoms in charge-density investigations will be dealt with in great detail in my investigation of the topic in Chapter 6.

3.2.1 Overfitting and cross-validation

Due to the large number of parameters potentially added in a MM refinement, one should ensure that all refined parameters actually carry physical meaning. If additional parameters merely improve the fit of random errors in the data, they can be expected to improve a variety of generally inspected quality indicators without actually contributing to the knowledge derivable from the resulting model. As a rule of thumb to avoid overfitting, a data-to-parameter ratio of at least 1:10 should be achieved in any model refinement. This ratio can however be deceptive, as different resolution shells of the data have different influences on the model, and it is quite possible to never fall below the 1:10 ratio for the entire dataset but still overfit the innermost data. The check for overfitting, a Python script by Krause *et al.*^[78] is employed, which divides the entire used dataset into 20 subsets. 95% of the data (the work set) are then used for the refinement, while the remaining 5% (the training set) are then used to determine quality indicators. Each set is then used once as training set, and the cross-validation residual value R_{cross} is determined, which takes into account the difference between F_o and F_c for all reflections as training reflections.

$$R_{\text{cross}} = \frac{\sum |F_o^2 - F_c^2|}{\sum F_o^2} \quad (\text{Eq. 22})$$

Any meaningful addition of parameters should then lead to an improvement in both the mean residual value of the work sets $\langle R_{\text{work}} \rangle$ as well as the R_{free} value. Contrary development of these quality indicators, specifically a decrease in $\langle R_{\text{work}} \rangle$ paired with increase in R_{free} can be seen as a sign for overfitting. A sample output for the script by Krause *et al.* is displayed below (Figure 3-3).

Every time new parameters beyond the starting refinement strategy were added, a cross-validation check for overfitting was conducted to ensure their addition leads to a valid model improvement. This includes, for example, the release of chemical constraints or the lowering of assumed local symmetry in certain atoms.

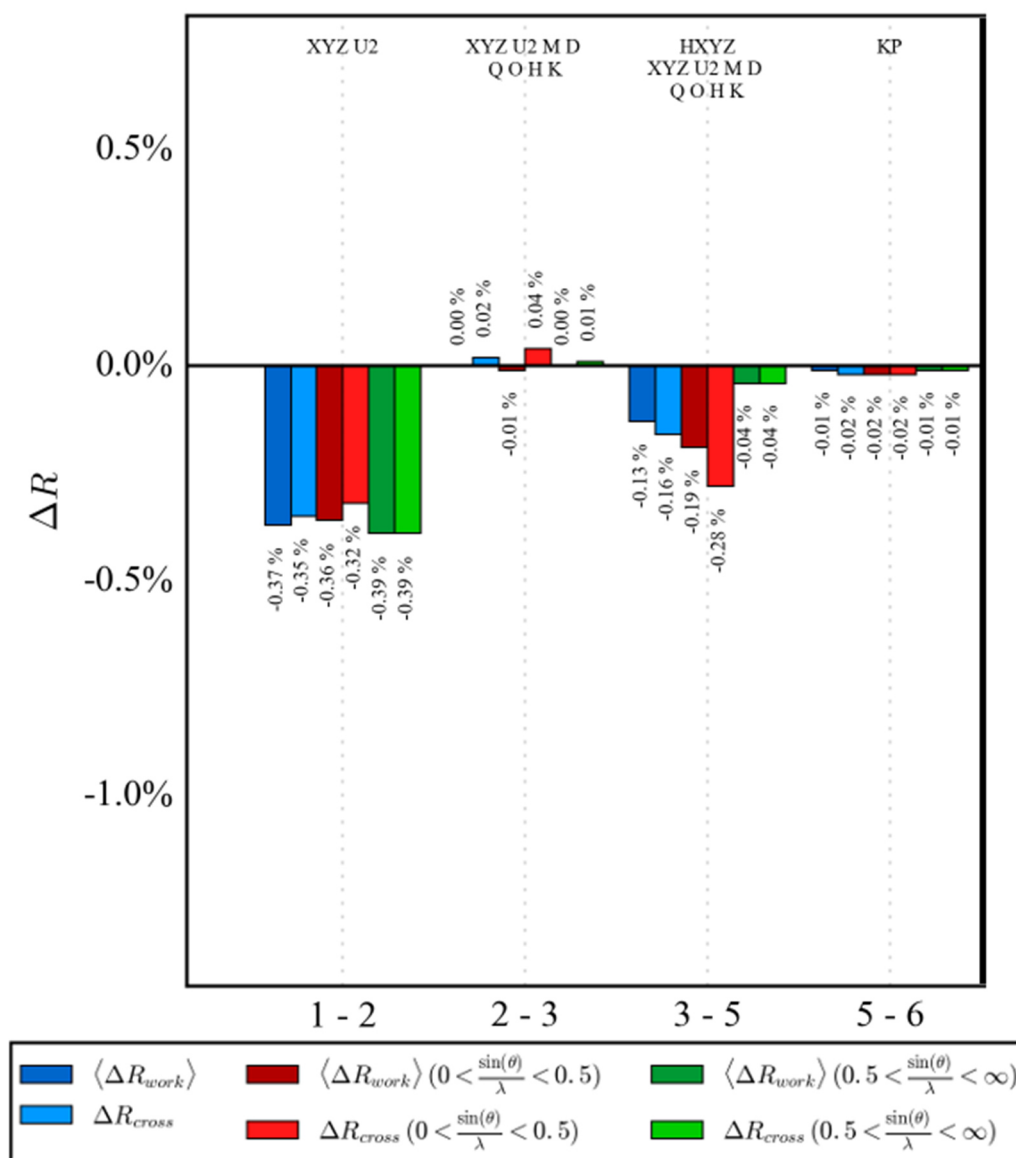


Figure 3-3: Example output plot of the script by Krause *et al.*^[78] Only refinement steps that improve both R_{work} and R_{cross} are chemically sound. In step 3, R_{cross} worsens, while the R_{work} slightly improves. This is a sign for overfitting. Image was reused from my master thesis.^[33]

3.2.2 Thermal Diffuse Scattering and other resolution-dependent errors

A foundational assumption of X-ray crystal structure analysis is that the intensities measured in SCXRD experiments are proportional in the structure factors. This is, however, only true if inelastic scattering is neglected. The most relevant component of inelastic scattering is the so-called *thermal diffuse scattering* (TDS),^[79] which is caused by the exchange of at least one photon with the crystal. While there are other sources of inelastic scattering in XRD experiments, for the sake of this explanation, they will be summarised under the umbrella term “TDS”. The actual measured intensities in a diffraction experiment with respect to TDS can be described by a Bragg intensity plus the additional TDS contribution

$$\begin{aligned} I_{\text{meas}} &= I_{\text{Bragg}} + I_{\text{TDS}} \\ &= I_{\text{Bragg}} \cdot (1 + \alpha) \end{aligned} \tag{Eq. 23}$$

The effects of TDS increase with resolution and can therefore not be ignored in data for charge-density investigations, which rely on high-resolution diffraction data for accurate deconvolution of thermal motion. The presence of TDS contamination in the outer data can usually be detected through a U-shaped structure factor plot within the *DRKPlot* program (see Chapter 2.5).^[53] Another indication of resolution-dependent errors in the data can be the presence of high residual ED around heavier atoms in the structure, such as the central metal ions of organometallic complexes. Two main correction methods for TDS in the data are known. In 2015, an empirical correction method for TDS was published by Niepötter *et al.*,^[80] in which a Python script tries to approximate the TDS term α with the polynomial term

$$\alpha = a \cdot \left(\frac{\sin(\theta)}{\lambda}\right)^2 + b \cdot \left(\frac{\sin(\theta)}{\lambda}\right)^3; a, b \in \mathbb{R} \tag{Eq. 24}$$

proposed by Stash and Zavodnik in 1995.^[81] For several compounds examined in this work, some form of resolution dependent errors hinting at TDS contamination were detected. While the script by Niepötter *et al.* was tested for all structures investigated for this thesis, it often terminated with convergence problems and did not surpass the second usual approach of excluding TDS contamination during the integration process. As the TDS intensities overlapping the Bragg intensities have a broader shape, it is possible to partially exclude them by using an integration box with fixed size (Figure 3-4). The optimal box size has to be identified based on experience and trial and error, which usually is more time consuming than the scripted empirical correction. While TDS contamination cannot be fully circumvented this way, omitting the majority of intensities primarily caused by TDS usually results in a noticeable increase in model quality. The most extensive testing of integration with fixed box size was performed on the first dataset for MnMeBOX (6), which was the first relevant dataset for this work without any systematic problems such as disorder (Chapter 4) or complications during the measurement (Chapter 5.3). The insights gained during this process turned out to be more or less generally applicable

to the other datasets collected for this work. As a general rule, all incidents of suspected TDS contamination in high-resolution datasets could be straightforwardly remedied by integration with a fixed box size of or close to 0.6, 0.6, 0.8 (see Chapter 10.4.2).

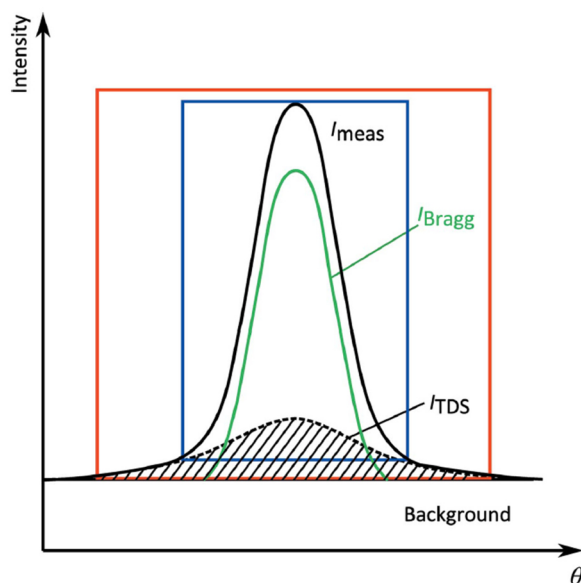


Figure 3-4: Schematic depiction of TDS on the measured intensities I_{meas} and the integration boxes used by SAINT. With the red integration box, the TDS errors are included in the integrated intensities. The smaller blue box omits a large portion of the errors. The background is corrected for in the data integration process. Image reused with permission by the International Union for Crystallography.^[80]

3.3 Quantum Theory of Atoms in Molecules (QTAIM)

Once a final model is obtained, a closer investigation of the modelled density can be performed by examining the static deformation density $\Delta\rho_{\text{static}}$, which is the difference between the density derived from the MM and the one taken from the IAM. This way, the contribution of the modelled aspherical ED can be clearly seen, which is normally dominated and eclipsed by the core ED.

$$\Delta\rho_{\text{static}}(\mathbf{r}) = \Delta\rho_{\text{MM}}(\mathbf{r}) - \Delta\rho_{\text{IAM}}(\mathbf{r}) \quad (\text{Eq. 25})$$

For a sound model, the deformation density should be found around the bonds and in other regions where electrons like lone pairs can be expected to be found. Beyond a visual inspection of the deformation density, an even more precise way of investigating chemical concepts based on modelled charge-density is the Quantum Theory of Atoms In Molecules (QTAIM) by Richard Bader.^[25] Bader demonstrated that a many-electron system can be partitioned into open quantum subsystems, the namesake atoms in molecules (AIM). By examining the ED distribution of two neighbouring atoms in the interatomic space between them, the bonding situation between these atoms can be analysed (Table 3-2). Each AIM can be defined by examining the gradient vector field of the ED function $\rho(\mathbf{r})$ (Figure 3-5, Figure 3-6).

$$\nabla\rho(\mathbf{r}) = \left(\frac{\partial\rho}{\partial x}, \frac{\partial\rho}{\partial y}, \frac{\partial\rho}{\partial z} \right)^T \quad (\text{Eq. 26})$$

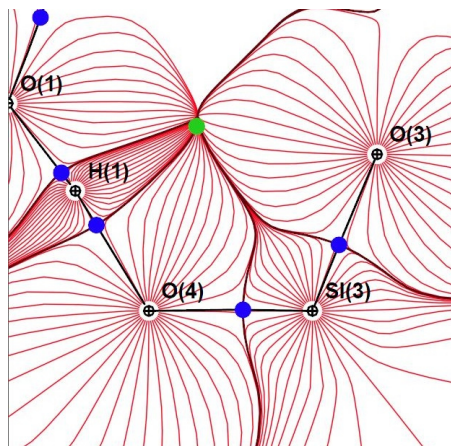


Figure 3-5: Sample trajectory plot. Trajectories drawn in red originate from atomic positions and follow the path of greatest ED descent, ending on the so-called *zero-flux surfaces* separating the different atomic basins according to QTAIM. Atomic positions are interconnected by bond paths, with end on a bond-critical point displayed as blue dot located on the zero-flux surfaces. A ring critical point displayed as green dot is situated in the middle of circular-shaped bond critical points.

Table 3-2: Classification of critical points, with m being the number of nonzero eigenvalues λ_i and n being the algebraic sum of the signs of λ_i .^[27]

(m, n)	Topology in $\rho(r)$	Type
(3, -3)	local maximum	nuclear position
(3, -1)	maximum in two directions minimum in one direction	bond critical point (BCP)
(3, +1)	maximum in one directions minimum in two directions	ring critical point (RCP)
(3, +3)	local minimum	Cage-critical point (CCP)

Each gradient vector is perpendicular to the topological contour lines of $\rho(\mathbf{r})$. Starting from the maximum ED within an AIM, they follow the path of greatest descent towards its outer boundaries. A gradient path that connects a saddle point with exactly two maxima of the ED is called *bond path*. Two atoms connected by a bond path can be considered bonded, however, the bond path itself is not equivalent to a chemical bond. Each AIM is surrounded by so-called *zero flux surfaces* S , which are never crossed by gradient vectors.

$$\nabla\rho(\mathbf{r}) \cdot \mathbf{n}(\mathbf{r}) = 0, \forall \mathbf{r} \in S, \mathbf{n}(\mathbf{r}) \perp S \quad (\text{Eq. 27})$$

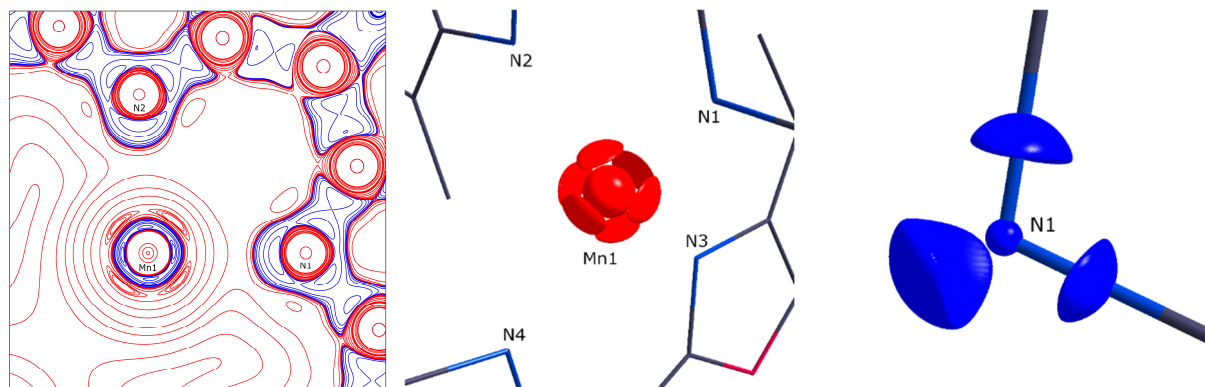


Figure 3-6: Examples for two-dimensional contour map (left) and three-dimensional iso-surface (middle and right) visualisation of the Laplacian. Red “clouds” indicate depletions in the ED, known as valence shell charge depletions (VSCDs). Blue clouds indicate concentrations in the ED, known as valence shell charge concentrations (VSCCs). Analysing the orientations of VSCDs and VSCCs towards each other is a useful tool for bond analysis. All examples are taken from Chapter 0.

According to Bader’s theory, the properties of a molecule can therefore be described as the sum of its atoms. The integrated charge of an atomic basin is called the *Bader charge* of the respective atom. All integrated charges of an examined fragment have to add up its total charge for the obtained charges to be meaningful.

3.3.1 Critical Points

Extrema in the ED function hold information about various properties about the ED distribution of the examined compound and are called *critical points* (CPs), which are determined from the second derivative of the ED function, the *Hessian Matrix* $H(\mathbf{r})$. The diagonalized Hessian Matrix $D(\mathbf{r})$, which can be obtained via the principle axis theorem, provides the three eigenvalues $\lambda_1, \lambda_2, \lambda_3$ (with $\lambda_1 < \lambda_2 < \lambda_3$).

$$H(\mathbf{r}) = \begin{pmatrix} \frac{\partial^2 \rho}{\partial x^2} & \frac{\partial^2 \rho}{\partial x \partial y} & \frac{\partial^2 \rho}{\partial x \partial z} \\ \frac{\partial^2 \rho}{\partial y \partial x} & \frac{\partial^2 \rho}{\partial y^2} & \frac{\partial^2 \rho}{\partial y \partial z} \\ \frac{\partial^2 \rho}{\partial z \partial x} & \frac{\partial^2 \rho}{\partial z \partial y} & \frac{\partial^2 \rho}{\partial z^2} \end{pmatrix} \quad D(\mathbf{r}) = \begin{pmatrix} \frac{\partial^2 \rho}{\partial x'^2} & 0 & 0 \\ 0 & \frac{\partial^2 \rho}{\partial y'^2} & 0 \\ 0 & 0 & \frac{\partial^2 \rho}{\partial z'^2} \end{pmatrix} = \begin{pmatrix} \lambda_1 & 0 & 0 \\ 0 & \lambda_2 & 0 \\ 0 & 0 & \lambda_3 \end{pmatrix} \quad (\text{Eq. 28})$$

The eigenvalues of the Hessian matrix are indicative of the curvature of $\rho(\mathbf{r})$ at the point \mathbf{r} and are used to differentiate four types of CPs, depending on the number of nonzero eigenvalues m and the algebraic sum n of the signs of the eigenvalues.^[27] To follow the mathematical rules of topology, the total number of critical points determined in topological analysis the so-called *Hopf-Poincaré* (HP) rule^[48]

$$n_{\text{Atoms}} - n_{\text{BCPs}} + n_{\text{RCPs}} - n_{\text{CCPs}} = 1 \quad (\text{Eq. 29})$$

has to be fulfilled, and all expected critical points should be found.

3.3.2 Bond Characterisation

Additional information can be obtained from the eigenvalues of $D(\mathbf{r})$. In order to accentuate minute features in the ED, derivatives of the experimental ED function are examined as well. The Laplacian $\nabla^2\rho(\mathbf{r})$ obtained from the trace of the second derivative of the electron density function is investigated to characterize bonding characteristics.

$$\nabla^2\rho(\mathbf{r}) = \text{tr}(D(\mathbf{r})) = \frac{\partial^2\rho}{\partial x'^2} + \frac{\partial^2\rho}{\partial y'^2} + \frac{\partial^2\rho}{\partial z'^2} = \lambda_1 + \lambda_2 + \lambda_3 \quad (\text{Eq. 30})$$

The Laplacian at a BCP can be used to characterize a bond. Values of $\nabla^2\rho(\mathbf{r}) > 0$ indicate so-called *Valence Shell Charge Depletion* (VSCDs), and therefore, an ionic closed-shell interaction. On the contrary, $\nabla^2\rho(\mathbf{r}) < 0$ indicates a charge concentration at the BCPs and is a sign for a covalent, shared-shell interaction. Concentrations of ED in non-bonding regions, on the other hand, are also called *Valence Shell Charge Concentrations* (VSCCs) and can give insight into atomic interaction other than the classical chemical bond.

A finer differentiation of bond character can be made with the $|V_{\text{CP}}|/G_{\text{CP}}$ descriptor proposed by Espinosa *et al.*,^[82] as expansion to the work of Cremer and Kraka.^[83] Herein, G_{CP} is the kinetic energy density, which can be obtained from the approximation by Abramov.^[84] From this, the potential energy density V_{CP} can be determined by applying the local virial theorem (Equation 31).^[85]

$$G(\mathbf{r}_{\text{CP}}) = \frac{3}{10}(3\pi^2)^{2/3}\rho^{5/3}(\mathbf{r}_{\text{CP}}) + \frac{1}{6}\nabla^2\rho(\mathbf{r}_{\text{CP}})$$

$$V(\mathbf{r}_{\text{CP}}) = \frac{\hbar}{4m}\nabla^2\rho(\mathbf{r}_{\text{CP}}) - 2G(\mathbf{r}_{\text{CP}}) \quad (\text{Eq. 31})$$

$$H(\mathbf{r}_{\text{CP}}) = G(\mathbf{r}_{\text{CP}}) + V(\mathbf{r}_{\text{CP}})$$

According to Espinosa *et al.*, a total energy density $H(\mathbf{r}_{\text{CP}}) < 0$ while $1 < |V_{\text{CP}}|/G_{\text{CP}} < 2$ is indicative of a mixed interaction with both closed-shell and open shell character.

Another useful bond descriptor available from the eigenvalues of $D(\mathbf{r})$ is the ellipticity ε , based on the quotient of the two negative eigenvalues at a BCP. The eigenvectors of these eigenvalues are perpendicular to the bond path.^[86]

$$\varepsilon = \frac{|\lambda_1|}{|\lambda_2|} - 1 \quad (\text{Eq. 32})$$

The ellipticity at a BCP can be used to gauge the deviation of the respective bond from cylindrical shape. An ideal single bond (σ -bond) has perfect rotational symmetry. Accordingly, in this case, ε is equal to zero. If the absolute value of ellipticity is significantly different from zero, this is indicative of limited rotational symmetry of the bond, which could be a sign of π -character in the bond.

3.3.3 Source function investigations

Introduced in 1998 by Bader and Gatti,^[87] the Source Function is a mathematical descriptor designed to express electron density at a reference point \mathbf{r} in terms of a *local source* $LS(\mathbf{r}, \mathbf{r}')$, which encompasses contributions from all other points \mathbf{r}' within the structure:

$$\rho(\mathbf{r}) = \int LS(\mathbf{r}, \mathbf{r}') \cdot d\mathbf{r}' \quad (\text{Eq. 33})$$

Herein, LS is defined as

$$LS(\mathbf{r}, \mathbf{r}') = -(4\pi \cdot |\mathbf{r} - \mathbf{r}'|)^{-1} \cdot \nabla^2 \rho(\mathbf{r}') \quad (\text{Eq. 34})$$

in which $-(4\pi \cdot |\mathbf{r} - \mathbf{r}'|)^{-1}$ is basically a Green's function, representing the influence of a cause $\nabla^2 \rho(\mathbf{r}')$ – the Laplacian of the electron density at a point \mathbf{r}' – on an effect, here, the electron density $\rho(\mathbf{r})$ at a reference point \mathbf{r} . If the local source is integrated over atomic basins according to QTAIM theory, the so-called *Source Function* for the respective basins is obtained. The electron density at the reference point can be written as a sum $S(\mathbf{r}; \Omega)$ of contributions from the basins Ω of individual atoms or a group of atoms in the structure. Therefore, the electron density at a point \mathbf{r} can then be written as the sum of the contribution of the atomic basin the respective point lies in, and the contributions from all other basins.

$$\rho(\mathbf{r}) = S(\mathbf{r}, \Omega) + \sum_{\Omega' \neq \Omega} S(\mathbf{r}, \Omega') \quad (\text{Eq. 35})$$

This descriptor can be used to quantify charge delocalisation within a structure, for example, in an aromatic or heteroaromatic system.

4 Investigation of a disordered Aluminium dihydride-BOX complex: A new approach to modelling molecular disorder?

During my investigation of aluminium dihydride BOX complexes, I encountered problematic disorder in two structures (Figure 4-1). While a disordered solvent molecule in **6** was determined to be the cause for insufficient maximum resolution during the SCXRD data collection (more details in Chapter 8.1), a dataset of sufficient quality could be collected for **5** (AlH₂MeBOX, short “AlH2” in this chapter). However, it turned out during early MM refinement that both molecules in the unit cell are affected by a small molecular disorder of below 5%. The unavailability of certain crystallographic analytical methods due to structural complications in a compound of interest is a common problem in SCXRD investigations.^[88] In this study, my goal was to investigate the extent to which an accurate modelling of the molecular disorder in AlH₂ is possible, with the goal of performing a meaningful topological analysis of the resulting model based on QTAIM. In so doing, a new method for modelling this kind of small-scale molecular disorder in charge-density refinement akin to the well-known *PLATON SQUEEZE* correction for disordered solvent was developed. It was then applied to AlH₂, as well as two additional model compounds for verification of the results. The results of this investigation will be summarized in this chapter.

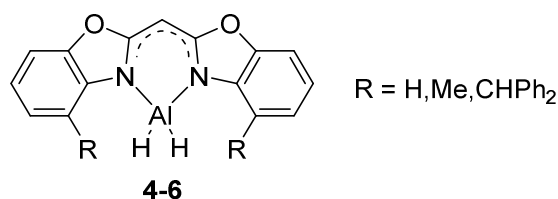


Figure 4-1: BOX-based alanes within the scope of this thesis. High-resolution measurements of **5** and **6** was attempted. The required maximum resolution of 0.5 Å could only be reached for **5**.

First, a brief introduction about the refinement of disordered structures in IAM and MM refinements will be given in 4.1. Used datasets will be examined in 4.2. Thoughts on the MM refinement strategy, as well as the both used disorder correction methods employed will be presented in 4.3. Results from the AlH₂ structure are summarized in 4.4, while 4.5 deals with the other used model compounds and a comparison of the tested disorder methods for all structures. Concluding remarks are provided in 4.6.

4.1 Disordered structures in charge-density analysis

On a base level, the occurrence of disorder in SCXRD studies can be explained by an averaging of obtainable structural information over the entire measuring time, as well as over the entirety of a real, non-ideal crystal. If, for example, a methyl group in a ligand is oriented in a certain way A in 85% of all unit cells, and in another way B in the remaining 15%, the derivable structure factors from experimental Bragg intensities contain averaged structural information from both unit cell variants A and B. When condensed into a single unit cell, this leads to the well-known phenomenon of seeing signs of 85% of said group being situated in position A, and 15% being placed in orientation B. In routine structure

determinations using the IAM, disorder is usually resolved by incorporation of both positions A and B into the model, usually using restraints and constraints to increase stability. A so-called *site occupation factor* (SOF) is then refined for both (or, in some cases, even more) positions, which gives the percentage to which each position is occupied in the model. The sum of all SOFs for one disordered part of a molecule is constrained to amount to 1 to ensure chemical plausibility. Given the availability of modern refinement programs and specific tools designed to aid in the refinement of disorder like DSR by Kratzert *et al.*^[56] or specific functionalities implemented in Olex2,^[89] today, the refinement of even moderately complex structures usually a relatively mundane task for an experienced crystallographer. While the refinement of disorder in charge-density investigations is notably more demanding than in standard IAM refinements, there are occasional successful reports of it. The main challenge of disorder refinement in charge-density investigations is that due to the usually high accuracy of the method if properly executed false conclusions might be drawn based on minor errors in the model. Even after disorder refinement, some artifacts caused by the disorder might remain, but in the scope of the IAM, they can generally be considered to be irrelevant. In charge-density investigations based on high-resolution data, on the other hand, this might not be the case, as even minor unresolved model uncertainties might falsify certain critical structural properties otherwise obtainable from a MM refinement with subsequent QTAIM analysis. This can for example occur when residual density remaining from a second component of disorder is attributed to ED in bonding regions, therefore potentially impacting the accuracy of bond characterisation.

Small-scale disorders such as the presence of two positions for the atoms of a methyl group are usually straightforwardly resolved.^[49] In the case of larger scale disorder, a usual strategy relies on the transferability of multipole parameters first proposed by Brock.^[90] In this case, a refinement with greatly reduced parametrisation of the disordered parts is conducted. Multipole parameters for one or both components of the disordered parts are then taken either from quantum chemical calculations carried out by oneself or obtained from one of several available databases such as the INVARIOM database by Dittrich *et al.*^[91] or the UBDB databank by Dominiak *et al.*,^[92] usually in conjunction with constraints for the affected atoms. A normal MM refinement can then be conducted for the rest of the structure. These approaches are generally preferable when the disordered region of a compound is far away from region of central interest, i.e. in a case where some peripheral alkyl rest is disordered while the main focus is on the metal centre of the investigated compound. In the Stalke group, a similar approach was chosen by Kratzert *et al.*^[93] for his investigation of two hexasilabenzene compounds. However, such databank approaches can only be applied if all atom types in an investigated compound are also present in the databank.

If disorder of an entire molecule (called “molecular disorder” in the following) is present instead, even the focal areas of the molecule are very likely to be affected by an overlap between the two components. In that case, a constrained refinement with two components usually is the preferred solution. In 2009, for their charge-density analysis of N-Phenylpyrrole, Meindl *et al.*^[94] used extensive constraints to refine

the minor component of approximately 10%, as rigid group, which lead to a MM refinement of remarkable quality. However, there are also attempts to use constraints in order to properly separate the main component from residual density features caused by the second without actually refining atoms on this position. In 2021, Shteingolts *et al.*^[95] published a charge-density analysis of 1,6-dimethyl-3-propargyl-2,4-pyrimidinedione conducted with the multipole refinement program *MoPro* instead of the XD software suite used by Meindl *et al.* *MoPro* is able to use restraints, which contrary to constraints do not have to be strictly fulfilled by the model.^[96] However, as the molecular disorder in this structure comprised a minor component of only 2.55%, a restrained refinement proved to be troublesome, nevertheless. In the end, an approach using a one-component model turned out to be the most successful. Restraints and constraints were used in order to idealize the geometry of the disordered part in on a one-component in order to disallow it from absorbing any residual density caused by the undescribed presence of the minor component. While resolving minor disorder by ignoring it, ensuring it does not compromise experimental results, might yield a satisfactory final model, this chapter will focus on approaches that actually describe the ED of all disordered components.

4.2 Experimental

4.2.1 Data collection and processing

The high-resolution diffraction data of AlH₂ were collected at 100(2) K on a Bruker D8 *Venture* three-circle goniometer equipped with a Smart APEX II CCD detector, a TXS Mo rotating anode, Incoatec Helios mirror optics and a Bruker Kryoflex II cooling device. A suitable crystal was selected in inert oil and then mounted on a MiTeGen Microloop. Data were collected using φ and ω scans up to a maximum resolution of 0.50 Å and integrated using Saint 8.40B.^[97] Maximum resolution was chosen separately in each run to minimize empty detector space on frames. In order to correct for resolution-dependent errors in the data, the outer data with $\sin \vartheta/\lambda \geq 1$ were integrated with a fixed integration box of size 0.6, 0.6, 0.8, while the integration box for the inner data was refined during integration. Even with this customized integration, the normal probability plot is slightly offset from the origin and the DRK-plot of the final model is not a straight line and shows small irregularities for the inner data. These effects are probably caused by remaining unresolved ED of the minor component. Nevertheless, the structure factor plot stays well within the $\pm 5\%$ boundaries. Scaling, absorption correction and error model determination were applied using *SADABS* 2016/2.^[98] Both error models described in Chapter 2.3 were tested, indicating that the use of experimental errors lead to better results.

The datasets of the two additional model structures NO₃-Heptacyclotetradecan (HCTD) and N-Phenylpyrrole (NPP) were not collected in own measurements. The data for HCTD was collected on a Bruker D8 *Venture* four-circle diffractometer equipped with a Photon III detector I μ S Mo Microfocus anode with Helios mirror optics by Christopher Golz, and integrated up to a maximum resolution of 0.43 Å with fixed box size of 0.6, 0.6, 0.8 for the entire data. During data reduction in *SADABS*, using an error model according to Chapter 2.3 was adjusted.

The original dataset for NPP was collected in 2001 by Meindl *et al.* on the same setup as AlH₂, except the previously installed APEXII detector, which was used back then. Scaling was repeated with the latest version of *SADABS*, using experimental errors. The integration, which was performed up to a maximum resolution of 0.41 Å, was left unchanged. While structure factor and normal probability plots of HCTD are unproblematic, the structure factor plot of NPP with the unchanged integration showed deviation of about -6 % for the inner data and up to +8% for the outermost data, which was deemed acceptable within the scope of this comparative study.

4.2.2 Theoretical study

In order to obtain transferable multipole parameters for the second component of both molecules and to validate the experimentally obtained structural properties, quantum chemical calculations at the B3LYP^[99] def2-TZVP^[100] level of theory were carried out in *ORCA* 5.^[101] A theoretical structure factor file for a theoretical multipole refinement (theoMM) in XD was then generated using the *DENPROP* program by Volkov *et al.*^[102] Additionally, a geometrically optimized calculation was conducted at the same level of theory in order to examine where experimental and theoretical molecular geometry differ.

4.2.3 Structure refinement

AlH₂ was solved in SHELXT^[44] using direct methods. There are two molecules in the asymmetric unit (AU), as displayed in Figure 4-2. In order to better identify residual density peaks caused by the second position, Hirshfeld atom refinement with aspherical form factors was conducted using *NoSpherA2* in Olex2.^[62,64,89] With this method, ED in bonding areas that would otherwise cause residual density peaks of the same order of magnitude as the disorder can be described. All remaining residual density peaks could be accounted to the disorder. Furthermore, Hirshfeld Atom Refinement is known to provide hydrogen bonding distances on par with neutron data, providing the best possible starting positions for the hydrogen atom around the aluminium. Starting model generation for MM refinement and initial modelling of the disorder were performed using SHELXL^[70] in the *ShelXle* GUI.^[71] For the final starting model, the second position of the molecule was inserted using the *ShelXle DSR* plugin^[56] based on the geometry of the compound obtained from a previous MM refinement. The second component for both molecules in the AU was refined as rigid group with restrained isotropic thermal displacement parameters, while anisotropic displacement parameters (ADPs) were refined for the main component. The resulting model was then used for another *NoSpherA2* refinement. The SOFs for the minor component of the two molecules refined to 0.0338(8) and 0.0413(7).

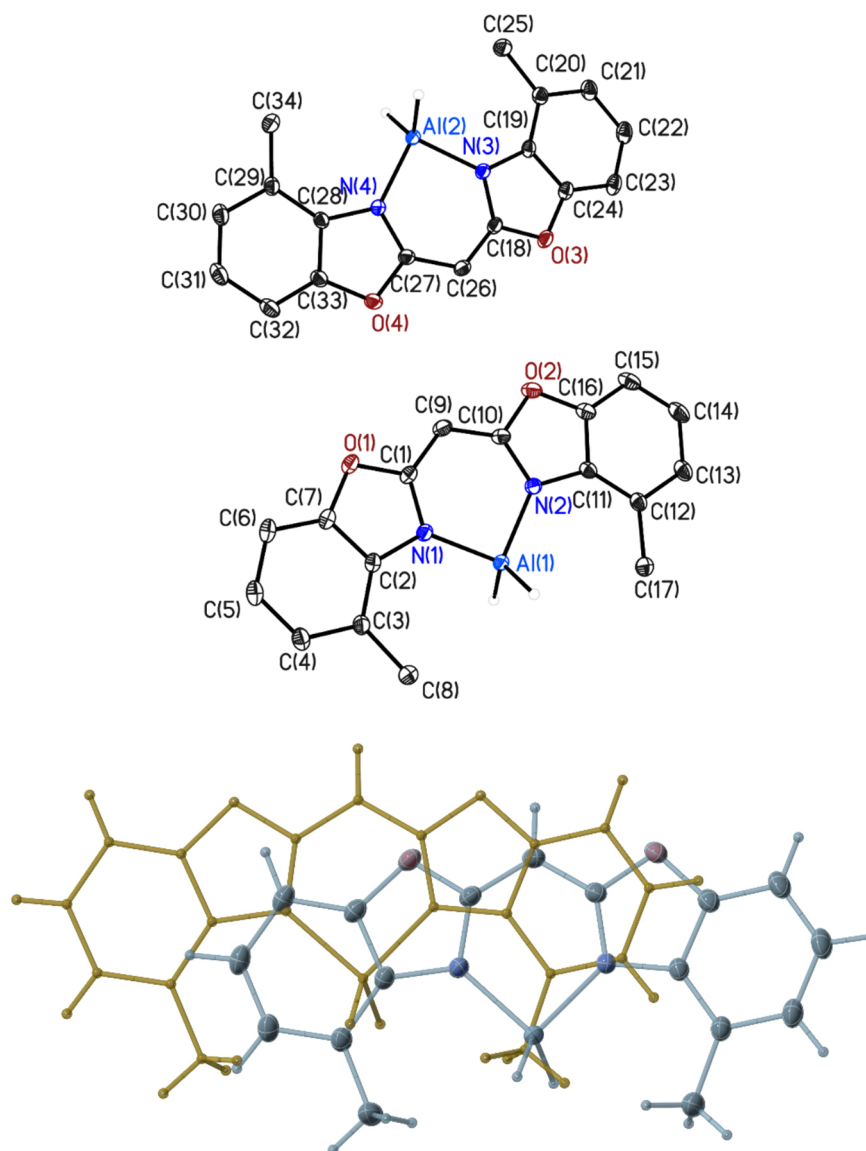


Figure 4-2: Top: Molecular structure of AlH₂ without disorder. Bottom: Schematic depiction of molecular disorder in the compound. The minor components were refined as rigid groups with isotropic displacement parameters. Occupancy of the minor component refined to 0.0338(8) for the first molecule and 0.0413(7) for the second molecule. Anisotropic displacement parameters are displayed at the 50% probability level. Non-Al-H hydrogen atoms and thermal ellipsoids of the minor component were omitted for clarity.

4.2.4 Additional model structures

The squeezelike correction of minor molecular disorder in the data was tested on two additional compounds, one with higher, and one with lower percentage of disorder. The former structure, N-phenylpyrrole (NPP), was published by Meindl *et al.* and was previously mentioned in the introductory Chapter 4.1 as an example for successful disorder refinement. As the disorder in this compound amounts to about 10%, it was possible for the authors to perform a full constrained refinement of both disordered positions in XD. Besides the relatively high SOF of the minor component and the fact that NPP is a small organic molecule with a total of merely 20 atoms including hydrogen, minor and major component are related by mirror symmetry, which yields additional correlations between a number of parameters

such as the ADPs. Given these extremely favourable circumstances, results from this refinement by Meindl *et al.* will be chosen as best possible conventional description of molecular disorder in a MM refinement. As such, the original refinement by Meindl *et al.* will be used for the comparisons in this chapter. The latter model compound, NO₃-Heptacyclo[6.6.0.0^{2,6}.0^{3,13}.0^{4,11}.0^{5,9}.0^{10,14}]tetradecane (HCTD),^[103] on the other hand, has a disorder with the inverted structure of about 1%. While residual density peaks from the minor component are clearly visible in a full IAM refinement not accounting for disorder, impact of this disorder on the charge-density refinement is noticeably lower than for the other compounds. Both NPP and HCTD only consist of small organic molecules. The impact of disorder of the respective amount can therefore be expected to be lower than if heavier elements were involved.

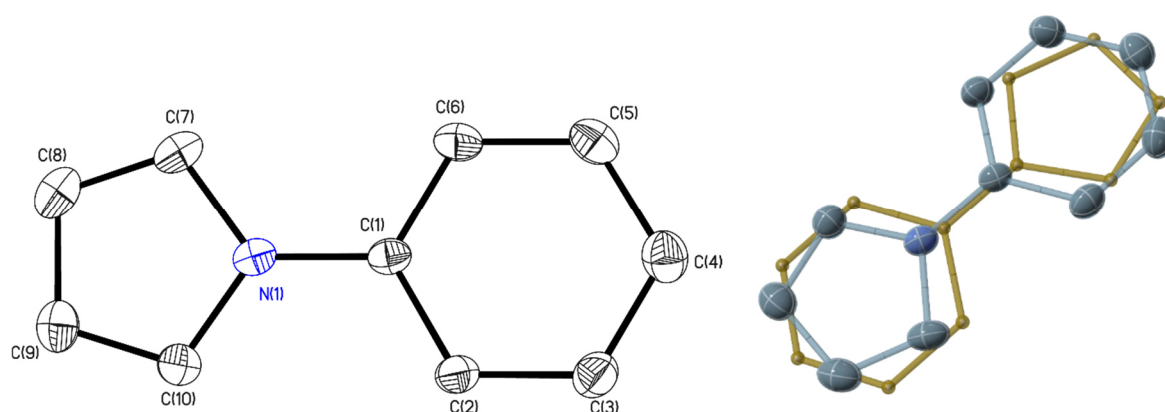


Figure 4-3: Left: Molecular structure of NPP without disorder. Right: Schematic depiction of molecular disorder in the compound. The minor component was refined as rigid groups. Occupancy of the minor component refined to 0.0913(15). It was set to 0.1 in the MM refinement by Meindl *et al.*^[94] Anisotropic displacement parameters are displayed at the 50% probability level. Hydrogen atoms and thermal ellipsoids of the minor component were omitted for clarity.

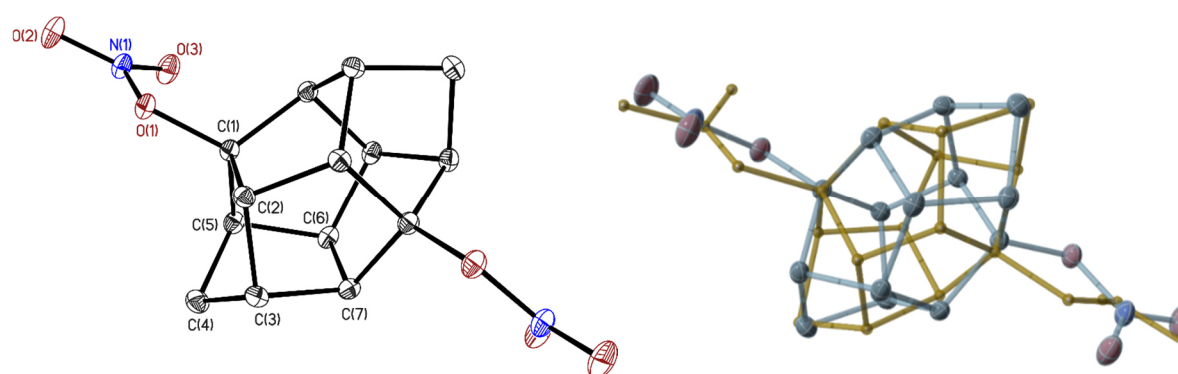


Figure 4-4: Left: Molecular structure of HCTD without disorder. Only the AU of the compound is labelled. Right: Schematic depiction of molecular disorder in the compound. The minor component was refined as rigid groups with isotropic displacement parameters. Occupancy of the minor component refined to 0.0086(5). Anisotropic displacement parameters are displayed at the 50% probability level. Hydrogen atoms and thermal ellipsoids of the minor component were omitted for clarity.

4.3 Multipole model refinement

MM refinements against F^2 using the Hansen & Coppens formalism^[24] were carried out in the *XD2016* software suite (in short: XD),^[69] utilizing multipolar expansion up to dipole level for hydrogen atoms and up to hexadecapole level for all heavier atoms. Gram-Charlier coefficients for anharmonic motion were refined for all methyl group carbon atoms in AlH₂. Analysis of the resulting probability density functions describing the position of respective atoms revealed no significant negative probability, and at least one parameter per atom is clearly significant. Furthermore, refinement of these GCCs is in agreement with Kuhs's rule.^[74] Full refinement strategies for all compounds can be found in the Appendix (10.1.1,10.1.2). Refinement of hydrogen ADPs was attempted with both a free refinement against the X-ray data as well as imported ADPs from the SHADE server.^[75] A detailed description of strategies for anisotropic hydrogen refinement can be found in Chapter 6. Both of the employed methods were deemed insufficient. While the former method led to unreasonably shaped ADPs, the latter led to negative DMSDA values for certain X-H bonds, indicating stronger vibration in a heavier atom. As this seems physically questionable and the impact of the SHADE refinement on the properties investigated in this chapter, final models with isotropic hydrogen atoms were used in this study. Additional information about the SHADE model of AlH₂ can be found in the Appendix (10.1.3).

XD, in contrast to the MM refinement program *MoPro*,^[96] does not allow for the implementation of restraints. However, the disorder of AlH₂ required severe constraining in the independent atom model (IAM) refinement. It can therefore be argued that AlH₂ is not well suited for a MM refinement with the less rigid restraints, compared to mathematically strict constraints. Two different refinement strategies were attempted, which will be described in the following. Both of these methods contain various non-standard manipulations of XD input files, which were carried out using a number of Python 3 scripts based on building blocks provided by Paul Niklas Ruth. In the following, these methods will be abbreviated by the number of positions included in the model. The traditional way of including two disordered molecules with a sum of site occupancy factors amounting to unity into the model is labelled "2Part"-approach. A newly developed way of correcting disorder in the data is labelled "1Part", because if the disorder is removed from the dataset before refinement, then only one component has to be included in the model itself.

4.3.1 "2Part" approach

In this approach, a starting model for MM refinement was generated from a IAM refinement of the disorder. In this, the minor component was refined as rigid group and with isotropic displacement parameters except for HCTD. After starting model generation with *XDINI*, multipole parameters from refinement against theoretical data were transferred to the starting model scaled by the SOF of the respective atom. For the final model, starting multipole parameters were transferred from the main component of a refinement against experimental data instead. A constrained refinement of the lesser component was attempted, but turned out to be impractical. Due to the large number of atoms per

molecule and the presence of two molecules in the AU, several hundred constraints have to be implemented. Not only did the setup of proper rigid body constraints and equivalent parameters of both components prove to be too extensive to do by hand, it surpassed the limits of XD with an extremely large number of required constraints even the most limited scripted version of this approach. While all parameters of the minor component therefore had to be kept fixed to their starting values, a normal MM refinement was carried out for the main component. A python script was then used to repeat this process with varied SOFs for both molecules in the AU, from which then the best model was chosen performing a residual density analysis. Details about this process can be found in the Appendix (10.1.4). The overall procedure used for this approach is summarized below. For determination of QTAIM properties, the multipole parameters of the main component were scaled up to a SOF of unity and then transferred to a XD parameter file with only one component.

1. Disorder refinement in *SHELXL*.
2. Hirshfeld Atom refinement of the disorder using *Olex2/NoSpherA2*.
3. Refinement of ADPs in *SHELXL* against high order data.
4. Starting model generation in *XDINI*.
5. Transfer of transferred multipoles from theoMM.
6. Iteration over several occupancies.
7. Final refinement with occupancies and transferred multipoles from 4.
8. Occupancy and multipoles of main component are scaled to 1 and written to a parameter file with only 1 component.

4.3.2 “1Part” approach

The final result of the 2Part approach was, in principle, a static correction for the molecular disorder. As the high degrees of freedom in the MM were therefore not used or required, an alternative correction of the disorder in the data itself was considered. As mentioned in the introduction, a method akin to the treatment of disordered solvent in crystal voids with the *PLATON SQUEEZE* procedure was chosen and implemented in Python 3.^[104] In standard IAM refinements, *SQUEEZE* can be used to automatically identify the part of the experimentally obtained structure factors that is caused by the disordered solvent, which are then written into a separate file and excluded from the refinement. The predecessor of *PLATON SQUEEZE*, named *BYPASS*,^[105] used a similar algorithm to determine areas with disordered solvent. Here, however, the determined contributions of the disordered solvent are flat-out subtracted from the structure factor file according to the formula:

$$F_{h,\text{corr}}^o = s \cdot |F_{h,\text{all}}^o| \cdot \exp(i\varphi_{h,\text{all}}^c) - F_{h,\text{solvent}}^c$$

Herein, $F_{h,\text{all}}^o$ denotes the experimentally obtained observed structure factors, $\varphi_{h,\text{all}}^c$ is the calculated phase for the respective reflection, and $F_{h,\text{solvent}}^c$ is the calculated structure factor of the disordered solvent, while s is a scaling factor that brings $F_{h,\text{all}}^o$ and $F_{h,\text{solvent}}^c$ on the same order of magnitude.

The authors rightfully stated that nowadays, SQUEEZE should always be used instead of BYPASS, which might obfuscate the original presence of disordered solvent in the data. However, a BYPASS-like approach was implemented for this study, as it allows for the more or less unchanged standard use of the XDLSM refinement program. Theoretical structure factors of the minor component were calculated using *SHELXL* and then subtracted from the experimental structure factors using the formula:

$$F_{h,\text{corr}}^o = s \cdot |F_{h,\text{all}}^o| \cdot \exp(i\varphi_{h,\text{all}}^c) - F_{h,\text{Part2}}^c$$

As such, the subtracted data remains available *via* the structure factor file read by the script. A MM refinement was then conducted based on a starting model containing only the major component. After an initial functional scaling factor s was determined using trial and error, it was thereafter optimized against $wR2$ for the final model of this approach. As intended, previously visible residual density features caused by the minor component vanished after this correction was applied.

4.3.3 Disorder in the Methyl Groups and Final Model

In both of the aforementioned strategies for treating the molecular disorder of AlH₂, unusual ring-shaped deformation density around the carbon atoms of the methyl groups was noticed (Figure 4-5). This effect was identified as a disorder of the hydrogen atoms bonded to these carbon atoms. As refinement of this disorder for both components in a modelled molecular disorder would be troublesome even by IAM standards, we chose to start from the 1Part approach to describe it. The subtraction of the structure factor contributions of the molecular disorder in *SHELXL* was done using the ABIN command normally associated with *PLATON SQUEEZE*. Disorder was refined for three of the four methyl groups, C8, C17 and C34. A constrained refinement of the disorder was conducted in the MM refinement. Even after modelling of the methyl disorder, the ring-shaped deformation density did not change into distinct concentrations around the six overall hydrogen atom positions of the respective methyl groups. In particular, for the hydrogen atoms of C8, even after refinement of the second positions of the hydrogen atoms, another suspicious residual density peak can be found directly between hydrogen atoms of both positions. This makes it likely that more than just two positions are present for at least one of the methyl groups, which, however, could not successfully be modelled.

Table 4-1: Selected figures of merit for the disorder treatment of AlH2.

Method	Uncorrected	2Part	1Part	1Part+H disorder
$R(F^2), wR(F^2)$	0.0612, 0.0662	0.0318, 0.0369	0.0289, 0.0332	0.0287, 0.0329
GOF	5.0373	2.8065	2.1002	2.0818
$\Delta\rho_{\min}, \Delta\rho_{\max}$ [$e\text{\AA}^{-3}$]	-0.713; 1.398	-0.722; 0.624	-0.325; 0.591	-0.256; 0.362
e_{gross} [e]	62.7	46	44.4	44.3

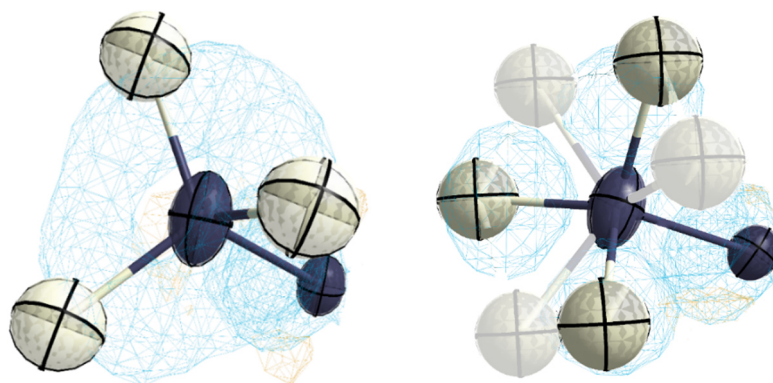


Figure 4-5: Hydrogen atom disorder around the methyl carbon atom C34, as refined in the 1Part model for the overlaying molecular disorder. Anisotropic displacement parameters are displayed at the 50% probability level. Left: Ring-shaped deformation density indicating the presence of disorder. Right: Refined methyl disorder, causing the ring-shaped deformation density to be replaced by discrete maxima. Major disorder component is highlighted. For the other two affected carbon atoms C8 and C25, the ring-shaped deformation density did not vanish even for refined methyl group disorder, hinting at the existence of further, even smaller disordered positions, which could not be modelled. The SOFs of the minor components are: 0.1113(14) (C8), 0.298(14) (C25) and 0.2743(14) (C34).

All relevant figures of merit of the final refinement of AlH2 for the uncorrected disorder and the 2Part and 1Part disorder approaches can be found in Table 4-1. Overall, the 1Part approach seems to yield to superior model quality in terms of the examined quality indicators. While additionally accounting for the disordered methyl groups lowers the extrema in the residual density map, it also leads to a slight worsening of the other examined quality indicators. Compared to differences between approaches of dealing with the molecular disorder, however, the impact is rather small. As refinement of this disorder lead to unreasonable Bader charges for the affected methyl groups, the 1Part model with unrefined methyl disorder was chosen as final model. Therefore, details about the process of refining this disorder are omitted here and can instead be found in the Appendix (Chapter 10.1.5).

4.4 Results and discussion: AlH2

At first, results for the two disorder methods will be analysed and compared for the BOX compound. A thorough examination of the other two model structures as well as a more in-depth comparison of the different disorder methods will follow in Chapter 4.5.

4.4.1 Residual density analysis

As previously mentioned in Chapter 2.5, for a successful MM refinement, the remaining residual density of the final model should be flat and featureless. A visual inspection of the residual density of the 2Part-approach reveals that while the overall level of the residual density map is relatively low, the areas of high residual density are mainly located around overlapping atom positions between the disorder components. This is especially pronounced around the methyl groups and the aluminium atoms in the structure, which heavily overlap with each other between the two components. Residual density concentrations can furthermore be found around the oxygen atoms of the minor component, even if they are not overlapping with parts of the main component. Another noticeable feature is the presence of residual density holes of approximately $0.3 \text{ e}\text{\AA}^{-3}$ around several atoms of the second component. The respective areas are highlighted in Figure 4-9. We attempted to reduce these effects by the aforementioned variation of the SOF parameters of both molecules for the final model. However, they could not be fully alleviated as any step that reduced positive residual density at one atom generally led to high residual density holes at atomic positions of another. Overall, this indicates that the mostly unchanged IAM model outfitted with transferred multipoles from theory or previous refinement against experimental data is not fully capable of describing the minor component ED in a MM refinement.

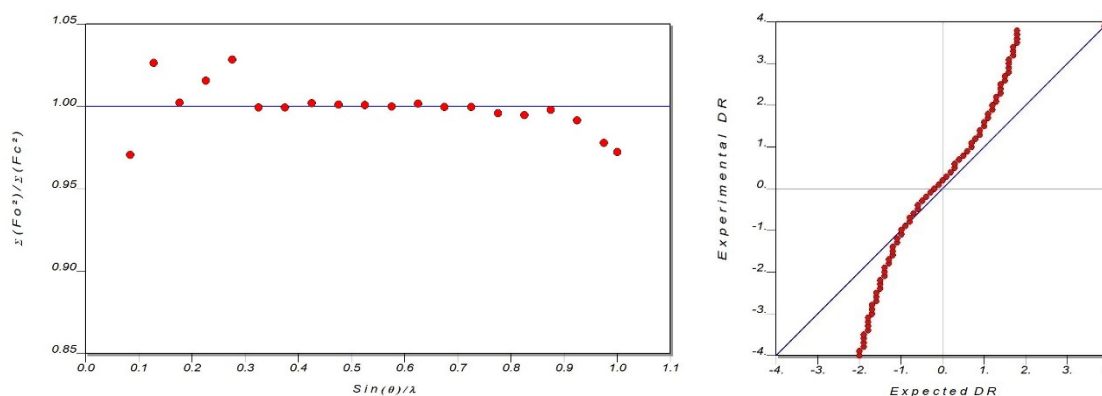


Figure 4-6: Structure factor plot and normal probability plot of AlH2 with corrected disorder. Plots do not significantly differ between disorder correction method, except an outlier in the outer data of the SQUEEZE-like 1Part approach described in Chapter 4.3.2 caused by truncation errors.

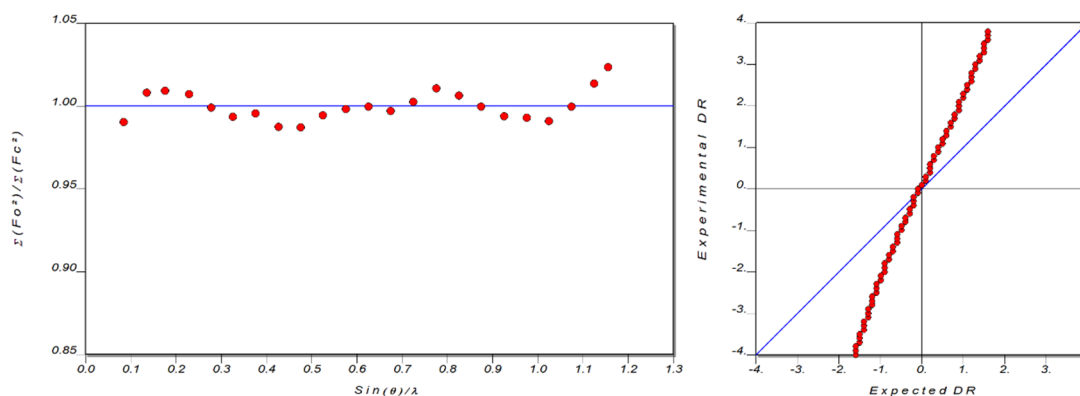


Figure 4-7: Structure factor plot and normal probability plot of HCTD with refined disorder.

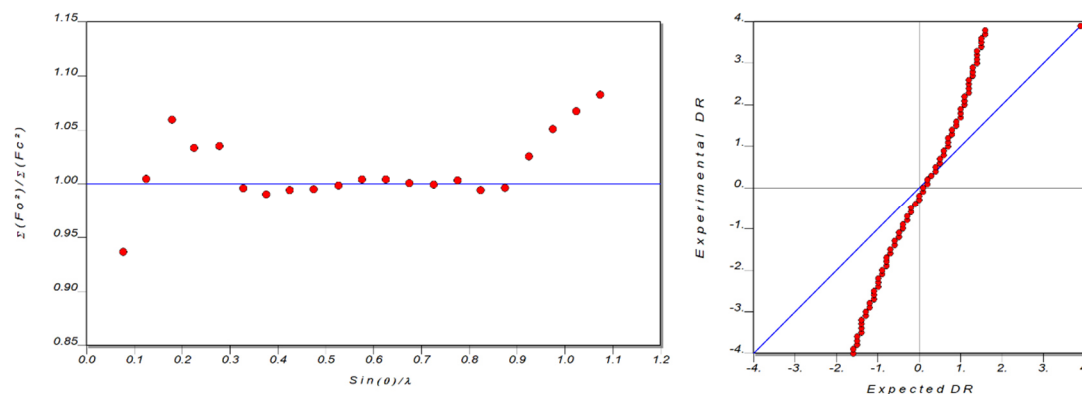


Figure 4-8: Structure factor plot and normal probability plot of NPP with corrected disorder, based on the original integration by Meindl *et al.*^[94]

For the 1Part model, on the other hand, residual density was still concentrated on areas of overlap between components, but slightly lower than for the 2Part model, as shown in Figure 4-10. No new features that indicate problems in the structure factor subtraction routine were found, such as the appearance of regions of unphysical negative ED. Structure factor plots and normal probability plots of the final refinements of all investigated compounds are depicted in Figures 4-7 to 4-8. Further details of residual density analysis can be found in Chapter 4.5.1, Figure 4-16.

4.4.2 Structural analysis

The overall structure of AlH₂ is in good agreement with the IAM model previously published by Kretsch *et al.*,^[16] with major differences only to be found in the Al-H distances, which are more apart in our MM refinement. A list of selected bond distances and angles can be found in Table 4-2. Compared to the geometrically optimized calculations, the largest difference between the experimental coordinates and the optimized structures lies mainly in the hydrogen atoms bonded to methyl groups and the aluminium atoms. In the optimized structure, all Al-H distances are of equal length, and the methyl groups are oriented in such a way that one hydrogen atom pointing away from the aluminium is in plane with the rest of the ligand. The experimental orientation does not match this, as all hydrogen atoms here are oriented slightly out of plane, even if the disorder in the methyl groups is accounted for. Differences in the methyl group hydrogen positions can be attributed to the presence of disorder in these groups. While different Al-H distances for aluminium dihydride complexes have been reported before,^[106] the specific origin of these differences in AlH₂ could not be deduced from the MM refinement. In addition, the aluminium atoms are situated around 0.16(2) Å out of plane compared to the N₂C₃ central part of the ligands, which is not the case for the theoretical structure.

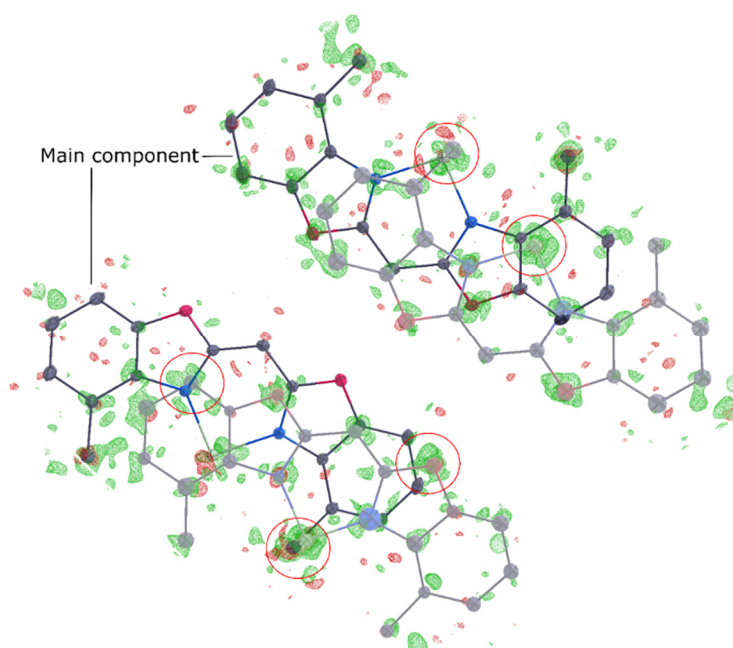


Figure 4-9: Residual density map of AlH₂ after refinement using the 2Part method. Areas of high residual density are highlighted. The isolevel of the residual density is $\pm 0.11 \text{ e}\text{\AA}^{-3}$. ADPs are displayed at the 50% probability level. Minor component is toned down, and hydrogen atoms were omitted for clarity.

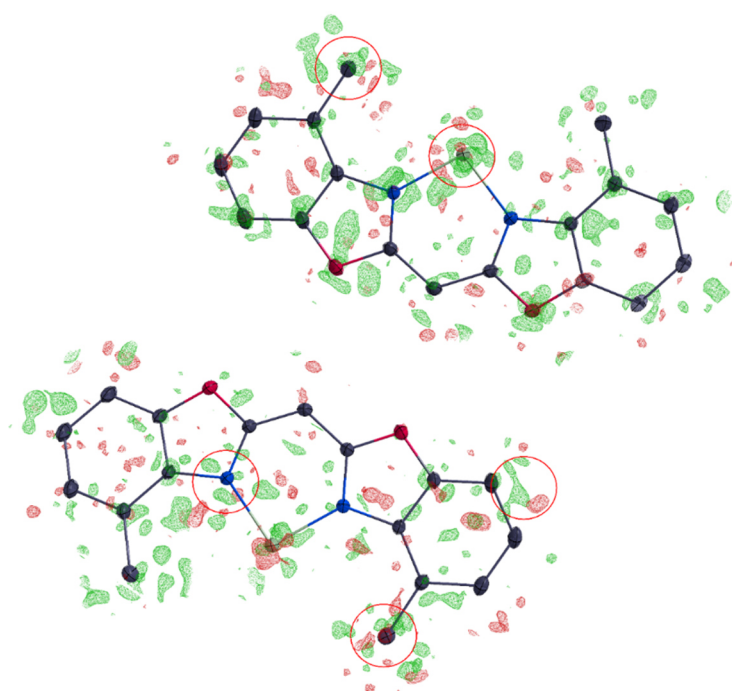


Figure 4-10: Residual density map of AlH₂ after refinement using the 1Part method. Highlighted areas had residual density extrema in the 2Part refinement, which are reduced in size or vanished compared to Figure 4-9. The isolevel of the residual density is $\pm 0.11 \text{ e}\text{\AA}^{-3}$. Green denotes positive, red denotes negative residual density. ADPs are displayed at the 50% probability level. Hydrogen atoms were omitted for clarity.

The deformation density around the aluminium centre was compared between the different disorder approaches. Contour maps of the various models can be found in Figure 4-12. This comparison shows that the deformation density is unreasonably warped around the N4-Al2 bond. This distortion is resolved in both corrections for the molecular disorder. Furthermore, a striking difference between the hydridic hydrogen atoms H37 and H38 can be seen for the 2Part model, whereas they have a more similar shape in the 1Part model. Overall, in the area around the aluminium atoms, deformation densities from the 1Part refinement have the best agreement with those taken from the theoMM refinement.

Table 4-2: Selected bond angles, distances and aluminium out of plane distances. Out-plane-distance of the aluminium atoms is determined relative to the mean plane defined by N1, N2, C1, C9 and C10 for Al1, and by the mean plane defined by N3, N4, C18, C26, C27 for Al2.

Bond distance [Å]		Bond distance [Å]	
Al1–N1	1.9307(3)	Al1–H35	1.55673(9)
Al1–N2	1.9229(3)	Al1–H36	1.72252(9)
Al2–N3	1.9314(3)	Al2–H37	1.55673(9)
Al2–N4	1.9251(3)	Al2–H38	1.72374(9)
Bond angle[°]		Out-of-plane distance [Å]	
N1–Al1–N2	95.418(15)	Al1	0.17(2)
N3–Al2–N4	94.906(15)	Al2	0.16(2)

4.4.3 Molecular Graph and Critical Points

While a decrease in residual density and improvement of R values is generally the sign of an improving model, care should be taken in the case of molecular disorder. Here, a decrease in residual ED might actually be caused by erroneous “absorption” of minor component ED into parameters of the major component, i.e. ADPs and multipole parameters. Therefore, several structural properties obtained from the experimental data were compared to properties from the theoMM refinement. While the theoMM should in no way be misunderstood as the “true structure”, properties obtained from it can be used as a guideline and reference point assisting in the assessment of the experimental model.

First off, we examined the molecular graph of all models, which can be found in Figure 4-11. All expected bond critical points in bonding regions are found for all models, and the Hopf-Poincaré (HP) rule is fulfilled for all refinements (for more details, see also 3.3). For this, however, a non-standard and more thorough search algorithm, increasing the computation time from below two minutes in the standard algorithm to around four hours. Still, there are discrepancies between the models regarding critical points in non-bonding regions of low ED, most predominantly, between the methyl groups and the aluminium centre of each respective complex in the AU. For the uncorrected model, between each methyl group and aluminium centre, six overall critical points are to be found from a refinement against structure factors from the geometrically optimised calculation: Two bond critical points (BCPs) with

associated bond paths between methyl carbon or hydrogen atoms and the hydrogen atoms connected to the aluminium, and then three ring critical points (RCPs) with one cage critical point (CCP) in the middle between them. Note that in this way, these critical points have no impact of the total of the HP equation,

$$n_{\text{Atoms}} - n_{\text{BCPs}} + n_{\text{RCPs}} - n_{\text{CCPs}} = 1,$$

which has to amount to 1 for a complete molecular graph by the mathematical laws of topology. The ED at these BCPs is roughly one order of magnitude smaller than the ED of a typical covalent C-C bond in the structure. In both the 2Part and the 1Part model, some of these CPs are absent, but always in a way that, again, does not affect the total of the HP equation. For the 2Part model, one RCP and one CCP are missing. For the 1Part model, one BCP, three RCPs and 2 CCPs in these regions could not be found. Furthermore, when compared between different molecular disorder models, the present bond paths partners of neighbouring methyl groups were intermingled. Therefore, regarding bond paths between two different methyl groups, what was detected as a H-H path in one of the models could be found as C-H path in another. The problems in these areas could partly arise due to the disorder in the methyl groups. A comparison between 20 cross validation sets revealed an overall large uncertainty for critical points in these regions. For different work-sets that omit 5 % of total data for the refinement, clear differences regarding location of bond paths and presence or absence of certain critical points could be observed. Furthermore, even in the theoMM refinement, not all critical points in these regions of low ED were consistently found. Therefore, we deem this inconsistency between different disorder approaches to negligible, as these regions apparently do not allow for a meaningful discussion of critical points either way.

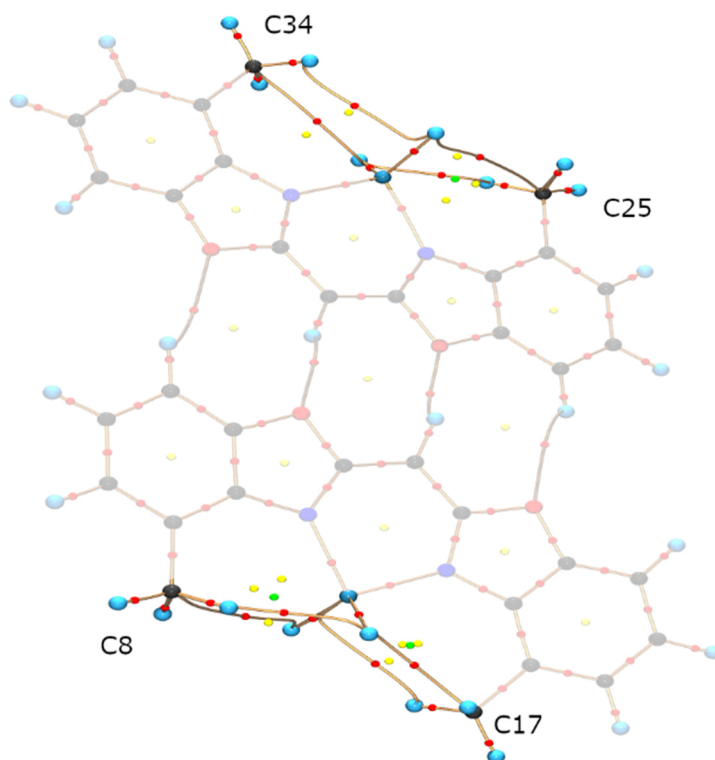


Figure 4-11: Molecular graph of AlH₂. The image presented here is taken from the 2Part model. Bond paths are displayed in golden, BCPs are displayed in red, RCPs are displayed in yellow, CCPs are displayed in green. Main differences between disorder approaches lie in the critical points in the highlighted regions. For example, for the 1Part example, one of the bond paths in this region is missing. Molecular graphs of all other approaches can be found in the Appendix (10.1.6).

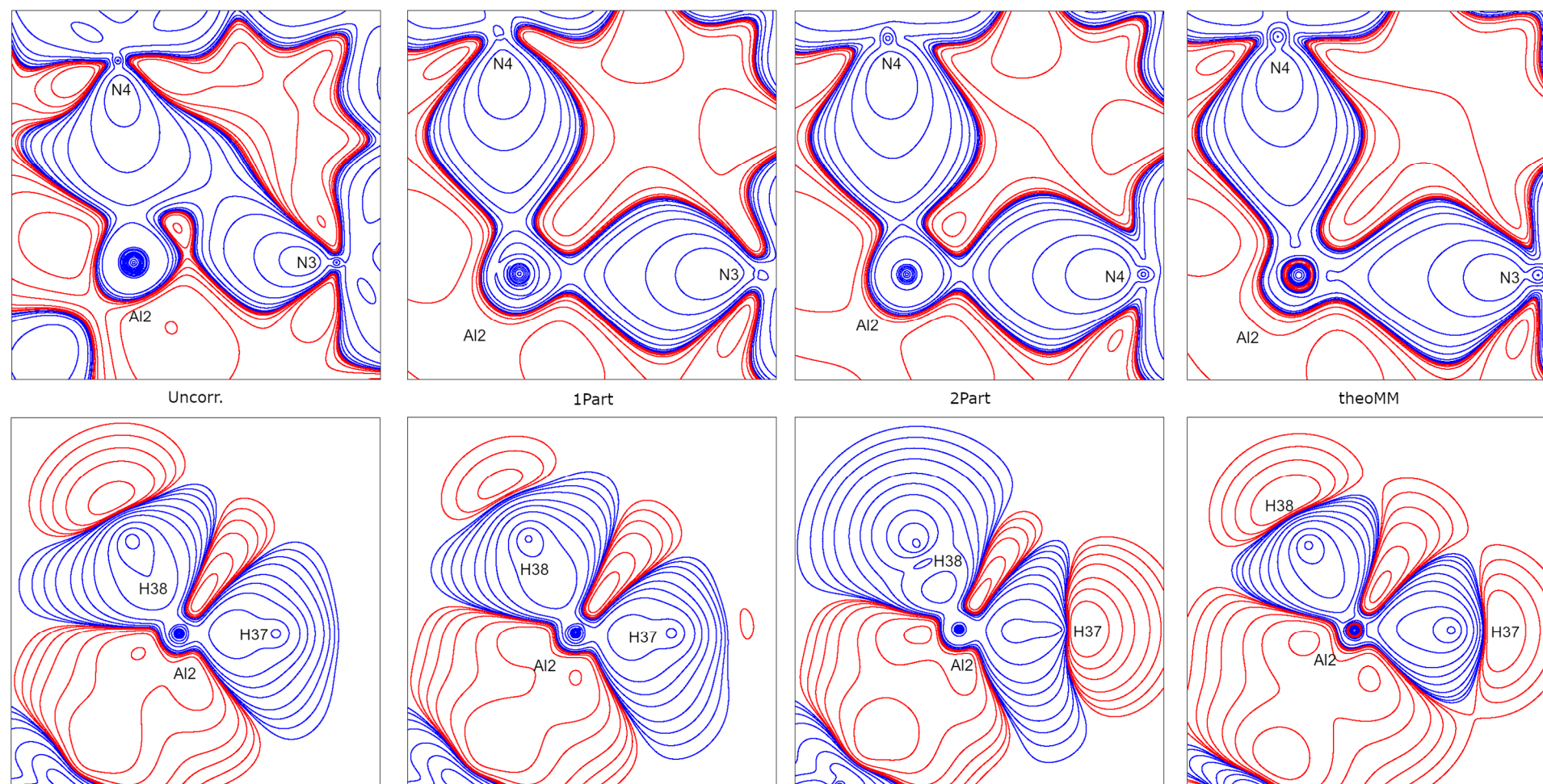


Figure 4-12: Static deformation density maps compared between different approaches for dealing with the molecular disorder. Top: Map of the N4-Al2-N3 plane of the second molecule in the AU. Multipole parameters of N3 and N4 are constrained to be equal. Bottom: Map of the H37-Al2-H38 plane of the second molecule in the AU. The contour intervals are $\pm(0.001, 0.002, 0.004, 0.008, 0.02, 0.04, 0.08, 0.2, 0.4, 0.8, 2.0, 4.0, 8.0, 20.0, 40.0, 80.0, 200.0, 400.0, 800.0) \text{ e}\text{\AA}^{-1}$.

Additionally, the ED ρ , the second derivative of the ED $\nabla^2\rho$ (Laplacian) and the ellipticity ε at all BCPs were compared between the models, with focus on the BCPs that describe the interactions between ligand and metal. Standard deviations for these properties were estimated by statistical analysis of results of 20 cross validation sets [78]. At the Al–N BCPs in the uncorrected model, a discrepancy of the ED was noticed when compared to the theoMM model. While in the theoMM refinement all of these BCPs have approximately the same BCP ED values, for the uncorrected model, there are significant differences between two of these BCPs in the same model. Furthermore, ellipticities, which quantify the rotational symmetry of a bond, differ clearly between the various, with the 2Part model closest to results from theoMM. Laplacians value are the most deviating of the examined BCP properties. These phenomena are noticeably diminished if disorder is accounted for in both described ways, which reveals these effects to be artifacts caused by residual density of the undescribed second component (see Table 4-3). A similar observation was made in the benzoxazole groups in the ligand, the detailed BCP properties for which can be found in the Appendix.

Table 4-3: Selected properties at BCPs around the aluminium atoms in the asymmetric unit. ρ is the electron density at the BCP. $\nabla^2\rho$ is the Laplacian of the ED, which is positive for ionic interactions and negative for covalent interactions. ε is the elipicity of the bond. Ellipticity is close to one for complete absence of rotational symmetry, which generally hints at a strong π -character.

BCP	Method	ρ	$\nabla^2\rho$	ε
Al1 – N1	Uncorr.	0.475(3)	5.93(13)	0.26(2)
	2Part	0.534(3)	5.09(13)	0.04(2)
	1Part	0.524(3)	5.53(13)	0.06(2)
	theoMM	0.549(3)	4.71(13)	0.07(2)
Al1 – N2	Uncorr.	0.595(3)	4.92(13)	0.37(2)
	2Part	0.566(3)	4.68(13)	0.06(2)
	1Part	0.533(3)	5.52(13)	0.14(2)
	theoMM	0.547(3)	4.62(13)	0.07(2)
Al2 – N3	Uncorr.	0.471(3)	5.80(13)	0.26(2)
	2Part	0.532(3)	5.02(13)	0.04(2)
	1Part	0.523(3)	5.50(13)	0.05(2)
	theoMM	0.545(3)	4.53(13)	0.08(2)
Al2 – N4	Uncorr.	0.594(3)	4.91(13)	0.37(2)
	2Part	0.564(3)	4.64(13)	0.06(2)
	1Part	0.531(3)	5.45(13)	0.13(2)
	theoMM	0.546(3)	4.60(13)	0.09(2)

While differences in the Laplacian of the ED are present between the different models, the overall conclusion these values lead to is the same for all approaches. The strongly positive values indicate, as expected, an ionic closed-shell interaction between the ligand and the aluminium. More details on the differences of BCP properties between the compared disorder methods can be found in Chapter 4.5.2, Table 4-5.

4.4.4 Bader charges and source function

Integrated atomic basin charges were calculated for all molecules, which should, if added up, amount to approximately zero for an accurate model of a non-charged compound. This can be confirmed by calculating these charges based on results of the theoMM refinement. The 1Part refinement comes close to a sum of zero as well. In the 2Part model, however this sum amounts to a value close to -1, with approximately equal contributions from both molecules in the AU. Two main areas of deviation from theoMM results were identified: The aluminium atoms and the methyl groups, along with bonded hydrogen atoms, respectively. These are, in fact, the areas of the molecule most heavily affected by overlap between major and minor component. A noteworthy deviation from the theoMM properties are the charges of methyl groups. Here, in all experimental approaches, the Bader charges of the associated hydrogen atoms are larger, while the charges of the carbon atoms are smaller than the theoMM results. However, for all but the uncorrected refinement, the sum over all atoms per methyl group and their mean is close to the expected value of zero. Overall, the Bader charges obtained from the 1Part model seem to fit the best with the expectations from the theoMM model (Table 4-4).

In addition, calculation of the integrated source function was attempted for both methods in order to quantify electron delocalisation within the compound. This method established by Gatti *et al.* [28] can be used to determine to what degree electron density at specific points in the structure is influenced by the atomic EDs. Most commonly, bond critical points are used as reference points. Results for the source function investigation could only be obtained from the 1Part approach. For the uncorrected refinement as well as the 2Part approach, the calculations of source function properties crashed when integrating source functions over certain atomic basins. The results show that ED close to the Aluminium atoms is influenced by carbon atoms across large parts of the ligand, while for BCPs in peripheral regions of the ligand are only affected by atoms nearby. This can be seen as indication for delocalisation of ED from the ligand the metal centre in order to stabilize the complex.

Table 4-4: Selected charges of integrated atomic basins (Bader charges) of all investigated disorder approaches. A full list can be found in the Appendix.

Bader charges	Uncorr.	2Part	1Part	theoMM
Al1	1.89	2.13	2.07	2.21
Al2	2.17	2.11	1.98	2.21
⟨Hydride H⟩	-0.99	-0.91	-0.79	-0.67
⟨Methyl Groups⟩	-0.48	-0.03	0.07	0.09
$\Sigma_{\text{Structure}}$	0.00	-1.00	0.06	0.04

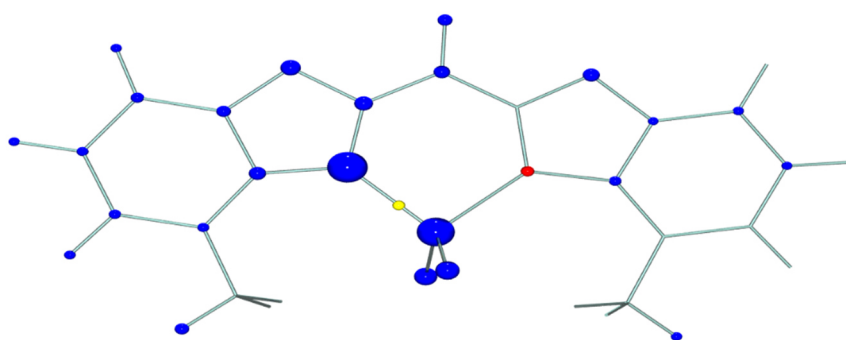


Figure 4-13: Visualisation of the integrated source function descriptor for electron delocalisation in the first molecule in the AU. Larger spheres denote a larger contribution of atomic ED to the electron density at the yellow reference point. Blue spheres denote positive contribution, red spheres denote negative contribution. Observations are similar for the second molecule.

4.5 Results and discussion: Additional model compounds

Structural discussion of the additional model compounds with lower (HCTD) and higher (NPP) SOF of the minor component allowed for some further insight into the capabilities of the 1Part correction method. Data reduction and refinement followed the same procedures described in Chapter 4.2. The discussion of selected criteria comparable to those introduced in the previous chapter for AlH₂ can be found below.

4.5.1 Residual density analysis

The observations in residual density analysis of AlH₂ hold generally true for both NPP and HCTD. In both cases, the application of the 1Part correction noticeable reduces the height of residual electron density peaks associated with the minor component. However, those peaks do not completely vanish, nor are they reduced to noise level. A comparison of all peak sizes over all three structures revealed a mean decrease in peak height of approximately 66% for AlH₂ and NPP, while for the significantly smaller second component in HCTD, an average decrease in height of 45% was noticed. Furthermore, the shape of the HM plot improved in all three cases, proportional to the size of the second component.

Specifically, for HCTD, the minor component is so small that its impact on various model quality indicators is barely visible. The HM plots for all compared refinements are displayed in Figure 4-16.

Regarding a more conventional description of disorder in a 2Part model, it became clearly apparent that a constrained refinement can be expected to yield superior results compared to the 1Part correction. While the 1Part correction of NPP does improve model quality indicators, the constrained 2Part description by Meindl *et al.* surpasses this improvement and reduces minor component peak height to noise level. For the very small minor component of HCTD, on the other hand, a classical 2Part description of the disorder did inexplicably fail and lead to a worsening of model quality indicators. While no input error in the usual XD starting model generation process could be identified, this error is likely caused by a program limitation of the XD suite. Taking this into account, the 1Part description was identified as best possible disorder description for HCTD.

4.5.2 Impact on the deformation density and structural properties

The observations regarding the deformation density maps and structural properties derivable from different disorder approaches of NPP and HCTD were comparable to those made for AlH₂ in proportionality of the percentage of disorder present. For HCTD, the agreement of the experimentally obtained deformation density with the theoMM equivalent improved slightly in the 1Part model in areas of direct overlap (Figure 4-14).

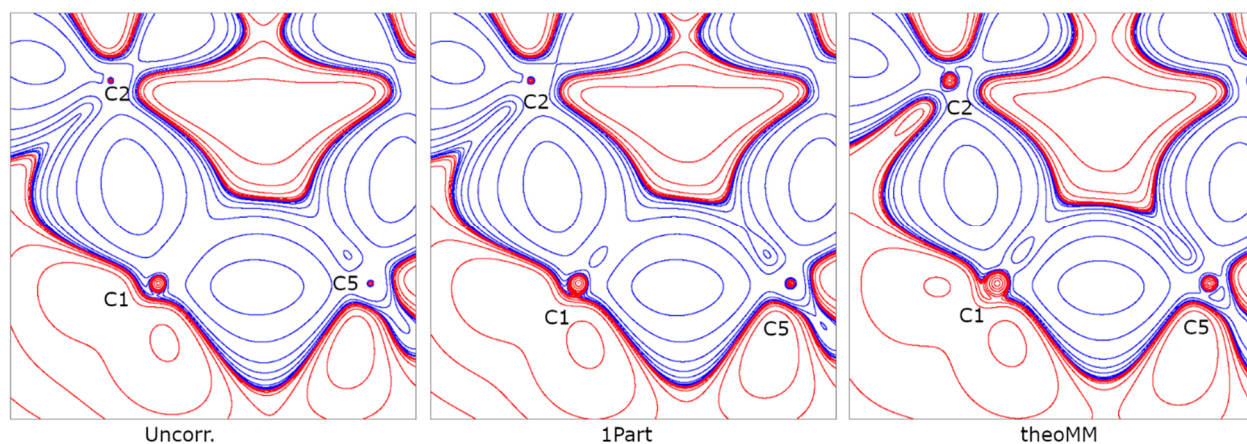


Figure 4-14: Static deformation density maps around the overlapping carbon atom C1 of HCTD. The 2Part approach was excluded from this comparison, as model quality significantly worsens when this method is applied. The contour intervals are $\pm(0.001, 0.002, 0.004, 0.008, 0.02, 0.04, 0.08, 0.2, 0.4, 0.8, 2.0, 4.0, 8.0, 20.0, 40.0, 80.0, 200.0, 400.0, 800.0) \text{ e}\text{\AA}^{-3}$.

For NPP, the deformation density of the uncorrected model exhibits irregularities in the bonding areas, caused the formerly described impact of undescribed minor component electron density. These effects are, again, diminished in both the constrained 2Part model as well as in the 1Part refinement. However, while the correction of irregularly shaped deformation density is near perfect for the 2Part model by Meindl *et al.*, it still remains visible to a problematic extent in the 1Part model (Figure 4-15).

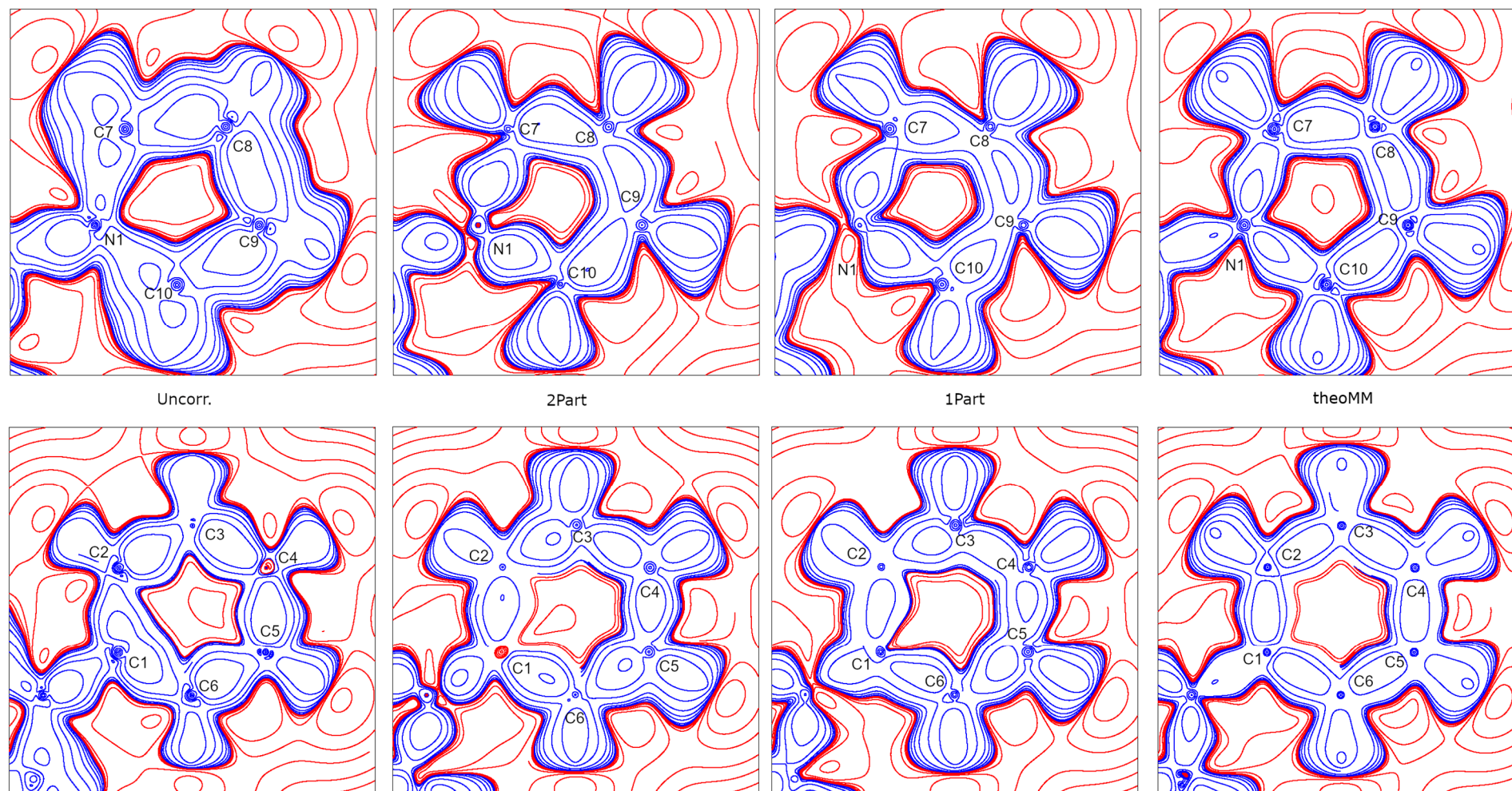


Figure 4-15: Static deformation density maps around the overlapping carbon atom C1. Left: Phenyl group, displayed in the C1 C3 C5 plane. Right: Picoline ring, displayed in the N1 C8 C9 plane. Full maps can be found in the Appendix. The contour intervals are $\pm(0.001, 0.002, 0.004, 0.008, 0.02, 0.04, 0.08, 0.2, 0.4, 0.8, 2.0, 4.0, 8.0, 20.0, 40.0, 80.0, 200.0, 400.0, 800.0) \text{ e}\text{\AA}^{-1}$.

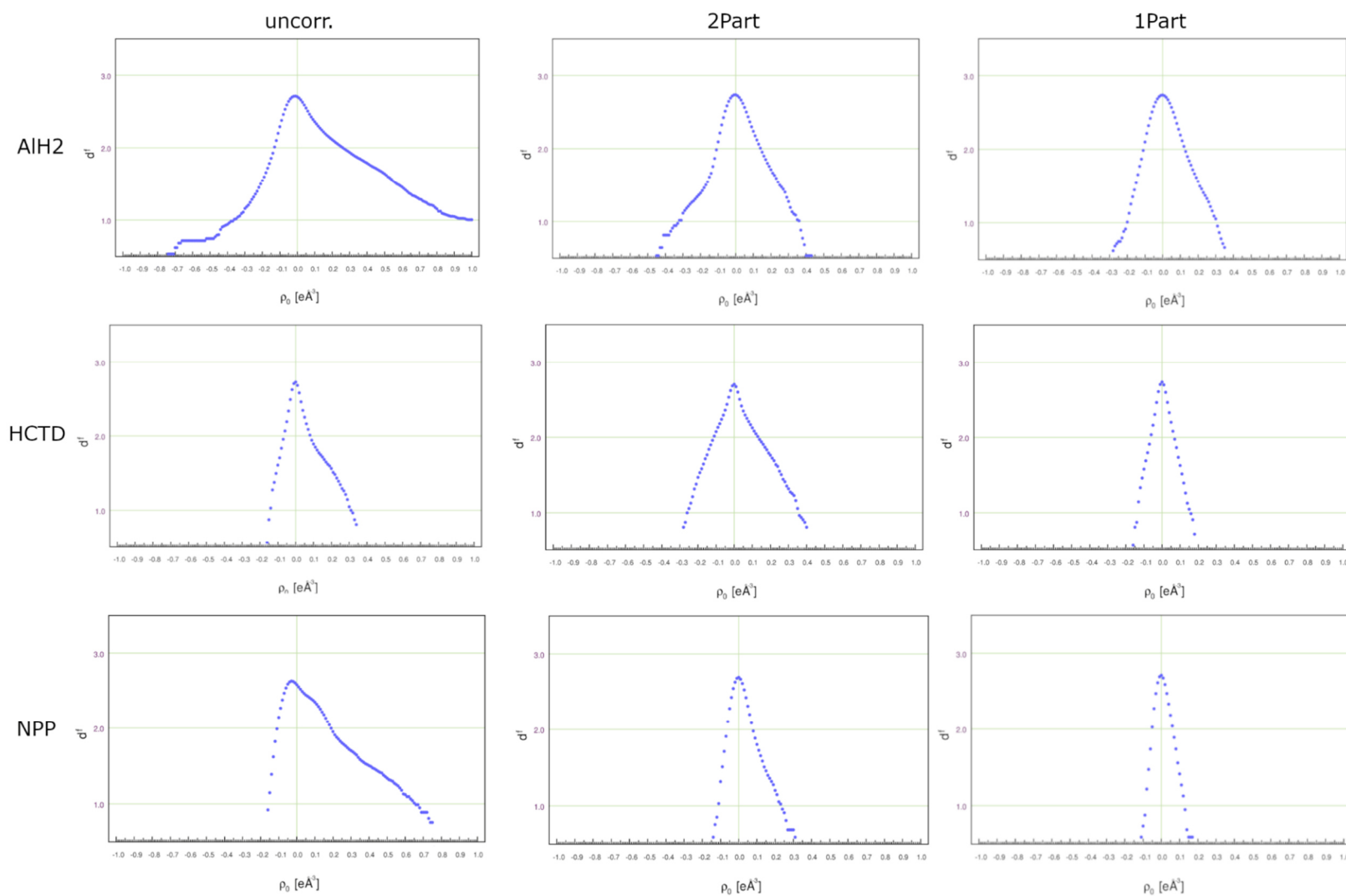


Figure 4-16: HM-plot for all compared refinement strategies. For reasonable residual density, the plot should be parabola-shaped without “shoulders” on either side.

Molecular Graphs of both NPP and HCTD are both complete and fulfil the HP rule for all correction methods, even in the case of the uncorrected model of the most strongly disordered NPP (Figure 4-17 Figure 4-18). Observations regarding topological properties at the BCPs mostly match those made for AlH₂. Like noted above, several crudities in the uncorrected model concerning BCP ED and ellipticities get reduced by 2Part and 1Part corrections. Electron density in bonding regions is systematically too high for the uncorrected models, for example, which is to be expected due to overlap of the second position with the bonding regions and amended after disorder treatment.

In order to quantify the extend the properties differ from each other in terms of agreement with theoMM results, the root mean square difference of BCP ED, Laplacian and ellipticity were determined, including no X-H BCPs except the Al-H BCPs in AlH₂. Results showed that while as noticed before the 2Part approach failed for HCTD, the differences between the correction methods are generally small. Interestingly, while the agreement of BCP electron density with the theoMM model is expectedly better for the constrained 2Part model, the agreement for the Laplacian is better for the 1Part model. Otherwise, while some irregularities remain in individual values for both 2Part and 1Part refinements, the overall accuracy of BCP property determination appears to be comparable between both methods, indicating that the 1Part method is able to provide those properties on par with the usual 2Part approach. Contrary to AlH₂, in which Bader charges did not amount to the expected value, no discrepancy in the Bader charges was observed for both NPP and HCTD, which in both cases were close to the expected value for the respective molecule.

Table 4-5: Root mean square deviations of BCP properties from theoMM values as reference.

Compound	Method	ρ	$\nabla^2\rho$	ε
AlH ₂	Uncorr.	0.07	3.33	0.12
	2Part	0.07	3.53	0.06
	1Part	0.07	3.33	0.06
HCTD	Uncorr.	0.92	0.78	0.26
	2Part	0.89	8.71	0.25
	1Part	0.08	0.79	0.03
NPP	Uncorr.	0.46	11.28	0.08
	2Part	0.09	5.11	0.04
	1Part	0.14	2.83	0.05

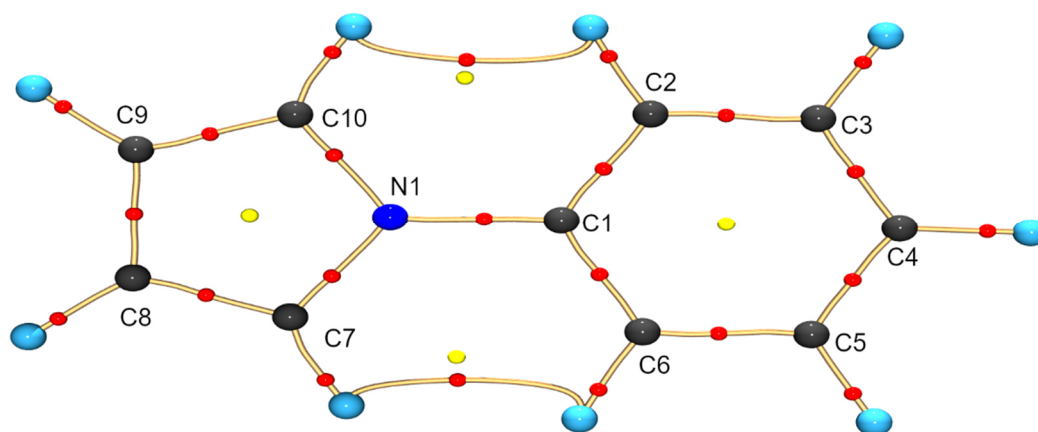


Figure 4-17: Molecular graph of the asymmetric unit of HCTD. The image presented here is taken from the 1Part model. Bond paths are displayed in golden, BCPs are displayed in red, RCPs are displayed in yellow.

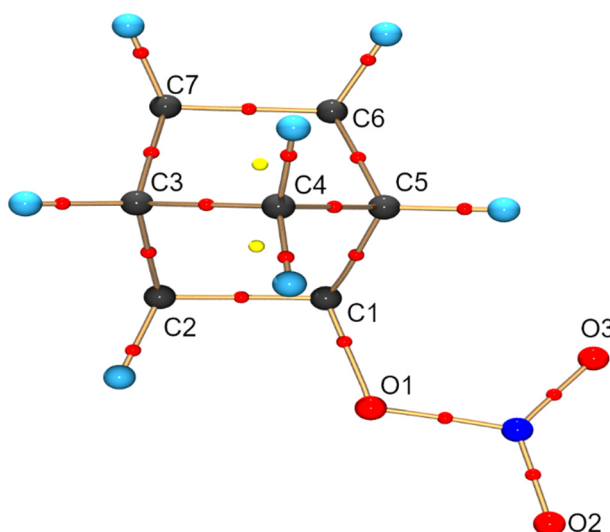


Figure 4-18: Molecular graph of the asymmetric unit of NPP. The image presented here is taken from the 1Part model. Bond paths are displayed in golden, BCPs are displayed in red, RCPs are displayed in yellow.

4.6 Conclusion and outlook

In this disorder study of three compounds with varying percentages of the minor second component, the merit of different ways of approaching disorder refinement in charge-density analyses could be evaluated. Comparison of the 1Part description of disorder with conventional 2Part description clearly showed that the latter approach, if feasible, is still the superior way of modelling the presence molecular disorder in two components. For this case, careful consideration of constraints is required. However, in this chapter, the two structures AlH₂ and HCTD were presented, where this kind of thorough description was not possible. The SQUEEZE-like 1Part method investigated in this chapter was able to enhance the model quality for both of these structures, with inferior 2Part models in both cases. Properties derived from these 1Part corrected models are reasonably well in line with expected values from the theoMM refinement. The remaining residual density peaks still leave a degree of uncertainty in the final model. Still, differences regarding the properties of the tested disorder approaches are mostly small. As it stands, successful disorder treatment in multipole model refinements is still considered the exception, and the work done in this thesis was not able nor meant to provide a generally applicable solution. However, the new method presented in this chapter could be a useful tool for other structures with small molecular disorder and is therefore worthy of further investigation.

5 Charge-Density Analysis of three d-metal BOX complexes with different magnetic properties

As mentioned in Chapter 1, among the most recent BOX complexes synthesised in the Stalke group are a number of highly stable d-metal compounds by Daniel Lüert and Christina Legendre. These complexes have demonstrated potential applications in the benchmarking of spectroscopic and magnetic properties.^[20] The synthesis and investigation of single-molecule magnets (SMM) is well established as an interdisciplinary topic, involving a wide field of chemical and physical concepts and a plethora of relevant analytical methods. SMMs are molecules which retain magnetization even after an applied magnetic field is removed, due to their high energy barrier to spin reversal.^[107] Contemporary SMMs retain magnetization generally only at low temperatures, and only for a limited amount of time. Some of the investigated compounds, the those dealt with in this chapter, only show *slow magnetic relaxation*. This means that magnetisation is lost approximately 10^6 times slower than for a usual paramagnetic compound

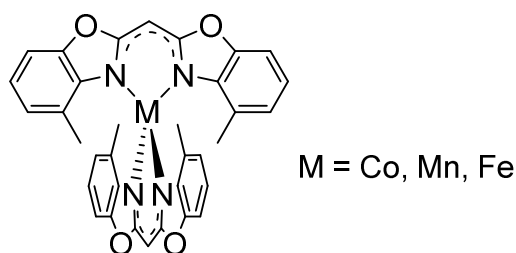


Figure 5-1: Structure formula of the investigated family of MeBOX compounds.

In this chapter, results from charge-density investigations of the manganese, iron and cobalt complexes of the MeBOX ligand from the publication by Lüert and Legendre are investigated. These complexes will be named MnMeBOX, FeMeBOX and CoMeBOX in the following (Figure 5-1). Being easily crystallised in superb quality and highly stable, these compounds are well-suited for performing advanced diffraction experiments, MM refinement and QTAIM analysis. Main focus of this investigation will be the identification of differences between various experimental structural properties, e.g. d-orbital populations, the results of quantum chemical calculations and MM refinement against theoretical structure factors derived from them (abbreviated “theoMM” refinements). Furthermore, QTAIM results were carefully examined for possible magneto-structural relations that might assist the design of future improved SMMs.

For this study, both the MnMeBOX and the FeMeBOX compound were recrystallised from toluene without the lattice solvent THF that was present in the original publication, leading to three isostructural compounds fit for direct comparison. All investigated complexes behave in different ways when exposed to a magnetic field: FeMeBOX has no magnetic properties, both MnMeBOX and CoMeBOX show slow magnetic relaxation. As pointed out by the authors, however, only CoMeBOX matches the textbook definition of an SMM, showing slow magnetic relaxation *via* the Orbach process.^[20,108] Magnetic

relaxation in MnMeBOX, on the other hand, occurs via a photon bottleneck process,^[109] which is not a usual SMM relaxation process. Specifically, MnMeBOX is also a rare example of a manganese compound showing slow magnetic relaxation that is not a cluster, like e.g. the first reported SMM (see Chapter 5.1). A more detailed description of the physics behind both relaxation processes is beyond the scope of this thesis focussed on charge-density analysis, and can be found in the cited literature.

The concept of molecular magnetism as well as a short overview over the corresponding research field will be presented in more detail in Chapter 5.1. In Chapter 5.2, the calculation of experimental d-orbital populations from MM refinements, which is a cornerstone of this study, is explained in detail. The experimental section 5.3 deals with the process of data collection and processing as well as the execution of quantum chemical calculations, while the process of obtaining the final MM refinement is presented in Chapter 5.4. Results of QTAIM analysis and comparison between experimental and theoMM properties can be found in Chapter 5.5, the conclusions of which can be found in Chapter 5.6.

5.1 Introduction to molecular magnetism

All traditional macroscopic magnetic materials consist of separate magnetic domains in which the spins of many atoms or molecules are aligned. In order to alter the magnetisation of a magnetic material, the domain walls separating have to be broken, which requires energy. Therefore, domains can persist even when an outside field is removed, and the magnetisation remains as the magnetic domains persist. In SMMs, these processes are similar, however, unlike traditional magnets, the magnetic domains consist of individual molecules. When an SMM is magnetised by an exterior field, the unpaired spins of the molecules align with this field, as this is the energetically most favourable orientation. If the field is then removed, magnetisation can be retained under certain conditions. In theory, with the possibility to encode data in an arrangement of “frozen” spin states, this effect can potentially be utilized in the development of highly efficient data storage media and in quantum computers,^[110] which are expected to be highly efficient in solving problems contemporary computers struggle with. Currently, however, SMMs operate only at very low temperatures, significantly hampering the use in all but the most controlled environments. Today, the highest reported blocking temperatures for SMMs are around 80 K, like for the Dysprosium complexes reported by Guo *et al.* in 2018,^[111] and Gould *et al.* in 2022.^[112]

In the light of the enormous possible benefits, the research area of SMMs gained an increasing amount of interest, with the main goal of reaching higher blocking temperatures. If unorthodox spin relaxation pathways such as quantum tunnelling are ignored, increasing the barrier to spin inversion U_B should be the feasible way of reaching this goal: The larger U_B is, the longer can magnetisation be retained, and the higher the temperature at which retention is still possible. While earlier SMM research focused on cluster compounds akin to the first reported SMM $[\text{Mn}_{12}\text{O}_{12}(\text{OAc})_{16}(\text{H}_2\text{O})_4]$ by Sessoli *et al.* in 1993,^[113] an ever-increasing number of mononuclear single-ion magnets (SIMs) based on lanthanides and d-block metals.^[114] These smaller compounds, especially the latter ones, are better suited to be investigated with computational methods and promise to obtain a more fundamental understanding of molecular

magnetism. In order to investigate molecular magnetism, a plethora of analytical methods are employed: While mainly physical magnetic properties like temperature dependency of magnetic hysteresis are usually characterized *via* SQUID magnetometer measurements (from Superconducting QUantum Interference Device), several chemical approaches are employed to provide insights in magneto-structural relationships with the goal of aiding the design of more potent SMMs. A key discovery for recent efforts in the design of SMMs is that a high magnetic anisotropy, meaning high differences in magnetic susceptibility from different direction, facilitates a slow magnetic relaxation. This is commonly referred to as the existence of an *easy axis* for magnetisation. Magnetic anisotropy is caused by unquenched orbital angular momentum within the compound. For d-metal compounds, this occurs as a first order effect when an uneven number of electrons is situated in degenerate ($d_{x^2-y^2}$, d_{xy}) and (d_{xz} , d_{yz}) orbital pairs.^[115] However, as the ligand field of d-metal complexes is heavily influenced by the ligand field, this is often not the case, hence the OAM is quenched. Even in this case, so called *second order unquenched OAM* can arise from an interaction between the required orbitals over a small energy gap. The existence of these interactions, in turn, leads to a phenomenon called *zero-field splitting* (ZFS), where both the ground state and an excited induced by mixing with a higher orbital are populated without the presence of an outside field. ZFS is quantified by the zero-field splitting parameter D , whereas $|D|$ is inversely proportional to the separation between two sets of orbitals with different populations. For example, a low energetic gap between the highest double occupied and the lowest single occupied d-orbital can facilitate a large spin-orbit coupling, which, in turn favours ZFS. Furthermore, it has been suggested by studies of Zadrozny *et al.* that magnetic anisotropy is fostered by ligands with a soft main group donor and a high covalent contribution in the metal-ligand bonding,^[116] making the nitrogen-coordinating BOX ligand worthwhile candidates. Due to the large influence of the ligand field on orbital energies in d-metal complexes, ligand design is one major tool for shaping d-orbital energies in a favourable way. In a recent publication, Legendre *et al.* reported that there is, in fact, an optimal bite angle for nitrogen-coordinating distorted tetrahedral cobalt complexes of 76-78°, which leads to the near-degeneracy and there, a near minimal aforementioned energy gap.^[117]

Lately, several studies of single crystal X-ray charge-density analyses of SMM compounds have been published.^[31,32] Charge-density analysis of high-resolution SCXRD datasets is a well-established method which is known to provide key structural insights like the characterization of chemical bonding and a more exact localisation of ED. Specifically, experimental d-orbital populations can be straightforwardly determined from the Hansen & Coppens MM, from the obtained relative populations of d-orbitals, from which the relative orbital energies can be concluded. Details on the calculation of the orbital populations can be found in Chapter 5.2. Using synchrotron data and the latest detector technology, a recent publication by Overgaard *et al.* demonstrated it is possible to obtain such experimental d-orbital populations with remarkable accuracy.^[32] While neither CoMeBOX nor MnMeBOX exhibit their magnetic properties without the application of an outside field, investigation of their ligand–metal interactions and d-orbital populations compared to the non-magnetic FeMeBOX

could still have merit for the unveiling of certain magneto-structural relations. An applied magnetic field generally only affects the spin of the electrons within the complex, but does not directly affect orbital populations. The method by which d-orbital populations can be obtained will be explained in the following.

5.2 Experimental d-orbital populations from the multipole model

Multipole parameters obtained from a MM refinement can be used to calculate d-orbital populations using the method of Holladay, Leung and Coppens.^[30] This approach utilizes the fact that the d-electron density in terms of atomic orbitals $\rho_{d,AO}$ can be written in terms of the same spherical harmonics used in the multipole model for describing the aspherical density component of total electron density $\rho_{d,MM}$.

$$\rho_{d,AO} = \sum_i \sum_{j \geq i} P_{ij} d_i d_j \quad (\text{Eq. 36})$$

$$\rho_{d,MM}(\mathbf{r}) = \sum_{l=0}^{l \max} \kappa'^3 R_l(\kappa' \mathbf{r}) \sum_{m=-l}^l P_{lm} d_{lm}(\theta, \Phi). \quad (\text{Eq. 37})$$

If the radial functions of d_i and d_{lm} are equal, they can be expected to cancel each other. If the respective d-orbital populations are written in form of a vector \mathbf{P}_{ij} and the multipole populations in vector \mathbf{P}_{lm} , obtaining in both cases the unique elements of the matrices defined by equations 36 and 37, there are therefore related by a conversion matrix M with

$$\mathbf{P}_{lm} = M \mathbf{P}_i \quad (\text{Eq. 38})$$

and it is therefore

$$\mathbf{P}_i = M^{-1} \mathbf{P}_{lm}. \quad (\text{Eq. 39})$$

Depending on the local symmetry of the d metal ion, only certain multipole parameters that correspond to the shape of the d-orbitals are considered, and therefore, only those multipoles should be refined. In the case of the isostructural compounds described in this chapter, these relevant multipole parameters are monopoles, quadrupoles and hexadecapoles. Like d-orbitals, but unlike dipoles and octupoles, they are centrosymmetric. The respective Matrix M^{-1} can be found in the publication by Holladay *et al.*^[30] In order to obtain d-orbital populations from this method that are comparable to those obtained by theoretical calculations, the same radial functions have to be used in both the calculation and the multipole refinement. As a default, the MM refinement program used for this work, *XDLSM* from the *XD2016* program suite (in short: XD),^[69] uses single-zeta Slater functions for the description of aspherical density (CSZD option). However, it was recently shown by Damgaard-Møller *et al.*^[32] that in order to obtain results comparable with theoretical d-orbital population from the widely used *ORCA*

software for quantum chemical calculations, radial functions based on Hartree-Fock calculations have to be chosen in XD instead (CHFW option).^[48] Additionally, special care has to be taken with the local coordinate system of the atom in question, as even minor changes in its orientation can lead to significant changes in the resulting populations.^[118]

5.3 Experimental

This chapter contains information about the data collection and reduction of MnMeBOX, FeMeBOX and CoMeBOX. Data collection of the analogue complexes of the similar ligand bis(4-H-benzoxazol-2-yl)methanide ligand replacing the methyl group attached to the benzoxazole moieties with hydrogen atoms, as published as well in the same publication by Lüert, Legendre *et al.*,^[20] was also attempted. While these compounds, too, are easily synthesised and crystallised, with maximum resolutions not higher than around 0.6 Å for even the most promising crystals, none of the structures reached the necessary resolution requirements for charge-density analysis.

5.3.1 Data collection and processing:

Crystals for all compounds were crystallised from toluene. In general, crystallisation was a straightforward process, and crystals of suitable size and quality were easily available. Data collection was performed at 100(2) K, mainly on a Bruker D8 *Venture* three-circle goniometer equipped with a PHOTON III detector, a TXS Mo rotating anode, Incoatec Helios mirror optics and a Bruker Kryoflex II cooling device. However, two additional datasets were collected for CoMeBOX, the data collection for which turned out significantly more challenging. A list of the different datasets discussed in this chapter can be found in Table 5-1 below.

Table 5-1: Setups and maximum resolutions used for the different datasets discussed in this chapter. While all datasets were initially collected up to a slightly higher resolution, due to data quality limitations, the limit given here was chosen for integration.

Structure	Radiation Source	Detector	Maximum resolution	Rrim / Rpim (all)
CoMeBOX 1	Mo TXS	APEXII	0.47 Å	0.0320 / 0.0077
CoMeBOX 2	Mo TXS	PHOTONIII	0.47 Å	0.0444 / 0.1090
CoMeBOX 3	Ag I μ S	PHOTONIII	0.47 Å	0.0341 / 0.0782
MnMeBOX	MoTXS	PHOTONIII	0.49 Å	0.0412 / 0.0104
FeMeBOX	MoTXS	PHOTONIII	0.49 Å	0.0365 / 0.0099

The first dataset for this project was collected for the CoMeBOX compound in early 2019, when the used Mo-TXS diffractometer was still equipped with an old APEXII detector. While a well-diffracting crystal could be quickly identified, all tested crystals turned out to be *too* well-diffracting instead. Even with the shortest reasonable exposure time of 1 second per 0.5° frame, most of the inner reflections were overexposed and could therefore not be reliably measured. In addition to resorting to an extremely low

exposure time, an aluminium attenuator had to be placed in the beam in order to collect these reflections. However, while the obtained “fast scans” included all previously missing reflections, they were of suboptimal quality compared to the other runs, leading to questionable d-orbital populations in the final MM refinement. Two additional data sets were collected together with Dr. Christopher Golz on diffractometers equipped with a new Photon III detector, once again with aforementioned Mo-TXS source and once with Ag-I μ S source. The new detector, equipped with a built-in attenuator as well as higher dynamic range and a higher detector area, yielded significantly better results. A comparison of various data and model quality indicators was used as a guideline to decide on a dataset for final evaluation. While both of these datasets showed reasonable model quality, the Mo dataset was used in the end due, among other factors, a more reasonable distribution of residual density in the final MM. A short comparison between the three datasets is presented in Table 5-2 below, while a full list can be found in the Appendix (10.6.1).

For both FeMeBOX and MnMeBOX, data collection was more straightforward. Both datasets were collected with the Mo-TXS Photon III setup, albeit to a slightly lower maximum resolution of 0.49 Å. All datasets were integrated with active masks for beamstop and parts of the cooling nozzle appearing on the frames. Resolution limits were chosen for each run separately to minimize empty detector space for runs with low exposure time intended to collect inner data. To account for resolution-dependent errors in the data as described in 3.2.2, an integration with fixed box size was performed for all compounds. For all measurements, an integration box with fixed size 0.6, 0.6, 0.8 turned out to provide the best results. In the case of the later discarded first CoMeBOX dataset, this fixed box size was only applied to the outer data with $\sin \vartheta / \lambda > 1$, while a refined integration box was used for inner the inner data. IAM structure refinement and starting model generation were handled as described in Chapter 4.2.3.

Table 5-2: Data and model quality indicators from MM refinement against all collected datasets of CoMeBOX. Model quality indicators are based on a Co²⁺ refinement with isotropic hydrogen atoms (see 5.4). Due to the highest completeness, reasonable GoF and overall lower e_{gross} value than the competing dataset 3, dataset 2 was chosen for final refinement and evaluation. Model quality indicators were determined based on refinement according to the strategy shown in Table 5-3.

CoMeBOX Dataset	1*	2	3
Rrim/ Rpim	0.0320 / 0.0077	0.0444 / 0.1090	0.0341 / 0.0782
Completeness	98.82	99.82	99.80
$wR(F^2)$	0.0328	0.0313	0.0243
GoF	3.0919	1.4769	1.4986
$\Delta\rho_{\text{min}}, \Delta\rho_{\text{max}}$ [$e\text{\AA}^{-3}$]	-0.441, 0.421	-0.450, 0.311	-0.429/0.126
e_{gross} [e]	39.7	43.4	53.2

*For dataset 1, the 3σ cutoff could not be fully released due to large refinement instability. Results here are from a 2σ cutoff refinement.

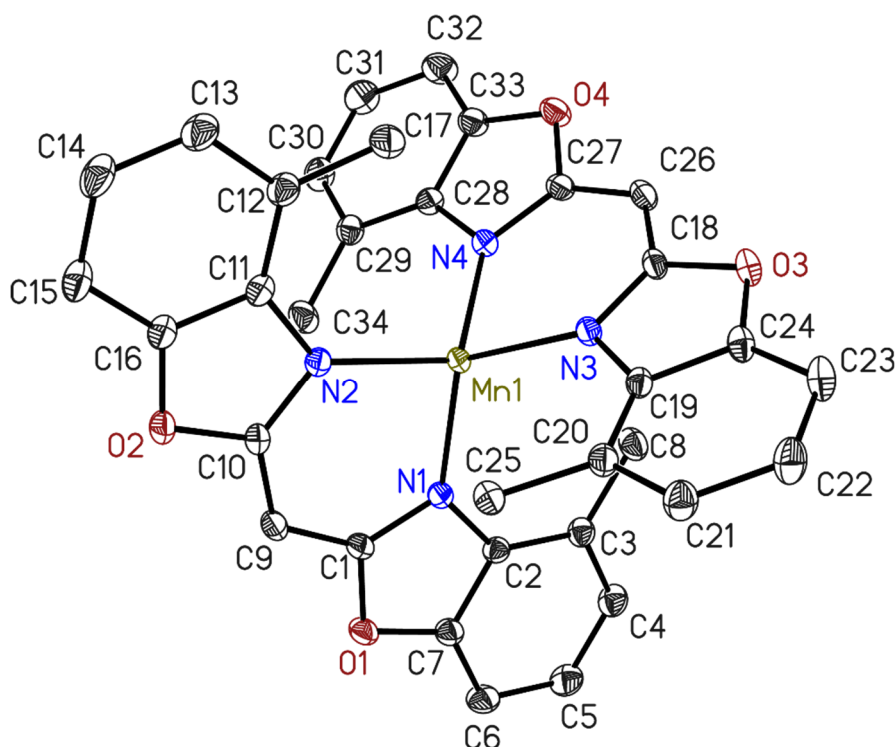


Figure 5-2: Molecular structure of MnMeBOX. Anisotropic displacement parameters are displayed at the 50% probability level. Hydrogen atoms are omitted for clarity. FeMeBOX and CoMeBOX are isostructural and follow the same labelling convention.

5.3.2 Temperature-dependent study of CoMeBOX

At the time when dataset 2 and dataset 3 were collected, the question was posed whether temperature wear on the crystal, beyond the aforementioned overexposed inner reflections and poor-quality fast scans, was an additional factor in the problematic data quality of the first measurement. At the time, the first measurement was interrupted by a filament break of the TXS rotating anode, which forced a postponement of about three months. The chosen crystal of CoMeBOX, being air-stable, was kept in inert oil for the time did not visibly suffer in quality over this time. Reflection shape and maximum resolution between measurements were compared and no deterioration was noticed.

During the process of measurement postponement, the crystal was mounted and de-mounted several times, and thus cooled down to 100 K and warmed up to room temperature. At the time of the other two measurements, before the actual measurements, a temperature-dependent measurement series was conducted to foreclose the possibility of a small-scale non-destructive phase transition that occurs in the cooling process. While an overlay of the room temperature structure with the one collected at 100 K revealed them to be identical, a small drop in the otherwise linearly decreasing unit cell volume was noticed, especially in the *a* and *c* cell lengths (Figure 5-3). While no phase transition could be detected, deteriorating data quality due to temperature strains in the crystal still remain a possibility.

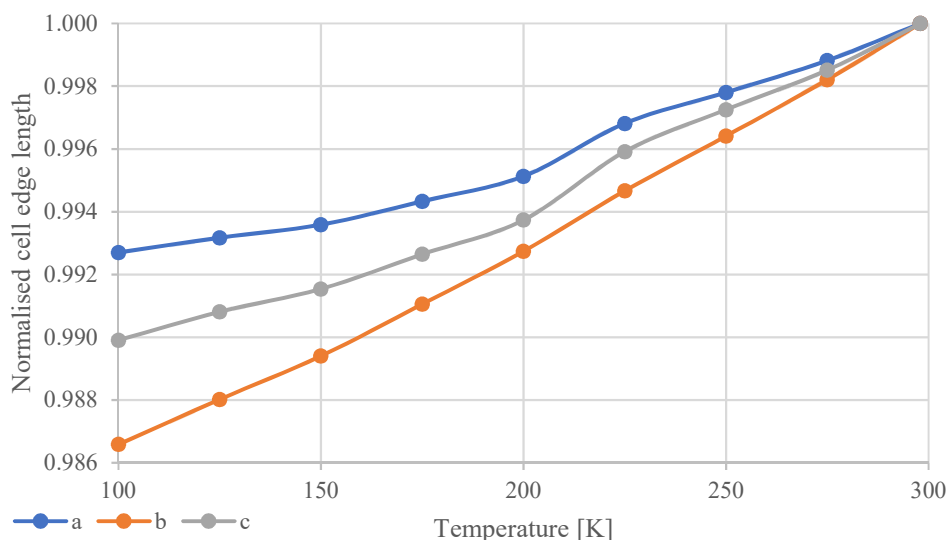


Figure 5-3: Unit cell edge lengths a, b, c plotted against temperature. Cell lengths are referenced on values at 298 K. A small deviation from otherwise linear descent can be seen between 225 K and 200 K. However, this change does not correspond with any changes in the arrangement of atoms in the unit cell.

5.3.3 Theoretical study

For all compounds, Complete Active Space Self-Consistent Field (CASSCF) calculations^[119] up to the def2-TZVP level and taking into account spin orbit coupling were performed in the *ORCA* 5 program with the help of Katharina Rachuy from the Stalke Group and Hannah Hedegaard Nielsen from the group of Prof. Jacob Overgaard.^[32] These calculations were used in order to obtain theoretical d-orbital energies, populations and theoretical structure factors. For CASSCF calculations, an active space is defined as the focus of the calculations. In the case of the investigated d-block complexes, the five d-orbitals were chosen, written in the following as CASSCF(5,5). Then, a wave function with contributions from all possible electronic configurations in these active orbitals is calculated. This method is sufficient to obtain adequate wave functions and geometries. However, in order to obtain accurate orbital energies, dynamic electron correlation has to be accounted for as well. In *ORCA* 5, the n-electron valence state perturbation theory (NEVPT2) option can be used to achieve this. From the resulting wave function files, theoretical structure factors were obtained with the method by Genoni *et al.*^[120] which, unlike the commonly used *DENPROP*,^[102] accounts for the spin-orbit-coupling component of the wavefunction. A previous attempt of generating theoretical structure factors in *DENPROP* led to unreasonable d-orbital populations and was therefore discarded. The resulting theoretical d-orbital populations will be presented and discussed in Chapter 5.5.4. Exact inputs such as the number of states (“Roots”) accounted for in the calculations per structure can be found in the Appendix (Chapters 10.4.7, 10.5.7, 10.6.7).

5.4 Multipole model refinement

Structure solution for all three compounds was done in *SHELXT* using direct methods.^[44] Starting models for MM refinement was generated from a standard IAM refinement with *SHELXL*^[70] in the *ShelXle* GUI.^[71] The multiple refinements were conducted in the *XD2016* program suite.^[69] As all three compounds are isostructural, very similar refinement strategies could be used for them (see Table 5-3). In particular, all structures used identical local coordinate systems for all atoms except the different metal centres. For these, local coordinate systems for d-orbital determination were taken exactly from the performed quantum chemical calculations. According to results, the z axis for manganese and cobalt is oriented roughly towards the centre point between the two nitrogen atoms of the first ligand. For Fe, it is instead oriented towards the centre of the longer edge of the distorted coordination tetrahedron, though not exactly on it (Figure 5-4). In accordance to Chapter 5.2, the CHFW radial function option was chosen for the aspherical valence density. While only quadrupole and hexadecapole parameters are considered for d-orbital determination, a refinement including the other multipole parameters was tested as well. Refining these parameters, while not relevant for orbital populations, could potentially “absorb” irregularly shaped ED around the metal centre and thus improve the obtained d-orbital populations. However, as dipole and octupole parameters expectedly refined to values near zero for all tested refinement strategies, in the end, only quadrupoles and hexadecapoles were refined for these atoms. A large number of different models for the central metal atom were tested for all compounds, only the most relevant of which will be discussed here. First testing was mainly performed on the CoMeBOX compound, which was first measured, but results from this testing held true for the other two compounds.

A major decision point was the way in which the charge of the ion should be handled. Refinements for the metal centre both with neutral M and M^{2+} scattering factors from the SCM databank^[121] were compared. On one hand, all compounds should contain high-spin metal ions with a charge of +2, while each of the ligands has a charge of -1. Due to the energetic sequence of the higher most orbitals of a d-metal, the 4s electrons can be expected to leave the central metal ion before any d electrons. To model this in the M^{2+} refinement, in the input files for XD, the two 4s electrons of the metal ion were moved to be valence electrons in the d shell instead. These two electrons were then equally distributed towards the coordinating nitrogen atoms. On the other hand, a model with M instead of M^{2+} should contain more degrees of freedom for the refinement and thus be better suited for intermediate states where the absolute value of transferred electrons is not quite an integer. For this, the two 4s electrons were placed in the spherical valence electrons of the metal centre instead of the nitrogen, which was then refined as neutral. Differences in model quality were small, as seen in Table 5-4.

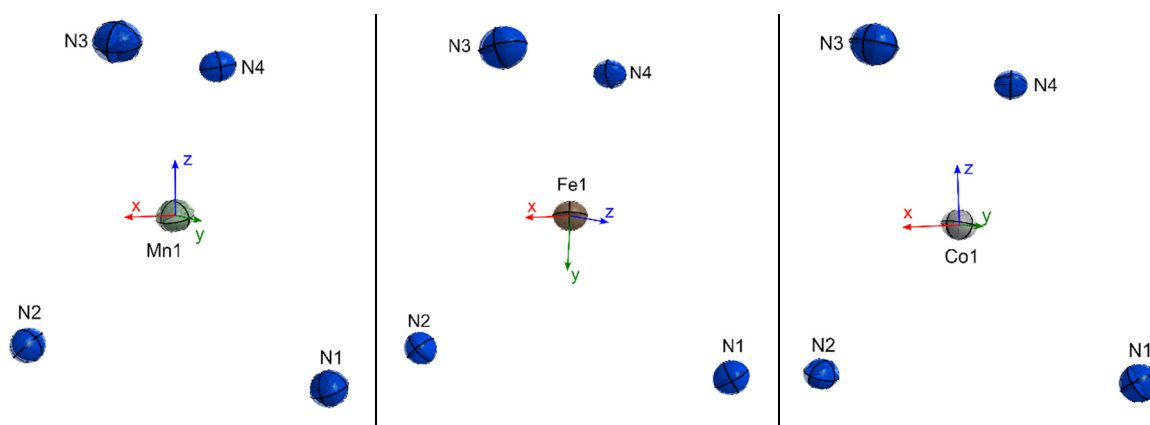


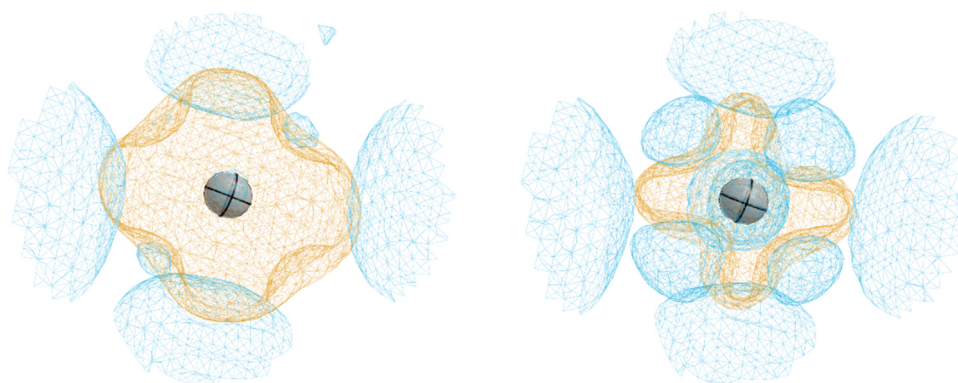
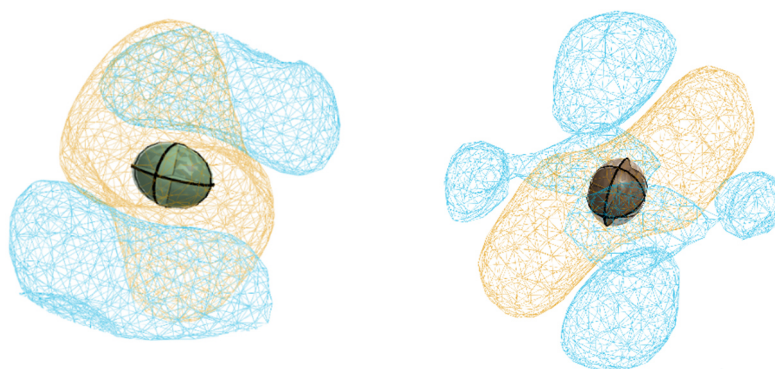
Figure 5-4: Local coordinate systems chosen for the three investigated compounds, which were taken directly from CASSCF(5,5)/NEVPT2 calculations. For MnMeBOX and CoMeBOX, the z axis is pointing roughly towards the midpoint between nitrogen atoms of the same ligand (N3/N4), while the y axis is pointing towards the midpoint between nitrogen atoms from different ligands (N1/N3). For FeMeBOX, the directions of z and y axis are switched.

Table 5-3: General refinement strategy for the three compared d metal compounds. Parameter names are the same as for the standard MM strategy introduced in Chapter 3.1. Step 12 and 13 highlighted in green were only valid for the manganese structure. Obviously, the last step was omitted when tabulated neutron ADPs from the SHADE server were used. Full details on the development of final strategies and the checking for overfitting can be found in the Appendix (10.4.4, 10.5.3, 10.6.3).

Step	Refined parameters (<i>new</i>)
1	SCALE
2	M
3	M DQOH
4	M DQOH U_{ij}
5	M DQOH U_{ij} xyz
6	M DQOH U_{ij} xyz κ
7	Hxyz
8	M DQOH U_{ij} xyz κ
9	κ'
10	M DQOH U_{ij} xyz κ
11	Sigobs 0
12	Nocon N3/N4
13	Nosymm N3/N4
14	AnisoH+Q0

Table 5-4: Model quality indicators in comparison for the various neutral M and M²⁺ refinements, based on a refinement with isotropic hydrogen atoms.

Model	Mn	Mn ²⁺	Fe	Fe ²⁺	Co	Co ²⁺
$wR(F^2)$	0.0278	0.0280	0.0273	0.0274	0.0310	0.0313
GOF	1.4710	1.4775	1.7068	1.7155	1.4661	1.4769
$\Delta\rho_{\min}, \Delta\rho_{\max}$ [eÅ ⁻³]	-0.339, 0.290	-0.353, 0.294	-0.567, 0.418	-0.590, 0.419	0.429, 0.308	-0.450, 0.311
e_{gross} [e]	41.8	41.8	47.1	47.2	43.2	43.4


 Figure 5-5: Deformation density at the $\pm 0.11 \text{ e}\text{\AA}^{-3}$ isolevel of the Co (left) and Co²⁺ (right) refinement detailed above, viewed from the y axis of the local coordinate system. Positive density is displayed in blue. Negative density is displayed in orange. Observations regarding the difference between M and M²⁺ models are comparable for the MnMeBOX and FeMeBOX structure.

 Figure 5-6: Deformation density around the central metal ion of MnMeBOX, viewed along the y axis (left, isolevel $\pm 0.14 \text{ e}\text{\AA}^{-3}$) and FeMeBOX, viewed along the z axis (right, isolevel $\pm 0.11 \text{ e}\text{\AA}^{-3}$). Positive density is displayed in blue. Negative density is displayed in orange.

As seen in the Table 5-4, all M refinements produce slightly better model quality indicators compared to the M^{2+} refinement. However, an inspection of the deformation density around the metal centre of all investigated as well. Here, in both M and M^{2+} refinements, the shape of deformation density is dictated by the d-orbitals modelled by the multipoles. When compared between the M and M^{2+} models, the deformation density for the M^{2+} model looked more in line with the expectations for d-orbital shape (Figure 5-5). As the differences in the properties of the two different model approaches were negligible, in the end, the M^{2+} approach was chosen for all compounds. Deformation density for the respective final models can be found in Figure 5-5 right and Figure 5-6.

Refinement started from a basic multipole refinement strategy which was then checked for possible expansion using the cross-validation routine by Krause *et al.* to check for validity.^[78] No signs of anharmonic motion were detected, and release of the usual chemical constraints only prove valid for two nitrogen atoms in the Mn structure: Here, independent multipole parameters were refined for the nitrogen atoms in the second ligand. An anisotropic description of hydrogen atoms was attempted in the final model. For this, ADPs from the SHADE server^[75] were compared to ADPs from free refinement against the X-ray data with added bond-directed Q0 quadrupoles for hydrogen atoms. As will be described in more detail in Chapter 6, the hydrogen ADPs from refinement against the high-resolution X-ray data were carefully checked for validity and found sufficient. No unreasonably elongated ellipsoids are visible, and the Hirshfeld test detected no unreasonable differences between ADPs of similar hydrogen atoms. For the manganese structure, the κ parameter associated with the methyl carbon atoms would not converge in the refinement with freely refined hydrogen ADPs, instead alternating at an order of magnitude of 0.02. Meanwhile, the refinement converged for the cobalt and iron compounds. For comparability with the other two models which benefit greatly from the anisotropic refinement compared to shade, this method was chosen for MnMeBOX as well. The properties of the SHADE refinement were nevertheless examined, and no grievous incongruence was noticed. Therefore, all properties discussed in 5.5 will be based on refinements with freely refined hydrogen ADPs. Model quality indicators for tested refinements with anisotropic hydrogen ADPs can be found in Table 5-5. As this study primarily focusses on properties of the metal centre and its surrounding nitrogen atoms, differences between the desired properties can be expected to be small for the different ADP approximation methods.^[51] X-H Hirshfeld test values for all hydrogen ADP refinements can be found in the Appendix (Chapters 10.4.5, 10.5.4, 10.6.4).

Table 5-5: Model quality indicators in comparison for the various refinements with hydrogen ADPs, based on the M^{2+} refinements discussed earlier in this chapter (see Table 5-4). ADPs for refinements labelled “SHADE” were taken from the SHADE2.1 server. Hydrogen ADPs for refinements labelled “Aniso” were freely refined against the high-resolution X-ray data with addition of Q0 quadrupoles, in accordance to Chapter 6 and the resulting publication.^[51]

Model	Mn (SHADE)	Mn (Aniso)	Fe (SHADE)	Fe (Aniso)	Co (SHADE)	Co (Aniso)
$wR(F^2)$	0.0278	0.0265	0.0271	0.0193	0.0304	0.0291
GOF	1.4697	1.4043	1.6955	1.6364	1.4345	1.3806
$\Delta\rho_{\min}, \Delta\rho_{\max}$ [eÅ ⁻³]	-0.357, 0.298	-0.382, 0.281	-0.570, 0.435	-0.602, 0.422	-0.434, 0.330	-0.461, 0.311
e_{gross} [e]	42.6	41.4	47.5	46.7	43.3	42.7

In the final refinement, the structure factor plots for Mn and Co are relatively straight and reveal no further problems. They can be found in the Appendix, together with the normal probability plots for all compounds, which were unproblematic as well (Chapters 10.4.6, 10.5.5, 10.6.5). For the structure factor plot of the iron compound, however, a strong drop-off for the outer data was noticed (Figure 5-7). This is presumably caused by weak outer data. While data for FeMeBOX was collected up to a resolution of 0.49 Å, and even for the outermost data, an I/σ value of 8.75 is reached, the mean intensities in the outer resolution shell is very low with a value of only 0.34. Further data quality information about all datasets can be found in the Appendix (Chapters 10.4.1, 10.5.1, 10.6.1). First, a refinement with 10 resolution-dependent scale factors was tested in order to correct this insufficiency in the outer data. Generally, refinement with ten scale factors (“10scale”) should only be used as a diagnose tool, as it will make a problematic structure factor plot near linear without directly resolving the problem that caused this shape. With the 10scale refinement, residuals dropped noticeably, and the residual electron density around the central iron atom was lowered. In the next step, a resolution cut-off at $\sin \theta/\lambda = 0.95$ was applied, which translates to a maximum resolution of roughly 0.53 Å. With this cut-off, the structure factor plot stays with $\pm 5\%$ of 1 for the entire resolution range. A comparable effect to the 10scale refinement could be reached. While this resolution is below the usual resolution limit required for charge-density investigation, it was decided that a refinement with slightly too low resolution was preferable to a refinement against weak outer data (Table 5-6). Doing so had a significant impact on structural properties derived from the final model, which will be discussed in more detail in 5.5.5. For each compound a final model with plausible quality indicators (seen in Table 5-7), reasonably shaped deformation density around the central metal atom and anisotropic hydrogen ADPs was obtained. As seen in Figure 5-8, the remaining residual density in all models is mainly centred discrete peaks around the metal centre. This is well in line with expectations, as these are the heaviest atom in the respective structures. Therefore, the obtained final models are well fit for QTAIM topological analysis.

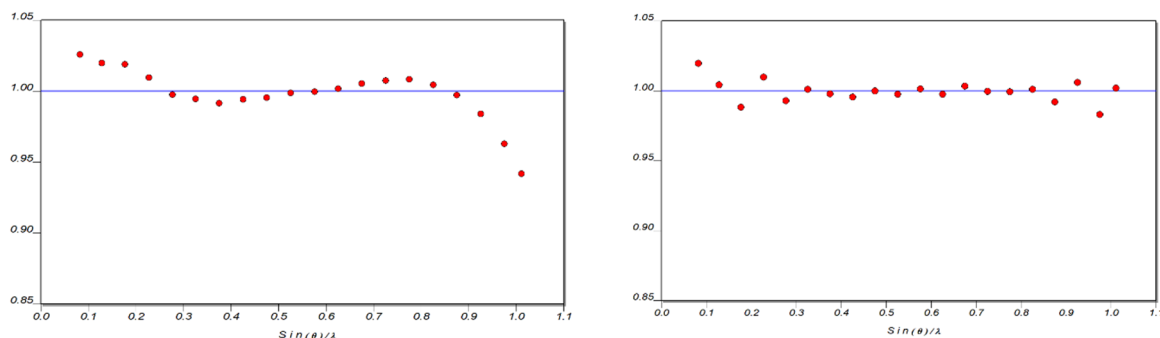


Figure 5-7: Structure factor plot for the Fe²⁺ refinement with anisotropic hydrogen ADPs, refined with one (left) and 10 resolution-dependent scale factors (right).

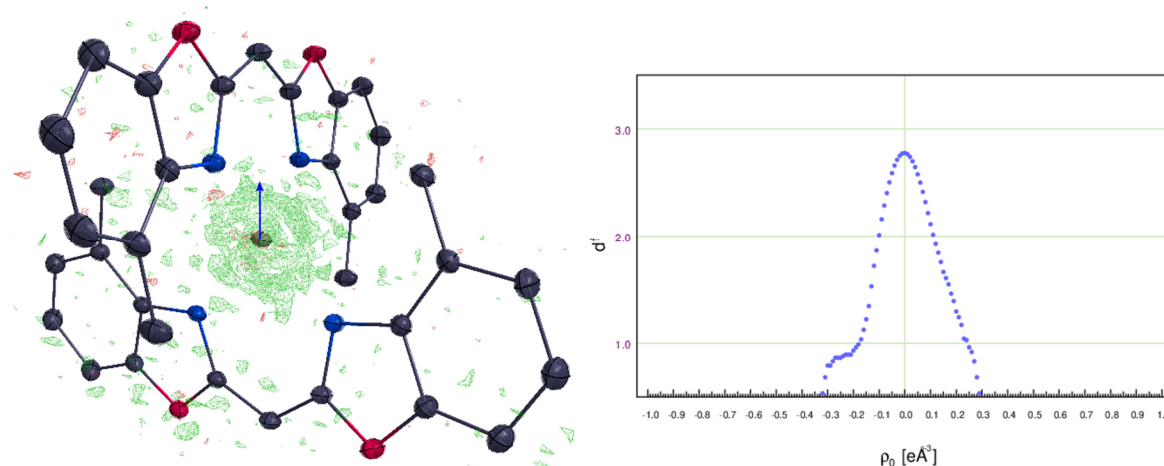
Table 5-6: Model quality indicators for the Fe²⁺ refinement with anisotropic hydrogen atom refinement. For the (10scale) column, a refinement with ten resolution-dependent scaling factors was conducted. For the (cut-off) column, a resolution cut-off at roughly 0.53 Å was applied to the refinement.

Model	Fe	Fe (10scale)	Fe (cut-off)
$wR(F^2)$	0.0273	0.0244	0.0238
GOF	1.7068	1.5301	1.6527
$\Delta\rho_{\min}, \Delta\rho_{\max}$ [$e\text{\AA}^{-3}$]	-0.567, 0.418	-0.205, 0.294	-0.195, 0.225
e_{gross} [e]	47.1	46.5	37.5

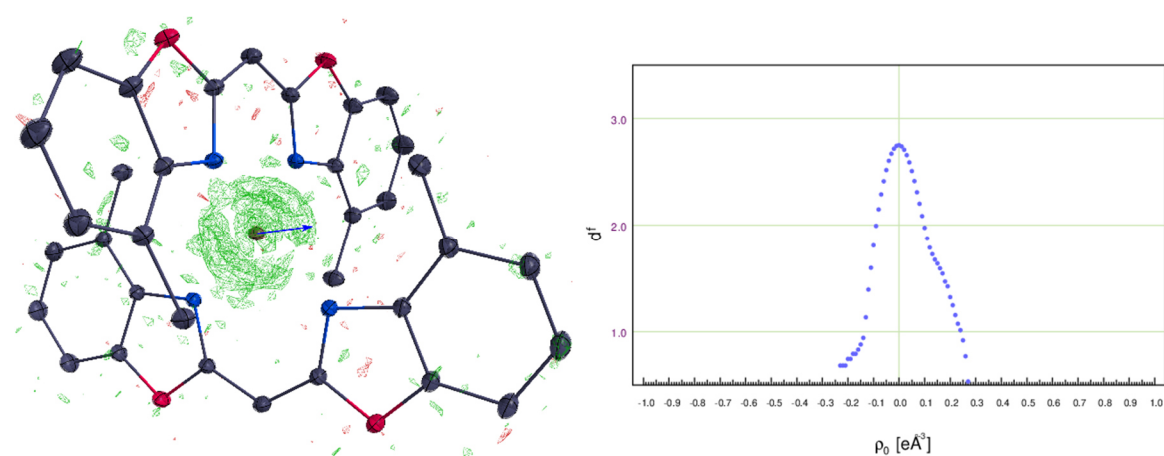
Table 5-7: Model quality indicators for the final models for each of the compounds, combined from the previous tables.

Model	Mn	Fe (cut-off)	Co
$wR(F^2)$	0.0265	0.0238	0.0291
GOF	1.4043	1.6527	1.3806
$\Delta\rho_{\min}, \Delta\rho_{\max}$ [$e\text{\AA}^{-3}$]	-0.382, 0.281	-0.195, 0.225	-0.461, 0.311
e_{gross} [e]	41.4	37.5	42.7

MnMeBOX



FeMeBOX



CoMeBOX

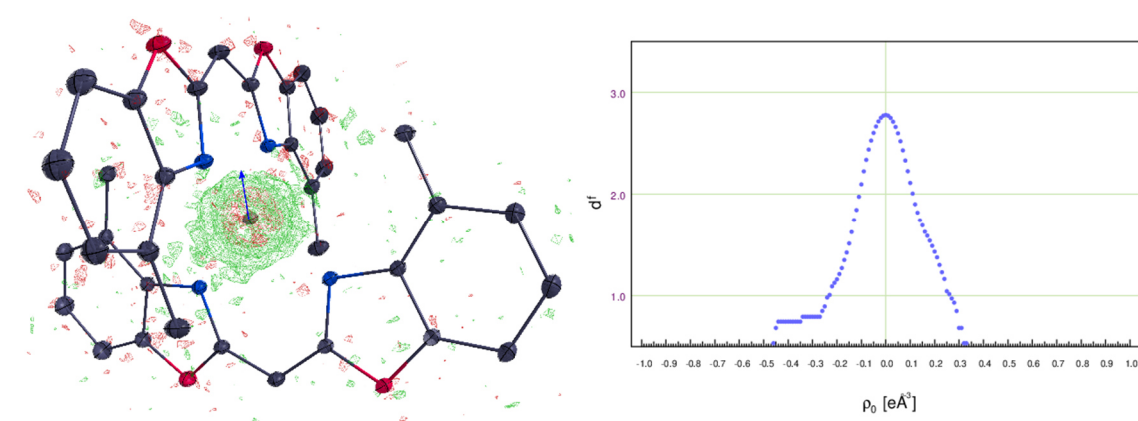


Figure 5-8: Residual density map and Henn-Meindl plot for the final refinement of investigated compounds. ADPs are displayed at the 50 % probability level. Hydrogen atoms were omitted for clarity. Residual density isolevel is $\pm 0.10 \text{ e}\text{\AA}^{-3}$ for MnMeBOX and CoMeBOX and $\pm 0.092 \text{ e}\text{\AA}^{-3}$ for FeMeBOX. Red denotes positive residual, green denotes negative residual density. The blue arrow indicates the z axis of the local coordinate system of the central metal ion.

5.5 Results and Discussion of structural properties

In Chapters 5.5.1 to 5.5.4, various structural properties of MnMeBOX, FeMeBOX and CoMeBOX are presented, discussed and compared. Then, in Chapter 5.5.5, the impact of the model choices described in 5.4 on these properties is evaluated.

5.5.1 Structural analysis

Selected bond lengths and angles around the metal centre were determined for all investigated structures, as well as the distance of the central ion to the mean plane defined by the ligand, as specified in the description of Table 5-8. As in each structure, one of the ligands appears near planar, while the other seems more bent. As a measure for this, four torsion angles were determined as a measure of to what extent the two benzoxazole moieties of each ligand are twisted against each other.

Table 5-8: Selected geometrical parameters for the compared structures. OOP denotes the out-of-plane distance of M from the mean plane through N1, N2, N1, C9, C10 for ligand 1 and N3, N4, C18, C26, C27 for ligand 2, respectively.

Angle [°]	Mn	Fe	Co
N1-M-N2	93.266(9)	95.636(9)	96.883(7)
N1-M-N3	118.847(8)	118.536(8)	113.489(7)
N1-M-N4	120.468(8)	118.462(8)	117.341(7)
N2-M-N3	119.468(8)	114.385(8)	118.465(6)
N2-M-N4	115.371(8)	117.433(8)	116.523(7)
N3-M-N4	91.804(9)	94.117(9)	95.616(7)
N1-C1-C10-N2	-2.46(5)	-2.70(5)	-1.93(4)
N3-C18-C27-N4	-10.55(5)	-10.28(5)	-9.04(4)
Distance [Å]			
M-N1	2.0966(2)	2.03442(19)	1.99191(17)
M-N2	2.0982(2)	2.0365(2)	1.99419(16)
M-N3	2.1028(2)	2.0346(2)	1.99022(16)
M-N4	2.1011(2)	2.03442(19)	1.99175(16)
OOP1	-0.0136(7)	0.0101(7)	0.0171(5)
OOP2	0.1469(6)	0.1216(7)	0.0956(5)

Bond lengths and angles for the CoMeBOX compound, which was identical to the structure published by Lüert, Legendre *et al.*, are in good agreement with values determined by their IAM refinement. While MnMeBOX and FeMeBOX were recrystallised without THF in the asymmetric unit, the loss of lattice solvent had only a minor impact on these angles and distances. The investigation of out-of-plane distances for the central metal ion arose from the fact that only for the manganese compound, the cross-

validation test for overfitting permitted the refinement of separate multipole parameters for the nitrogen atoms of both ligands. Complementing this observation, the out-of-plane distance for the central ion in MnMeBOX is the highest one of the investigated compounds, while it is the lowest for CoMeBOX. In a similar fashion to this out-of-plane distance, the twist angle between the benzoxazole moieties of the second ligand decreases from the manganese to the cobalt compound. It appears that the different OOP distances partly result from different degrees of twisting of the benzoxazole moieties in the different compounds. The bite angles of all investigated compounds are significantly higher than the reported optimal bite angle for S–N cobalt complexes. Compared to the more flexible S–N SMM complexes, the BOX ligand system provides only little room for bite angle tuning, as the only way of influencing it is by switching the substituents at the benzoxazole moieties. A comparison of CoMeBOX N–M–N bite angles between CoMeBOX and the analogue complex of the bis(4-H-benzoxazol-2-yl)methanide ligand ($92.89(12)^\circ / 92.80(12)^\circ$) published by Lüert, Legendre *et al.*,^[20] for example, reveals a mean difference near 4° . This difference is caused just by absence of the methyl groups, with no clear way of achieving intermediate steps in the angle.

5.5.2 Molecular Graph and Critical points

From the final MM refinements of the three investigated compounds, a topological analysis according to QTAIM was performed. Analysis of bond paths and critical points revealed that the molecular graph of all structures is generally complete and fulfils the HP rule, with one small exception in regions of low ED. The only BCPs in a low ED region are found on eight H–N bond paths between a nitrogen atom from one ligand and a methyl hydrogen atom of the other. Due to the twisting of the benzoxazole groups of the second ligand against each other, all these H–N bond paths are of slightly different lengths, with differences increasing with said twist angle. For the MnMeBOX structure, one RCP in these regions is not found, which leads to one additional CCP missing as well. As discussed in more detail in Chapter 4, this has no influence on the total of the HP equation, and topological parameters at these points are too low compared to estimated standard deviations to be meaningfully discussed in this work. Therefore, the molecular graphs were deemed sensible for all structures. The molecular graph of MnMeBOX is displayed in Figure 5-9. As the molecular graphs of FeMeBOX and CoMeBOX are quite similar to observation from a static, printed image, they have been omitted here and can be found in the Appendix instead (Chapters 10.5.6, 10.6.6). Properties of critical points between the ligands and the respective central ion can be found in Table 5-9 below.

A comparison between the structures reveals that as expected, electron density and Laplacian at the BCP slightly increase from the manganese to the cobalt compound with rising electronegativity. Likewise, the length of the bond path overall, as well as the distance of the BCP to the metal centre decreases in this order. The former decrease in length specifically outweighs the latter, meaning that the shortening of total bond path length between the structures is not merely caused by a decreasing distance between BCP and metal centre. Highly positive values of the Laplacian indicate, as expected, a mainly ionic bond character between the metal centre and the ligand for all compounds. Examination of the $|V_b|/G_b$

descriptor based on the method of Espinosa *et al.*, however, reveals quotients slightly below 1.00 for the N-Fe bonds, while the values slightly above 1.00 for the N-Co bonds and noticeably higher for one N-Mn bond per ligand, while they are close to 1.00 for the other two bonds. By the definition of Espinosa *et al.*, this therefore displays a covalent contribution the metal-ligand bond of CoMeBOX and especially MnMeBOX. Meanwhile, the metal-ligand interaction of FeMeBOX can be seen as purely ionic. While the discussed differences in the $|V_b|/G_b$ quotients are indeed small, they could be shown to be significant by examining the distribution of values over 20 cross validation sets for all compounds.

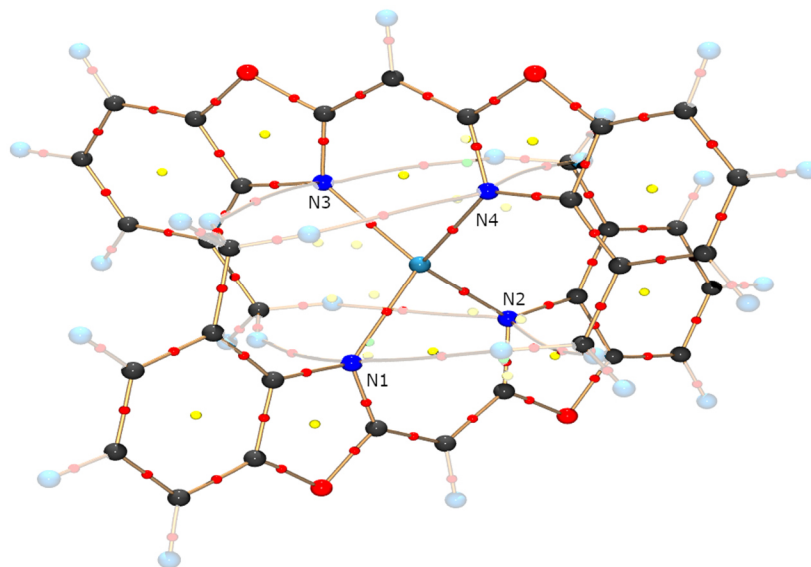


Figure 5-9: Molecular graph of MnMeBOX. Bond paths are displayed in golden, BCPs are displayed in red, RCPs are displayed in yellow, CCPs are displayed in green. Bond paths originating from/ending at hydrogen atoms are toned down for clarity. Molecular graphs of the other two structures are of very similar form and are only differentiated by minute details like slightly different bents in the H–N bond paths and one additional RCP and CCP, which is missing here.

In an attempt to further investigate these minor differences in the bonding situations, Laplacian maps in the N–M–N plane of each ligand were generated to investigate valence-shell charge concentrations (VSCCs) and depletions (VSCDs). From a three-dimensional visualisation, three distinctively different shapes of VSCDs around the compared central metal ions can be identified, which are shown in Figure 5-10. These different shapes correspond to the differently shaped deformation density in the three compounds. The total number of identified VSCDs around the metal centre is 6 for MnMeBOX, 4 for FeMeBOX and 8 for CoMeBOX. The two-dimensional Laplacian maps displayed in Figure 5-11, on the other hand, provide additional validation for the different amounts of covalent contribution to the mainly ionic ligand–metal interactions. For FeMeBOX and CoMeBOX, the VSCCs of the nitrogen atoms point towards a VSCD of the metal centre. For the N1/N4–Mn bonds in MnMeBOX, however, which show a small but noticeable amount of covalency, the VSCC of the respective nitrogen atom is aligned with a VSCCs of the manganese ion. A possible explanation for this is that the broad shape of the VSCDs of the manganese ion, which could facilitate an ionic interaction between nitrogen VSCC

an d metal VSCD even when the respective concentrations and depletions in ED are not exactly aligned. While this alignment can be found for the N2/N3 atoms in this compound as well, the VSCCs aligned with N1/N4 is stronger. A further possible explanation for the different amounts of covalency in the M-L bond of the investigated compounds are the different covalent radii of the central metal ions. With 1.37 Å, the covalent radius of manganese is clearly higher than the covalent radii of iron (1.24 Å) and cobalt (1.25 Å).

In the theoMM refinement derived from the performed CASSCF(5,5)/NEVPT2 calculations, the respective VSCCs and VSCDs are significantly less pronounced, as the extrema in the Laplacian of the theoMM ED around the metal centre appear to have a lower overall absolute value. Specifically, the peculiar differences in VSCC/VSCD alignment between the three investigated compounds as shown in figure Figure 5-11 were not reproducible from the theoMM refinement. This difference can be mainly attributed to the fact that the CASSCF(5,5)/NEVPT2 calculations do not account for metal-ligand interactions.

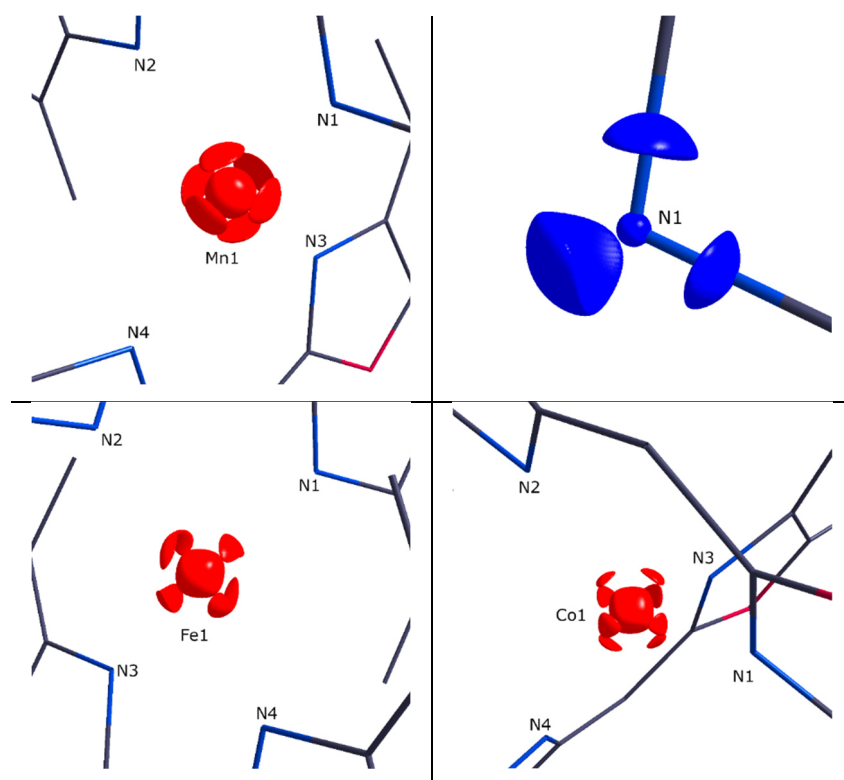


Figure 5-10: Laplacian iso surface representation of VSCCs and VSCDs around the central metal ion of the investigated compounds. Top left: VSCDs in MnMeBOX around Mn1, isolevel is $-105 \text{ e}\text{\AA}^{-5}$. Top right: VSCCs in MnMeBOX around N1. All VSCCs around nitrogen atoms in the three investigated complexes are of similar shape. Isolevel is $40 \text{ e}\text{\AA}^{-5}$. Bottom left: VSCDs in FeMeBOX around Fe1, isolevel is $-150 \text{ e}\text{\AA}^{-5}$. Right: VSCDs in CoMeBOX around Co1, isolevel is $-230 \text{ e}\text{\AA}^{-5}$.

Table 5-9: Selected parameters at the BCPs around the metal centre of investigated compounds. $\rho(r_{\text{BCP}})$: Charge-density at the BCP, $\nabla^2\rho(r_{\text{BCP}})$: Laplacian at the BCP, d_{BP} : Length of the bond path, $d_{l/2\text{BC}}$: distance of atom 1/2 to the BCP, $H_{\text{b}}(r_{\text{BCP}})$: Total electrical energy density at the BCP, $G_{\text{b}}(r_{\text{BCP}})$: Kinetic energy density at the BCP, $V_{\text{b}}(r_{\text{BCP}})$: potential energy density at the BCP. Values are rounded to the last significant decimal, which was estimated from the standard deviation of the respective values over 20 cross-validation sets.

A1	A2	$\rho(r_{\text{BCP}})$ [eÅ ⁻³]	$\nabla^2\rho(r_{\text{BCP}})$ [eÅ ⁻⁵]	d_{BP} [Å]	$d_{l/2\text{BC}}$ [Å]	$d_{2\text{BCP}}$ [Å]	$H_{\text{b}}(r_{\text{BCP}})$ [E _h Å ⁻³]	$G_{\text{b}}(r_{\text{BCP}})$ [E _h Å ⁻³]	$V_{\text{b}}(r_{\text{BCP}})$ [E _h Å ⁻³]	$ V_{\text{b}}/G_{\text{b}} $
Mn1	N1	0.50	8.52	2.097	1.043	1.054	-0.05	0.65	-0.70	1.08
	N2	0.45	8.41	2.098	1.030	1.071	-0.02	0.61	-0.63	1.03
	N3	0.46	8.49	2.103	1.033	1.070	-0.02	0.62	-0.64	1.03
	N4	0.48	8.46	2.101	1.036	1.065	-0.04	0.63	-0.67	1.06
Fe1	N1	0.47	10.12	2.035	0.992	1.043	0.01	0.7	-0.69	0.99
	N2	0.48	10.12	2.037	0.996	1.041	0.01	0.71	-0.70	0.99
	N3	0.45	10.33	2.036	0.983	1.052	0.03	0.69	-0.66	0.96
	N4	0.48	10.27	2.038	0.997	1.041	0.01	0.71	-0.71	1.00
Co1	N1	0.55	11.32	1.992	0.968	1.024	-0.03	0.82	-0.85	1.04
	N2	0.54	11.27	1.994	0.966	1.028	-0.02	0.81	-0.83	1.02
	N3	0.54	11.42	1.991	0.965	1.026	-0.02	0.82	-0.84	1.02
	N4	0.53	11.48	1.992	0.962	1.030	-0.01	0.81	-0.82	1.01

Table 5-10: Selected Bader charges of the three investigated compounds. Results from theoMM refinement are written in brackets behind the respective values. Last significant decimals were estimated from comparison between 20 cross-validation sets. All values have an estimated ESD of 0.02.

	Mn	Fe	Co
M	+1.76(+1.72)	+1.76 (1.68)	+1.71(+2.12)
⟨N⟩	-1.13 (-1.12)	-1.02 (-1.12)	-0.97 (-1.12)
⟨O⟩	-1.01 (-1.13)	-1.02 (-1.09)	-1.00(-1.12)
Σ_{Ligands}	-0.85, -0.89 (-0.85, -0.85)	-0.87, -0.85 (-0.83, -0.83)	-0.86, -0.83 (-1.02, -1.03)
Σ_{Total}	+0.03 (+0.02)	+0.04 (+0.01)	+0.02 (+0.06)

5.5.3 Bader charges and Source function

Atomic basins were integrated for all atoms in the three investigated compounds. Bader charges of the central metal ions as well as the coordinating nitrogen atoms can be found in Table 5-10 above. Notably, positive Bader charges at all three central metal ions are lower than the expected charge of +2. Accordingly, the total negative charge of each ligand is slightly lower than the expected value of -1. The sums of all atoms within each of the structures therefore still amounts close to zero, which fits the expectations for neutral compounds. For the manganese structure, the Bader charges of the coordinating nitrogen atoms are slightly, but significantly higher than for the other two compounds. This higher mean value is caused by a general increase of Bader charges for all nitrogen atoms, not by single atoms with significantly higher charge. In particular, while N1/4 and N2/3 show slightly different bonding situations with the central metal ion, no differences in Bader charges were noticed between these two groups of nitrogen atoms. To counteract this, the positive charge at the adjacent carbon atoms linking the two benzoxazole groups is slightly lower, while Bader charges in other parts of the ligand remain unchanged compared to the ligands in the other two structures. A possible explanation for this could be that the higher covalent contribution to metal ligand bonding causes a stronger concentration of ED around the nitrogen atoms.

In order to gain additional insight into charge delocalisation within the compounds, the source function descriptor by Gatti *et al.* was used.^[87] As previously described in Chapter 3.3.3, the source function descriptor can be used to analyse delocalisation of electron density within in a structure. For each atom, the integrated source function provides a measure for the influence of atomic ED towards the ED at a pre-determined reference point. Usually, BCPs are chosen as these reference points. Choosing the N-M BCPs as reference points reveals a slight contribution from all atoms of both ligands, which is comparable for all three compounds. This effect can be seen as sign for delocalisation of ED from the ligand towards the stabilisation of the metal centre, and appears to be ligand-specific rather than dependent on the metal ion. Values are comparable between all three d-metal BOX complexes as well as the AlH₂MeBOX compound investigated in the previous chapter. Therefore, a comparison of these values with analogue complexes with slightly altered BOX ligands would be extremely worthwhile. However, as previously mentioned in Chapter 5.3, it was not possible to collect sufficient high-resolution diffraction data of the analogue complexes of the BOX ligand without methyl groups. When comparing the impacts of different central metal ions on reference points throughout the molecule, the most apparent discrepancies, albeit small, can be found in their contribution to the BCPs of the M-N bonds. Determining the integrated source function in XD, contributions towards reference point ED can be differentiated in their core density and valence density component. While relatively high estimated standard deviations for these percentage contributions makes a further separation generally infeasible for small contributions, contributions of atoms to directly neighbouring BCPs should be sufficiently large so that even small differences become significant. A list of contributions towards BCP_{N-M} reference points can be found in Table 5-11.

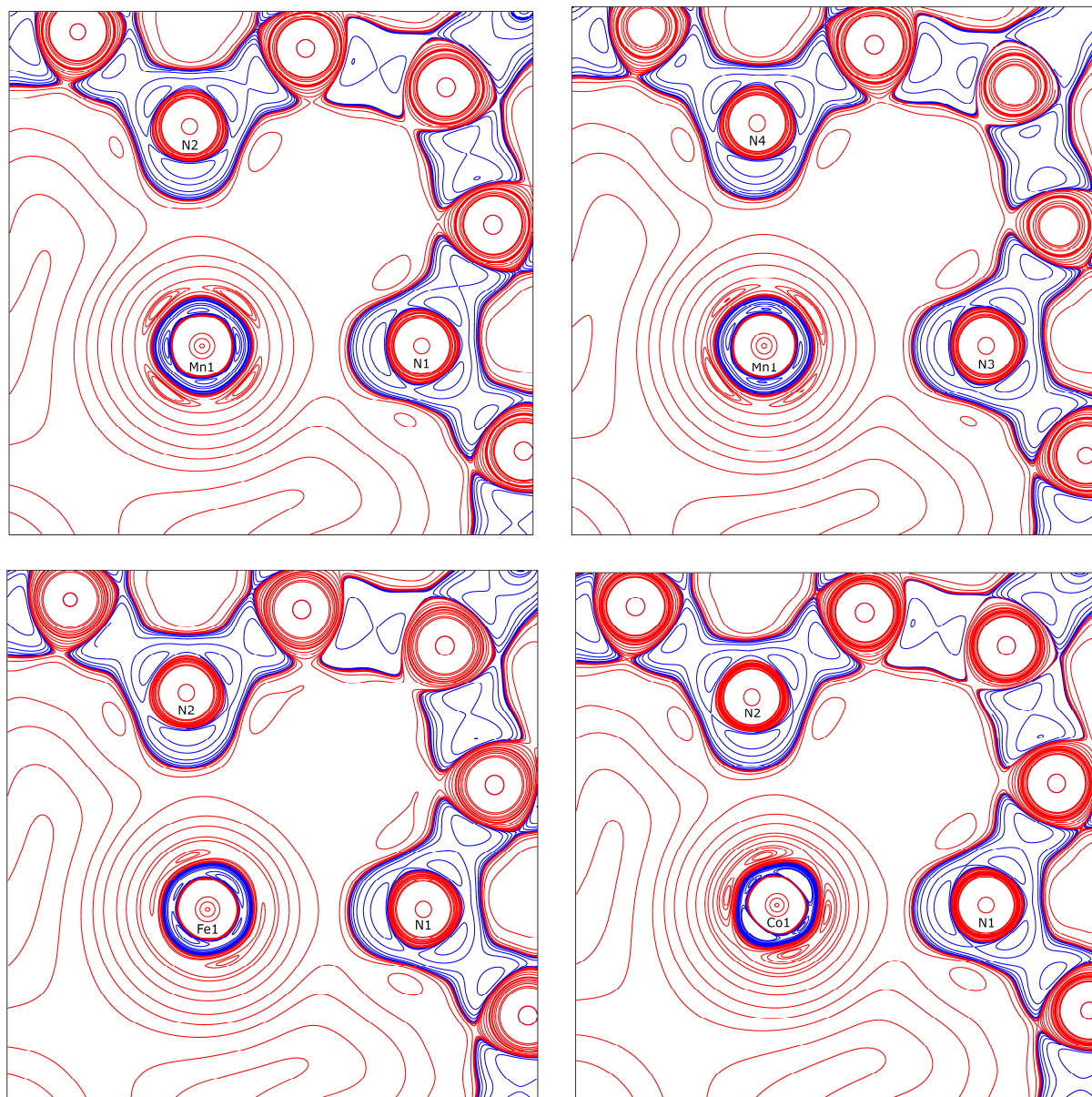


Figure 5-11: Two-dimensional Laplacian maps in the N1–M–N2 layer of the investigated compounds. Top left and right: MnMeBOX, contour levels are $\pm\{0.2, 0.4, 0.8, 2, 4, 8, 20, 40, 80, 100, 105, 110, 120, 130, 250, 350, 500, 600\}$ $\text{e}\text{\AA}^{-5}$. Bottom left: FeMeBOX, contour levels are $\pm\{0.2, 0.4, 0.8, 2, 4, 8, 20, 40, 80, 100, 150, 160, 170, 250, 350, 600, 800\}$ $\text{e}\text{\AA}^{-5}$. Bottom right: CoMeBOX, contour levels are $\pm\{0.2, 0.4, 0.8, 2, 4, 8, 20, 40, 80, 100, 140, 180, 200, 230, 240, 250, 260, 350, 500, 600\}$ $\text{e}\text{\AA}^{-5}$. M–N bond path run in near-straight lines from the respective nitrogen atoms to the metal centre in the displayed planes.

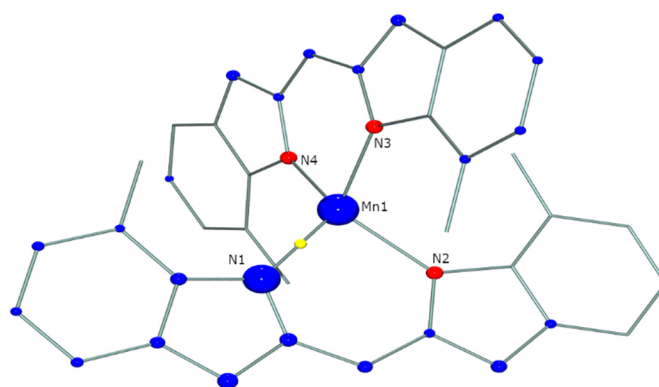


Figure 5-12: Visualisation of the integrated source function descriptor for electron delocalisation in MnMeBOX. Larger spheres denote a larger contribution of atomic ED to the electron density at the yellow reference point. Blue spheres denote positive contribution, red spheres denote negative contribution. Observations are similar for the other two investigated compounds.

Table 5-11: Percentage contribution of the central metal ions in the investigated compounds towards ED at reference BCPs on N–M bonds, differentiated into contributions from core, valence density and total contribution. Last significant decimals were estimated from comparison between 20 cross-validation sets. All values have an estimated ESD of 0.3%.

	Mn			Fe			Co		
	Valence	Core	Total	Valence	Core	Total	Valence	Core	Total
N1–M	5.9%	34.2%	40.2%	5.6%	34.4%	40.0%	7.5%	29.1%	36.7%
N2–M	–3.8%	38.6%	34.8%	3.3%	30.9%	34.2%	7.6%	30.8%	38.4%
N3–M	–0.5%	37.9%	37.4%	1.7%	36.1%	37.8%	4.4%	28.6%	33.0%
N4–M	–6.3%	29.0%	22.7%	5.5%	32.6%	38.0%	7.1%	32.5%	39.7%

As can be seen in the table, all metal ions have similar total contributions to the N–M BCP electron density, except for one outlier in the N4–Mn bond. On the contrary, the contributions from the valence electrons for cobalt is slightly, but significantly higher than for the other two ions. This indicates a slightly input from d-orbital electrons compared to the manganese and iron complexes. For the manganese compound, on the other hand, this ED appear to be mainly dominated by input from core electrons. Overall, however, due to the remaining uncertainty in relatively minute differences between the compared structures, these source function results should be merely seen as one part of the puzzle and might not be reliable enough for a quantitative differentiation between core and valence contributions.

5.5.4 Determination of d-Orbital populations

Orbital populations for all three structures were determined based on the method of Holladay, Leung and Coppens, and then compared to theoMM results and the different energy levels of the respective structures obtained from CASSCF(5,5)/NEVPT2 calculations in *ORCA* 5. The calculated orbital energies are visualized in the diagrams in Figure 5-13. A comparison of the resulting populations can be found in Table 5-12 below. The theoretical energies are in good agreement with observed magnetic behaviour of the compounds: For the iron compound, while the two lowest orbitals have a sufficiently low energy gap to show a slight mixing between them. However, due to the different orientation of the d-orbitals within the complex, the wrong sets of orbitals are near-degenerate, leading to the absence of magnetic anisotropy. For both the manganese and the cobalt compound, while the correct pairs of orbitals are neighbouring in terms of their energy level, the energy gap between the $3d_{x^2-y^2}$ and $3d_{xy}$ orbital is significantly higher than for the “optimal angle” SMM by Legendre *et al.*, which explains the absence of ZFS.

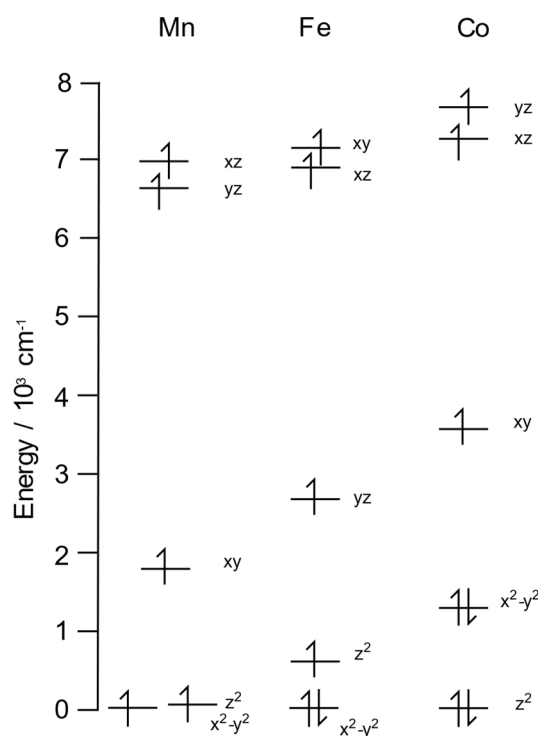


Figure 5-13: Energy diagrams of the calculated d-orbital energies for all three investigated compounds determined from CASSCF(5,5)/NEVPT2 calculations.

The experimentally derived d-orbital populations are in good overall agreement with the theoMM results when considering that the calculations take neither ligand–metal transfer nor mixing between 4s and 3d-orbitals into account. Occupancies of certain orbitals are noticeably higher than expected values, while others are lower. For example, all investigated structures exhibit some deviations from the expected d-population of 1 electron in at least one antibonding orbital. For the cobalt and manganese compounds, one of these orbitals has rounded occupancy values of 1.2 e (exact values in Tables 18-20), while for

the iron compound, the d_{xy} orbital amounts to about 0.8 electrons, while the d_{xz} has an occupancy near 1.2 e. It is reasonable to assume that these differences from one electron are caused by ligand–metal interaction, e.g. electron transfer from ligand to the metal centre in case of higher occupancies or π backbonding in case of a lower one.

On the other hand, the respectively lowest orbitals of the iron and cobalt compounds exhibit a lower population than the expected value of 2. In the case of the iron compound, this can be partly explained with interactions between the $d_{x^2-y^2}$ and the d_{z^2} orbitals, which are even predicted by theory. However, with a value of about 2.8 electrons in these two orbitals together, this value is still slightly too low. This leads to the assumption of an interaction between to normally empty 4s orbital. For the cobalt compound, a similar observation applies. In addition to the d_{z^2} orbital showing a population of less than 2, it has a lower population than the energetically slightly higher $d_{x^2-y^2}$ orbital. Judging by the experimental populations, this could be explained by mixing between 4s and 3d-orbitals in conjunction with a theoretically forbidden interaction between the $3d_{z^2}$ and $3d_{x^2-y^2}$ orbital.

As the manganese compound contains five d electrons in five d-orbitals, the expected distribution would be one electron per orbital. However, beyond the phenomena described above, the d_{z^2} and d_{xy} are slightly below this expected value as well. A possible explanation is, again interaction between these orbitals and the slightly lower 4s orbitals. The energetic difference between the lowest nearly degenerate $3d_{z^2}$ and $3d_{x^2-y^2}$ orbitals the only slightly higher d_{xy} orbital is lower than the differences between the lowest and second-to-lowest orbital energies of the other two compounds. Therefore, an orbital interaction between those two different energy levels is a consideration to explain the slightly lower population in not on the former two, but also the latter of these three orbitals. An electronic structure with an occupied 4s orbital also is in good agreement with the fact that Bader charges for all central metal ions are noticeably lower than the expected value of +2. Additional electrons are “stashed away” in the lower 4s orbitals, while electron transfer from the ligands to the metal still results in a d-orbital population close to the expected value of 5, 6, or 7 respectively.

While data collection for all structures was performed with nitrogen cooling to 100 K as opposed to the even lower temperatures of 15 K that can be reached with helium cooling, d-orbital populations from these experiments can still be expected to be largely unaffected by the Boltzmann distribution. According to the conducted quantum chemical calculations, all excited states that pose a change in orbital populations compared to the ground state have negligible Boltzmann populations at this temperature. While there are excited states that might legitimately affected by the Boltzmann distribution at 100 K, these only pertain spin flipping and therefore have no impact on orbital populations.

Table 5-12: d-orbital populations from refinement against experimental and theoretical structure factors of MnMeBOX, compared with results from CASSCF(5,5)/NEVPT2 calculations. Values are given as tuples of absolute population in electron a percentage per orbital of the total population. Orbitals are ordered in order of decreasing calculated energy level. Last significant decimals of the absolute electron numbers were estimated for from comparison between 20 cross validation sets. The estimated standard deviation for them is 0.02.

Mn	experimental		theoMM		CASSCF/NEVPT2	
xz	1.16	22.9%	1.04	20.4%	1.00	20.0%
yz	1.06	20.8%	1.02	19.9%	1.00	20.0%
xy	0.94	18.6%	1.04	20.3%	1.00	20.0%
z^2	0.88	17.3%	1.01	19.7%	1.00	20.0%
x^2-y^2	1.04	20.5%	1.00	19.6%	1.00	20.0%
Total d electrons	5.09		5.12		5.00	
Fe	experimental		theoMM		CASSCF/NEVPT2	
xy	0.84	13.9%	1.06	17.3%	1.00	16.7%
xz	1.19	19.7%	1.07	17.3%	1.00	16.7%
yz	1.18	19.4%	1.02	16.6%	1.00	16.7%
z^2	1.32	21.8%	1.15	18.7%	1.14	19.0%
x^2-y^2	1.52	25.1%	1.85	30.1%	1.86	31.0%
Total d electrons	6.06		6.15		6.00	
Co	experimental		theoMM		CASSCF/NEVPT2	
xz	1.04	14.8%	0.96	14.5%	1.00	14.3%
yz	1.19	16.8%	0.98	14.8%	1.00	14.3%
xy	1.01	14.2%	0.98	14.7%	1.00	14.3%
x^2-y^2	1.93	27.4%	1.86	28.0%	2.00	28.6%
z^2	1.90	26.9%	1.86	28.0%	2.00	29.6%
Total d electrons	7.07		6.63		7.00	

5.5.5 Impact of model decisions on structural properties

Throughout the various model and data processing adjustments described in Chapter 5.4, the impact of the changes on the various QTAIM properties was monitored as well. Compared to standard IAM structure refinement, the Hansen & Coppens MM contain significantly higher number of potentially influential parameters, and many different permutations of these parameters were tested during this project. The main takeaway from this comparison is the relatively low impact and an overwhelming number of these parameters on the properties of interest for this comparison study. As a main example, experimental d-orbital populations prove to be nearly invariant to all compared ways of modelling the central metal ion, which the main exception being to obviously impactful choice of local coordinate

system. Data quality, on the other hand, was paramount to the validity of obtained QTAIM parameters, with the first suboptimal dataset of CoMeBOX yielding vastly different and unphysical d-orbital populations. Reducing the maximum resolution for FeMeBOX from 0.5 Å to 0.53 Å significantly improved properties such as the experimental d-orbital populations.

5.6 Conclusion and outlook

Three d-metal BOX complexes with different behaviour in an applied magnetic field were subjected to an extensive study using the method of charge-density investigation. Topological analysis according to QTAIM revealed slight covalent contributions in the primarily ionic, closed-shell interaction between ligand and metal centre for MnMeBOX and CoMeBOX. This covalent component is absent in FeMeBOX. These differences were first noticed inspecting the $|V_{CP}|/G_{CP}$ descriptor proposed by Espinosa *et al.* at the respective BCPs, and then validated by an investigation of VSCCs and VSCDs of the central d metal ions and the coordinating nitrogen atoms, which could be obtained from Laplacian maps with astonishing resolution. Furthermore, using local coordinate systems obtained from quantum chemical CASSCF(5,5)/NEVPT2 calculations, experimental d-orbital populations were obtained and subsequently compared with results from MM refinements against theoretical structure factors. Differences between theoretical and experimental values were then used to identify different forms of ligand–metal interactions, which are not accounted for by the calculations. The resulting populations, in conjunction from examination of Bader charges of both ligands and central ions, suggest that contrary to its higher energy level, the 4s orbital of all complexes is indeed slightly occupied. Here, the lower-than-expected number of electrons in the d-orbitals with the lowest orbital energy is in good agreement with the lower-than-expected positive Bader charge of around +1.7 for all compounds.

The source function descriptor by Gatti *et al.* could be used to demonstrate that electron density transfer from ligand to metal centre is comparable for all three structures. Differences between its core and valence density contributions to ED at neighbouring BCPs, however, remain inconclusive. While crystallographers should strive towards the best possible final model when during the highly sensitive method of QTAIM evaluation of MM refinements, a large number of supposedly relevant parameters like the refinement of anisotropic hydrogen atoms or the choice between M and M²⁺ structure factors had very little impact on the investigated properties. In this particular study, these to some extent minor model adjustments were by and large outweighed by the impact and importance of excellent data quality. Using a wide range of correction methods like the use of a fixed integration box size, a plausible final model based with acceptable quality indicators could be obtained even for the first collected and unfortunately flawed dataset of CoMeBOX – resulting, however, in unphysical d-orbital populations. While the toolbox of crystallographic correction methods is constantly growing, this goes to show that these methods should be used for the specifically identified problems they are built to tackle, not to salvage models based on bad data.

The findings from the three high-resolution datasets collected on in-house sources, overall represented the observed slow magnetic relaxation in MnMeBOX and CoMeBOX in an applied field, as well as the absence thereof in FeMeBOX. The main difference between the former two compounds was a differing amount of covalent contribution in the mainly ionic metal-ligand bond. While the different degrees of covalency in M-L bonding are worthwhile for further investigation, a direct connection between them and the different forms of slow magnetic relaxation is unlikely to be drawn from MM and QTAIM investigations. One possible way of accessing additional information about the magnetic properties of the three MeBOX complexes would be the method of polarized neutron diffraction. While this would require an advanced setup at a large-scale reactor facility, the highly stable crystals of CoMeBOX and FeMeBOX would definitely be up the challenge.

6 Comparison of different strategies for modelling hydrogen atoms in charge-density analyses

The project of comparing different approximation strategies for hydrogen atoms in charge-density analyses started with my master thesis but was only finished in the first years of my PhD, where many of the central conclusions were made. For my master thesis, I used the model structures 9-diphenylthiophosphoranyl anthracene (SPANH) and 9,10-bis-diphenylthiophosphoranyl anthracene (SPANPS) to compare approximate hydrogen anisotropic displacement parameters (H-ADPs) from the *SHADE* webserver, the INVARIOM^[122] based approach of *APD-Toolkit*,^[76] and free refinement of H-ADPs with high-resolution SCXRD data with the perceived “gold standard” for investigating hydrogen atoms, the refinement of hydrogen atoms against neutron data.^[123] These results will only be sparingly mentioned, while focus will be put on the new investigations conducted during my PhD, namely, comparison with H-ADPs from Hirshfeld Atom Refinement (HAR)^[58] results and the correlation of ADP approximation quality and the presence of anharmonic motion within the structure. Furthermore, two additional HAR methods that were not published at the time of my master thesis were included in the comparison study.

Chapter 6.1 will provide a brief introduction to the central challenges of modelling H-ADPs based on X-ray diffraction data and the compared approximation methods for them. In Chapter 6.2, criteria for H-ADP comparison that were used in this work will be introduced. The model compounds SPANH and SPANPS, as well as their MM refinement will be presented in Chapter 6.3. This presentation will be kept rather short, as work on the multipole model refinements was mainly done for and covered in my master thesis. The used methods from and the latest developments in the field of Hirshfeld Atom Refinement will be summarized in Chapter 6.4. Results of the comparison study can be found in Chapter 6.5, while final conclusions from them are drawn in Chapter 6.6.

Parts of this chapter have already been published in C. Köhler, J. Lübben, L. Krause, C. Hoffmann, R. Herbst-Irmer, D. Stalke, *Acta Cryst.*, **2019**, B75, 434.^[51]

6.1 Treatment of Hydrogen atoms in charge-density analyses

As X-rays are scattered at the electrons in the crystal, hydrogen atoms, having only one single electron, are consequently hard to detect and describe in SCXRD studies. Furthermore, the ED of a hydrogen atom in a structure is usually heavily shifted towards a bonded heavy atom, which causes X-H distances from XRD data to be systematically underestimated.



Figure 6-1: Schematic depiction of ED in the bonding region between a H-atom and a carbon atom after subtracting the contribution of the carbon atom. The maximum density marks the hydrogen position estimated in the standard refinement procedure for X-ray data. Therefore, the bonding distance is systematically underestimated.

In IAM investigations, hydrogen atoms are usually described with the riding model, where distances are set based on an idealized geometry and H-ADPs based on the ADPs of bonded heavy atoms. In charge-density investigations, it might be advisable to apply an anisotropic description of hydrogen atoms to improve model quality. Hydrogen distances from neutron diffraction experiments are considered to be the “gold standard”, and the complementary use of data obtained from neutron diffraction experiments has been shown to yield highly accurate parameters for hydrogen atoms.^[123,124] The method of neutron diffraction is, however, still of limited availability due to the small number of available facilities where these measurements can be performed. Additionally, the larger crystal size required for neutron measurements frequently cannot be matched. Even if sufficiently large crystals can be grown, the crystal size often leads to systematic errors caused by absorption effects. Due to differences between X-ray and neutron diffraction for effects like extinction, absorption or thermal diffuse scattering as well as possibly different experiment temperatures, ADPs obtained from neutron data first have to be corrected to be comparable to those obtained from X-ray data.^[125] To allow for the accurate determination of H-ADPs and positions even in the absence of neutron data, a variety of alternative approximation methods have been developed, tested and incrementally improved over the last years. A common approach for these methods is to approximate the hydrogen positions by using tabulated bond distances from neutron experiments.^[126] The respective H-ADPs U^{ij} are then assumed to be separated into the external vibrations U_{external}^{ij} of the asymmetric unit of a crystal as rigid body and the internal vibrations U_{internal}^{ij} of the atoms within the asymmetric unit themselves.

$$U^{ij} = U_{\text{external}}^{ij} + U_{\text{internal}}^{ij} \quad (\text{Eq. 40})$$

While the external vibrations are generally determined *via* TLS-fit^[127], the strategies for determination of internal vibrations vary. The *SHADE* method uses tabulated ADPs from neutron experiments to approximate the H-ADPs of any given structure and is readily available in form of the *SHADE* webserver^[75,128]. The program *APD-Toolkit*, published in 2015 by Lübben *et al.*^[129] utilizes pre-calculated frequency information stored in the INVARIOM database^[91] for the calculation of internal vibrations. The used theoretical data are obtained from DFT calculations with *GAUSSIAN*^[130] on a number of model compounds. Hirshfeld atom refinement (HAR) is an alternate refinement technique to IAM or MM refinement which utilizes additional input from quantum chemical calculations.^[58,131] Aspherical scattering factors are acquired using Hirshfeld’s stockholder atom partitioning of tailor-made *ab initio* quantum mechanical molecular electron densities^[59]. Based on these scattering factors, a

conventional least-squares refinement of atomic positions and U^{ij} is conducted. The resulting model is then used as starting point for new *ab initio* calculations. This two-step process is iterated until convergence. More details on the method of HAR are presented in Chapter 2.7.

For this comparative study, the aforementioned approximation methods are applied to the hydrogen atoms of the model structures 9,10-bis-diphenylthiophosphoranyl anthracene (SPANPS) and 9-diphenylthiophosphoranyl anthracene (SPANH) [132]. In 2004, Roversi and Destro stated that the refinement of quadrupole parameters for H-atoms improved the model quality in a chemically and physically feasible way.[133] Two years later, Mata *et al.* [134] reported similar results with the refinement bond-directed quadrupoles for all H-Atoms (H-Q0) improved the model quality in a chemically and physically feasible way. Therefore, the impact of introducing these quadrupole parameters into the hydrogen refinement against X-ray data is herein examined as well. The free refinement against experimental X-ray data will be labelled “Aniso”, while the same approach with added quadrupole parameters will be labelled “Aniso+Q0”.

6.2 Methods for comparison of ADPs

Due to the high accuracy of results in terms of hydrogen atom parameters derived from neutron data, the quality of any approximation method can be judged by comparing the respective results with neutron values. The *similarity index* S_{12} introduced by Whitten and Spackman[135] in 2006 as

$$S_{12} = 100(1 - R_{12}), R_{12} = \int [p_1(\mathbf{x})p_2(\mathbf{x})]^{1/2} d^3\mathbf{x} \quad (\text{Eq. 41})$$

is a mathematical figure constructed to calculate the percentage difference between two ADP matrices \mathbf{U}_1 and \mathbf{U}_2 . Herein, $p(\mathbf{x})$ denotes the probability density function for finding an atom at displacement \mathbf{x} from its core position. The similarity index can be used to illustrate the deviation of a given approximation method from neutron results, and hence should be as small as possible to indicate a minimal deviation. As the similarity index provides no information in which direction the inspected ADPs differ, other relations have to be examined as well. The systematic differences between two ADPs can be inspected by examining the mean difference of the equivalent isotropic displacement parameters $\langle |\Delta U_{X-N}^{ii}| \rangle$ and the mean absolute anisotropic difference $\langle |\Delta U_{X-N}^{ij}| \rangle$, as well as their mean anisotropic ratio $\langle U_X^{ii}/U_N^{ii} \rangle$. The error-weighted root means-square difference of two ADPs

$$w\text{RMSD} = \left((\Delta U_{X-N}^{ij})^2 / [s.u.^2(U_X^{ij}) + s.u.^2(U_N^{ij})] \right)^{1/2} \quad (\text{Eq. 42})$$

additionally takes into account that both neutron and X-ray diffraction experiments are affected by experimental errors (see Table 6-1 in Chapter)^[58]. A visual inspection using a molecular viewer such as *MoleCoolQT* by Hübschle & Dittrich^[136] can then reveal problematic ADPs. Using the *PEANUT* program by Hummel *et al.*^[137], the difference between the ADPs derived from X-ray data by the described approaches and those derived from neutron data can be directly visualized *via* the difference

of the root mean square surfaces of the subtracted ADPs. Contrary to the commonly used *ORTEP* representation,^[138] the *PEANUT* visualization is capable of depicting non-positive definite ADP matrices. The resulting visual representation of differences is often shaped like a peanut hence the name of the program.

When performing an anisotropic refinement of H-atoms against high resolution X-ray data (abbreviated “Aniso” refinement in the following), various quality indicators can be expected to improve. However, caution has to be taken as these improvements might not be chemically sound. The residual density originating from other physical effects and errors in the data might be “absorbed” into freely refined H-ADPs, resulting in a significant decrease of examined figures of merit.^[139] The direction of all H-ADPs must be carefully examined. Reasonable thermal vibrations of H-atoms should have a similar orientation as the bonded heavy atoms, vibration should specifically not extend in the direction of bonding. Tests like the Hirshfeld or DMSDA test (from “difference of mean square displacement amplitudes”, see Chapter 3.1.2) should be used to validate the resulting ADPs.^[140] While the Hirshfeld test was designed to analyse bonding partners of similar weight, the results for atoms in comparable chemical surroundings should still be similar. Furthermore, the so-called *BEEF* formalism by Jens Lübben can be used to calculate mass corrected DMSDA values.^[141] As for the other examined H-atom parameters, results from the neutron data can be used as a reference to judge the DMSDA. As the free anisotropic refinement of hydrogen atoms is the only method for modelling H-ADPs that does introduce new refined parameters, the presence of overfitting should be examined as well via cross-validation.^[78]

6.3 Model compounds and MM refinement

For this comparative study, the aforementioned approximation methods are applied to the hydrogen atoms of the model structures 9-diphenylthiophosphoranyl anthracene (SPANH) and 9,10-bis-diphenylthiophosphoranyl anthracene (SPANPS).^[142] For both structures, neutron data as well as high-resolution X-ray datasets for MM refinement were available, allowing for the comparison of various hydrogen ADP approximation methods with the perceived “gold standard”.

The datasets for both SPANH and SPANPS were provided for my master thesis. The development of a refinement strategy for SPANPS was part of my master thesis as well, while a finished refinement strategy for SPANH was taken from a previous publication by Herbst-Irmer *et al.*, where it was used as model compound to investigate the implications of anharmonic motion for MM refinements and charge-density analysis.^[72] Structure solution for both model compounds was done in *SHELXT* using direct methods.^[44] Starting models for MM refinement were generated from a standard IAM refinement with *SHELXL*^[70] in the *ShelXle* GUI.^[71] The multiple refinements were conducted in the *XD2016* program suite.^[69] In the case of both of these structures, anharmonic motion of the sulphur and phosphorus caused problems during the refinement. Both structures were first refined with isotropic hydrogen atoms. Then, hydrogen ADPs from the compared methods were applied. An exception are ADPs from HAR methods, which were directly evaluated from the respective refinement and not additionally included in the MM

refinement. No signs of overfitting were detected for any of the employed methods. Used refinement strategies and additional quality indicators can be found in the Appendix (subchapters 1-3 of Chapter 10.4 for SPAnH and 10.8 SPAnPS).

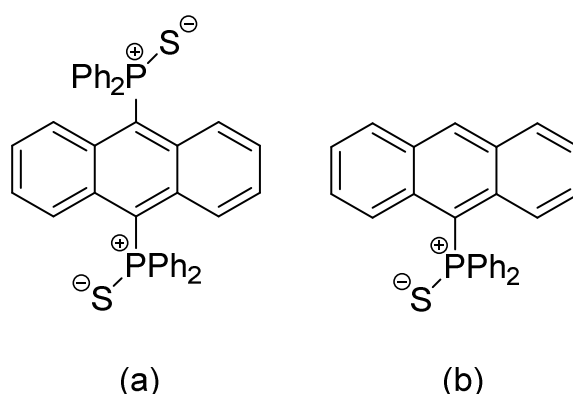


Figure 6-2: Lewis structure SPAnPS (a) and SPAnH (b). Image reused with permission by the International Union for Crystallography.^[51]

6.4 Hydrogen atom ADPs from Hirshfeld atom refinement: Old and contemporary methods

The method of HAR and the programs and tools for applying the method have been continuously developed and expanded over the last few years. The first implementations and noteworthy interfaces built for the method relied on the *Tonto* software for both scattering factor calculation and refinement. At the time of publication of this project, one of these recent interfaces, Hirshfeld Atom Refinement terminal (*HARt*) in *Olex2*^[89] as published by Fugel *et al.* in 2018, was used.^[62] As mentioned in Chapter 2.7, hydrogen ADP determination from *HARt* was shown to improve the already high accuracy of X-H distances, but can regularly yield ADPs of unphysical shapes.^[60,63] Since then, several advancements to the method have been made, two of which will be highlighted in this chapter. In 2021, the *NoSpherA2* (“Non-spherical Atoms in *Olex2*”) system was published by Kleemiss *et al.*,^[64] which expanded the capabilities of and replaced the aforementioned *HARt* package in *Olex2*. Among other improvements, *NoSpherA2* replaces *Tonto* in both calculation of scattering factors and subsequent refinement, thereby circumventing several limitations of the program. It allows the quantum-mechanical calculations to be conducted in *ORCA* or Gaussian, and replaces the refinement of *Tonto* with the *olex.refine* routine.^[45] For the use of the *NoSpherA2* system in this thesis, *ORCA* 5 was chosen.^[101] Recently, Ruth *et al.*^[66] published a HAR Python package with a different approach based on periodic calculations. While the previously mentioned HAR methods relied on single molecule calculations, or used cluster charges to model the solid-state surroundings in the crystal, the *XHARPy* (“X-ray diffraction data Hirshfeld atom refinement in Python”) package uses densities derived from projector augmented wave densities in computationally more demanding periodic DFT calculations in GPAW.^[143] Compared to the publication in 2019, hydrogen ADPs from *NoSpherA2* using *ORCA* and *XHARPy* were included in the comparison for this chapter as well. A new version of *Olex2* now furthermore allows for the refinement of Gram

Charlier anharmonic motion parameters during the *olex.refine* procedure. However, this only allows all GCCs up to fourth order to be enabled for each individual atom, or none at all. As this not only violated Kuhs's rule for the majority of affected carbon atoms,^[74] but also caused jarring refinement instabilities and a significant worsening of overall model quality indicators, this approach was discarded.

6.5 Results and discussion

As seen in Table 6-1 by judging the mean isotropic ADP ratio $\langle U_X^{ii}/U_N^{ii} \rangle$, both the database approaches and the refinements against the high-resolution X-ray data underestimate the hydrogen ADPs, especially in the case of *SHADE*. Surprisingly, the mean similarity indices suggest that the ADPs determined with the Aniso+Q0 approach outperforms both *SHADE* and *APD-Toolkit* in both model compounds and even yields the best mean agreement with neutron data for SPAnH. Without addition of H-Q0, the agreement suffers significantly, especially in the case of SPAnH. Evaluation of the modified mean similarity index $\langle S_{NX}^* \rangle$, which excludes hydrogen atoms bonded to carbon atoms with refined anharmonic motion, can be used as a guideline on how much ADP agreement with neutron data was impaired by anharmonic components in the ADP transmitted from a bonded heavier atom. Especially for *SHADE*, this seems to be the root cause for the underestimation of ADPs, as the *SHADE* server does not take GCCs from the multipole refinements into account for the determination of approximate ADPs.

On the other hand, while *HARt* slightly overestimated the H-ADPs in both model structures, results are not that unanimous for the newer HAR methods. Even though *NoSpherA2* HAR was performed with a larger basis set, the resulting ADPs have a slightly worse overall agreement with neutron data. While the H-ADPs of SPAnPS are clearly overestimated with a mean isotropic ratio of 1.19(12), the mean isotropic ratio for SPAnH appears fine as it is close to unity. A later visual inspection however revealed that here, H-ADPs are mostly overestimated (see Figure 6-3). The recently published *XHARPy*, while requiring a significantly longer calculation time, yields a greatly improved S_{12} value, while ADP ratios and differences are comparable to the *HARt* results. Both *NoSpherA2* and *XHARPy* ADPs reach significantly lower *BEEF*-corrected DMSDA values than the *Tonto*-based *HARt*.

6.5.1 Visual comparison of approximate ADPs using PEANUT

During the beginnings of my work on this project during my Master thesis, the relatively straightforward molecular viewer *MoleCoolQT* was used for a visual comparison of approximate ADPs among each other and with their neutron data equivalents. The *PEANUT* representation of ADP differences used during the first year of my PhD emphasizes the differences previously noted from a direct comparison of *ORTEP* ADPs: Both database approaches show a significant overestimation of the ADPs especially in the phenyl moieties of SPAnH and SPAnPS. The same observation of overestimated ADPs in these regions can be made for the anisotropic refinement against X-ray data as well, although less pronounced. The addition of bond-directed Q0 quadrupoles additionally enhances overall agreement with neutron data. Rather than improving all H-ADPs equally, this occurs because of large improvements to select H-ADPs with problematic shapes such as a large bond-directed vibration. These problematic ADP

shapes create a large deviation from neutron APDs, which is remedied by introduction of an additional parameter describing bond-directed ED in the anisotropic refinement with quadrupoles.

Table 6-1: Examined figures of merit for the H-atoms of both inspected model compounds. $\langle S_{NX} \rangle$ is the percentage mean deviation between X-ray and neutron data calculated with *APD-Toolkit* (see equation 3). $\langle S_{NX}^* \rangle$ is the respective mean value for H-atoms not bonded to carbon atoms with refined anharmonic motion. Given mean DMSDA values of H-Atoms are multiplied by 10^5 and include the *BEEF*-correction by Jens Lübben. wRMSD is defined in equation 42 in Chapter 6.2. Since *SHADE* and *APD-Toolkit* ADPs are estimated from tabulated neutron data or INVARIOMs, they have no standard uncertainties. Entries in bold font were newly added compared to the publications from 2019.^[51]

Compound	Method	$\langle \text{DMSDA} \rangle$	$\langle S_{NX} \rangle$	$\langle S_{NX}^* \rangle$	$\langle U_X^{ii}/U_N^{ii} \rangle$	$\langle \Delta U_{X-N}^{ii} \rangle$	$\langle \Delta U_{X-N}^{ij} \rangle$	wRMSD
SPAnPS	Neutron	89	-	-	-	-	-	-
	<i>SHADE</i>	45	2.95	1.32	0.830(13)	0.0141(9)	0.0089(7)	-
	<i>APD-Toolkit</i> *	60	3.52	4.65	0.885(13)	0.0080(9)	0.0059(7)	-
	Aniso (no Q0)	122	1.71	3.26	0.94(7)	0.000(4)	0.000(3)	10.81
	Aniso + Q0	124	1.58	1.06	0.96(7)	0.002(4)	0.002(3)	11.10
	<i>HARt</i> **	186	1.91	1.75	1.16(11)	0.007(5)	0.003(5)	2.60
	<i>NoSpherA2</i>	107	2.36	2.82	1.19(12)	0.011(8)	0.007(6)	6.37
	<i>XHARPy</i>	111	0.96	1.16	1.13(8)	0.007(6)	0.004(4)	7.82
SPAnH	Neutron	43	-	-	-	-	-	-
	<i>SHADE</i>	36	1.79	0.97	0.84(3)	0.007(1)	0.004(1)	-
	<i>APD-Toolkit</i>	51	0.97	0.57	0.84(3)	0.007(1)	0.004(1)	-
	Aniso (no Q0)	129	3.09	3.45	0.92(9)	0.004(3)	0.002(3)	8.29
	Aniso + Q0	83	0.92	0.76	1.00(9)	0.000(3)	0.000(3)	7.54
	<i>HARt</i> **	131	1.67	1.60	1.08(12)	0.002(4)	0.002(4)	2.06
	<i>NoSpherA2</i>	28	2.03	1.65	1.01(9)	0.000(4)	0.000(3)	7.17
	<i>XHARPy</i>**	27	1.03	0.53	1.09(8)	0.003(4)	0.002(4)	9.02

APD-Toolkit* is not optimized to treat structures with molecules on special positions like SPAnPS. The used functionalities are still regarded to be experimental. ** *HARt* and *XHARPy* does not take GC-Parameters into account. * Refinement with GC parameters was attempted, but discarded due to a significant worsening of quality indicators and a non-converging refinement (see 6.4).

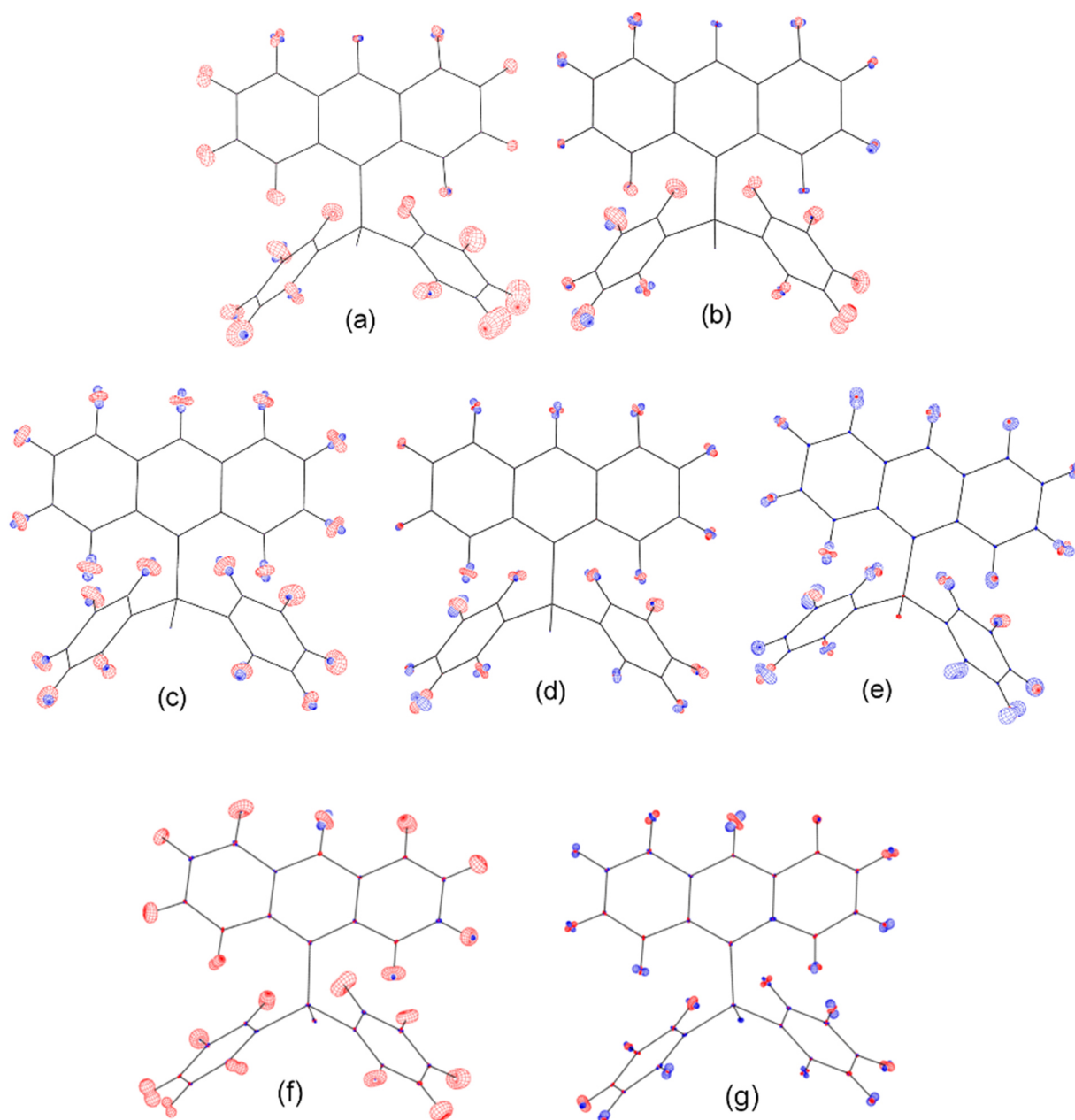


Figure 6-3: PEANUT plots (X-N) of the second molecule in the asymmetric unit of SPAnH. SHADE (a), APD-Toolkit (b), Aniso (no Q0) (c), Aniso+Q0 (d), HART (e), NoSpherA2 (f), XHARPy (g). Red denotes negative difference, indicating larger neutron ADPs, blue positive difference, indicating larger X-ray ADPs. For accentuation differences are multiplied by the factor of 2.0. Part (a)-(e) of this graphic was reused with permission by the International Union for Crystallography.^[51]

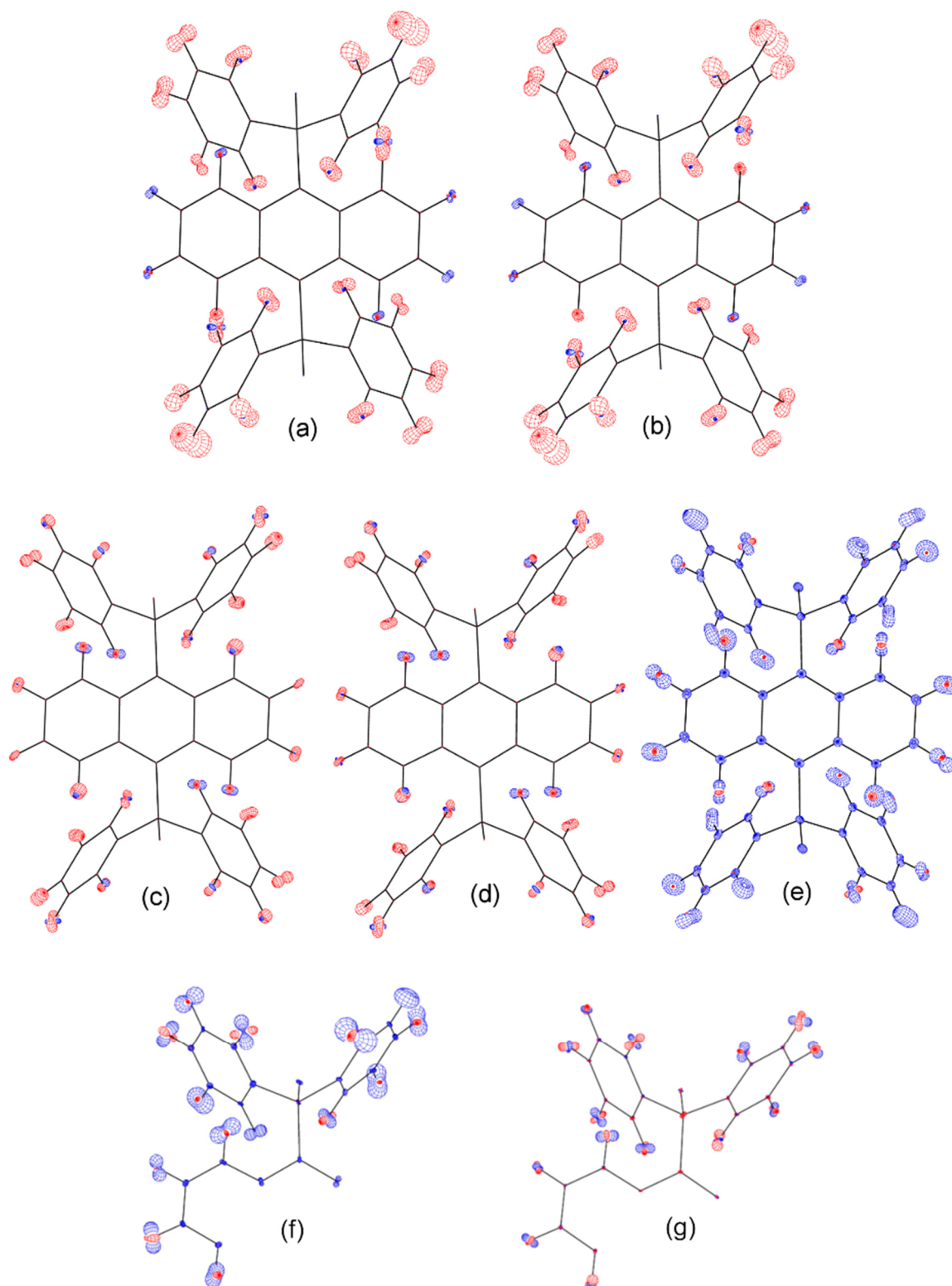


Figure 6-4: *PEANUT* plots (X-N) for SPAnPS. *SHADE* (a), *APD-Toolkit* (b), Aniso (no Q0) (c), Aniso+Q0 (d), *HART* (e), *NoSpherA2* (f), *XHARPy* (g). Red denotes negative difference, indicating larger neutron ADPs, blue positive difference, indicating larger X-ray ADPs. For accentuation differences are multiplied by the factor of 2.0. Due to an unknown error with the *PEANUT* program, only the asymmetric unit could be displayed for (f) and (g), which were added to this study compared to the original publication. Part (a)-(e) of this graphic was reused with permission by the International Union for Crystallography.^[51]

6.5.2 Comparison of X-H distances

The fact that the refinement of hydrogen positions against X-ray data without the aid of theoretical supplementation like HAR is not feasible is generally considered common knowledge.^[144] For this study, the results of a free refinement of hydrogen positions against X-ray data will be compared for different treatments of H-ADPs. For the *SHADE*, *APD-Toolkit* and both Aniso refinement strategies, a final refinement step was added in which constraints resetting all C-H bond distances to fixed values were released. All hydrogen positions were refined in addition to all previously refined parameters. The results were compared with neutron distances and the HAR results. For both SPAnPS and SPAnH, the bond distances determined with H-ADPs from all approximation methods except the three HAR methods were severely underestimating the bond distances (see Table 6-2). This was the case even for the best approximation method for the respective structures (Aniso+HQ0). However, the deviation from neutron distances seems to be related to the quality of the obtained ADPs. In both cases, the distances from the HAR approaches were in overall best agreement with neutron distances. *HARt* and *XHARPy* yield very comparable distances, while those from *NoSpherA2* differ more strongly. Curiously, while the former methods are superior for SPAnPS, while the latter yields better agreement with neutron data for SPAnH. For SPAnPS, while all HAR methods slightly underestimate X-H distances compared to neutron values, *NoSpherA2* ADPs still come relative close to them, while *HARt/XHARPy* results are more clearly too low. In both cases, this underestimation does not just appear to be mainly caused by problematic X-H distances in the toluene molecule, which is affected by strong anharmonic motion. Instead, the underestimation seems to be generally present within the SPAnPS compound as well, with the mean X-H distance within the molecule amounting to 1.078(4) Å in the *XHARPy* results versus 1.088(3) for the neutron values. For SPAnH, on the other hand, observations are the other way around: A systematic underestimation of distances can be seen for *NoSpherA2*, while *HARt/XHARPy* results seem in good agreement. This, again, appears to be a general problem for the entire compound that cannot simply be remedied by excluding X-H distances with involvement of anharmonic motion. A slight underestimation of X-H bond lengths with HAR methods such as *XHARPy* has previously been reported by Ruth *et al.* The deviations from neutron distances observed for this investigation is roughly within the same bonds as those reported by the authors.^[66]

Table 6-2: Examined figures of merit for C-H bond distances in both model compounds $\langle r(C-H) \rangle$ and $\langle |\Delta r_{X-N}| \rangle$ are given in Å. Entries in bold font were newly added compared to the publications from 2019.^[51]

Compound	Method	$\langle r(C-H) \rangle$	$\langle r_X/r_N \rangle$	$\langle \Delta r_{X-N} \rangle$	wRMSD
SPAnPS	Neutron	1.0872(6)	-	-	-
	<i>SHADE</i>	1.055(5)	0.971(5)	0.037(6)	7.42
	<i>APD-Toolkit</i>	1.061(5)	0.976(5)	0.032(5)	7.37
	Aniso without H-Q0	1.058(4)	0.974(4)	0.034(5)	8.04
	Aniso with H-Q0	1.060(4)	0.985(4)	0.032(5)	7.58
	<i>HARt</i>	1.077(6)	0.991(6)	0.012(6)	2.72
	<i>NoSpherA2</i>	1.083(4)	1.002(4)	0.002(5)	3.95
	<i>XHARPy</i>	1.074(5)	0.994(4)	0.007(5)	2.92
SPAnH	Neutron	1.0863(2)	-	-	-
	<i>SHADE</i>	1.064(4)	0.979(4)	0.023(4)	5.90
	<i>APD-Toolkit</i>	1.069(3)	0.984(4)	0.017(4)	4.71
	Aniso without H-Q0	1.042(4)	0.960(4)	0.044(4)	11.11
	Aniso with H-Q0	1.072(4)	0.987(4)	0.014(4)	3.98
	<i>HARt</i>	1.088(5)	1.002(5)	0.007(5)	1.73
	<i>NoSpherA2</i>	1.078(4)	0.992(3)	0.009(4)	2.32
	<i>XHARPy</i>	1.088(4)	1.002(3)	0.002(4)	1.49

6.5.3 Comparison of Interaction Energies

To quantify the impact of varying accuracy of H-atom parameters on the determination of structural properties of intermolecular interactions, intermolecular bond critical points and the intermolecular interaction energies were investigated using the *XDPROP* program in the *XD2016* program suite. Due to theoretical limitations, only the electrostatic term of the interaction energy is to be determined reasonably.^[145] As *XDPROP* calculates properties based on the multipole parameters refined with the *XD* program suite, this investigation was not possible for the results from HAR methods.

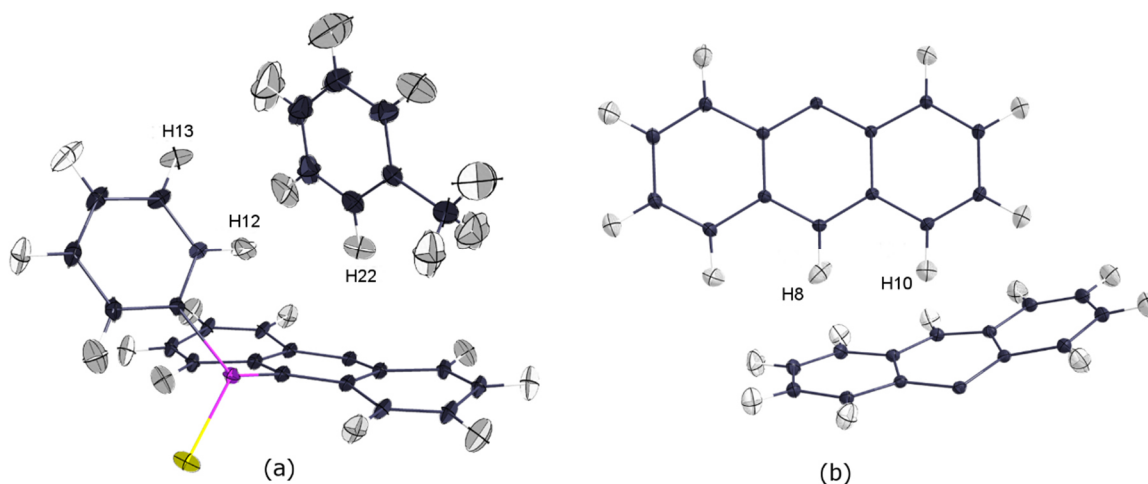


Figure 6-5: (a): Depiction of hydrogen atoms that have intermolecular BCPs between the anthracene moiety and the toluene molecule. (b): Depiction of atoms involved in the fishbone-shaped intermolecular interactions between the anthracene moieties of two neighbouring SPAnH molecules. BCPs were found between H8/C30 and H10/C28, respectively. The carbon atoms are part of the neighbouring molecule generated by cell symmetry. ADPs are taken from the Aniso+Q0 refinement and depicted at 50 % probability level. Image reused with permission by the International Union for Crystallography.^[51]

In the case of SPAnPS, the sample energies were calculated for the interaction between the guest toluene molecule and the anthracene moiety. For SPAnH, sample interaction energies of neighbouring SPAnH molecules in suitable positions for fishbone-shaped π -stacking were investigated. To test whether observed differences to neutron data are solely based on different C-H distances, the results for neutron ADPs with the same distances used for the other approximation methods were determined as well. The alignments of the respective molecules and moieties are displayed in Figure 6-5. The investigations show that the intermolecular BCPs were mostly invariant to different H-ADP methods. As expected, only small electron densities around $0.05 \text{ e} \cdot \text{\AA}^{-3}$ with errors of approximately the same order of magnitude were obtained, rendering the respective absolute values rather unreliable. While differences between the respective interaction energies were observed, they are well below the expected experimental errors of $\sim 5 \text{ kJ/mol}$.^[146] All determined bond critical points and interaction energies can be found in the Appendix (subchapters 4 and 5 of Chapter 10.4 for SPAnH and 10.8 for SPAnPS).

6.6 Conclusion and Outlook

Our comparison study revealed a variety of specific features of the investigated approximation methods. Specifically, anharmonic motion had a significant impact on the obtainable agreement with neutron data. The agreement of H-ADPs derived from the above-discussed approaches with those derived from neutron data improved for nearly all of them when H atoms bonded to C atoms with refined anharmonic motion were excluded. It could be demonstrated that the *SHADE* approach in particular significantly underestimated the full extent of H-ADPs of these atoms. While results from *APD-Toolkit*, like for *SHADE*, showed a number of outlier atoms with high deviations, their overall agreement with neutron

data turned out to be better. In terms of the *BEEF* DMSDA test, *SHADE* and *APD-Toolkit* exhibited comparable results. While the ADP-method had a significant impact on the model quality, its impact on derivable structural properties of interest was negligible considering the estimated standard deviations of said properties. In particular, it was shown that for the examined weak intermolecular interactions, deviation of both BCPs and intermolecular interaction energies were not significant. Therefore, approximation methods for hydrogen ADPs in charge-density analyses should generally be used to improve model quality as a whole, but not with the specific goal of obtaining the best possible interaction energies from the multipole model.

When my comparison study of different approximation methods for hydrogen ADPs was first published, taking ADPs from Tonto-based Hirshfeld Atom Refinement resulted in generally better agreement than both *APD-Toolkit* and *SHADE*, but worse results than free refinement against the X-ray data. However, fuelled by both the exploration of new approaches to the computational part of the method and the increasing availability of more powerful desktop computers, the field of HAR has undergone rapid development over a timespan of less than 5 years. While calculations using *HARt* took about two days on my old office work station used during my master thesis, *NoSpherA2* calculation times with a current generation computer now took below an hour for both compounds. The more demanding *XHARPy* calculation, on the other hand, took around 9 hours to complete on the same computer, but yielded clearly superior overall agreement to neutron data, as indicated by the respective S_{12} values. As expected, only HAR methods provided acceptable X-H distances on par with those obtained from neutron data. However, for each model structure, one of the newly investigated HAR methods slightly underestimated the distances, with *XHARPy* underestimating them for SPAnPS and *NoSpherA2* underestimating them for SPAnH. While some inconsistencies to neutron distances are still prevalent, the promising improvement in H-ADPs from contemporary HAR methods great potential for further developments, leading to even more accurate structure determinations from this method.

7 Summary an Outlook

In this thesis, extensive investigations of various complexes of the BOX ligand family were conducted. A significant portion of my time spent on this thesis was dedicated to the collection of high-resolution SCXRD datasets for subsequent MM refinement and QTAIM analysis. As should be expected when screening a structure class in search of candidates for a specific analysis method, not all investigated compounds were suitable for MM refinement. Among the originally chosen BOX ligands, only the MeBOX ligand yielded metal complexes with sufficient maximum resolution for charge-density analysis – while unfortunately not meeting this criterion itself as free ligand. Among initially targeted BOX-based alanes, the only compound with suitable data quality turned out to be affected by a small disorder of the entire compound.

Nevertheless, even the disordered AlH_2MeBOX compound could successfully be used in a method development study exploring new approaches to dealing with the presence of such small molecular disorders. While classical description of the disorder, modelling both disordered components in the MM, turned out to be severely limited by the size of the structure as well as the low occupancy of the second disorder positions, a new approach for treating the disorder within the data showed great promise. Using several Python 3 scripts for non-standard XD input file modification, a description of the minor disorder component in the data, akin to the well-known SQUEEZE description of disordered solvents, could be implemented. Testing of this new “1Part” disorder description was performed on AlH_2MeBOX as well as two additional model compounds. For small molecular disorders below 5%, the 1Part correction resulted in a significant improvement in many vital model quality indicators when compared to a more standard disorder description. While some ambiguity regarding the final model of AlH_2MeBOX still remained due to *additional* disorder in the methyl groups of the ligand, the method overall appears worthwhile for future testing on similar problems.

The most successful measurements for this work were conducted on three MeBOX complexes of the d-metals manganese, iron and cobalt. After some initial problems with overexposures in the first CoMeBOX dataset were remedied by the use of a new PHOTON III detector, datasets of great quality could be obtained for all three compounds, especially for MnMeBOX and CoMeBOX. While the general resolution limit of 0.50 Å for MM refinement could not be reached by a small margin for FeMeBOX, the data quality was still deemed to be sufficient for comparison with the other two datasets. Besides standard QTAIM analysis, yielding highly accurate Laplacian maps, experimental d-orbital populations could be calculated for all three compounds. From the Laplacian, as well as certain properties at the metal-ligand BCPs, differences in the covalent contributions towards the mainly ionic metal-ligand bond could be identified, which might be partly caused by the different covalent radii of the three metals. Determined d-orbital populations are in good agreement with calculated d-orbital energies obtained from CASSCF(5,5)/NEVPT2 calculations. Differences between experimental and theoretical d-populations could mainly be attributed to the fact that metal-ligand interactions are not accounted for by the

calculations. As all three compounds are easily crystallised and relatively air stable, they are well suited for additional benchmarking experiments.

In 2019, the results of my master thesis regarding a comparison between different approaches for modelling hydrogen ADPs in charge-density studies, including ADPs taken from Hirshfeld Atom Refinement, were published. Due to rapid developments in the field, the main HAR method used in this publication, Hirshfeld Atom Refinement terminal (*HARt*) was turned obsolete in merely less than three years. Like in the original publication, ADPs from the two contemporary HAR methods *NoSpherA2* and *XHARPy* were compared to those obtained from neutron diffraction. It turned out that the more computationally demanding *XHARPy*, modelling the crystal environment using projector augmented wave densities, was able to surpass all other HAR in terms of neutron agreement of ADPs. For one of the two anthracene derivatives employed as model compounds, it surpassed the previously (surprisingly) best approach of free ADP refinement against the SCXRD data. As even more advanced HAR methods are currently in development, the method has great potential for highly accurate structure models in the future, with potential applications e.g. for the treatment of pathological disorder in standard structure refinement.

The presented work on charge-density studies on BOX ligands encompasses a near exhaustive investigation on currently available complexes of the contemporary ligands and metal complexes suitable for the method. For future studies on the promising ligand family, complexes of BOX ligands other than MeBOX could be worthwhile in order to quantify and compare the impact of substituents on charge-delocalisation within the complex using the source function descriptor.

8 Other Projects

Besides the extensive charge-density presented in the main Chapters 4-6 of this work, a number of further smaller or unfinished projects were part of my PhD as well. These projects, including work on BOX compounds that turned out unfit for charge-density investigation, will be briefly presented in this chapter. This includes a number of charge-density investigations for which sufficient data quality was available, but from which no satisfactory conclusion could be drawn. In the interest of brevity, quality indicators and refinement details for these datasets and structures will be presented in a shortened fashion.

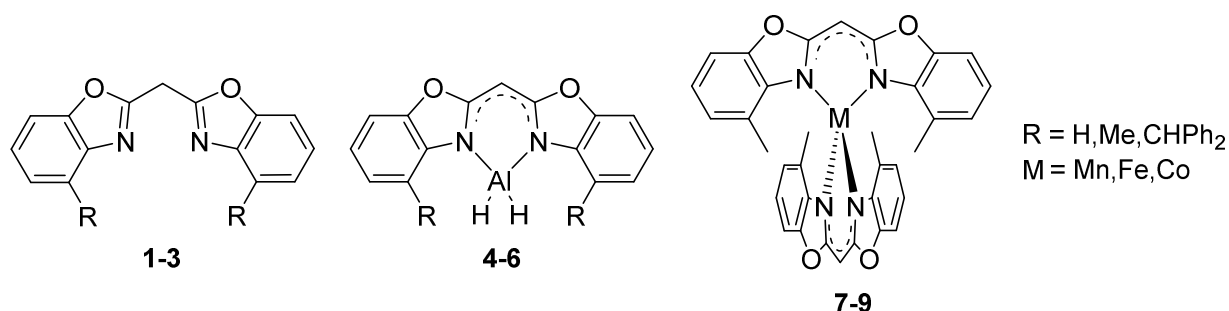
8.1 Attempted Data collection for other BOX ligands and their metal complexes

This thesis deals mainly with charge-density studies of compounds of the MeBOX ligand. This chapter will briefly summarize the attempted data collection for various other box complexes that were synthesized during my time in the Stalke group. A large number of possible candidates for investigation in this work, while providing crystals sufficient for standard IAM investigation, did not fulfil the requirements for a charge-density study.

8.1.1 Free Ligands

For all three free BOX ligands mentioned in the introductory Chapter 1, collection high resolution SCXRD datasets was attempted. Unfortunately, while a dataset of sufficient resolution and data quality could be obtained for **1**, this compound is disordered with the nitrogen and oxygen atoms of one benzoxazole moiety switching positions in a minor component of approximately 20%, which matches the original publication by Dauer *et al.* from 2014.^[6] It was not possible to recrystallise the compound without this disorder.

For **2** on the other hand, no crystals of sufficient quality for the high-resolution experiments could be obtained. Recrystallisation was attempted several times with varying parameters such as temperature and concentration of the solution. Crystallisation by evaporation was attempted as well as *via* cooling of a saturated solution of toluene as well as ethyl acetate. The main issue was not crystal size, but rather their overall structure. Crystals generally grew as slightly intergrown needles. Even the largest and most promising of them did not exceed a maximum resolution around 0.70 Å, making the compound unfit for MM refinement.



A high-resolution with sufficient quality of **3** could be successfully collected. While the final integration was performed up to a resolution of 0.50 Å, quality indicators for the outermost data are just barely still in acceptable ranges. Starting model generation was performed as described in Chapter 3. A 3λ correction according to Krause *et al.* was performed on the data.^[42] Third order Gram-Charlier coefficients for anharmonic motion were refined for several carbon atoms in the ligand, as seen in the final refinement strategy shown in Table 8-1. A list of selected quality indicators of the final model is shown in Table 8-2 below, as well as in Figure 8-1. However, lacking MM refinements of proper structures fit for comparison like another free BOX ligand or a metal complex of the same ligand, no further conclusions were drawn from these results.

Table 8-1: Final refinement strategy for **3**.

Step	Refined parameters (new)
1	SCALE
2	M
3	M DQOH
4	M DQOH Uij
5	M DQOH Uij xyz
6	M DQOH Uij xyz κ
7	Hxyz
8	M DQOH Uij xyz κ
9	κ'
10	M DQOH Uij xyz κ
11	Sigobs 0
12	U3 (C11-C14, C32-34, C38-39)
13	U3 (C3-4, C17-19, C31)

Table 8-2: Selected quality indicators for the final refinement of **3**.

	BOX3
$wR(F^2)$	0.0337
GOF	2.3727
$\Delta\rho_{\min}, \Delta\rho_{\max}$	-0.235,
$[e\text{\AA}^{-3}]$	0.345
$e_{\text{gross}} [e]$	41.5

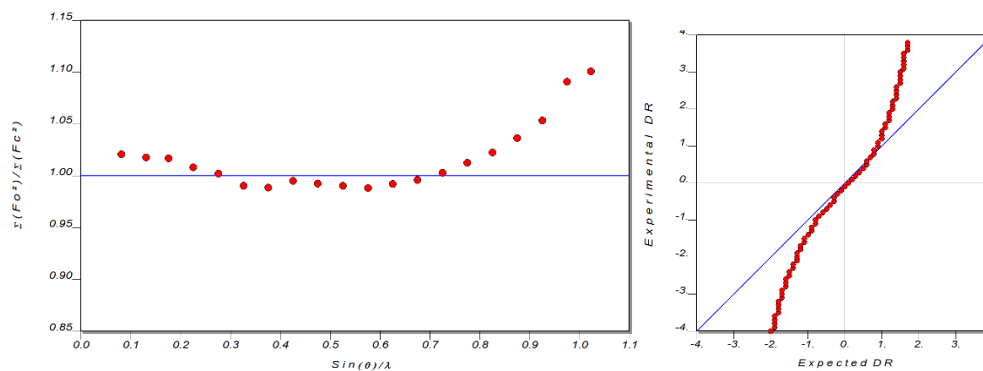


Figure 8-1: Structure factor plot and normal probability plot final model of **3**. The steep increase in the structure factor plot could not be fully remedied even with a integration with fixed box size.

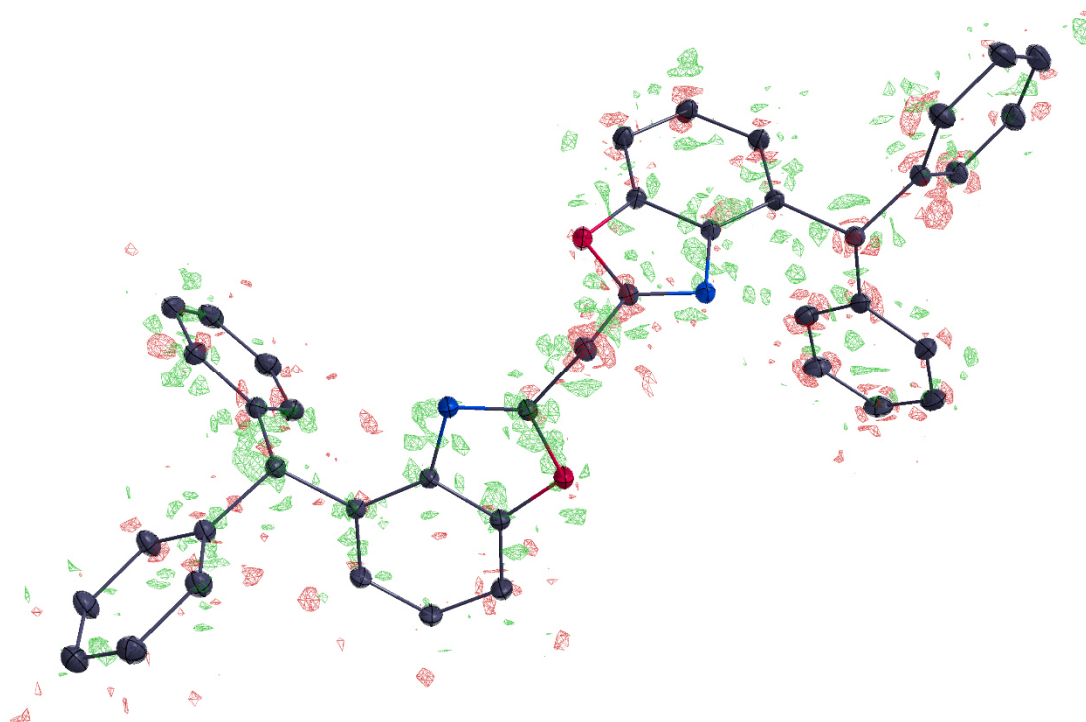


Figure 8-2: Residual density map and HM plot of the final model. Isolevel of residual density is $\pm 0.098 \text{ e}\text{\AA}^{-3}$.

8.1.2 Additional aluminium dihydride and group 13 complexes

The collection of high-resolution datasets of two additional aluminium BOX complexes was attempted besides the slightly disordered **5**. After the dataset of **3** was successfully collected, the goal was set to find a metal complex of this ligand suitable for MM refinement. The first investigated candidate was compound **6**. However, as the compound was first synthesized by Johannes Kretsch and crystallized from fluorobenzene, it turned out that heavily disordered solvent was present in the unit cell, making the compound unfit for MM refinement. Recrystallisation from a 1:1 mixture of n-hexane and benzene was attempted as well as recrystallisation from toluene. In the former case, the same site previously occupied by a positional disorder of fluorobenzene was now occupied by a substitutional disorder of the two mixed solvents. In the latter case, the toluene, while occupying the same spot in the unit cell as the other solvents, had only slightly enlarged ADPs, which were indicating of a rather small disorder that was no deal breaker for MM refinement per se. However, as the presence of disorder in a crystal causes electron density in a crystal to be less localised, which can be expected to impair the achievable maximum resolution. As such, besides the usual problems of disorder in MM refinements and charge-density analysis explained in Chapter 4, it was not possible to reach the required maximum resolution of 0.50 Å. Searching for an alternative to alane complex of **3**, the chemically less interesting **6'** was investigated as well. Starting from toluene, which was the most promising solvent for **6**, the complex turned out to have the same problems with disordered solvents that **6** showed. As was not possible to obtain a complex of **3** without disordered solvent, the focus of my PhD shifted from BOX-based alanes to the d-block compounds by Lüert and Legendre, as described in Chapter 0. The successfully collected dataset of the disordered **4** was instead used as sample structure for the development of a new approach to modelling small molecular disorders in MM refinements, as described in Chapter 4.

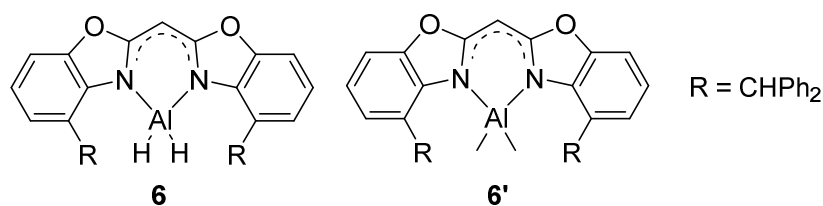


Figure 8-3: The two aluminium complexes of **3**, for which collection of high-resolution datasets was attempted. Crystals grown from toluene, fluorobenzene and a 1:1 mixture of n-hexane and benzene all contained disordered solvent to some degree in the asymmetric unit, impairing maximum resolution and/or making the compound generally unfit for MM refinement.

8.2 Charge-density Investigation on Si-O bonds in two different structures

The investigation of **10** and **11** was the most extensive side project I undertook during my PhD. The high-resolution X-ray datasets for this investigation were provided by the group of Professor Carsten Strohmann from Dortmund. The structures **10** and **11**, while bearing some structural similarities, behave very different chemically. While **12**, a comparable compound to **11**, is catalytically active in Si-C bond cleavage, **10** is not.^[147] The focus of the investigation of these structures was put on Si-O bond characterisation and in how far differences between the two compounds can be observed. As high-resolution diffraction data for focal compound **12** could not be obtained, further work on this study was ended after the comparison of Si-O bonding characters in **10** and **11** exhibited no noticeable differences.

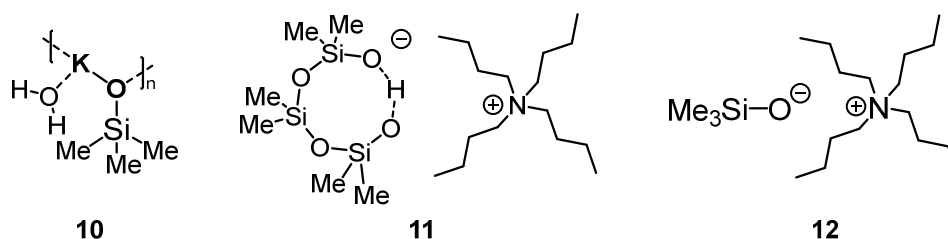


Figure 8-4: Silicon compounds within the scope of this project. High-resolution datasets for **10** and **11** were provided the group of Prof. Strohmann.

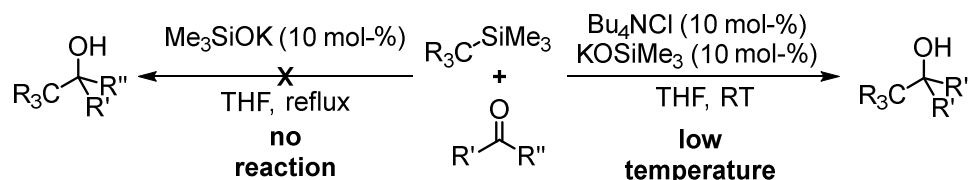


Figure 8-5: Different reactivities of compounds **10** and **12**.^[147]

8.2.1 Data collection

The data used for the refinements of both **10** and **11** was collected on a Bruker D8 Venture four-circle goniometer equipped with a Photon 100 detector and an Incoatec Mo I μ S source. For **10**, a dataset collected with the same setup except the use of a newer I μ S 3.0 source was available as well.

8.2.2 Data reduction

The available datasets were integrated with default settings in SAINT 8.40B. Afterwards, scaling absorption correction and error model determination were applied with *SADABS* 2016/2. An error model as described in Chapter 2.3 was applied. Tables of the dataset of **10** and the two datasets of **11** can be found in Table 8-3 below. As the first dataset for **11**, collected on the overall older setup, shows slightly higher completeness than the second, it was ultimately chosen for the final refinement. While further comparisons between both datasets were conducted during the multipole refinement process, only results from the superior dataset will be discussed in detail.

8.2.3 Model refinement

The general procedure for starting model generation and MM refinement was akin to the one described in Chapter 3. The detailed refinement strategies for **10** and **11** can be found in Table 8-4 and Table 8-5, respectively.

Table 8-3: Selected quality indicators of the final models for **10** and **11**, differentiating the two available high-resolution datasets for **11**. As the first dataset using the older X-ray source had a superior completeness, it was chosen for the final model.

	10	11(1)	11(2)
Maximum Res. [\AA]	0.47	0.48	0.48
Rrim/ Rpim	0.1028/0.0311	0.0405/0.0040	0.0339/0.0042
Completeness	99.55	99.87	96.81
$wR(F^2)$	0.0205	0.0212	0.0262
GoF	2.5091	2.9353	2.7975
$\Delta\rho_{\min}, \Delta\rho_{\max}$ [$e\text{\AA}^{-3}$]	-0.470/0.402	-0.261, 0.192	-0.290, 0.235
e_{gross} [e]	9.48	32.6	32.5

Table 8-4: Final refinement strategy for **10**. Potassium was refined as K^+ . Half an electron from its valence shell was moved to each of the adjacent oxygen atoms in the starting model for MM refinement. Strategy was checked for overfitting using the script by Krause *et al.*^[78]

Step	Refined parameters (new)
1	SCALE
2	M
3	M DQOH
4	M DQOH Uij
5	M DQOH Uij xyz
6	M DQOH Uij xyz κ
7	Hxyz
8	M DQOH Uij xyz κ
9	κ'
10	M DQOH Uij xyz κ
11	Sigobs 0
12	U3 (C1-3)

Table 8-5: Final refinement strategy for **11**. Strategy was checked for overfitting using the script by Krause *et al.*^[78]

Step	Refined parameters (new)
1	SCALE
2	M
3	M DQOH
4	M DQOH Uij
5	M DQOH Uij xyz
6	M DQOH Uij xyz κ
7	Hxyz
8	M DQOH Uij xyz κ
9	κ'
10	M DQOH Uij xyz κ
11	Sigobs 0
12	U3 (C4, C6, C10, C14, C18, C22)
13	U3 (C3, C13, C17)
14	Nocon Si
15	Nosymm Si
16	Nocon O

8.2.4 Discussion and results

The QTAIM analysis of both compounds was conducted in XDPROP in the XD2016 programme suite. A critical point search of the entire structure was conducted for both **10** and **11**. Furthermore, maps of the Laplacian around the silicon atoms were generated in the search for VSCCs. Analysis of the Laplacian at the BCPs between oxygen and silicon atoms for both structures reveals two basic types of similar bonding situation. The bonds between Si2-O2 and Si2-O3 have slightly lower Laplacian values and a lower kinetic energy densities and lower negative potential energy density than all other compared Si-O bonds. Nevertheless, it is $\nabla^2\rho(r_{BCP}) \gg 0$ for all compared bonds. Therefore, the aforementioned decrease in the Laplacian merely indicates a slightly less pronounced closed-shell character in a group of strongly distinctively ionic bonds. As described by Espinosa *et al.*, the negative values of $V_b(r_{BCP})$ indicate a significant covalent contribution in the overall ionic character of the bonds. Inspection of Laplacian maps revealed no additional insights into differences in the bonding situations.

Table 8-6: Selected topological parameters at the BCPs of Si-O Bonds in Structures **10** and **11**. Values in the last row are taken from structure **11**. $\rho(r_{\text{BCP}})$: Charge-density at the BCP, $\nabla^2\rho(r_{\text{BCP}})$: Laplacian at the BCP, d_{BP} : Length of the bond path, $dI/2_{\text{BC}}$: distance of atom 1/2 to the BCP, $H_{\text{b}}(r_{\text{BCP}})$: Total electrical energy density at the BCP, $G_{\text{b}}(r_{\text{BCP}})$: Kinetic energy density at the BCP, $V_{\text{b}}(r_{\text{BCP}})$: potential energy density at the BCP.

A1	A2	$\rho(r_{\text{BCP}})$ [eÅ ⁻³]	$\nabla^2\rho(r_{\text{BCP}})$ [eÅ ⁻⁵]	d_{BP} [Å]	dI_{BCP} [Å]	$d2_{\text{BCP}}$ [Å]	$H_{\text{b}}(r_{\text{BCP}})$ [E _h Å ⁻³]	$G_{\text{b}}(r_{\text{BCP}})$ [E _h Å ⁻³]	$V_{\text{b}}(r_{\text{BCP}})$ [E _h Å ⁻³]	$ V_{\text{b}} /G_{\text{b}}$
Si1	O1	1.14	14.22	1.6078	0.6819	0.9259	-0.67	1.66	-2.33	1.4036
Si1	O2	1.01	11.63	1.6491	0.6933	0.9558	-0.55	1.36	-1.91	1.4044
Si2	O2	1.05	14.07	1.6287	0.6868	0.9419	-0.54	1.52	-2.06	1.3553
Si2	O3	1.02	15.06	1.6273	0.6866	0.9407	-0.48	1.53	-2.01	1.3137
Si3	O3	0.98	11.99	1.6539	0.6949	0.9590	-0.49	1.33	-1.83	1.3759
Si3	O4	1.19	15.37	1.5947	0.6774	0.9173	-0.72	1.79	-2.51	1.4022
Si1*	O1*	1.13	15.23	1.6116	0.6833	0.9283	-0.63	1.69	-2.32	1.3728

*:taken from structure **11**

8.2.5 Conclusion and outlook

Overall from the inspected BCPs alone, and lacking a suitable dataset of the catalytic compound **12** itself, no conclusive evidence for the difference in chemical behaviour for **10** and **12** can be gleaned. While this study could demonstrate that the investigated compound **11** is not a sufficient model system for investigation of the catalytic activity of **12**, the conducted work on it could prove useful for comparison in future charge-density studies of Si-O bonding in similar compounds. The necessary groundwork for future uses of the MM refinements on structures **10** and **11**, such as determination of the best dataset for **11** and determination of a suitable refinement strategy, is now concluded.

8.3 Development of a Crystallisation strategy for growing [2.2]paracyclophane crystals of sufficient size for neutron and benchmarking experiments

[2.2]Paracyclophane (PCP) is a compound widely used in synthetic chemistry,^[148] making investigation of its reactivity a worthwhile endeavour.^[149] Furthermore, as PCP is air stable and commercially available at a relatively low price, making it interesting as a potential benchmarking substance for diffraction experiments. This use requires a highly reproducible strategy for producing near-identical crystals is required. The aforementioned benchmarking crystals are usually cut to spherical shape to ensure an equal beam intersection from all orientations. Crystallisation of PCP is an uncomplicated task per se, as crystals can be easily obtained from cooling an oversaturated solution of toluene. Alternatively, the solution can be evaporated as well for a similar effect. As an anecdotal advice on this project goes, good quality PCP crystals are supposedly best obtained by “placing a beaker with solution on a warm vacuum pump and forgetting it over lunch”. However, crystals obtained in either of these ways are generally relatively small, around 100 μm in diameter. This is generally sufficient for standard SCXRD experiments, although even here, better results can be expected from slightly larger crystal, as the purely organic PCP is purely organic and lacks heavier elements with large numbers of electrons. During the first year of my PhD, I experimented with different approaches for reproducible crystallisation of large paracyclophane crystals of sufficient size for cutting into spherical shape and/or neutron diffraction experiments requiring crystals sizes around 1 mm at minimum. In order to obtain larger crystals, it was concluded that the best approach we be slowing down the crystallisation process in order to facilitate the growth of a smaller number of larger crystals. Slowing down the cooling of saturated solution of heated toluene had only limited success, as the number forming initial nuclei was still too large. This lead, again, to a large number of small crystals. A similar problem was encountered when slow evaporation of a non-heated saturated solution was attempted under a fume hood. Even slow evaporation in a beaker at room temperature, further slowed down by limiting the size of its opening using two glass microscope slides still lead to a comparable problem. The latter method however showed a more promising outlook, as prolonging evaporation over an even longer time is more feasible than prolonging the cooling process of a heated solution.

In order to provide an even more controlled crystallisation environment, a continuous flow table cryostat with isopropanol as coolant was used for keeping a constant temperature in the crystallisation batch. Custom-made double-walled beakers from the glass workshop were used, permitting a consistent flow of coolant between the two walls. Constant temperatures at 20 °C and 15 °C still did not lead to sufficiently large crystals, producing a number of larger plates instead. Slow evaporation of a saturated solution of PCP in toluene at 10 °C, including the previously used microscope slides finally yielded crystals of desired size and quality. With 100 mL of starting solution, the process of evaporation and crystal growth takes between two and three weeks and is highly reproducible, resulting in PCP crystal of approximately 1-2 mm in size. The method described here is now routinely used by the technical staff of the Stalke group.

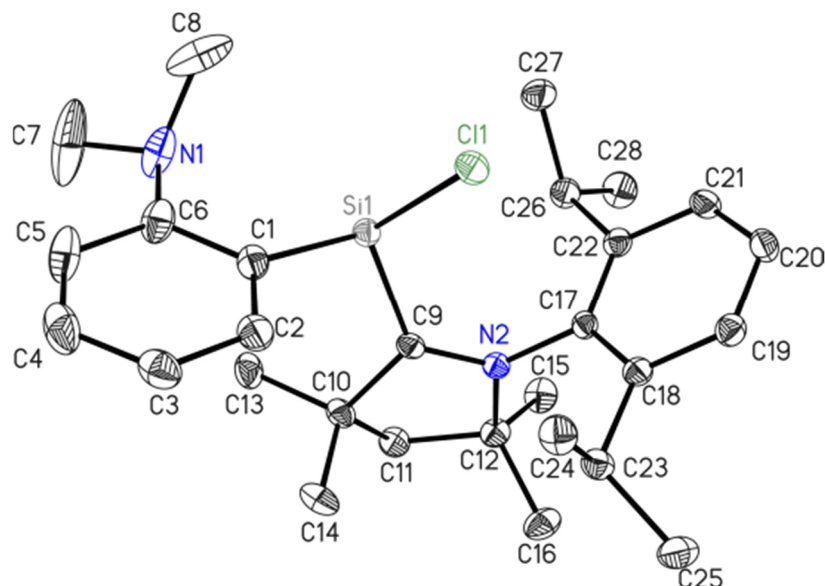


Figure 8-6: Left: Setup with the cryostat on the floor and the double-walled beaker on the bench. Isopropanol at 10 °C is constantly pumped through the beaker. Middle: Close-up of the beaker setup. Two microscope slides are used to even further limit evaporation speed, and thus, crystal growth speed. Right: First batch of paracyclophane crystals grown with the reported crystallisation. Crystal diameter lies between 1-2 mm.

9 Crystal Structure Determination in Collaboration

9.1 Structures determined for Dr. Wenling Li

9.1.1 CK_WL2



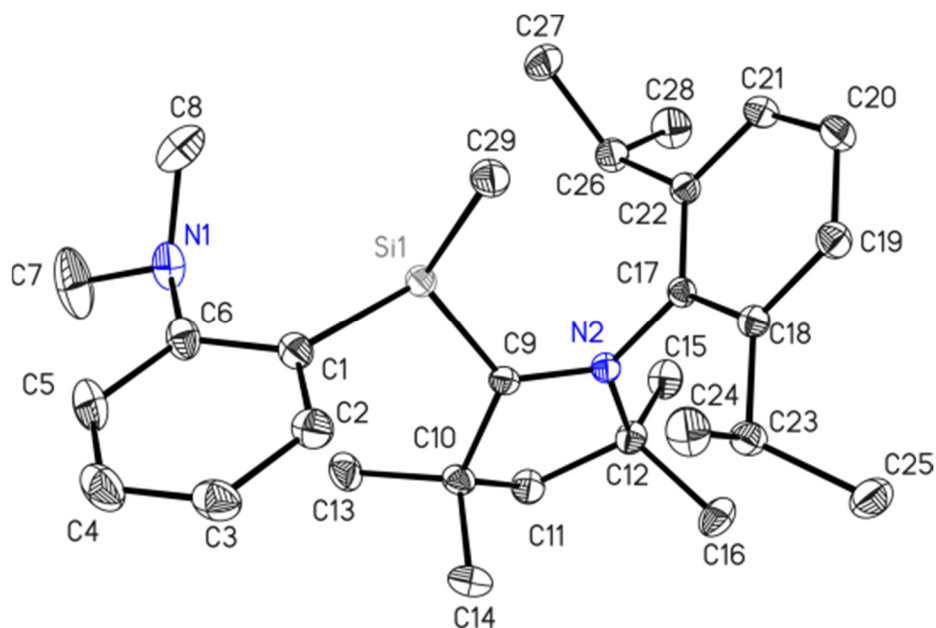
Graphical representation of the asymmetric unit. Hydrogen atoms are omitted for clarity..

This structure was published in:

Wenling Li, C.Köhler, Zhi Yang, D.Stalke, R.Herbst-Irmer, H.W.Roesky, *Chem.-Eur. J.*, **2019**, *25*, 1193. Structural information CIF format available with CSD number: **1873888**

Structure code	CK_WL2	ρ_{calc} [g cm ⁻³]	1.166
Empirical formula	C ₂₈ H ₄₁ ClN ₂ Si	μ [mm ⁻¹]	0.206
Formula Weight [g mol ⁻¹]	469.17	F(000)	508
Temperature [K]	100(2)	Crystal Size [mm]	0.196 x 0.187 x 0.117
Wavelength [Å]	0.71073	θ range [°]	1.563 to 27.234
Crystal System	Triclinic	Reflections Collected	78277
Space Group	P $\bar{1}$	Unique reflections	5970
Unit cell dimensions [Å]	a = 9.986(2) b = 10.647(2) c = 13.658(3) α = 76.47(2)° β = 75.99(2) γ = 74.78(2)	Completeness to θ_{max} :	100.0 %
Volume [Å ³]	1336.8(5)	Data/Restraints/Parameters	5970 / 0 / 299
Z	2	R_{int}	0.0302
		$R1$ [$I > 2\sigma(I)$]	0.0313
		wR2 (all data)	0.0831
		Goof	1.049
		Largest Diff. peak and hole [e Å ⁻³]	0.378 and -0.228

9.1.2 CK_WL5



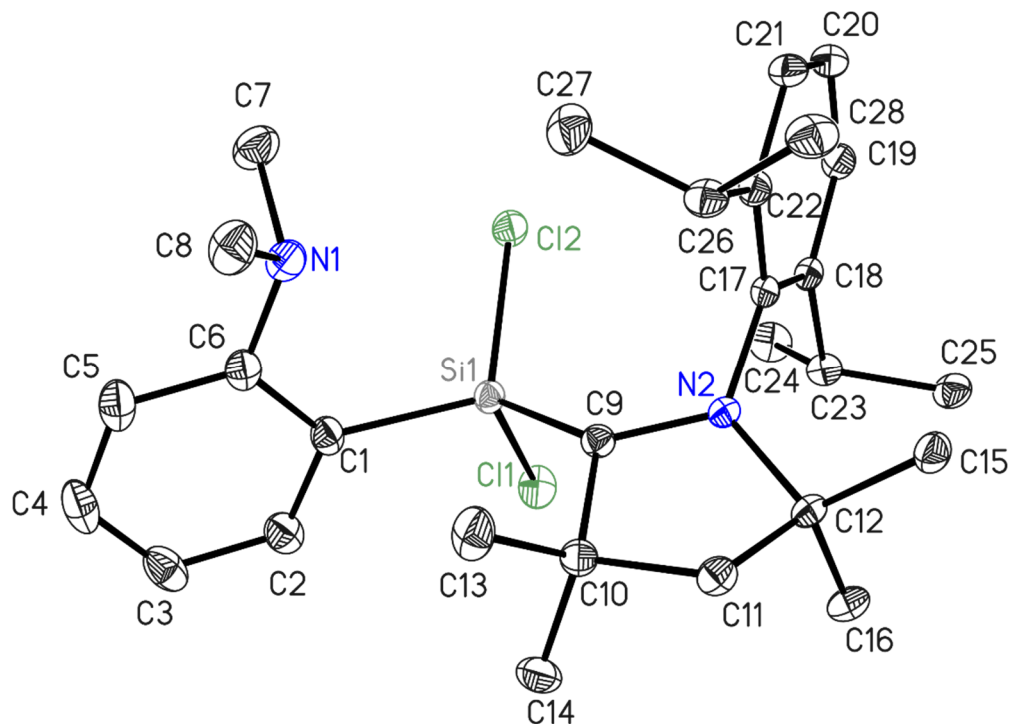
Graphical representation of the asymmetric unit. Hydrogen atoms are omitted for clarity. ADPs are displayed at the 50% probability level.

This structure was published in:

Wenling Li, C.Köhler, Zhi Yang, D.Stalke, R.Herbst-Irmer, H.W.Roesky, *Chem.-Eur. J.*, **2019**, *25*, 1193. Structural information CIF format available with CSD number: **1873889**

Structure code	CK_WL5	ρ_{calc} [g cm ⁻³]	1.106
Empirical formula	C ₂₉ H ₄₄ N ₂ Si	μ [mm ⁻¹]	0.105
Formula Weight [g mol ⁻¹]	448.75	F(000)	492
Temperature [K]	100(2)	Crystal Size [mm]	0.196 x 0.187x 0.117
Wavelength [Å]	0.71073	θ range [°]	1.562 to 30.496
Crystal System	Triclinic	Reflections Collected	105094
Space Group	P $\bar{1}$	Unique reflections	8215
Unit cell dimensions [Å]	a = 10.042(2) b = 10.659(2) c = 13.649(3) α = 76.48(2) β = 76.36(2) γ = 74.84(2)	Completeness to θ_{max} :	100.0 %
Volume [Å ³]	1347.1(5)	Data/Restraints/Parameters	8215 / 0 / 300
Z	2	R_{int}	0.0427
		$R1$ [$I > 2\sigma(I)$]	0.0362
		$wR2$ (all data)	0.01029
		$Goof$	1.045
		Largest Diff. peak and hole [e Å ⁻³]	0.428 and -0.228

9.1.3 CK_WL8



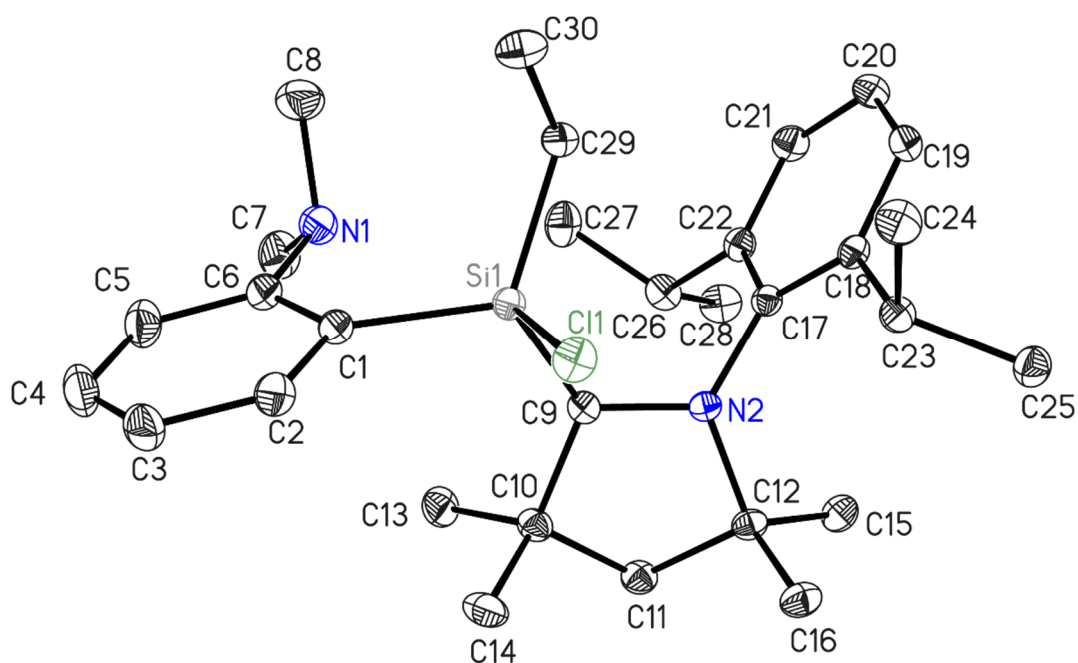
Graphical representation of the asymmetric unit. Hydrogen atoms are omitted for clarity. ADPs are displayed at the 50% probability level.

This structure was published in:

Wenling Li, Subrata Kundu, Christian Köhler, Jiancheng Li, Sayan Dutta, Zhi Yang, Dietmar Stalke, Regine Herbst-Irmer, A. Claudia Stückl, Brigitte Schwederski, Debasis Koley, Wolfgang Kaim, Herbert W. Roesky, *Organometallics*, **2019**, *38*, 1939. Structural information CIF format available with CSD number: **1891825**

Structure code	CK_WL8	ρ_{calc} [g cm ⁻³]	1.204
Empirical formula	C ₂₈ H ₄₁ Cl ₂ N ₂ Si	μ [mm ⁻¹]	0.295
Formula Weight [g mol ⁻¹]	504.62	F(000)	492
Temperature [K]	100(2)	Crystal Size [mm]	0.371 x 0.245x 0.182
Wavelength [Å]	0.71073	θ range [°]	2.159 to 27.125
Crystal System	Triclinic	Reflections Collected	164135
Space Group	P $\bar{1}$	Unique reflections	6144
Unit cell dimensions [Å]	a = 9.003(2) b = 9.189(2) c = 19.079(3) α = 93.40(2) β = 95.54(2) γ = 116.86(2)	Completeness to θ_{max} :	100.0 %
Volume [Å ³]	1392.1(5)	Data/Restraints/Parameters	6144 / 0 / 308
Z	2	R_{int}	0.0250
		$R1$ [$I > 2\sigma(I)$]	0.0260
		wR2 (all data)	0.0695
		Goof	1.045
		Largest Diff. peak and hole [e Å ⁻³]	0.420 and -0.195

9.1.4 CK_WL9



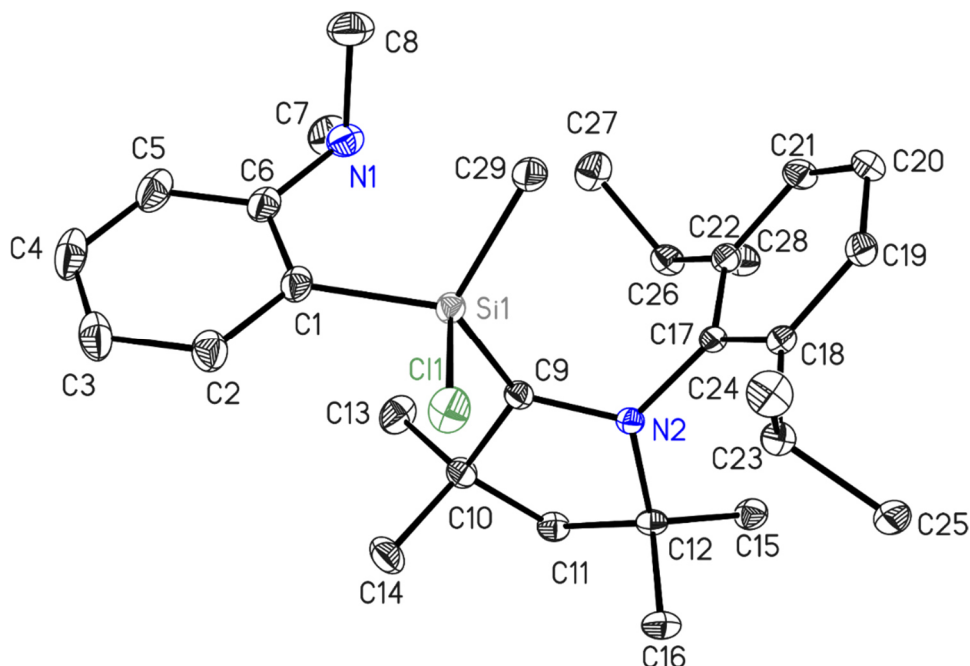
Graphical representation of the asymmetric unit. Hydrogen atoms are omitted for clarity. ADPs are displayed at the 50% probability level.

This structure was published in:

Wenling Li, Subrata Kundu, Christian Köhler, Jiancheng Li, Sayan Dutta, Zhi Yang, Dietmar Stalke, Regine Herbst-Irmer, A. Claudia Stückl, Brigitte Schwederski, Debasis Koley, Wolfgang Kaim, Herbert W. Roesky *Organometallics*, **2019**, *38*, 1939. Structural information CIF format available with CSD number: **1891826**

Structure code	CK_WL9	ρ_{calc} [g cm ⁻³]	1.140
Empirical formula	C ₃₀ H ₄₆ ClN ₂ Si	μ [mm ⁻¹]	0.193
Formula Weight [g mol ⁻¹]	498.23	F(000)	1084
Temperature [K]	100(2)	Crystal Size [mm]	0.204 x 0.178x 0.130
Wavelength [Å]	0.71073	θ range [°]	2.060 to 27.141
Crystal System	Monoclinic	Reflections Collected	252354
Space Group	P2 ₁ /c	Unique reflections	6415
Unit cell dimensions [Å]	a = 9.158(2)	Completeness to θ_{max} :	100.0 %
	b = 39.540(2)	Data/Restraints/Parameters	6415 / 0 / 318
	c = 9.204(3)	R_{int}	0.0401
	α = 90	RI [$I > 2\sigma(I)$]	0.0310
	β = 119.45(2)	$wR2$ (all data)	0.0774
	γ = 90	$Goof$	1.045
Volume [Å ³]	2902.2(13)	Largest Diff. peak and hole [e Å ⁻³]	0.375 and -0.261
Z	4		

9.1.5 CK_WL10



Graphical representation of the asymmetric unit. Hydrogen atoms are omitted for clarity. ADPs are displayed at the 50% probability level.

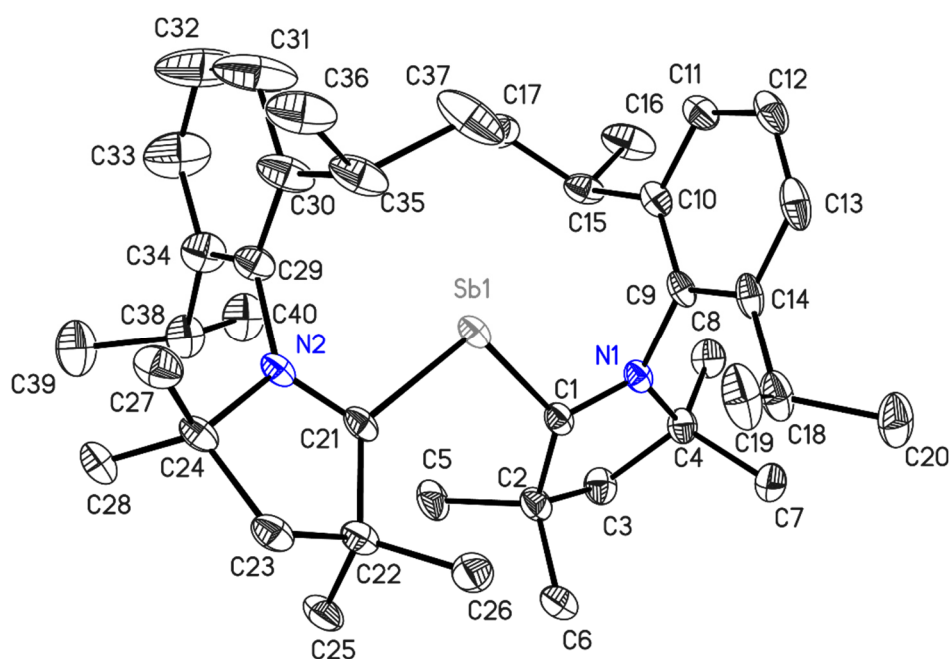
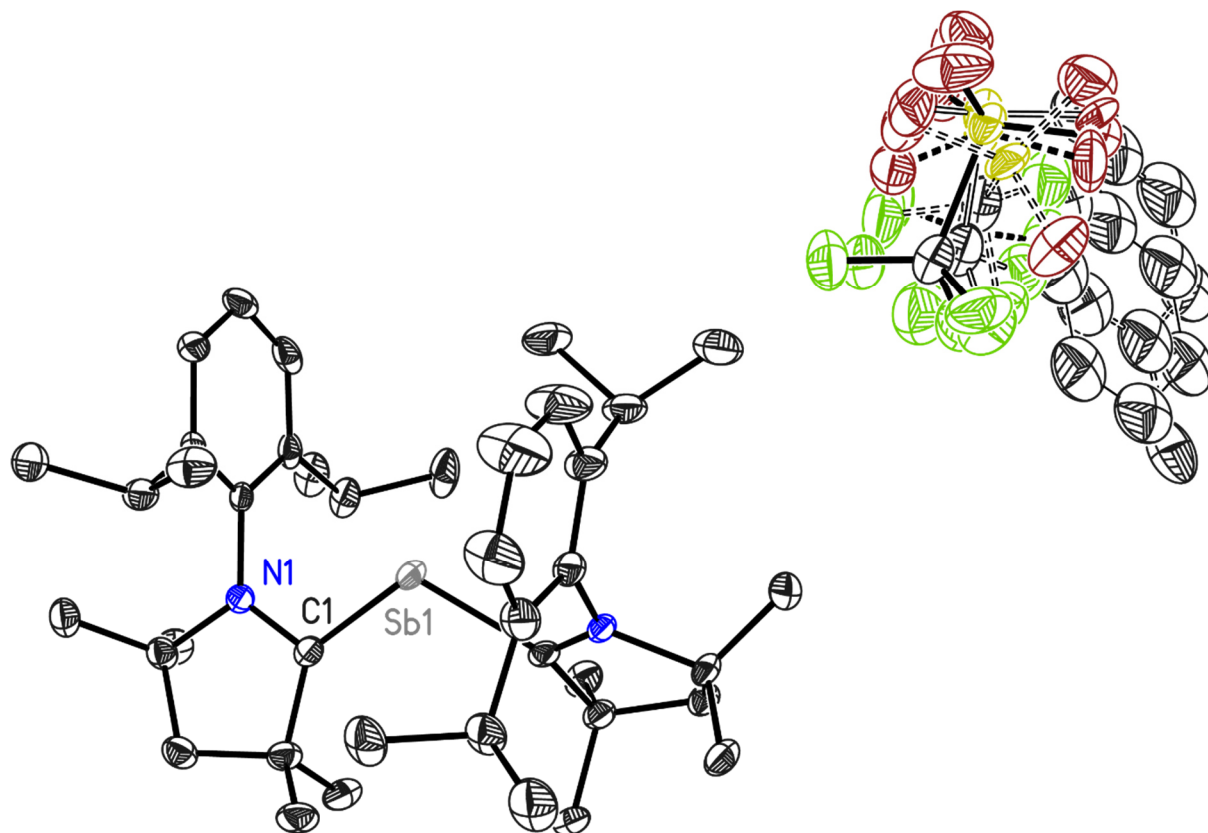
This structure was published in:

Wenling Li, Subrata Kundu, Christian Köhler, Jiancheng Li, Sayan Dutta, Zhi Yang, Dietmar Stalke, Regine Herbst-Irmer, A. Claudia Stückl, Brigitte Schwederski, Debasis Koley, Wolfgang Kaim, Herbert W. Roesky, *Organometallics*, **2019**, *38*, 1939. Structural information CIF format available with CSD number: **1891827**

Structure code	CK_WL10	ρ_{calc} [g cm ⁻³]	1.150
Empirical formula	C ₂₉ H ₄₄ ClN ₂ Si	μ [mm ⁻¹]	0.199
Formula Weight [g mol ⁻¹]	484.20	F(000)	526
Temperature [K]	100(2)	Crystal Size [mm]	0.298 x 0.137x 0.080
Wavelength [Å]	0.71073	θ range [°]	1.072 to 27.110
Crystal System	Triclinic	Reflections Collected	91697
Space Group	P $\bar{1}$	Unique reflections	6160
Unit cell dimensions [Å]	a = 9.064(2) b = 9.159(2) c = 19.190(3) α = 93.49(2) β = 94.93(2) γ = 117.57(2)	Completeness to θ_{max} :	100.0 %
Volume [Å ³]	1397.8(5)	Data/Restraints/Parameters	6160 / 0 / 309
Z	2	R_{int}	0.0386
		$R1$ [$I > 2\sigma(I)$]	0.0299
		wR2 (all data)	0.0799
		<i>Goof</i>	1.047
		Largest Diff. peak and hole [e Å ⁻³]	0.482 and -0.241

9.2 Structures determined for Dr. Majahuddin Siddiqui

9.2.1 CK_MM268



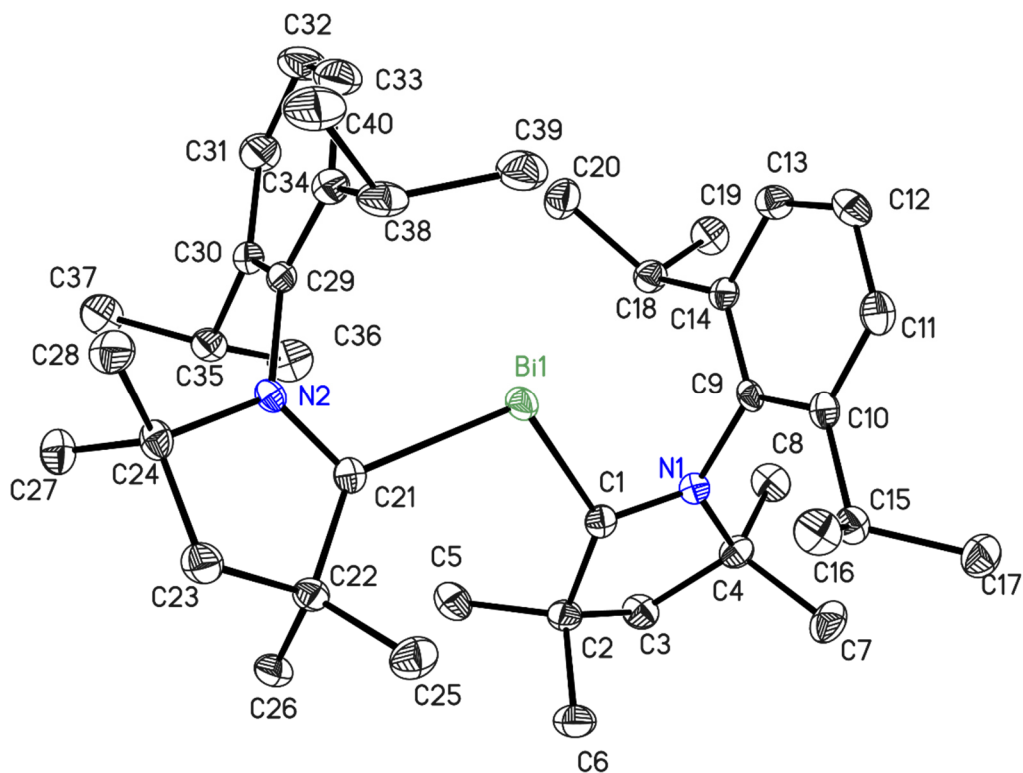
Graphical representation of the asymmetric unit. Hydrogen atoms are omitted for clarity. ADPs are displayed at the 50% probability level.

This structure was published in:

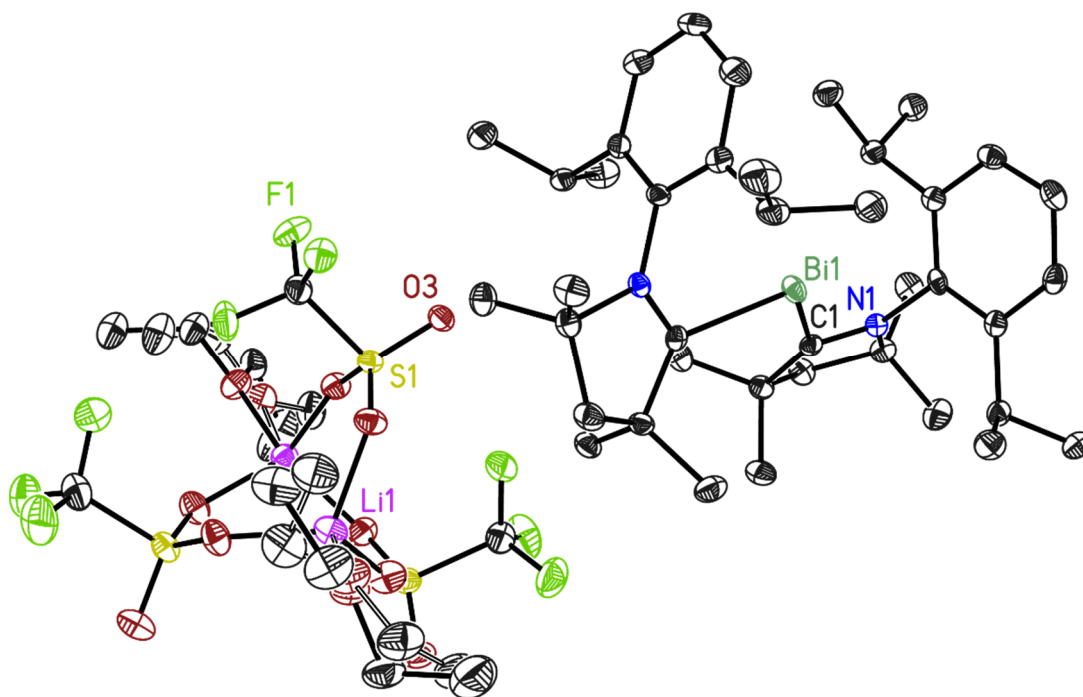
Mujahuddin M. Siddiqui, Samir Kumar Sarkar, Mohd Nazish, Massimiliano Morganti, Christian Köhler, Jiali Cai, Lili Zhao, Regine Herbst-Irmer, Dietmar Stalke, Gernot Frenking, Herbert W. Roesky, *Journal of the American Chemical Society*, **2021**, 143, 1301. Structural information CIF format available with CSD number: **2023671**

Structure code	CK_MM268	ρ_{calc} [g cm ⁻³]	1.298
Empirical formula	C _{44.50} H ₆₆ F ₃ N ₂ O ₃ S Sb	μ [mm ⁻¹]	0.704
Formula Weight [g mol ⁻¹]	887.80	F(000)	1860
Temperature [K]	100(2)	Crystal Size [mm]	0.704 x 0.109x 0.040
Wavelength [Å]	0.71073	θ range [°]	1.263 to 27.160
Crystal System	Monoclinic	Reflections Collected	80806
Space Group	P2 ₁ /n	Unique reflections	10055
Unit cell dimensions [Å]	a = 9.187(2)	Completeness to θ_{max} :	100.0 %
	b = 15.327(2)	Data/Restraints/Parameters	10055 / 2064 / 823
	c = 32.277(4)	R_{int}	0.0498
	$\alpha = 90$	$R1$ [$I > 2\sigma(I)$]	0.0274
	$\beta = 92.02(2)$	$wR2$ (all data)	0.0648
	$\gamma = 90$	$Goof$	1.025
Volume [Å ³]	4542.1(13)	Largest Diff. peak and hole [e Å ⁻³]	0.800 and -0.364
Z	4		

9.2.2 CK_MM290



Graphical representation of the central compound. Hydrogen atoms are omitted for clarity. ADPs are displayed at the 50% probability level.



Graphical representation of the asymmetric unit. Hydrogen atoms are omitted for clarity. ADPs are displayed at the 50% probability level.

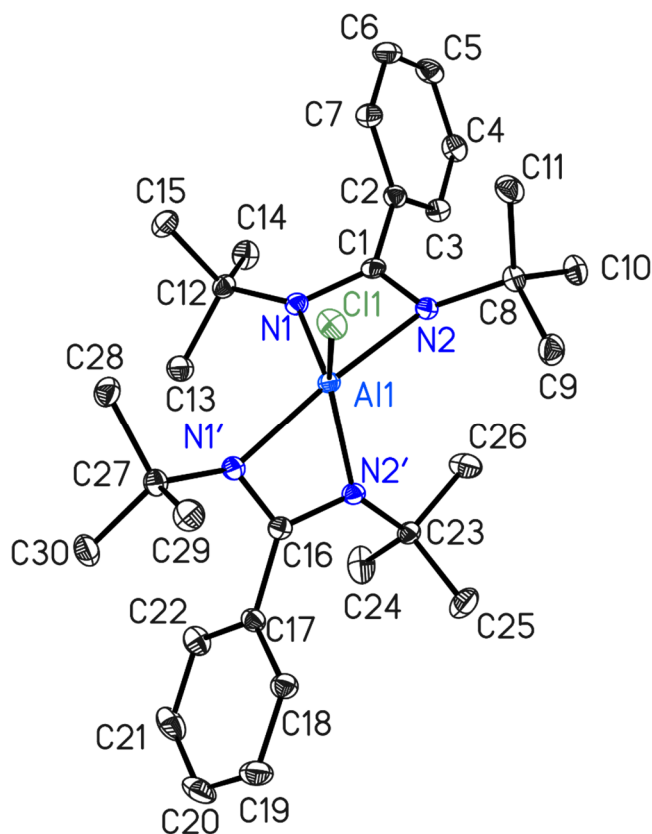
This structure was published in:

Mujahuddin M. Siddiqui, Samir Kumar Sarkar, Mohd Nazish, Massimiliano Morganti, Christian Köhler, Jiali Cai, Lili Zhao, Regine Herbst-Irmer, Dietmar Stalke, Gernot Frenking, Herbert W. Roesky, Journal of the American Chemical Society, **2021**, 143, 1301. Structural information CIF format available with CSD number: **2023670**

Structure code	CK_MM290	ρ_{calc} [g cm ⁻³]	1.461
Empirical formula	C ₅₁ H ₈₂ BiF ₉ Li ₂ N ₂ O ₁₁ S ₃	μ [mm ⁻¹]	2.971
Formula Weight [g mol ⁻¹]	1389.22	F(000)	2832
Temperature [K]	100(2)	Crystal Size [mm]	0.184 x 0.084x 0.045
Wavelength [Å]	0.71073	θ range [°]	1.192 to 25.033
Crystal System	Monoclinic	Reflections Collected	126568
Space Group	P2 ₁ /n	Unique reflections	11157
Unit cell dimensions [Å]	a = 24.689(2)	Completeness to θ_{max} :	100.0 %
	b = 9.342(2)	Data/Restraints/Parameters	11157 / 426 / 820
	c = 27.653(3)	R_{int}	0.0721
	$\alpha = 90$	$R1$ [$I > 2\sigma(I)$]	0.0253
	$\beta = 98.07(2)$	$wR2$ (all data)	0.0512
	$\gamma = 90$	$Goof$	1.014
Volume [Å ³]	6314.9(16)	Largest Diff. peak and hole [e Å ⁻³]	0.616 and -0.475
Z	4		

9.3 Structures determined for Dr. Chowan Ashok

9.3.1 CK_CAK_CISiAlSiCl



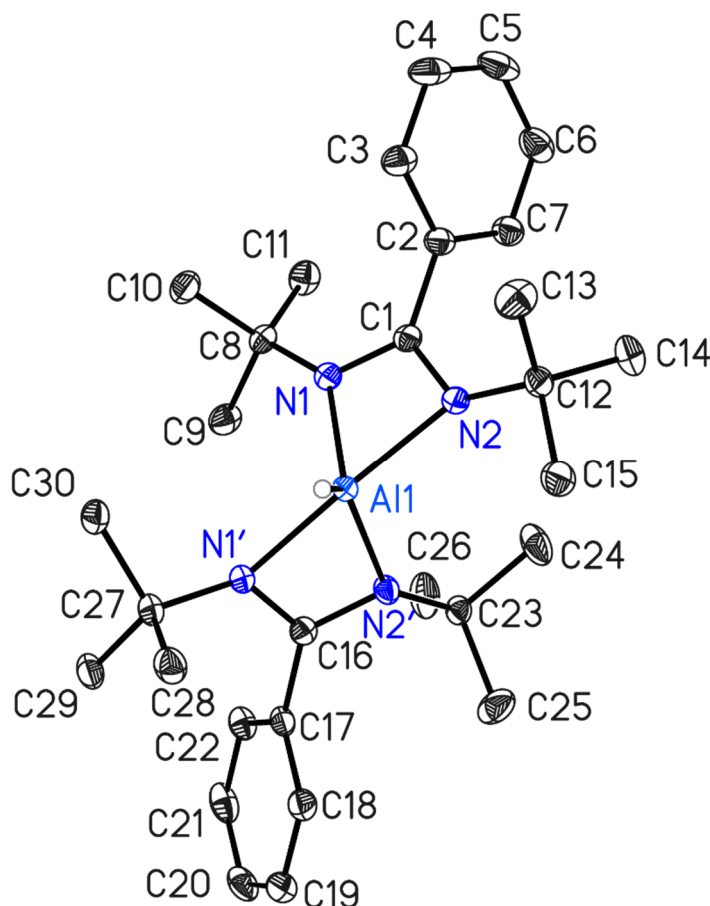
Graphical representation of the asymmetric unit. Hydrogen atoms are omitted for clarity. ADPs are displayed at the 50% probability level.

This structure was published in:

Samya Banerjee, Chowan Ashok Kumar, Sanjoy Bose, Samir Kumar Sarkar, Sandeep K Gupta, Nico Graw, Christian Köhler, Regine Herbst-Irmer, Dietmar Stalke, Sayan Dutta, Debasis Koley, Herbert W. Roesky: "Preparation and Reactivity Studies of Four and Five coordinated Amidinate Aluminum Compounds", *Z. Anorg. Allg. Chem.*, **2021**, 647, 1735–1743. Structural information CIF format available with CSD number: **2063441**

Structure code	CK_CAK_CISiAlSiCl	ρ_{calc} [g cm ⁻³]	1.172
Empirical formula	C ₃₀ H ₄₆ AlClN ₄	μ [mm ⁻¹]	0.183
Formula Weight [g mol ⁻¹]	525.14	F(000)	568
Temperature [K]	100(2)	Crystal Size [mm]	0.200 x 0.100 x 0.100
Wavelength [Å]	0.71073	θ range [°]	1.751 to 27.107
Crystal System	Triclinic	Reflections Collected	55948
Space Group	P $\bar{1}$	Unique reflections	6569
Unit cell dimensions [Å]	a = 11.225(2)	Completeness to θ_{max} :	100.0 %
	b = 12.534(2)	Data/Restraints/Parameters	6569 / 0 / 337
	c = 12.718(3)	R_{int}	0.0326
	α = 67.23(2)	R_I [$I > 2\sigma(I)$]	0.0294
	β = 74.52(3)	wR2 (all data)	0.0770
	γ = 65.42(2)	Goof	1.041
Volume [Å ³]	1488.4(6)	Largest Diff. peak and hole [e Å ⁻³]	0.366 and -0.251
Z	2		

9.3.2 CK_CAK67



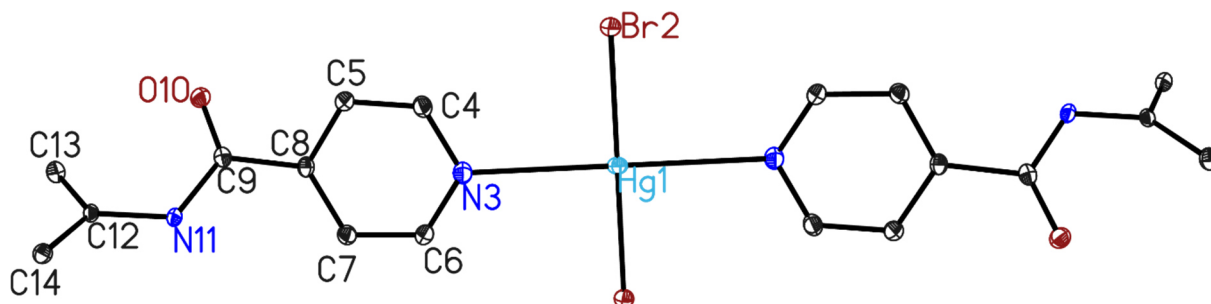
Graphical representation of the asymmetric unit. Hydrogen atoms are omitted for clarity. ADPs are displayed at the 50% probability level.

Structure code	CK_CAK67	ρ_{calc} [g cm ⁻³]	1.121
Empirical formula	C ₃₀ H ₄₇ AlN ₄	μ [mm ⁻¹]	0.094
Formula Weight [g mol ⁻¹]	490.69	F(000)	536
Temperature [K]	100(2)	Crystal Size [mm]	0.393 x 0.214 x 0.090
Wavelength [Å]	0.71073	θ range [°]	1.755 to 27.041
Crystal System	Triclinic	Reflections Collected	84242
Space Group	P $\bar{1}$	Unique reflections	6355
Unit cell dimensions [Å]	a = 11.018(2)	Completeness to θ_{max} :	100.0 %
	b = 12.590(2)	Data/Restraints/Parameters	6355 / 0 / 332
	c = 12.828(3)	R_{int}	0.0247
	α = 65.43(2)	RI [$I > 2\sigma(I)$]	0.0348
	β = 74.76(3)	$wR2$ (all data)	0.0921
	γ = 64.51(3)	$Goof$	1.032
Volume [Å ³]	1453.2(7)	Largest Diff. peak and hole [e Å ⁻³]	0.343 and -0.221
Z	2		

9.4 Structures determined for Arghavan Abolghasempour

All of these structures except EI3 were collected together with Katharina Rachuy for her Bachelor thesis.

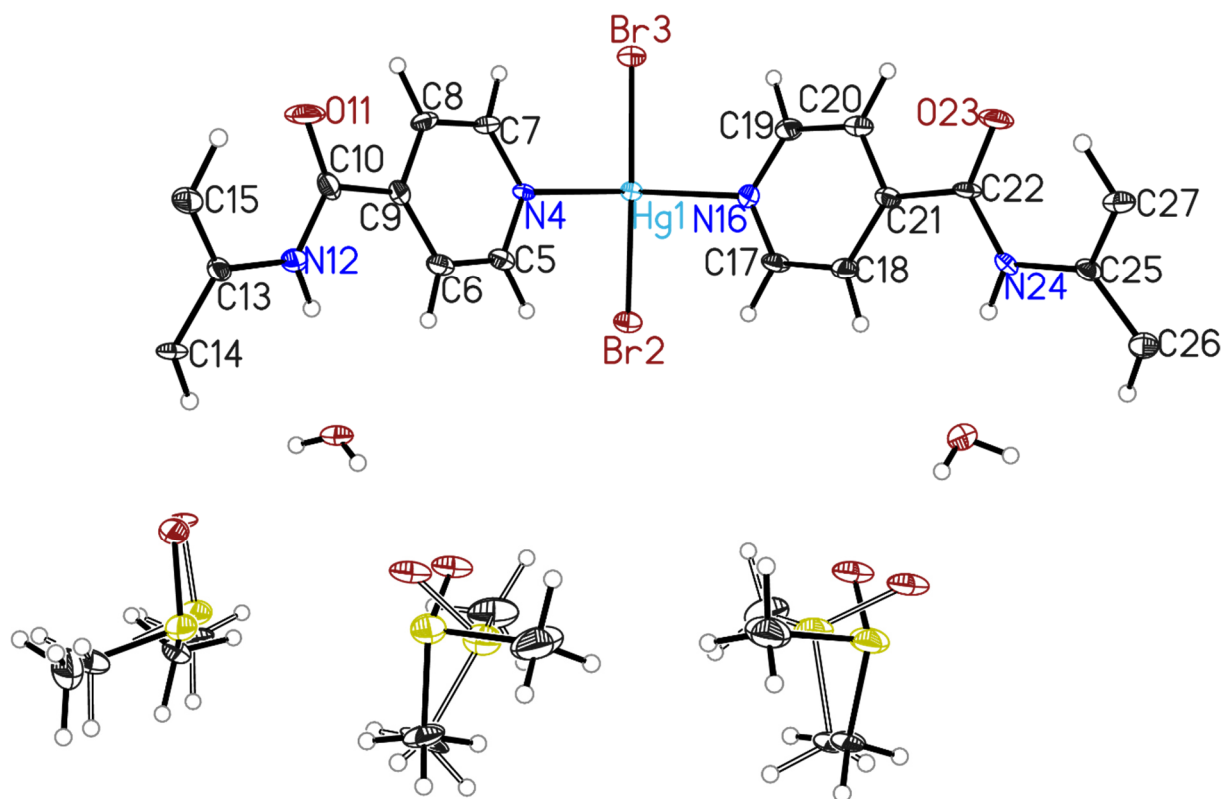
9.4.1 KR_CK_18



Graphical representation of the asymmetric unit. Hydrogen atoms are omitted for clarity. ADPs are displayed at the 50% probability level.

Structure code	KR_CK_A18	ρ_{calc} [g cm ⁻³]	2.502
Empirical formula	C ₁₈ H ₁₄ Br ₂ HgN ₄ O ₂	μ [mm ⁻¹]	13.000
Formula Weight [g mol ⁻¹]	678.74	F(000)	632
Temperature [K]	100(2)	Crystal Size [mm]	0.125 x 0.087 x 0.061
Wavelength [Å]	0.71073	θ range [°]	2.817 to 30.527
Crystal System	Monoclinic	Reflections Collected	39067
Space Group	P2 ₁ /n	Unique reflections	2749
Unit cell dimensions [Å]	a = 8.463(2)	Completeness to θ_{max} :	100.0 %
	b = 9.390(2)	Data/Restraints/Parameters	2749 / 1 / 128
	c = 11.363(3)	R_{int}	0.0271
	α = 90	RI [$I > 2\sigma(I)$]	0.0123
	β = 93.89(2)	$wR2$ (all data)	0.0309
	γ = 90	$Goof$	1.063
Volume [Å ³]	900.9(4)	Largest Diff. peak and hole [e Å ⁻³]	0.719 and -0.560
Z	2		

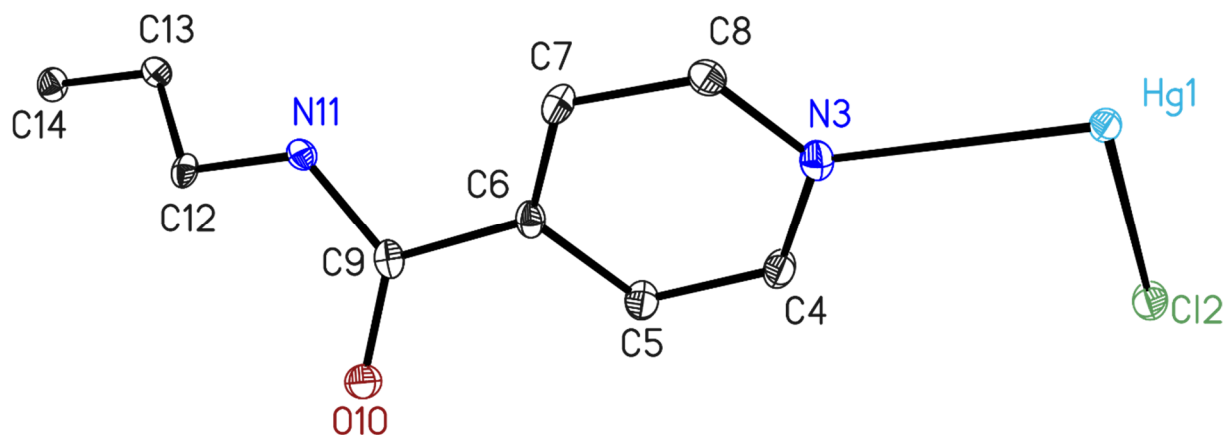
9.4.2 A18_twin



Graphical representation of the asymmetric unit. Hydrogen atoms are omitted for clarity. ADPs are displayed at the 50% probability level.

Structure code	KR_CK_A18_twin	ρ_{calc} [g cm ⁻³]	1.920
Empirical formula	C ₂₄ H ₃₆ Br ₂ HgN ₄ O ₇ S ₃	μ [mm ⁻¹]	7.358
Formula Weight [g mol ⁻¹]	949.16	F(000)	1848526
Temperature [K]	100(2)	Crystal Size [mm]	0.145 x 0.109 x 0.097
Wavelength [Å]	0.71073	θ range [°]	1.809 to 30.550
Crystal System	Monoclinic	Reflections Collected	10039
Space Group	P2 ₁ /c	Unique reflections	10039
Unit cell dimensions [Å]	a = 11.267(2)	Completeness to θ_{max} :	56.5 %
	b = 9.159(2)	Data/Restraints/Parameters	10039 / 518 / 492
	c = 28.204(3)	<i>BASF</i>	0.54512
	α = 90	<i>RI</i> [$I > 2\sigma(I)$]	0.0421
	β = 92.03(2)	<i>wR2</i> (all data)	0.0696
	γ = 90	<i>Goof</i>	1.037
Volume [Å ³]	3283.4(9)	Largest Diff. peak and hole [e Å ⁻³]	1.684 and -0.916
Z	4		

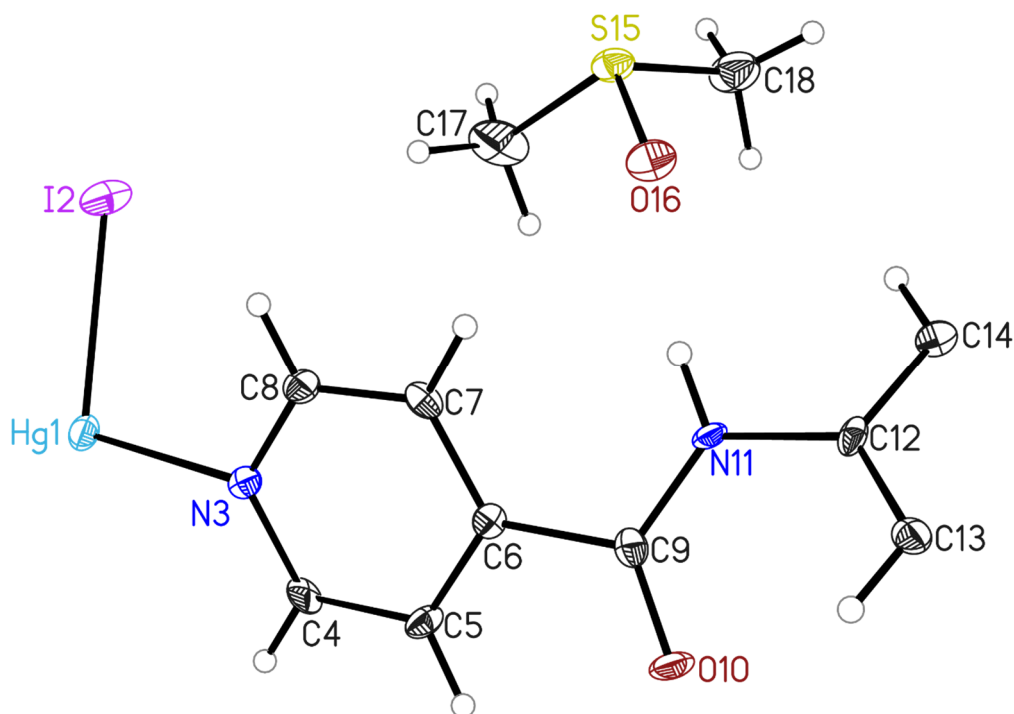
9.4.3 KR_CK_AFC



Graphical representation of the asymmetric unit. Hydrogen atoms are omitted for clarity. ADPs are displayed at the 50% probability level.

Structure code	KR_CK_AFC	ρ_{calc} [g cm ⁻³]	2.255
Empirical formula	C ₁₈ H ₁₄ Cl ₂ HgN ₄ O ₂	μ [mm ⁻¹]	5.020
Formula Weight [g mol ⁻¹]	589.82	F(000)	560
Temperature [K]	100(2)	Crystal Size [mm]	0.160 x 0.100 x 0.055
Wavelength [Å]	0.71073	θ range [°]	2.247 to 23.644
Crystal System	Monoclinic	Reflections Collected	23335
Space Group	P2 ₁ /c	Unique reflections	2650
Unit cell dimensions [Å]	a = 8.314(2)	Completeness to θ_{max} :	100.0 %
	b = 9.215(2)	Data/Restraints/Parameters	2650 / 0 / 128
	c = 11.374(3)	R_{int}	0.0401
	α = 90	$R1$ [$I > 2\sigma(I)$]	0.0151
	β = 94.41(2)	$wR2$ (all data)	0.0326
	γ = 90	$Goof$	1.035
Volume [Å ³]	868.8(4)	Largest Diff. peak and hole [e Å ⁻³]	0.575 and -0.436
Z	2		

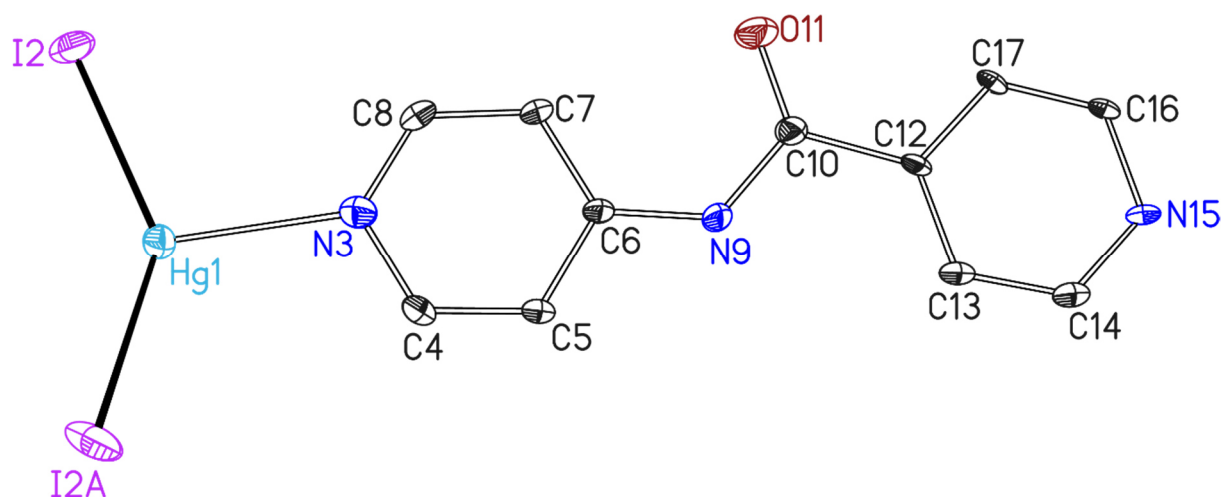
9.4.4 KR_CK_AFI



Graphical representation of the asymmetric unit. Hydrogen atoms are omitted for clarity. ADPs are displayed at the 50% probability level.

Structure code	KR_CK_AFI	ρ_{calc} [g cm ⁻³]	2.128
Empirical formula	C ₂₂ H ₂₆ HgI ₂ N ₄ O ₄ S ₂	μ [mm ⁻¹]	4.126
Formula Weight [g mol ⁻¹]	928.98	F(000)	1744
Temperature [K]	100(2)	Crystal Size [mm]	0.121 x 0.058 x 0.058
Wavelength [Å]	0.56086	θ range [°]	1.479 to 20.560°
Crystal System	Monoclinic	Reflections Collected	30113
Space Group	C2/c	Unique reflections	2980
Unit cell dimensions [Å]	a = 16.632(2)	Completeness to θ_{max} :	100.0 %
	b = 8.023(2)	Data/Restraints/Parameters	2980 / 1 / 166
	c = 21.930(3)	R_{int}	0.1098
	α = 90	$R1$ [$I > 2\sigma(I)$]	0.0325
	β = 97.72(2)	$wR2$ (all data)	0.0552
	γ = 90	$Goof$	1.012
Volume [Å ³]	2899.8(9)	Largest Diff. peak and hole [e Å ⁻³]	0.838 and -0.989
Z	4		

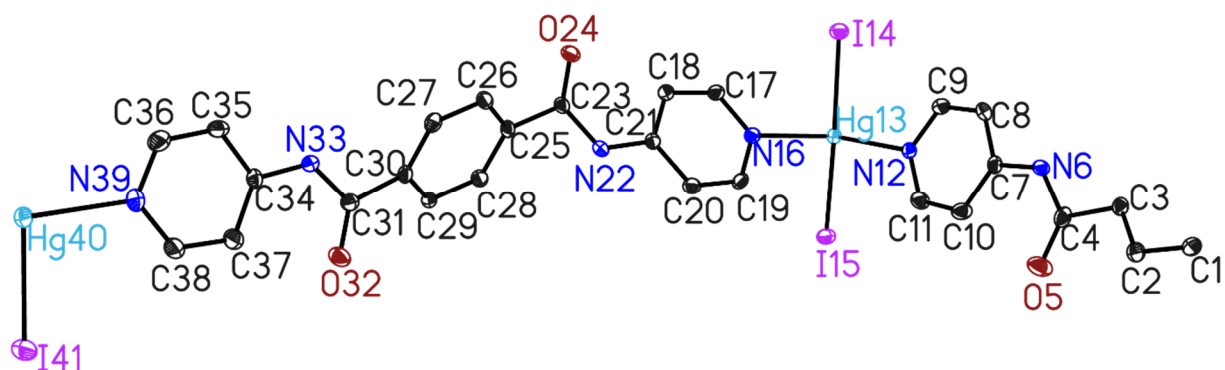
9.4.5 KR_CK_AI3



Graphical representation of the asymmetric unit. Hydrogen atoms are omitted for clarity. ADPs are displayed at the 50% probability level.

Structure code	KR_CK_AI3	ρ_{calc} [g cm ⁻³]	2.916
Empirical formula	C ₁₁ H ₉ HgI ₂ N ₃ O	μ [mm ⁻¹]	7.850
Formula Weight [g mol ⁻¹]	653.60	F(000)	1160
Temperature [K]	100(2)	Crystal Size [mm]	0.106 x 0.106 x 0.059
Wavelength [Å]	0.56086	θ range [°]	2.270 to 23.647
Crystal System	Orthorhombic	Reflections Collected	26239
Space Group	Pnma	Unique reflections	2274
Unit cell dimensions [Å]	a = 8.233(2)	Completeness to θ_{max} :	99.9 %
	b = 13.046(2)	Data/Restraints/Parameters	2274 / 225 / 150
	c = 13.862(3)	R_{int}	0.0464
	α = 90	$R1$ [$I > 2\sigma(I)$]	0.0377
	β = 90	$wR2$ (all data)	0.0853
	γ = 90	$Goof$	1.190
Volume [Å ³]	1488.9(5)	Largest Diff. peak and hole [e Å ⁻³]	2.252 and -1.841
Z	4		

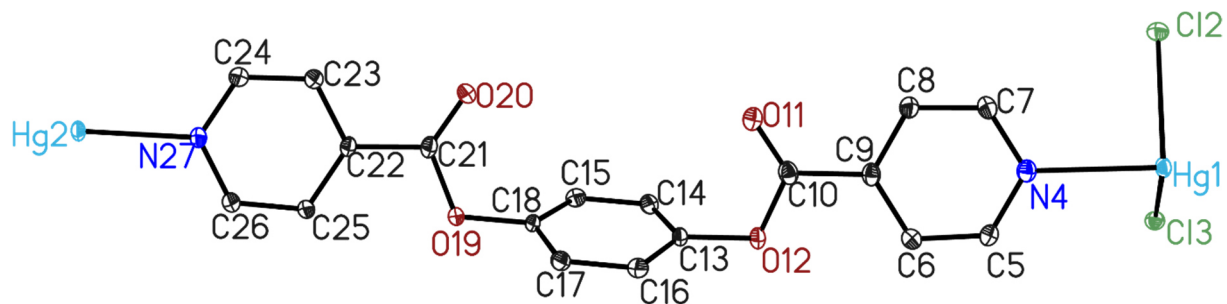
9.4.6 KR_CK_ANI



Graphical representation of the asymmetric unit. Hydrogen atoms are omitted for clarity. ADPs are displayed at the 50% probability level.

Structure code	KR_CK_ANI	ρ_{calc} [g cm ⁻³]	2.537
Empirical formula	C ₁₈ H ₁₄ HgI ₂ N ₄ O ₂	μ [mm ⁻¹]	10.679
Formula Weight [g mol ⁻¹]	772.72	F(000)	4224
Temperature [K]	100(2)	Crystal Size [mm]	0.300 x 0.100 x 0.100
Wavelength [Å]	0.71073	θ range [°]	0.965 to 27.925
Crystal System	Monoclinic	Reflections Collected	63066
Space Group	C2/c	Unique reflections	7228
Unit cell dimensions [Å]	a = 42.768(3)	Completeness to θ_{max} :	99.9 %
	b = 5.383(2)	Data/Restraints/Parameters	7228 / 9 / 378
	c = 26.709(2)	R_{int}	0.0298
	α = 90	$R1$ [$I > 2\sigma(I)$]	0.0344
	β = 99.17(2)	$wR2$ (all data)	0.0784
	γ = 90	$Goof$	1.360
Volume [Å ³]	6070(2)	Largest Diff. peak and hole [e Å ⁻³]	2.610 and -1.985
Z	12		

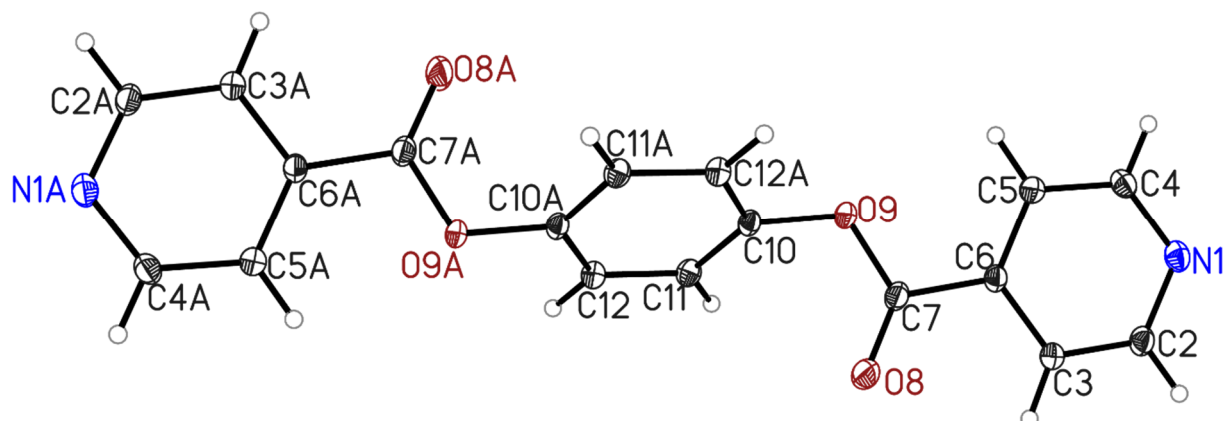
9.4.7 KR_CK_EC



Graphical representation of the asymmetric unit. Hydrogen atoms are omitted for clarity. ADPs are displayed at the 50% probability level.

Structure code	KR_CK_EC	ρ_{calc} [g cm ⁻³]	2.232
Empirical formula	C ₁₈ H ₁₂ Cl ₂ HgN ₂ O ₄	μ [mm ⁻¹]	9.073
Formula Weight [g mol ⁻¹]	591.79	F(000)	560
Temperature [K]	100(2)	Crystal Size [mm]	0.232 x 0.071 x 0.069
Wavelength [Å]	0.71073	θ range [°]	1.307 to 30.523
Crystal System	Triclinic	Reflections Collected	59351
Space Group	P $\bar{1}$	Unique reflections	5361
Unit cell dimensions [Å]	a = 7.424(2)	Completeness to θ_{max} :	100.0 %
	b = 7.614(2)	Data/Restraints/Parameters	5361 / 0 / 247
	c = 15.895(3)	R_{int}	0.0424
	α = 95.64(2)	$R1$ [$I > 2\sigma(I)$]	0.0178
	β = 99.82(3)	$wR2$ (all data)	0.0442
	γ = 91.09(2)	$Goof$	1.015
Volume [Å ³]	880.4(4)	Largest Diff. peak and hole [e Å ⁻³]	2.146 and -1.068
Z	2		

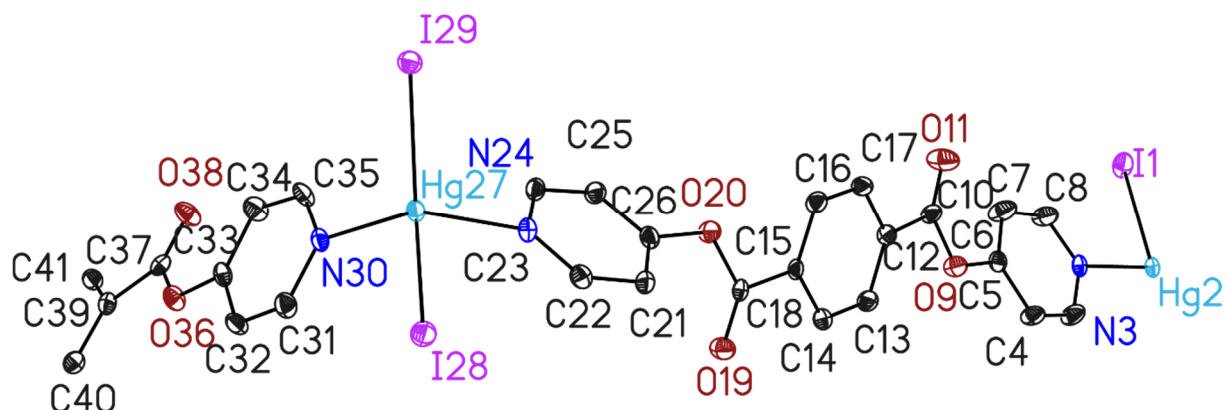
9.4.8 KR_CK_EF1



Graphical representation of the asymmetric unit. Hydrogen atoms are omitted for clarity. ADPs are displayed at the 50% probability level.

Structure code	KR_CK_EF1	ρ_{calc} [g cm ⁻³]	1.473
Empirical formula	C ₁₈ H ₁₂ N ₂ O ₄	μ [mm ⁻¹]	0.106
Formula Weight [g mol ⁻¹]	320.30	F(000)	332
Temperature [K]	100(2)	Crystal Size [mm]	0.380 x 0.366 x 0.170
Wavelength [Å]	0.71073	θ range [°]	2.351 to 30.549
Crystal System	Monoclinic	Reflections Collected	44841
Space Group	P2 ₁ /c	Unique reflections	2202
Unit cell dimensions [Å]	a = 17.325(3)	Completeness to θ_{max} :	99.8 %
	b = 5.586(2)	Data/Restraints/Parameters	2202 / 0 / 109
	c = 7.463(2)	R_{int}	0.0206
	α = 90	$R1$ [$I > 2\sigma(I)$]	0.0373
	β = 90.19(2)	$wR2$ (all data)	0.1093
	γ = 90	$Goof$	1.057
Volume [Å ³]	722.2(3)	Largest Diff. peak and hole [e Å ⁻³]	0.502 and -0.234
Z	2		

9.4.9 EI2



Graphical representation of the asymmetric unit. Hydrogen atoms are omitted for clarity. ADPs are displayed at the 50% probability level.

Structure code	CK_EI2	ρ_{calc} [g cm ⁻³]	2.558
Empirical formula	C ₁₈ H ₁₂ HgI ₂ N ₂ O ₄	μ [mm ⁻¹]	10.749
Formula Weight [g mol ⁻¹]	774.69	F(000)	4224
Temperature [K]	100(2)	Crystal Size [mm]	0.090 x 0.060x 0.050
Wavelength [Å]	0.71073	θ range [°]	0.970 to 27.179
Crystal System	Monoclinic	Reflections Collected	81693
Space Group	C2/c	Unique reflections	6684
Unit cell dimensions [Å]	a = 42.390(12) b = 5.267(2) c = 27.293(2) α = 90 β = 98.05(2) γ = 90	Completeness to θ_{max} :	100.0 %
Volume [Å ³]	6034(3)	Data/Restraints/Parameters	6684 / 0 / 366
Z	12	R_{int}	0.0697
		$R1$ [$I > 2\sigma(I)$]	0.0274
		$wR2$ (all data)	0.0657
		$Goof$	1.064
		Largest Diff. peak and hole [e Å ⁻³]	3.302 and -1.471

10 Appendix

10.1 Additional details about the structure refinement of AlH₂MeBOX

10.1.1 Local coordinate systems, symmetry and chemical constraints

Table S1: Local coordinate systems and chemical constraints for the 1Part refinement. For the 2Part refinement, local coordinate systems and κ parameters for the minor component are the same as for their main component counterparts

ATOM	ATOM0	AX1	ATOM1	ATOM2	AX2	R/L	KAP	Symm	CHEMCON
Al(1)	N(1)	Z	Al(1)	N(2)	Y	R	1	no	
Al(2)	N(3)	Z	Al(2)	N(4)	Y	R	1	no	Al(1)
O(1)	C(1)	Z	O(1)	C(7)	Y	R	2	mx	
O(2)	C(10)	Z	O(2)	C(16)	Y	L	2	mx	O(1)
O(3)	C(18)	Z	O(3)	C(24)	Y	R	2	mx	O(1)
O(4)	C(27)	Z	O(4)	C(33)	Y	L	2	mx	O(1)
N(1)	C(1)	Z	N(1)	Al(1)	Y	R	3	mx	
N(2)	C(10)	Z	N(2)	Al(1)	Y	L	3	mx	N(1)
N(3)	C(18)	Z	N(3)	Al(2)	Y	R	3	mx	N(1)
N(4)	C(27)	Z	N(4)	Al(2)	Y	L	3	mx	N(1)
C(1)	N(1)	Z	C(1)	O(1)	Y	R	4	mx	
C(2)	C(7)	Z	C(2)	C(3)	Y	R	4	mx	
C(3)	C(6)	Z	C(3)	C(4)	Y	R	4	mx	
C(4)	C(7)	Z	C(4)	C(5)	Y	R	4	mx	
C(5)	C(2)	Z	C(5)	C(6)	Y	R	4	mx	
C(6)	C(3)	Z	C(6)	C(7)	Y	R	4	mx	
C(7)	C(6)	Z	C(7)	C(2)	Y	R	4	mx	
C(8)	C(3)	Z	C(8)	H(8A)	Y	R	5	3m	
C(9)	H(9)	Z	C(9)	C(10)	Y	R	4	mm2	
C(10)	N(2)	Z	C(10)	O(2)	Y	L	4	mx	C(1)
C(11)	C(16)	Z	C(11)	C(12)	Y	L	4	mx	C(2)
C(12)	C(15)	Z	C(12)	C(13)	Y	L	4	mx	C(3)
C(13)	C(16)	Z	C(13)	C(14)	Y	L	4	mx	C(4)
C(14)	C(11)	Z	C(14)	C(15)	Y	L	4	mx	C(5)
C(15)	C(12)	Z	C(15)	C(16)	Y	L	4	mx	C(6)
C(16)	C(15)	Z	C(16)	C(11)	Y	L	4	mx	C(7)

C(17)	C(12)	Z	C(17)	H(17A)	Y	L	5	3m	
C(18)	N(3)	Z	C(18)	O(3)	Y	R	4	mx	C(1)
C(19)	C(24)	Z	C(19)	C(20)	Y	R	4	mx	C(2)
C(20)	C(23)	Z	C(20)	C(21)	Y	R	4	mx	C(3)
C(21)	C(24)	Z	C(21)	C(22)	Y	R	4	mx	C(4)
C(22)	C(19)	Z	C(22)	C(23)	Y	R	4	mx	C(5)
C(23)	C(20)	Z	C(23)	C(24)	Y	R	4	mx	C(6)
C(24)	C(23)	Z	C(24)	C(20)	Y	R	4	mx	C(7)
C(25)	C(20)	Z	C(25)	H(25A)	Y	R	5	3m	
C(26)	H(26)	Z	C(26)	C(27)	Y	R	4	mm2	C(9)
C(27)	N(4)	Z	C(27)	O(4)	Y	L	4	mx	C(1)
C(28)	C(33)	Z	C(28)	C(29)	Y	L	4	mx	C(2)
C(29)	C(32)	Z	C(29)	C(30)	Y	L	4	mx	C(3)
C(30)	C(33)	Z	C(30)	C(31)	Y	L	4	mx	C(4)
C(31)	C(28)	Z	C(31)	C(32)	Y	L	4	mx	C(5)
C(32)	C(29)	Z	C(32)	C(33)	Y	L	4	mx	C(6)
C(33)	C(32)	Z	C(33)	C(28)	Y	L	4	mx	C(7)
C(34)	C(29)	Z	C(34)	H(34A)	Y	L	5	3m	
H(35)	Al(1)	Z	H(35)	H(17A)	Y	R	6	cyl	
H(36)	Al(1)	Z	H(36)	H(35)	Y	R	6	cyl	
H(4)	C(4)	Z	H(4)	C(5)	Y	R	6	cyl	
H(5)	C(5)	Z	H(5)	C(4)	Y	R	6	cyl	H(4)
H(6)	C(6)	Z	H(6)	C(7)	Y	R	6	cyl	H(4)
H(8A)	C(8)	Z	H(8A)	H(8C)	Y	R	6	cyl	
H(8B)	C(8)	Z	H(8B)	H(8A)	Y	R	6	cyl	H(8A)
H(8C)	C(8)	Z	H(8C)	H(8A)	Y	R	6	cyl	H(8A)
H(9)	C(9)	Z	H(9)	C(10)	Y	R	6	cyl	
H(13)	C(13)	Z	H(13)	C(12)	Y	R	6	cyl	H(4)
H(14)	C(14)	Z	H(14)	C(15)	Y	R	6	cyl	H(4)
H(15)	C(15)	Z	H(15)	C(16)	Y	R	6	cyl	H(4)
H(17A)	C(17)	Z	H(17A)	H(17B)	Y	R	6	cyl	H(8A)
H(17B)	C(17)	Z	H(17B)	H(17C)	Y	R	6	cyl	H(8A)
H(17C)	C(17)	Z	H(17C)	H(17B)	Y	R	6	cyl	H(8A)
H(37)	Al(2)	Z	H(37)	H(38)	Y	R	6	cyl	

H(38)	Al(2)	Z	H(38)	H(37)	Y	R	6	cyl	
H(21)	C(21)	Z	H(21)	C(20)	Y	R	6	cyl	H(4)
H(22)	C(22)	Z	H(22)	C(23)	Y	R	6	cyl	H(4)
H(23)	C(23)	Z	H(23)	C(24)	Y	R	6	cyl	H(4)
H(25A)	C(25)	Z	H(25A)	H(25C)	Y	R	6	cyl	H(8A)
H(25B)	C(25)	Z	H(25B)	H(25C)	Y	R	6	cyl	H(8A)
H(25C)	C(25)	Z	H(25C)	H(25B)	Y	R	6	cyl	H(8A)
H(26)	C(26)	Z	H(26)	C(27)	Y	R	6	cyl	H(9)
H(30)	C(30)	Z	H(30)	C(31)	Y	R	6	cyl	H(4)
H(31)	C(31)	Z	H(31)	C(30)	Y	R	6	cyl	H(4)
H(32)	C(32)	Z	H(32)	C(33)	Y	R	6	cyl	H(4)
H(34A)	C(34)	Z	H(34A)	H(34B)	Y	R	6	cyl	H(8A)
H(34B)	C(34)	Z	H(34B)	H(34A)	Y	R	6	cyl	H(8A)
H(34C)	C(34)	Z	H(34C)	H(34A)	Y	R	6	cyl	H(8A)

10.1.2 Test for overfitting and final refinement strategies

Table S2: Refinement strategy used for cross validation.^[78] Steps without tint constitute a usual “standard” MM refinement strategy. Residuals are calculated based on the lPart approach. The scale factor is refined in every step. At the beginning of the refinement, only reflections with a significance of at least 3σ are taken into account (“sigobs 3”). This limitation is released in step 11. Refinement steps tinted green were accepted into the final refinement strategy. Steps tinted red show signs of overfitting or provide no enhancement of model quality and were therefore rejected. Abbreviations: M: monopoles; D: dipoles; Q: quadrupoles; O: octupoles; H: hexadecapoles, U: Uij, k: kappa, U3/4 (atom name): Gram Charlier 3rd/4th order, nosymm: no local symmetry constraints, nocon: no chemical constraints, d/p : data to parameter ratio, d_1/p_m : ratio of low resolution data (up to 1 Å) to multipole parameter.

Step	Parameters	#param	#data	d/p	d_1/p_m	$R(F^2)$
1	SCALE	1	17675	17675	588.6	0.0651
2	M	16	17675	1104.69	183.94	0.0631
3	MDQOH	184	17675	96.06	28.57	0.0384
4	MDQOHU	448	17675	39.45	28.57	0.0363
5	MDQOHU _{xyz}	580	17675	30.47	28.57	0.0337
6	MDQOHU _{xyz} κ	585	17675	30.21	27.25	0.0331

7	xyz(H)	91	2942	32.33	None	0.0315
8	MDQOHUxyzκ	585	17675	30.21	27.25	0.0314
9	κ'	6	17675	2945.83	None	0.0311
10	MDQOHUxyzκ	585	17675	30.21	27.25	0.0308
11	Sigobs 0	585	22678	38.77	28.53	0.0309
12	MDQOHUxyzκ U3 (C8, C25)	605	22678	37.48	28.53	0.0306
13	MDQOHUxyzκ U3 (C17, C34)	625	22678	36.28	28.53	0.0305
14	Nocon Methyl	646	22678	35.11	25.68	0.0296
15	Nosymm Methyl	718	22678	31.58	19.75	0.0293
16	Nocon H35–38	724	22678	31.32	19.02	0.0289
17	Q0 H35–38	728	22678	31.15	19.02	0.0289
18	Nocon N1 N2	758	22678	29.92	17.31	0.0289
19	Nocon N3 N4	773	22678	29.34	16.56	0.0289
20	Nocon A1	798	22678	28.42	15.48	0.0286
21	Chemcons per molecule	927	22678	24.46	11.45	0.0283
22	Nocon	1167	22678	19.43	7.76	0.0274
23	Nosymm	1559	22678	14.55	5.21	0.026

Figure S1: R_{cross} -validation of experimental data.

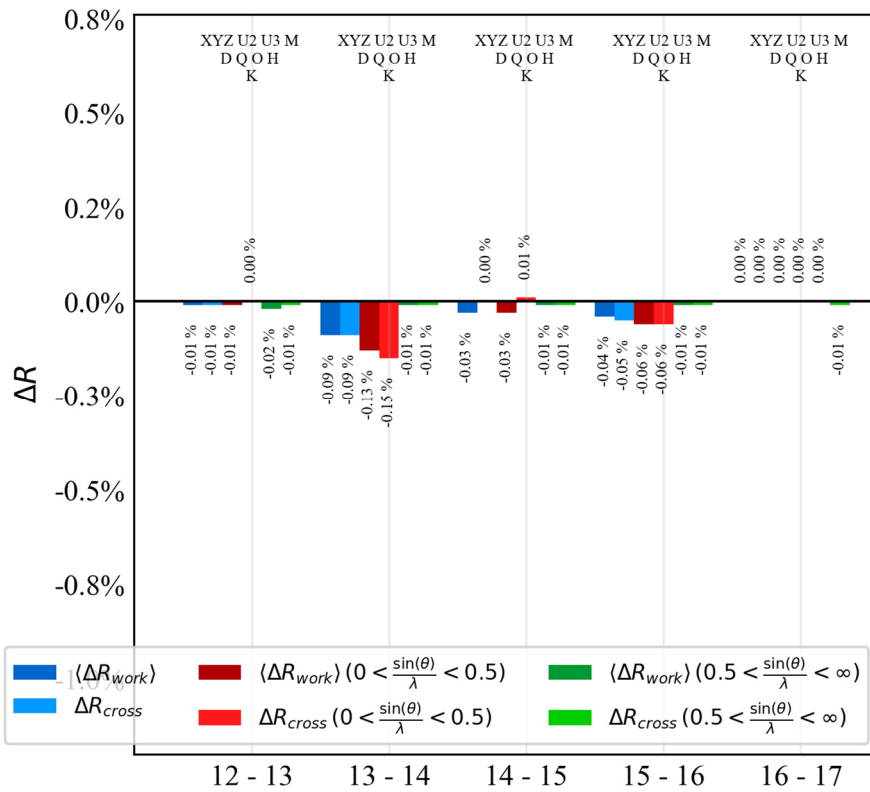
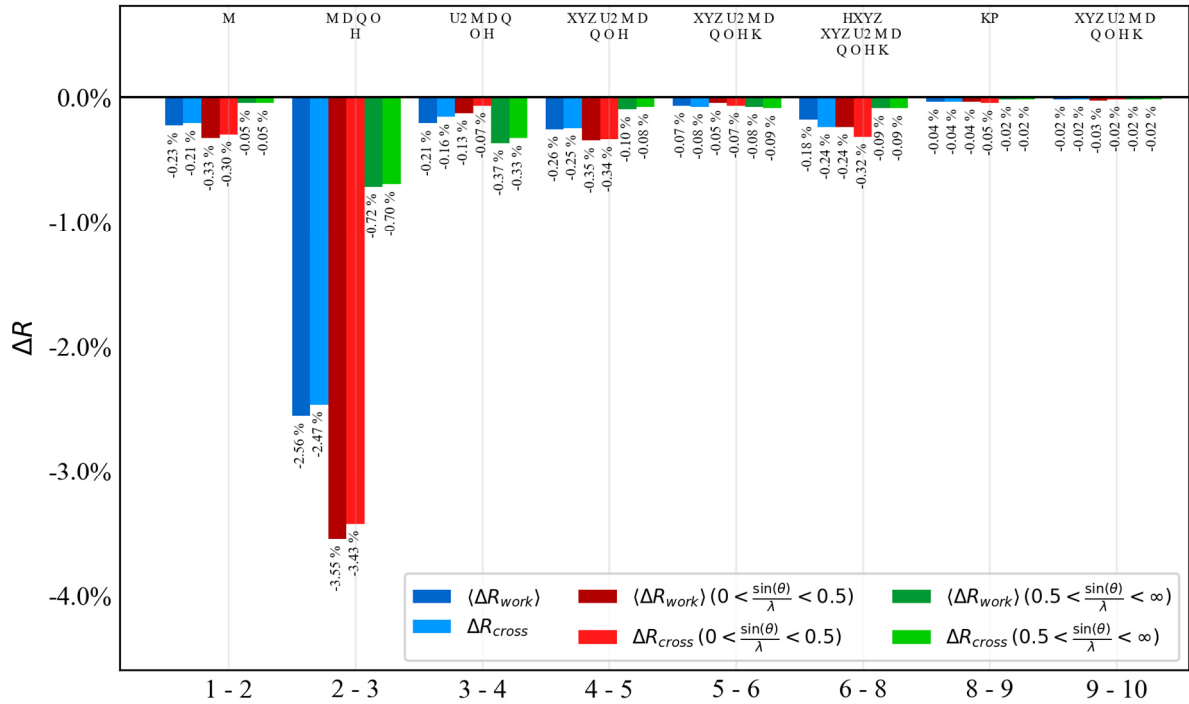


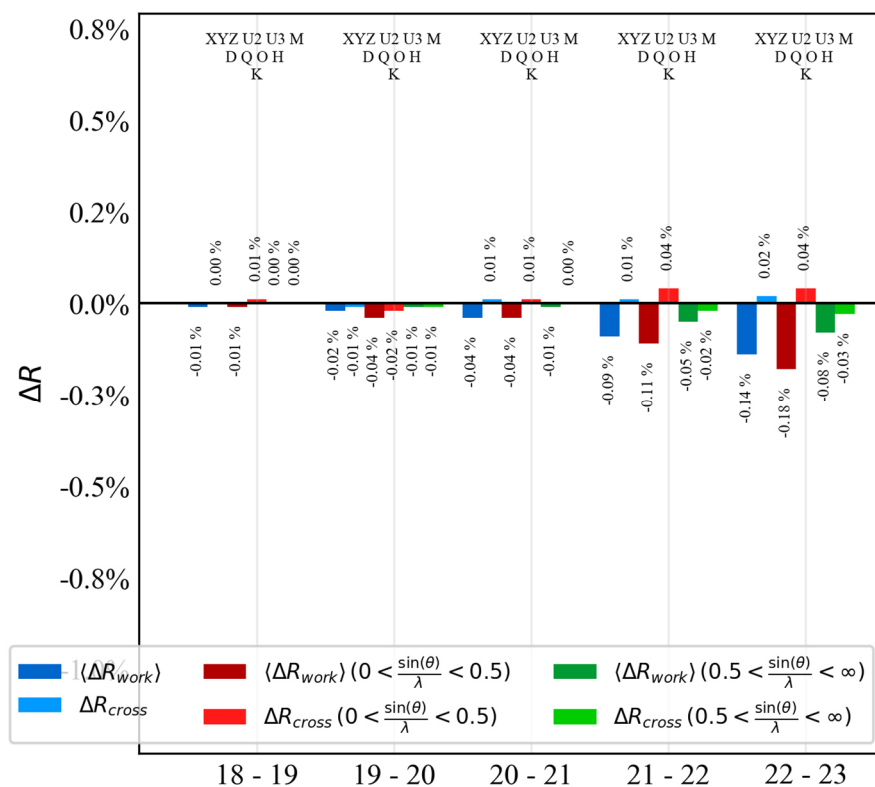
Figure S2: R_{cross} -validation of experimental data, continued.

Table S3: Final refinement strategy for the theoMM model. As the refinement is performed against theoretical data, no positions and vibrational parameters are refined. Abbreviations: d/p: data-to parameter ratio; d_1/p_m : Ratio of low-res data to multipole parameters; SCALE: overall scale factor; M: monopoles; D: dipoles; Q: quadrupoles; O: octupoles; H: hexadecapoles.

Step	Parameters	#param	#data	d/p	d_1/p_m	$R(F^2)$
1	SCALE	1	192670	192670	None	0.0337
2	M	15	192670	12844.67	1138.4	0.0322
3	MDQOH	182	192670	1058.63	169.07	0.0104
4	MDQOH κ	187	192670	1030.32	161.09	0.0083
5	κ'	6	192670	32111.67	None	0.008
6	MDQOH κ	187	192670	1030.32	161.09	0.0078

Table S4: Final strategy for refinement against experimental data. Abbreviations: d/p: data-to parameter ratio; d_1/p_m : Ratio of low-res data to multipole parameters; SCALE: overall scale factor; M: monopoles; D: dipoles; Q: quadrupoles; O: octupoles; H: hexadecapoles; U: U_{ij} ; xyz(H): free refinement of hydrogen atom positions against the inner data; U3: third-order Gram-Charlier coefficients for anharmonic motion. Until “Sigobs 0”, reflections below 3σ are excluded from the refinement. Residuals are calculated based on the 1Part approach.

Step	Parameters	#param	#data	d/p	d_1/p_m	$R(F^2)$
1	SCALE	1	17675	17675	None	0.0832
2	M	19	17675	930.26	154.89	0.0804
3	MDQOH	205	17675	86.22	25.59	0.0457
4	MDQOHU	475	17675	37.21	24.32	0.0423
5	MDQOHUxyz	607	17675	29.12	24.32	0.0384
6	MDQOHUxyz κ	612	17675	28.88	23.36	0.0375
7	xyz(H)	91	2942	32.33	None	0.0361
8	MDQOHUxyz κ	612	17675	28.88	23.36	0.0345
9	κ'	6	17675	2945.83	None	0.0339
10	MDQOHUxyz κ	612	17675	28.88	23.36	0.0334
11	Sigobs 0	612	22678	37.06	24.45	0.0338
12	MDQOHUxyz κ U3 (C8, C25)	632	22678	35.88	24.45	0.0334
13	MDQOHUxyz κ U3 (C34)	642	22678	35.32	24.45	0.0333
14	MDQOHUxyz κ U3 (C17)	652	22678	34.78	24.45	0.0332

10.1.3 Treatment of hydrogen atoms

The distance of hydrogen atoms to their bonded heavy atom(s) was reset to tabulated neutron distances after each refinement step including atomic positions. An exception are the hydrogen atoms bonded to aluminium, whose bond Al-H bond distances form two sets of different lengths at approximately 1.55 Å and 1.72 Å, compared to a uniform Al-H distance of 1.588 Å for all atoms. Until the free refinement of hydrogen positions against the inner data, these distances are reset to values obtained from Hirshfeld atom refinement in *Olex2* using aspherical form factors from *NoSpherA2*. In the following refinement steps, the distances are no longer reset.

For hydrogen anisotropic displacement parameters (ADPs), a free refinement against the X-ray data was attempted, however, as we expected beforehand, it led to a large number of unreasonably shaped ADPs. Next, tabulated hydrogen ADPs from neutron data were transferred from the SHADE server. The Hirshfeld test was used as a criterion for the quality of the approximate ADPs. While the Hirshfeld test is primarily designed to judge the ADPs of bonded atoms with equal molecular weight, it can still be used as a criterion for X-H bonds. Here, hydrogen atoms in similar surrounding should, in theory, all have comparable DMSDA (“Difference of Mean-Square Displacement Amplitudes”) values.

Table S5: DMSDA values of the 1Part refinement

Bond	Bond length	DMSDA value
C(4) - H(4)	1.083	-6
C(5) - H(5)	1.083	43
C(6) - H(6)	1.083	37
C(8) - H(8A)	1.077	-84
C(8) - H(8B)	1.077	-67
C(8) - H(8C)	1.077	25
C(9) - H(9)	1.083	77
C(13) - H(13)	1.083	-40
C(14) - H(14)	1.083	53
C(15) - H(15)	1.083	11
C(17) - H(17A)	1.077	-7
C(17) - H(17B)	1.077	32
C(17) - H(17C)	1.077	32
C(21) - H(21)	1.083	7
C(22) - H(22)	1.083	63
C(23) - H(23)	1.083	25

C(25) - H(25A)	1.077	39
C(25) - H(25B)	1.077	11
C(25) - H(25C)	1.077	-44
C(26) - H(26)	1.083	74
C(30) - H(30)	1.083	-11
C(31) - H(31)	1.083	63
C(32) - H(32)	1.083	-1
C(34) - H(34A)	1.077	-2
C(34) - H(34B)	1.077	-70
C(34) - H(34C)	1.077	36

The difference between the various hydrogen ADPs are quite significant, and the differences in the model quality is not especially large. Furthermore, we examined a list of molecular properties from the SHADE refinement and compared it to the refinement with isotropic hydrogen atoms. The impact on critical points and Bader charges compared in the main paper is also relatively small. The most significant change affects the Bader charges of methyl groups. Specifically, it lessens the feature of a shift in charge between carbon and hydrogen atoms compared to the theoMM refinement described in the main paper. However, as the effect of SHADE-ADPs on the compared properties was small and ultimately did not affect any of the overall results of the discussion, we decided to choose a model with isotropic hydrogen ADPs as final model.

Table S6: Selected properties at BCPs around the aluminium atoms in the asymmetric unit for the SHADE refinements. ρ is the electron density at the BCP. $\nabla^2\rho$ is the Laplacian of the ED, which is positive for ionic interactions and negative for covalent interactions. ε is the ellipticity of the bond. Ellipticity is close to one for complete absence of rotational symmetry, which generally hints at a strong π -character.

BCP	Method	ρ	$\nabla^2\rho$	ε
Al(1) – N(1)	Uncorr.	0.469(3)	5.90(13)	0.25(2)
	2Part	0.534(3)	5.01(13)	0.04(2)
	1Part	0.521(3)	5.48(13)	0.06(2)
	theoMM	0.549(3)	4.71(13)	0.07(2)
Al(1) – N(2)	Uncorr.	0.588(3)	4.90(13)	0.39(2)
	2Part	0.566(3)	4.69(13)	0.06(2)
	1Part	0.524(3)	5.61(13)	0.17(2)
	theoMM	0.547(3)	4.62(13)	0.07(2)
Al(2) – N(3)	Uncorr.	0.466(3)	5.78(13)	0.26(2)
	2Part	0.532(3)	5.02(13)	0.04(2)
	1Part	0.520(3)	5.46(13)	0.05(2)
	theoMM	0.545(3)	4.53(13)	0.08(2)
Al(2) – N(4)	Uncorr.	0.587(3)	4.89(13)	0.39(2)
	2Part	0.564(3)	4.642(13)	0.06(2)
	1Part	0.522(3)	5.541(13)	0.16(2)
	theoMM	0.546(3)	4.60(13)	0.09(2)

Table S7: Selected charges of integrated atomic basins (Bader charges) of all investigated disorder approaches from the SHADE refinement.

Bader charges	Uncorr.	2Part	1Part	theoMM
Al(1)	1.94	1.97	2.05	2.21
Al(2)	2.11	1.92	1.99	2.21
\langle Hydride H \rangle	1.27	-0.79	-0.79	-0.67
\langle Methyl Groups \rangle	-0.43	0.00	0.05	0.09
$\Sigma_{\text{Structure}}$	-0.01	-0.94	0.04	0.04

10.1.4 Iteration of occupancy factors in the 2Part approach

For the 2Part approach, a python script was used to emulate a refinement of the site occupation factor in XD. It was quickly identified that the starting SOFs appeared to be too large. Occupation factors were iterated from 0.02 to 0.035 separately in steps of 0.025. For each SOF tuple, a full refinement of the data against the final refinement strategy was conducted. Residual density analysis was performed for SOF pair and chosen as the main criterion to judge different SOFs by. Residual values did generally increase with an increase in SOFs for both molecules. With the chosen optimum SOF of 0.0275 for each molecule, there was still positive residual density located around some areas of overlap and the oxygen atoms of the minor component. However, increasing the SOF of any molecule from this point on lead to egregious residual density holes directly on top of other atomic positions of the minor component. Figures of merit from selected discarded SOF refinements can be found below.

Table S8: Figures of merit for additional site occupancy factors in the 2Part model. Best results were obtained at 0.0275/0.0275. Decreasing SOFs from this point leads to higher residuals and GOF values, while increasing any SOF causes unreasonably high minima in the residual density.

SOFs Mol1/Mol2	0.0275/0.0275	0.0338/0.0413	0.0200/0.0200	0.0275/0.0350
$R(F^2)$, $wR(F^2)$	0.0318, 0.0369	0.0340, 0.4016	0.0362, 0.0402	0.0326, 0.0383
GOF	2.8065	3.1634	3.0556	2.9122
$\Delta\rho_{\min}$, $\Delta\rho_{\max}$	-0.722; 0.624	-1.499; 0.673	-0.636; 0.596	-1.108; 0.647
e_{gross}	46	47.1	47.7	46.2

10.1.5 Attempted Refinement of Disordered Methyl Groups

The disordered methyl groups were first modelled in *SHELXL*. For this, the ABIN command and a custom .fab-file were used to implement the 1Part correction of the molecular disorder. This command is usually used in conjunction with *PLATON SQUEEZE*. Hydrogen positions of the disorder in the standard refinement were set using idealized geometry using the AFIX 127 command. A separate site occupancy factor was refined for every methyl group against low-order data. Disorder refinement was attempted for C8, C17 and C34, with the peaks corresponding to the disorder for C8 were the lowest. The occupancies for the minor positions refined to 0.11(4), 0.25(4) and 0.30(4), respectively. With the disorder refined, small signs of disorder around C25 became visible as well. However, the respective residual density peaks there were so low that modelling this disorder was deemed unnecessary.

For the starting model generation for multipole model (MM) refinement, the carbon atoms of affected methyl groups were split by the site occupancy of their respective hydrogen atoms in order to adjust local coordinate systems for minor and major component. All occupancy factors were taken from IAM refinement. Positions, of the split atoms, as well as monopole and multipole parameters were constrained to each other with respect to their different occupancies. During step 7 of the refinement strategy,

however, only the positions of hydrogen atoms of C17 and C34 could be freely refined against the low order data. Doing this for the hydrogen atoms of C8 caused egregious divergence in their coordinates.

10.1.6 Molecular Graphs for all molecular disorder approaches

For all approaches, the Hopf-Poincaré rule for the number of critical points is fulfilled. However, differences are visible in the highlighted regions of low electron density in the following figures.

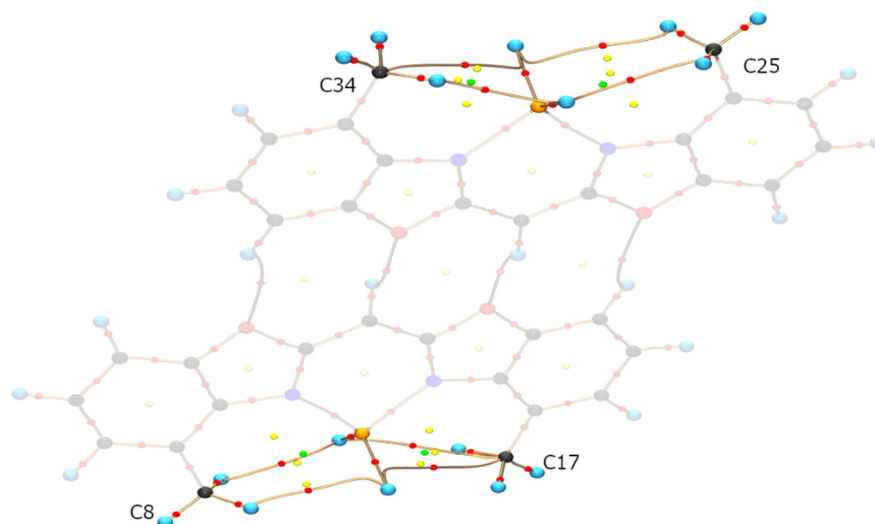


Figure 10-1: Molecular graph of AL2 for the uncorrected model. Bond paths are displayed in golden, BCPs are displayed in red, RCPs are displayed in yellow, CCPs are displayed in green. Bond paths originating from/ending at hydrogen atoms are toned down for clarity.

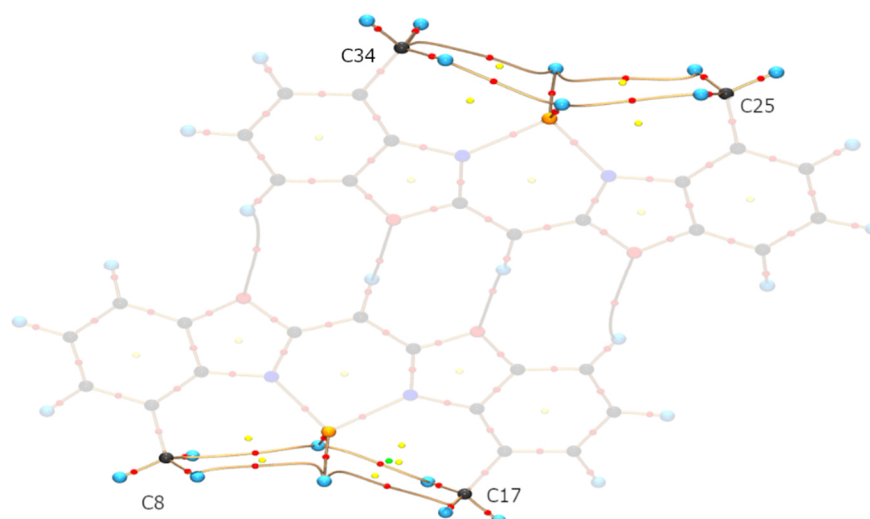


Figure 10-2: Molecular graph of AL2 for the 2Part model. Bond paths are displayed in golden, BCPs are displayed in red, RCPs are displayed in yellow, CCPs are displayed in green. Bond paths originating from/ending at hydrogen atoms are toned down for clarity.

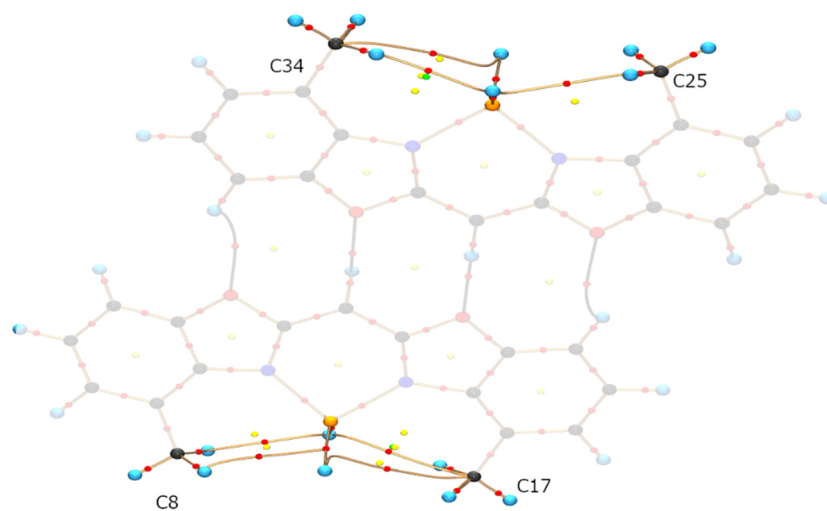


Figure 10-3: Molecular graph of AL2 for the 1Part model. Bond paths are displayed in golden, BCPs are displayed in red, RCPs are displayed in yellow, CCPs are displayed in green. Bond paths originating from/ending at hydrogen atoms are toned down for clarity.

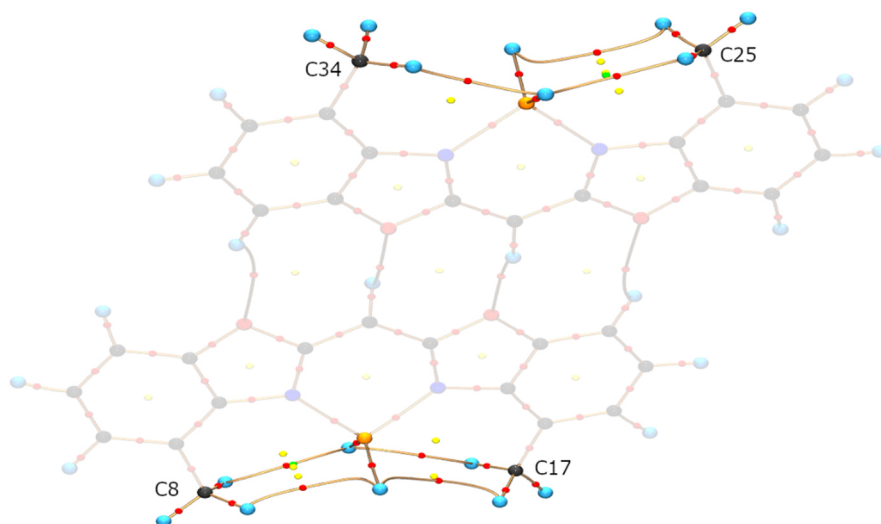


Figure 10-4: Molecular graph of AL2 for the theoMM model. Bond paths are displayed in golden, BCPs are displayed in red, RCPs are displayed in yellow, CCPs are displayed in green. Bond paths originating from/ending at hydrogen atoms are toned down for clarity.

10.2 Additional details about the structure Refinement of HCTD

10.2.1 Local coordinate systems, symmetry and chemical constraints

Table S9: Local coordinate systems and chemically invariant constraints for the 1Part refinement. For the 2Part refinement, local coordinate systems and κ parameters for the minor component are the same as for their main component counterparts

ATOM	ATOM0	AX1	ATOM1	ATOM2	AX2	R/L	KAP	Symm	CHEMCON
O(1)	N(1)	Z	O(1)	C(1)	Y	R	1	mx	
O(2)	N(1)	Z	O(2)	O(3)	Y	R	1	mx	
O(3)	N(1)	Z	O(3)	O(2)	Y	R	1	mx	O(2)
N(1)	O(3)	Z	N(1)	O(2)	Y	R	2	mx	
C(1)	O(1)	Z	C(1)	C(5)	Y	R	3	3z	
C(2)	H(2)	Z	C(2)	C(3)	Y	R	3	3z	
C(3)	H(3)	Z	C(3)	C(4)	Y	R	3	3z	
C(4)	C(3)	Z	C(4)	C(5)	Y	R	3	mx	
C(5)	H(5)	Z	C(5)	C(4)	Y	R	3	3z	
C(6)	H(6)	Z	C(6)	C(5)	Y	R	3	3z	
C(7)	H(7)	Z	C(7)	C(3)	Y	R	3	3z	
H(2)	C(2)	Z	H(2)	C(3)	Y	R	4	cyl	
H(3)	C(3)	Z	H(3)	C(2)	Y	R	4	cyl	H(2)
H(4A)	C(4)	Z	H(4A)	H(4B)	Y	R	4	cyl	
H(4B)	C(4)	Z	H(4B)	H(4A)	Y	R	4	cyl	H(4A)
H(5)	C(5)	Z	H(5)	C(6)	Y	R	4	cyl	H(2)
H(6)	C(6)	Z	H(6)	C(5)	Y	R	4	cyl	H(2)
H(7)	C(7)	Z	H(7)	C(6)	Y	R	4	cyl	H(2)

10.2.2 Final refinement strategy

Table S10: Final strategy for refinement against experimental data. Abbreviations: d/p: data-to parameter ratio; d_1/p_m : Ratio of low-res data to multipole parameters; SCALE: overall scale factor; M: monopoles; D: dipoles; Q: quadrupoles; O: octupoles; H: hexadecapoles; U: U_{ij} ; xyz(H): free refinement of hydrogen atom positions against the inner data; U3: third-order Gram-Charlier coefficients for anharmonic motion. Until “Sigobs 0”, reflections below 3σ are excluded from the refinement. Residuals are calculated based on the 1Part approach.

Step	Parameters	#param	#data	d/p	d_1/p_m	$R(F^2)$
1	SCALE	1	7447	7447	None	0.0485
2	M	13	7447	620.58	53.5	0.0456
3	MDQOH	107	7447	70.25	10.7	0.0224
4	MDQOHU	180	7447	43.3	10.7	0.0212
5	MDQOHU _{xyz}	213	7447	36.33	10.7	0.0201
6	MDQOHU _{xyz} κ	216	7447	35.8	10.19	0.0196
7	xyz(H)	22	642	29.18	None	0.0195
8	MDQOHU _{xyz} κ	216	7447	35.8	10.19	0.0195
9	κ'	4	7447	1861.75	None	0.0194
10	MDQOHU _{xyz} κ	216	7447	35.8	10.19	0.0186
11	Sigobs 0	216	7920	38.08	10.24	0.0186
12	MDQOHU _{xyz} κ U3 (O2, O3)	236	7920	34.74	10.24	0.0181

Table S11: Final refinement strategy for the theoMM model. As the refinement is performed against theoretical data, no positions and vibrational parameters are refined. Abbreviations: d/p: data-to parameter ratio; d_1/p_m : Ratio of low-res data to multipole parameters; SCALE: overall scale factor; M: monopoles; D: dipoles; Q: quadrupoles; O: octupoles; H: hexadecapoles.

Step	Parameters	#param	#data	d/p	d_1/p_m	$R(F^2)$
1	SCALE	1	98347	98347	992.89	0.0443
2	M	9	98347	10927.44	229.13	0.0403
3	MDQOH	74	98347	1329.01	217.95	0.0137
4	MDQOH κ	76	98347	1294.04	None	0.0092
5	κ'	3	98347	32782.33	217.95	0.0092
6	MDQOH κ	76	98347	1294.04	992.89	0.009

10.3 Additional details about the structure Refinement of NPP

The refinement strategy for NPP was directly taken from the publication by Meindl *et al.* and not further modified for this work.^[94] For convenience, however, certain aspects of it will be listed here, as well.

10.3.1 Local coordinate systems, symmetry and chemical constraints

Table 10-1: Local coordinate systems and chemical constraints for the 1Part refinement. For the 2Part refinement, local coordinate systems and κ parameters for the minor component are the same as for their main component counterparts

ATOM	ATOM0	AX1	ATOM1	ATOM2	AX2	R/L	KAP	Symm	CHEMCON
N(1)	C(10)	X	N(1)	C(1)	Y	R	1	mm2	
C(1)	N(1)	X	C(1)	C(2)	Y	R	2	mm2	
C(2)	C(3)	X	C(2)	C(1)	Y	R	3	mm2	
C(3)	C(4)	X	C(3)	C(2)	Y	R	3	mm2	
C(4)	C(5)	X	C(4)	C(3)	Y	R	3	mm2	
C(5)	C(4)	X	C(5)	C(6)	Y	R	3	mm2	C(3)
C(6)	C(5)	X	C(6)	C(1)	Y	R	3	mm2	C(2)
C(7)	N(1)	X	C(7)	C(8)	Y	R	4	mm2	C(10)
C(8)	C(7)	X	C(8)	C(9)	Y	R	5	mm2	C(9)
C(9)	C(10)	X	C(9)	C(8)	Y	R	5	mm2	
C(10)	N(1)	X	C(10)	C(9)	Y	R	4	mm2	
H(2)	C(2)	Z	H(2)	C(3)	Y	R	6	cyl	
H(3)	C(3)	Z	H(3)	C(4)	Y	R	6	cyl	H(2)
H(4)	C(4)	Z	H(4)	C(5)	Y	R	6	cyl	H(2)
H(5)	C(5)	Z	H(5)	C(6)	Y	R	6	cyl	H(2)
H(6)	C(6)	Z	H(6)	C(7)	Y	R	6	cyl	H(2)
H(7)	C(7)	Z	H(7)	C(8)	Y	R	6	cyl	
H(8)	C(8)	Z	H(8)	C(9)	Y	R	6	cyl	H(7)
H(9)	C(9)	Z	H(9)	C(10)	Y	R	6	cyl	H(7)
H(10)	C(10)	Z	H(10)	C(2)	Y	R	6	cyl	H(7)

10.3.2 Final refinement strategy

Table S12: Final strategy for refinement against experimental data. Abbreviations: d/p: data-to parameter ratio; d_1/p_m : Ratio of low-res data to multipole parameters; SCALE: overall scale factor; M: monopoles; D: dipoles; Q: quadrupoles; O: octupoles; H: hexadecapoles; U: U_{ij} ; xyz(H): free refinement of hydrogen atom positions against the inner data; U3: third-order Gram-Charlier coefficients for anharmonic motion. Until “Sigobs 0”, reflections below 3σ are excluded from the refinement. Residuals are calculated based on the 1Part approach.

Step	Parameters	#param	#data	d/p	d_1/p_m	$R(F^2)$
1	SCALE	1	3994	3994	None	0.1139
2	M	9	3994	443.78	54.22	0.109
3	MDQOH	74	3994	53.97	12.51	0.0847
4	MDQOHU	140	3994	28.53	12.51	0.0467
5	MDQOHU $_{xyz}$	173	3994	23.09	12.51	0.0398
6	MDQOHU $_{xyz\kappa}$	178	3994	22.44	11.09	0.0391
7	xyz(H)	28	488	17.43	None	0.0364
8	MDQOHU $_{xyz\kappa}$	178	3994	22.44	11.09	0.0344
9	κ'	6	3994	665.67	None	0.0336
10	MDQOHU $_{xyz\kappa}$	178	3994	22.44	11.09	0.0329
11	Sigobs 2	178	4167	23.41	11.11	0.0329

Table S13: Final refinement strategy for the theoMM model. As the refinement is performed against theoretical data, no positions and vibrational parameters are refined. Abbreviations: d/p: data-to parameter ratio; d_1/p_m : Ratio of low-res data to multipole parameters; SCALE: overall scale factor; M: monopoles; D: dipoles; Q: quadrupoles; O: octupoles; H: hexadecapoles.

Step	Parameters	#param	#data	d/p	d_1/p_m	$R(F^2)$
1	SCALE	1	98347	98347	None	0.0292
2	M	12	98347	8195.58	744.67	0.0275
3	MDQOH	106	98347	927.8	148.93	0.0096
4	MDQOH κ	109	98347	902.27	141.84	0.0085
5	κ'	4	98347	24586.75	None	0.0079
6	MDQOH κ	109	98347	902.27	141.84	0.0076

10.4 Additional details about the structure Refinement of MnMeBOX

10.4.1 Selected data quality indicators

Table S14: Quality indicators for different resolution shells from the final integration of AlH₂MeBOX.

d [Å]	#Data	#hkl (theory)	%Comp	Redundancy	Rrim	Rpim
Inf - 2.04	391	391	100.00	24.54	0.0318	0.0070
2.04 - 1.35	914	914	100.00	23.29	0.0351	0.0075
1.35 - 1.06	1335	1335	100.00	19.29	0.0291	0.0064
1.06 - 0.93	1248	1248	100.00	15.40	0.0234	0.0060
0.93 - 0.84	1372	1372	100.00	15.59	0.0321	0.0082
0.84 - 0.78	1278	1278	100.00	15.10	0.0394	0.0101
0.78 - 0.73	1401	1401	100.00	14.54	0.0477	0.0125
0.73 - 0.69	1451	1451	100.00	13.90	0.0516	0.0138
0.69 - 0.66	1333	1333	100.00	13.31	0.0586	0.0161
0.66 - 0.64	1017	1017	100.00	12.68	0.0712	0.0199
0.64 - 0.61	1819	1819	100.00	12.14	0.0795	0.0227
0.61 - 0.59	1377	1377	100.00	11.61	0.0897	0.0262
0.59 - 0.58	800	800	100.00	11.27	0.0989	0.0294
0.58 - 0.56	1733	1733	100.00	10.90	0.1195	0.0361
0.56 - 0.55	951	951	100.00	10.54	0.1357	0.0415
0.55 - 0.54	1027	1027	100.00	10.32	0.1504	0.0468
0.54 - 0.52	2301	2301	100.00	9.97	0.1741	0.0548
0.52 - 0.51	1306	1306	100.00	9.23	0.1981	0.0652
0.51 - 0.50	1401	1401	100.00	8.53	0.2208	0.0749
0.50 - 0.49	1456	1520	95.79	3.23	0.2211	0.1157

10.4.2 Comparison of integration options

A standard refinement strategy without anisotropic hydrogen ADPs was used for the comparison of integration options. For scaling in sadabs, experimental errors were used. Integration with a fixed box size of 0.6, 0.6, 0.8 in SAINT yielded the best combination of low residuals and e_{gross} and was therefore chosen as final integration. In later exploration of data reduction refinement, it was concluded that application of an error model in SADABS lead to better results. This prove true for all datasets in this thesis collected with a PHOTON III detector. (see Chapter 2.3).

(Fixed) Box size	inner box refinement?	$wR(F^2)$	GOF	$\Delta\rho_{\text{min}}, \Delta\rho_{\text{max}}$ [eÅ ⁻³]	e_{gross} [e]
Refined	On	0.0230	2.1891	-0.33, 0.39	52.1
0.3, 0.3, 0.6	On	0.0491	2.7757	-0.61, 0.37	63.7
	Off	0.0337	2.5445	-1.24, 0.52	49.8
0.5, 0.5, 0.7	On	0.0382	1.4450	-0.44, 0.44	50.3
	Off	0.0308	2.6469	-1.18, 0.78	59.8
0.6, 0.6, 0.8	On	0.0199	2.0468	-0.43, 0.42	42.9
	Off	0.0192	1.9732	-0.60, 0.40	37.1
0.6, 0.6, 0.5	On	0.0205	1.9231	-0.78, 0.47	43.1
0.7, 1.0, 1.0	Off	0.0225	1.9667	-0.92, 0.66	50.7

10.4.3 Local coordinate systems, symmetry and chemical constraints

ATOM	ATOM0	AX1	ATOM1	ATOM2	AX2	R/L	TP	TBL	KAP	LMX	SITESYM	CHEMCON
MN(1)	DUM1	Z	MN(1)	DUM0	Y	R	2	1	1	1	mx	
O(1)	C(1)	Z	O(1)	C(7)	Y	R	2	2	2	2	mx	
O(2)	C(10)	Z	O(2)	C(16)	Y	R	2	2	2	2	mx	O(1)
O(3)	C(18)	Z	O(3)	C(24)	Y	R	2	2	2	2	mx	O(1)
O(4)	C(27)	Z	O(4)	C(33)	Y	R	2	2	2	2	mx	O(1)
N(1)	C(1)	Z	N(1)	MN(1)	Y	R	2	3	3	3	mx	
N(2)	C(10)	Z	N(2)	MN(1)	Y	R	2	3	3	3	mx	N(1)
N(3)	C(18)	Z	N(3)	MN(1)	Y	R	2	3	3	3	mx	
N(4)	C(27)	Z	N(4)	MN(1)	Y	R	2	3	3	3	mx	
C(1)	N(1)	Z	C(1)	O(1)	Y	R	2	4	4	4	mx	
C(2)	C(7)	Z	C(2)	C(3)	Y	R	2	4	4	4	mx	
C(3)	C(6)	Z	C(3)	C(4)	Y	R	2	4	4	4	mx	
C(4)	C(7)	Z	C(4)	C(5)	Y	R	2	4	4	4	mx	
C(5)	C(2)	Z	C(5)	C(6)	Y	R	2	4	4	4	mx	
C(6)	C(3)	Z	C(6)	C(7)	Y	R	2	4	4	4	mx	
C(7)	C(6)	Z	C(7)	C(2)	Y	R	2	4	4	4	mx	
C(8)	C(3)	Z	C(8)	H(8A)	Y	R	2	5	5	5	3m	
C(9)	H(9)	Z	C(9)	C(10)	Y	R	2	4	4	4	mx	
C(10)	N(2)	Z	C(10)	O(2)	Y	R	2	4	4	4	mx	C(1)
C(11)	C(16)	Z	C(11)	C(12)	Y	R	2	4	4	4	mx	C(2)
C(12)	C(15)	Z	C(12)	C(13)	Y	R	2	4	4	4	mx	C(3)
C(13)	C(16)	Z	C(13)	C(14)	Y	R	2	4	4	4	mx	C(4)
C(14)	C(11)	Z	C(14)	C(15)	Y	R	2	4	4	4	mx	C(5)
C(15)	C(12)	Z	C(15)	C(16)	Y	R	2	4	4	4	mx	C(6)
C(16)	C(15)	Z	C(16)	C(11)	Y	R	2	4	4	4	mx	C(7)
C(17)	C(12)	Z	C(17)	H(17A)	Y	R	2	5	5	5	3m	C(8)
C(18)	N(3)	Z	C(18)	O(3)	Y	R	2	4	4	4	mx	C(1)
C(19)	C(24)	Z	C(19)	C(20)	Y	R	2	4	4	4	mx	C(2)

C(20)	C(23)	Z	C(20)	C(21)	Y	R	2	4	4	4	mx	C(3)
C(21)	C(24)	Z	C(21)	C(22)	Y	R	2	4	4	4	mx	C(4)
C(22)	C(19)	Z	C(22)	C(23)	Y	R	2	4	4	4	mx	C(5)
C(23)	C(20)	Z	C(23)	C(24)	Y	R	2	4	4	4	mx	C(6)
C(24)	C(23)	Z	C(24)	C(20)	Y	R	2	4	4	4	mx	C(7)
C(25)	C(20)	Z	C(25)	H(25A)	Y	R	2	5	5	5	3m	C(8)
C(26)	H(26)	Z	C(26)	C(27)	Y	R	2	4	4	4	mx	C(9)
C(27)	N(4)	Z	C(27)	O(4)	Y	R	2	4	4	4	mx	C(1)
C(28)	C(33)	Z	C(28)	C(29)	Y	R	2	4	4	4	mx	C(2)
C(29)	C(32)	Z	C(29)	C(30)	Y	R	2	4	4	4	mx	C(3)
C(30)	C(33)	Z	C(30)	C(31)	Y	R	2	4	4	4	mx	C(4)
C(31)	C(28)	Z	C(31)	C(32)	Y	R	2	4	4	4	mx	C(5)
C(32)	C(29)	Z	C(32)	C(33)	Y	R	2	4	4	4	mx	C(6)
C(33)	C(32)	Z	C(33)	C(28)	Y	R	2	4	4	4	mx	C(7)
C(34)	C(29)	Z	C(34)	H(34A)	Y	R	2	5	5	5	3m	C(8)
H(4)	C(4)	Z	H(4)	C(3)	Y	R	2	6	6	6	cyl	
H(5)	C(5)	Z	H(5)	C(4)	Y	R	2	6	6	6	cyl	H(4)
H(6)	C(6)	Z	H(6)	C(7)	Y	R	2	6	6	6	cyl	H(4)
H(8A)	C(8)	Z	H(8A)	H(8B)	Y	R	2	6	6	6	cyl	
H(8B)	C(8)	Z	H(8B)	H(8A)	Y	R	2	6	6	6	cyl	H(8A)
H(8C)	C(8)	Z	H(8C)	H(8A)	Y	R	2	6	6	6	cyl	H(8A)
H(9)	C(9)	Z	H(9)	C(10)	Y	R	2	6	6	6	cyl	H(4)
H(13)	C(13)	Z	H(13)	C(14)	Y	R	2	6	6	6	cyl	H(4)
H(14)	C(14)	Z	H(14)	C(13)	Y	R	2	6	6	6	cyl	H(4)
H(15)	C(15)	Z	H(15)	C(14)	Y	R	2	6	6	6	cyl	H(4)
H(17A)	C(17)	Z	H(17A)	H(17C)	Y	R	2	6	6	6	cyl	H(8A)
H(17B)	C(17)	Z	H(17B)	H(17C)	Y	R	2	6	6	6	cyl	H(8A)
H(17C)	C(17)	Z	H(17C)	H(17B)	Y	R	2	6	6	6	cyl	H(8A)
H(21)	C(21)	Z	H(21)	C(22)	Y	R	2	6	6	6	cyl	H(4)
H(22)	C(22)	Z	H(22)	C(23)	Y	R	2	6	6	6	cyl	H(4)

H(23)	C(23)	Z	H(23)	C(22)	Y	R	2	6	6	6	cyl	H(4)
H(25A)	C(25)	Z	H(25A)	H(25C)	Y	R	2	6	6	6	cyl	H(8A)
H(25B)	C(25)	Z	H(25B)	H(25C)	Y	R	2	6	6	6	cyl	H(8A)
H(25C)	C(25)	Z	H(25C)	H(25B)	Y	R	2	6	6	6	cyl	H(8A)
H(26)	C(26)	Z	H(26)	C(18)	Y	R	2	6	6	6	cyl	H(4)
H(30)	C(30)	Z	H(30)	C(29)	Y	R	2	6	6	6	cyl	H(4)
H(31)	C(31)	Z	H(31)	C(32)	Y	R	2	6	6	6	cyl	H(4)
H(32)	C(32)	Z	H(32)	C(31)	Y	R	2	6	6	6	cyl	H(4)
H(34A)	C(34)	Z	H(34A)	H(34C)	Y	R	2	6	6	6	cyl	H(8A)
H(34B)	C(34)	Z	H(34B)	H(34A)	Y	R	2	6	6	6	cyl	H(8A)
H(34C)	C(34)	Z	H(34C)	H(34A)	Y	R	2	6	6	6	cyl	H(8A)

10.4.4 Test for overfitting and final refinement strategies

Table S15: Refinement strategy used for cross validation. Steps without tint constitute a usual “standard” MM refinement strategy. Refinement steps tinted green were accepted into the final refinement strategy. Steps tinted red show signs of overfitting or provide no enhancement of model quality and were therefore rejected. Abbreviations: M: monopoles; D: dipoles; Q: quadrupoles; O: octupoles; H: hexadecapoles, U: Uij, κ : kappa, U3/4 (atom name): Gram Charlier 3rd/4th order, nosymm: no local symmetry constraints, nocon: no chemical constraints, d/p : data to parameter ratio, d_1/p_m : ratio of low resolution data (up to 1 Å) to multipole parameter.

Step	Parameters	#param	#data	d/p	d_1/p_m	$R(F^2)$
1	SCALE	1	20097	20097	582.4	0.0528
2	M	14	20097	1435.5	208	0.0497
3	MDQOH	170	20097	118.22	31.31	0.0329
4	MDQOHU	428	20097	46.96	31.31	0.0246
5	MDQOHU _{xyz}	557	20097	36.08	31.31	0.0238
6	MDQOHU _{xyz} κ	562	20097	35.76	29.71	0.0219
7	xyz(H)	79	2912	36.86	None	0.0216
8	MDQOHU _{xyz} κ	562	20097	35.76	29.71	0.0215
9	κ'	6	20097	3349.5	None	0.0212
10	MDQOHU _{xyz} κ	562	20097	35.76	29.71	0.0209

11	Sigobs 0	562	23680	42.14	30.24	0.0209
12	Nocon N1 N2	592	23680	40	26	0.0208
13	Nosymm N1 N2	612	23680	38.69	23.9	0.0208
14	Nocon N3 N4	627	23680	37.77	22.45	0.0208
15	Nosymm N3 N4	647	23680	36.6	20.87	0.0207
16	Nocon methyl groups	668	23680	35.45	19.25	0.0206
17	Nosymm methyl groups	740	23680	32	15.6	0.0205
18	Chemcons per molecule	854	23680	27.73	11.76	0.0204
19	Free H-ADPS	1010	23680	23.45	11.76	0.0202
20	H Q0	1012	23680	23.4	11.76	0.0196
21	Nocon	1267	23680	18.69	7.64	0.0192
22	Nosymm	1629	23680	14.54	5.22	0.0189

Figure S3: R_{cross} -validation of experimental data.

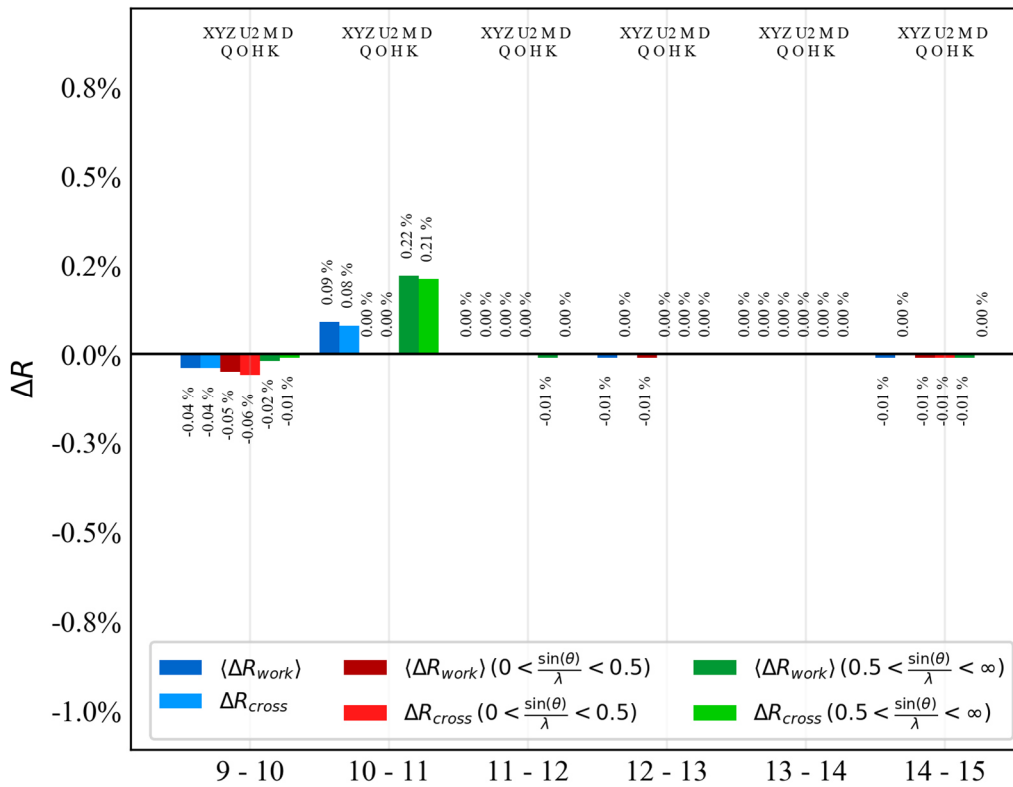
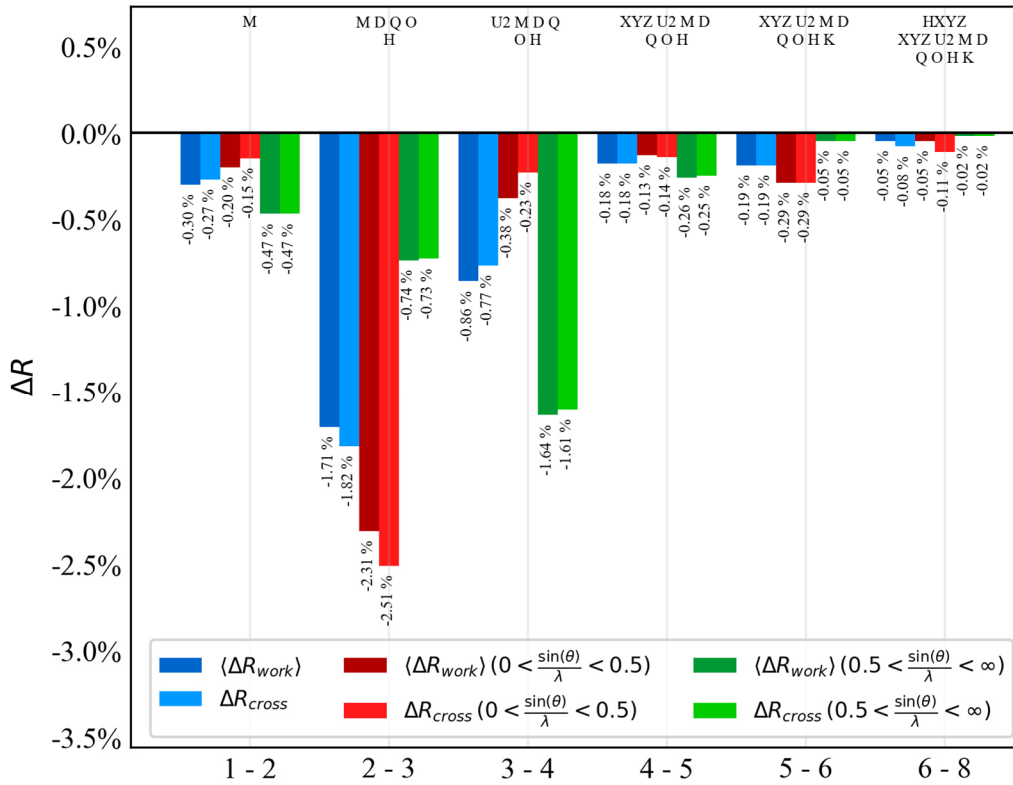


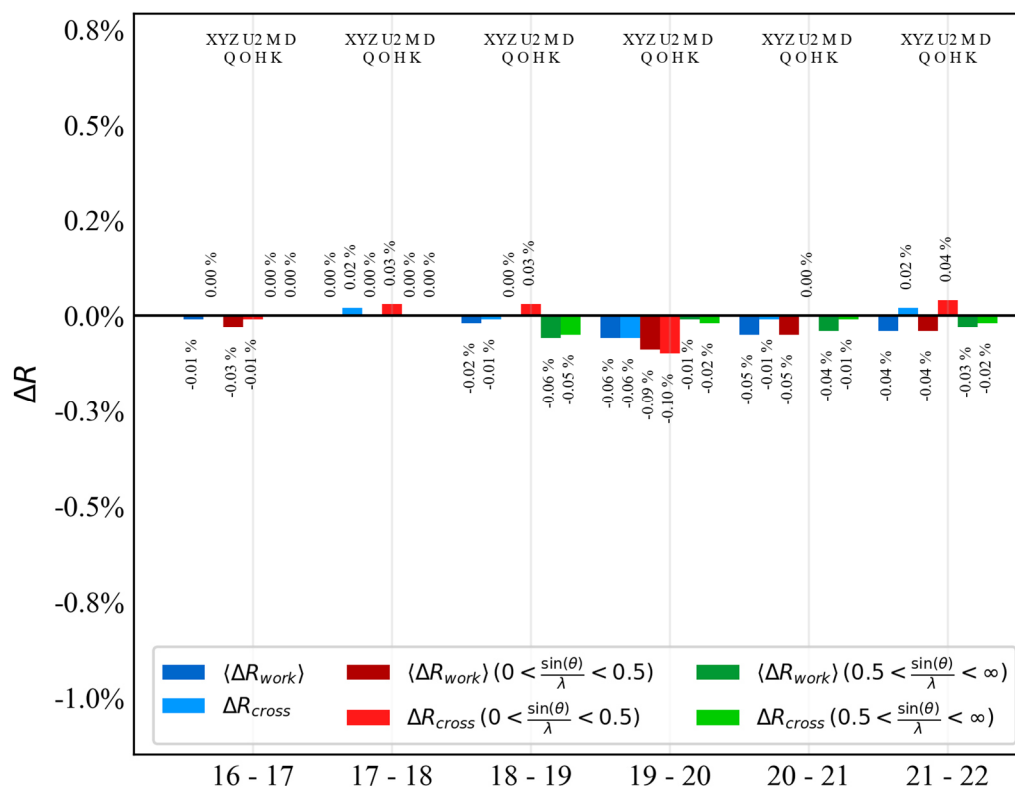
Figure S4: R_{cross} -validation of experimental data, continued.

Table S16: Final refinement strategy for the theoMM model. As the refinement is performed against theoretical data, no positions and vibrational parameters are refined. Abbreviations: d/p: data-to parameter ratio; d_1/p_m : Ratio of low-res data to multipole parameters; SCALE: overall scale factor; M: monopoles; D: dipoles; Q: quadrupoles; O: octupoles; H: hexadecapoles.

Step	Parameters	#param	#data	d/p	d_1/p_m	$R(F^2)$
1	SCALE	1	162443	162443	None	0.0209
2	M	15	162443	11603.07	1237.79	0.0196
3	MDQOH	182	162443	955.55	186.33	0.0083
4	MDQOH κ	187	162443	928.25	176.83	0.0087
5	κ'	6	665465	110910.83	None	0.0075
6	MDQOH κ	187	162443	928.25	176.83	0.0083

Table S17: Final strategy for refinement against experimental data. Abbreviations: d/p: data-to parameter ratio; d_1/p_m : Ratio of low-res data to multipole parameters; SCALE: overall scale factor; M: monopoles; D: dipoles; Q: quadrupoles; O: octupoles; H: hexadecapoles; U: U_{ij} ; xyz(H): free refinement of hydrogen atom positions against the inner data; U3: third-order Gram-Charlier coefficients for anharmonic motion. Until “Sigobs 0”, reflections below 3σ are excluded from the refinement. Residuals are calculated based on the 1Part approach.

Step	Parameters	#param	#data	d/p	d_1/p_m	$R(F^2)$
1	SCALE	1	20097	20097	None	0.0491
2	M	14	20097	1435.5	208	0.047
3	MDQOH	170	20097	118.22	31.31	0.0305
4	MDQOHU	428	20097	46.96	31.31	0.0264
5	MDQOHU _{xyz}	557	20097	36.08	31.31	0.0244
6	MDQOHU _{xyz} κ	562	20097	35.76	29.71	0.0223
7	xyz(H)	79	2912	36.86	None	0.0218
8	MDQOHU _{xyz} κ	562	20097	35.76	29.71	0.0217
9	κ'	6	20097	3349.5	None	0.0213
10	MDQOHU _{xyz} κ	562	20097	35.76	29.71	0.021
11	Sigobs 0	562	20948	37.27	29.94	0.021
12	Nocon N3 N4	562	23680	42.14	30.24	0.021
13	Nosymm N3 N4	612	23680	38.69	23.9	0.0208
14	Free H-ADPS+Q0	770	23680	30.75	23.9	0.0199

10.4.5 DMSDA values of freely refined hydrogen ADPS

Table S18: DMSDA values for the free refinement of hydrogen ADPs against the X-ray data of MnMeBOX.

Bond	Bond length	DMSDA value
C(4) - H(4)	1.0830	142
C(5) - H(5)	1.0830	104
C(6) - H(6)	1.0830	205
C(8) - H(8A)	1.0770	228
C(8) - H(8B)	1.0770	204
C(8) - H(8C)	1.0770	169
C(9) - H(9)	1.0830	127
C(13) - H(13)	1.0830	209
C(14) - H(14)	1.0830	120
C(15) - H(15)	1.0830	135
C(17) - H(17A)	1.0770	174
C(17) - H(17B)	1.0770	246
C(17) - H(17C)	1.0770	151
C(21) - H(21)	1.0830	134
C(22) - H(22)	1.0830	132
C(23) - H(23)	1.0830	211
C(25) - H(25A)	1.0770	167
C(25) - H(25B)	1.0770	148
C(25) - H(25C)	1.0770	179
C(26) - H(26)	1.0830	152
C(30) - H(30)	1.0830	166
C(31) - H(31)	1.0830	142
C(32) - H(32)	1.0830	96
C(34) - H(34A)	1.0770	147
C(34) - H(34B)	1.0770	208
C(34) - H(34C)	1.0770	198

10.4.6 Additional model quality indicator plots

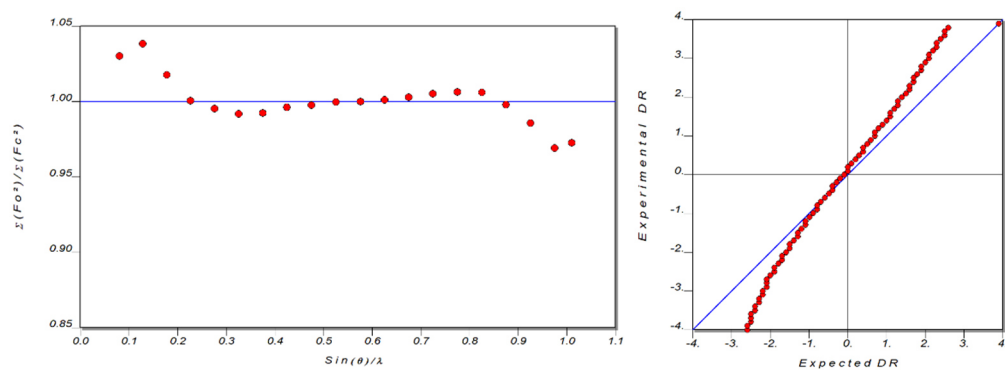


Figure S5: Structure factor plot and normal probability plot for the final refinement of MnMeBOX.

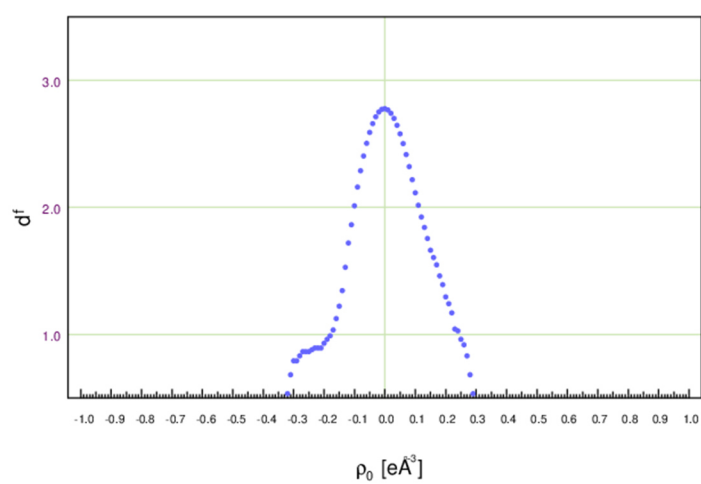


Figure S6: Henn-Meindl plot of the final refinement of MnMeBOX.

10.4.7 ORCA 5 input for CASSCF/NEVPT2 calculations

```

! def2-TZVP def2-TZVP/C PAL4 PATOM tightscf Keepdens
! SlowConv KDIIS SOSCF
%maxcore 62500

%casscf nel 5
  norb 5 #5 electrons in 5 d orbitals
  mult 6,4 # 10 quartet and 40 doublet states
  nroots 1,24
  trafostep RI
  #-----
  nevpt2 SC #Perform the SC-NEVPT2 correction
  actorbs dorbs #Makes the ab initio LFT analysis
  #-----
  rel #flag for relativistic properties
    printlevel 3 #Control the amount of printing
    dosoc true #Do the SOC calculation
    nroots 4
    #-----
    mcd true # Request the MCD calculation
    NInitStates 28 # Number of Donor SOC states
    # for the ABS and MCD spectra evaluation
    NPointsTheta 10 # Number of integration point for
    NPointsPhi 10 # Euler angles
    NPointsPsi 10 #
    B 5000 # Experimental Magnetic field (in Gauss)
    Temperature 10 # Experimental temperature (in K)
    #-----
    domagnetization true
    dosusceptibility true
    LebedevPrec 5 # Precision of the grid for different field
    # directions (meaningful values range from 1
    # (smallest) to 10 (largest))
    nPointsFStep 5 # number of steps for numerical differentiation
    # (def: 5, meaningful values are 3, 5 7 and 9)
    MAGFieldStep 100.0 # Size of field step for numerical differentiation
    # (def: 100 Gauss)
    MAGTemperatureMIN 4.0 # minimum temperature (K) for magnetization
    MAGTemperatureMAX 4.0 # maximum temperature (K) for magnetization
    MAGTemperatureNPoints 1 # number of temperature points for magnetization
    MAGFieldMIN 0.0 # minimum field (Gauss) for magnetization
    MAGFieldMAX 70000.0 # maximum field (Gauss) for magnetization
    MAGNpoints 15 # number of field points for magnetization
    SUSTempMIN 1.0 # minimum temperature (K) for susceptibility
    SUSTempMAX 300.0 # maximum temperature (K) for susceptibility
    SUSNPoints 300 # number of temperature points for susceptibility
    SUSStatFieldMIN 0.0 # minimum static field (Gauss) for susceptibility
    SUSStatFieldMAX 0.1 # maximum static field (Gauss) for susceptibility
    SUSStatFieldNPoints 2 # number of static fields for susceptibility
    #-----
    gtensor true # Request the G-tensor Calculation
    #-----
    dtensor true # Request the ZFS-tensor Calculation
    #(default if dosoc true)
    #-----
  end
end
!Printbasis
%scf print[p_mos] 1
end

```

10.5 Additional details about the structure Refinement of FeMeBOX

10.5.1 Selected data quality indicators

Table S19: Quality indicators for different resolution shells from the final integration of AlH₂MeBOX.

d [Å]	#Data	#hkl (theory)	%Comp	Redundancy	Rrim	Rpim
Inf - 2.03	394	394	100.00	11.67	0.0254	0.0081
2.03 - 1.34	921	921	100.00	19.10	0.0261	0.0063
1.34 - 1.06	1309	1309	100.00	19.84	0.0235	0.0052
1.06 - 0.92	1356	1356	100.00	16.02	0.0218	0.0054
0.92 - 0.84	1227	1227	100.00	15.53	0.0280	0.0071
0.84 - 0.78	1266	1266	100.00	15.16	0.0321	0.0082
0.78 - 0.73	1412	1412	100.00	14.64	0.0397	0.0102
0.73 - 0.69	1431	1431	100.00	14.09	0.0446	0.0117
0.69 - 0.66	1300	1300	100.00	13.56	0.0502	0.0134
0.66 - 0.63	1577	1577	100.00	13.10	0.0598	0.0163
0.63 - 0.61	1237	1237	100.00	12.49	0.0681	0.0190
0.61 - 0.59	1384	1384	100.00	11.89	0.0753	0.0214
0.59 - 0.58	776	776	100.00	11.68	0.0816	0.0235
0.58 - 0.56	1709	1709	100.00	11.07	0.0974	0.0289
0.56 - 0.55	949	949	100.00	10.92	0.1194	0.0356
0.55 - 0.53	2147	2147	100.00	10.24	0.1378	0.0422
0.53 - 0.52	1164	1164	100.00	9.98	0.1549	0.0483
0.52 - 0.51	1280	1280	100.00	9.47	0.1773	0.0566
0.51 - 0.50	1397	1397	100.00	9.30	0.1953	0.0629
0.50 - 0.49	1656	1691	97.93	8.09	0.2082	0.0701

10.5.2 Local coordinate systems, symmetry and chemical constraints

Save for the different metal centre and different dummy positions referred to in Chapter 5.4, local coordinate systems, symmetry and chemical constraints for FeMeBOX were identical to MnMeBOX (see 10.4.3) and CoMeBOX.

10.5.3 Test for overfitting and final refinement strategies

Table S20: Refinement strategy used for cross validation. Steps without tint constitute a usual “standard” MM refinement strategy. Refinement steps tinted green were accepted into the final refinement strategy. Steps tinted red show signs of overfitting or provide no enhancement of model quality and were therefore rejected. Abbreviations: M: monopoles; D: dipoles; Q: quadrupoles; O: octupoles; H: hexadecapoles, U: Uij, k: kappa, U3/4 (atom name): Gram Charlier 3rd/4th order, nosym: no local symmetry constraints, nocon: no chemical constraints, d/p : data to parameter ratio, d_1/p_m : ratio of low resolution data (up to 1 Å) to multipole parameter.

Step	Parameters	#param	#data	d/p	d_1/p_m	$R(F^2)$
1	SCALE	1	20303	576.4	576.4	0.0553
2	M	14	20303	205.86	205.86	0.0501
3	MDQOH	170	20303	30.99	30.99	0.0409
4	MDQOHU	428	20303	30.99	30.99	0.0229
5	MDQOHU _{xyz}	557	20303	30.99	30.99	0.0223
6	MDQOHU _{xyz} κ	562	20303	29.41	29.41	0.021
7	xyz(H)	79	2881	None	None	0.0209
8	MDQOHU _{xyz} κ	562	20303	29.41	29.41	0.0208
9	κ'	6	20303	None	None	0.0205
10	MDQOHU _{xyz} κ	562	20303	29.41	29.41	0.0202
11	Sigobs 0	562	23773	29.99	29.99	0.0202
12	Nocon N1 N2	592	23773	25.78	25.78	0.0202
13	Nosymm N1 N2	612	23773	23.7	23.7	0.0202

14	Nocon N3 N4	627	23773	22.27	22.27	0.0201
15	Nosymm N3 N4	647	23773	20.7	20.7	0.0201
16	Nocon methyl groups	668	23773	19.08	19.08	0.0201
17	Nosymm methyl groups	740	23773	15.47	15.47	0.02
18	Chemcons per molecule	782	23773	13.61	13.61	0.0201
19	Free H-ADPS	924	23773	14.13	14.13	0.0199
20	H Q0	926	23773	14.13	14.13	0.0194
21	Nocon	1195	23773	8.35	8.35	0.0193
22	Nosymm	1629	23773	5.17	5.17	0.0191

Figure S7: R_{cross} -validation of experimental data.

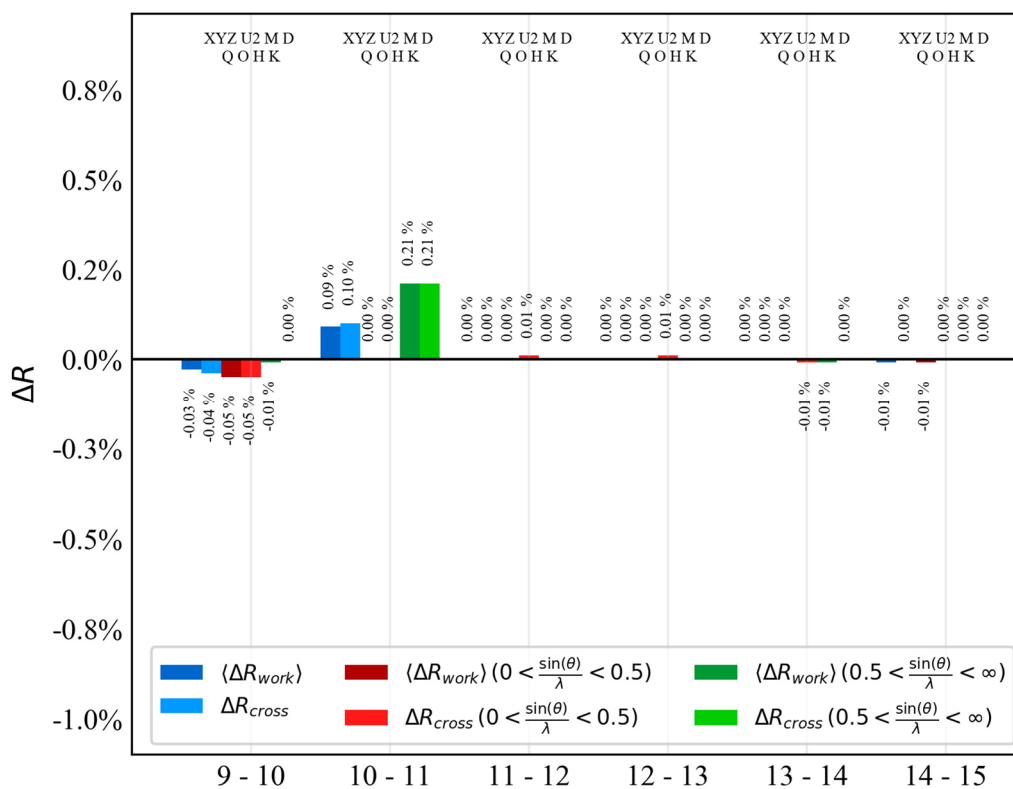
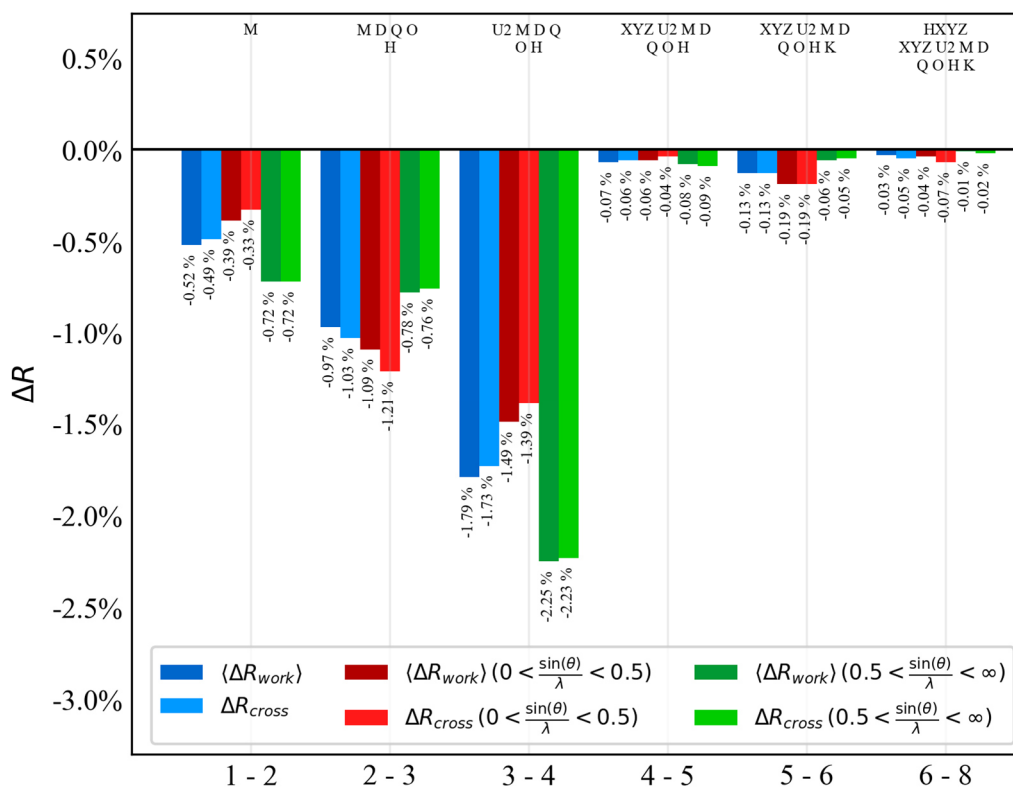


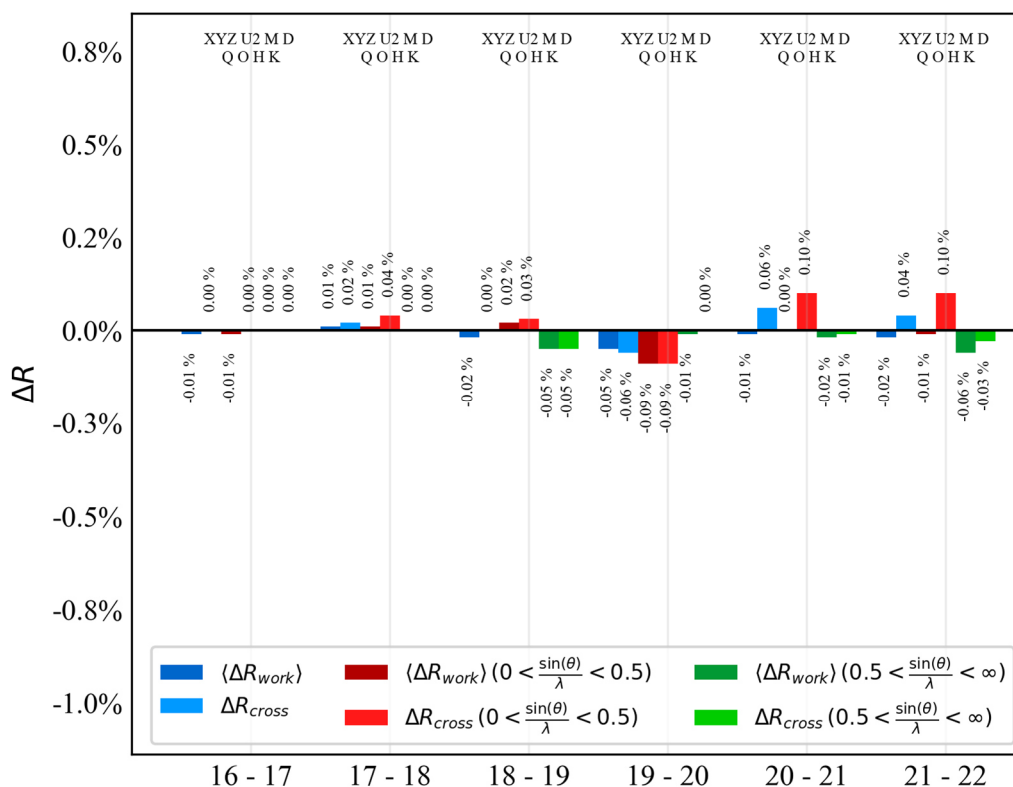
Figure S8: R_{cross} -validation of experimental data, continued.

Table S21: Final refinement strategy for the theoMM model. As the refinement is performed against theoretical data, no positions and vibrational parameters are refined. Abbreviations: d/p: data-to parameter ratio; d_1/p_m : Ratio of low-res data to multipole parameters; SCALE: overall scale factor; M: monopoles; D: dipoles; Q: quadrupoles; O: octupoles; H: hexadecapoles.

Step	Parameters	#param	#data	d/p	d_1/p_m	$R(F^2)$
1	SCALE	1	141865	141865	None	0.0226
2	M	14	141865	10133.21	1191.29	0.0217
3	MDQOH	170	141865	834.5	179.33	0.0084
4	MDQOH κ	175	141865	810.66	170.18	0.0092
5	κ'	6	141865	23644.17	None	0.009
6	MDQOH κ	175	141865	810.66	170.18	0.0088

Table S22: Final strategy for refinement against experimental data. Abbreviations: d/p : data-to parameter ratio; d_1/p_m : Ratio of low-res data to multipole parameters; SCALE: overall scale factor; M: monopoles; D: dipoles; Q: quadrupoles; O: octupoles; H: hexadecapoles; U: U_{ij} ; xyz(H): free refinement of hydrogen atom positions against the inner data; U3: third-order Gram-Charlier coefficients for anharmonic motion. Until “Sigobs 0”, reflections below 3σ are excluded from the refinement. Residuals are calculated based on the 1Part approach.

Step	Parameters	#param	#data	d/p	d_1/p_m	$R(F^2)$
1	SCALE	1	17207	17207	None	0.0502
2	M	14	17207	1229.07	205.86	0.0463
3	MDQOH	170	17207	101.22	30.99	0.0352
4	MDQOHU	428	17207	40.2	30.99	0.0239
5	MDQOHU _{xyz}	557	17207	30.89	30.99	0.0226
6	MDQOHU _{xyz} κ	562	17207	30.62	29.41	0.0214
7	xyz(H)	79	2881	36.47	None	0.0211
8	MDQOHU _{xyz} κ	562	17207	30.62	29.41	0.021
9	κ'	6	17207	2867.83	None	0.0207
10	MDQOHU _{xyz} κ	562	17207	30.62	29.41	0.0204
11	Sigobs 0	562	19339	34.41	29.99	0.0204
12	Free H-ADPS+Q0	720	19339	26.86	29.99	0.0195

10.5.4 DMSDA values of freely refined hydrogen ADPS

Table S23: DMSDA values for the free refinement of hydrogen ADPs against the X-ray data of FeMeBOX.

Bond	Bond length	DMSDA value
C(4) - H(4)	1.0830	101
C(5) - H(5)	1.0830	110
C(6) - H(6)	1.0830	137
C(8) - H(8A)	1.0770	230
C(8) - H(8B)	1.0770	155
C(8) - H(8C)	1.0770	148
C(9) - H(9)	1.0830	110
C(13) - H(13)	1.0830	169
C(14) - H(14)	1.0830	153
C(15) - H(15)	1.0830	161
C(17) - H(17A)	1.0770	223
C(17) - H(17B)	1.0770	205
C(17) - H(17C)	1.0770	132
C(21) - H(21)	1.0830	262
C(22) - H(22)	1.0830	141
C(23) - H(23)	1.0830	142
C(25) - H(25A)	1.0770	201
C(25) - H(25B)	1.0770	119
C(25) - H(25C)	1.0770	135
C(26) - H(26)	1.0830	131
C(30) - H(30)	1.0830	125
C(31) - H(31)	1.0830	178
C(32) - H(32)	1.0830	126
C(34) - H(34A)	1.0770	171
C(34) - H(34B)	1.0770	163
C(34) - H(34C)	1.0770	154

10.5.5 Additional model quality indicator plots

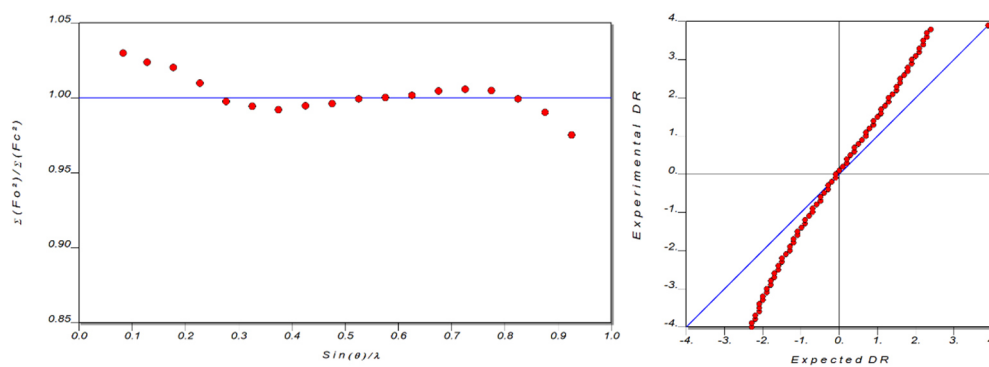


Figure S9: Structure factor plot and normal probability plot for the final refinement of FeMeBOX.

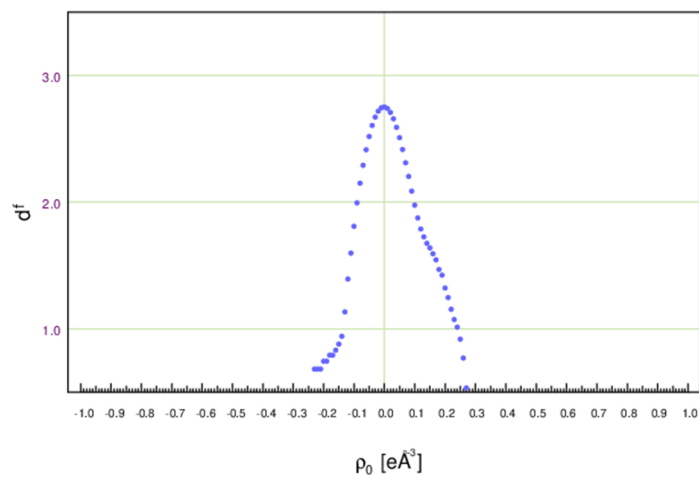


Figure S10: Henn-Meindl plot of the final refinement of FeMeBOX.

10.5.6 Molecular Graph

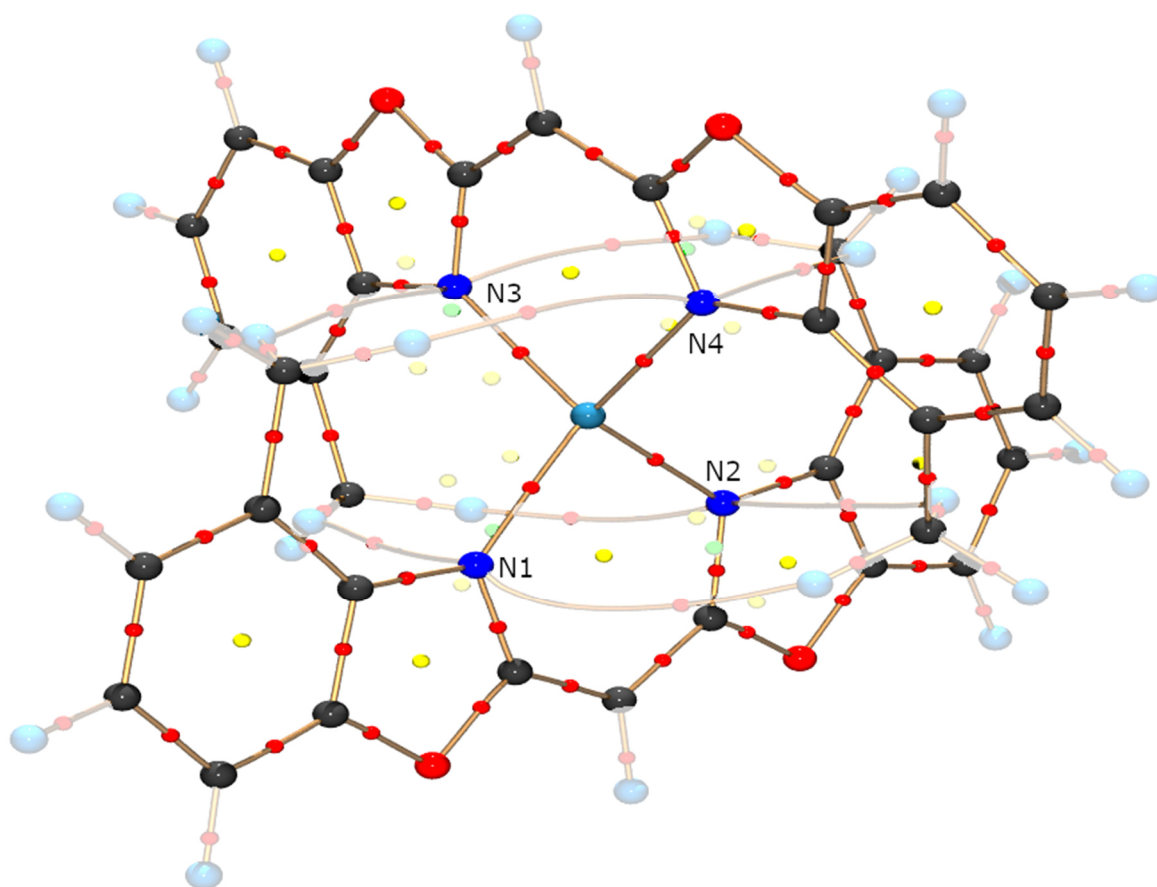


Figure S11: Molecular graph of FeMeBOX. Bond paths are displayed in golden, BCPs are displayed in red, RCPs are displayed in yellow, CCPs are displayed in green. Bond paths originating from/ending at hydrogen atoms are toned down for clarity.

10.5.7 ORCA 5 input for CASSCF/NEVPT2 calculations

```

! def2-TZVP def2-TZVP/C PAL4 PATOM tightscf Keepdens
! SlowConv KDIIS SOSCF
%maxcore 62500

%casscf nel 6
  norb 5 #6 electrons in 5 d orbitals
  mult 5,3 # 5 quintet and 45 triplet states
  nroots 5,45
  trafostep RI
  #-----
  nevpt2 SC #Perform the SC-NEVPT2 correction
  actorbs dorbs #Makes the ab initio LFT analysis
  #-----
  rel #flag for relativistic properties
    printlevel 3 #Control the amount of printing
    dosoc true #Do the SOC calculation
    nroots 4
    #-----
    mcd true # Request the MCD calculation
    NInitStates 28 # Number of Donor SOC states
    # for the ABS and MCD spectra evaluation
    NPointsTheta 10 # Number of integration point for
    NPointsPhi 10 # Euler angles
    NPointsPsi 10 #
    B 5000 # Experimental Magnetic field (in Gauss)
    Temperature 10 # Experimental temperature (in K)
    #-----
    domagnetization true
    dosusceptibility true
    LebedevPrec 5 # Precision of the grid for different field
    # directions (meaningful values range from 1
    # (smallest) to 10 (largest))
    nPointsFStep 5 # number of steps for numerical differentiation
    # (def: 5, meaningful values are 3, 5 7 and 9)
    MAGFieldStep 100.0 # Size of field step for numerical differentiation
    # (def: 100 Gauss)
    MAGTemperatureMIN 4.0 # minimum temperature (K) for magnetization
    MAGTemperatureMAX 4.0 # maximum temperature (K) for magnetization
    MAGTemperatureNPoints 1 # number of temperature points for magnetization
    MAGFieldMIN 0.0 # minimum field (Gauss) for magnetization
    MAGFieldMAX 70000.0 # maximum field (Gauss) for magnetization
    MAGNpoints 15 # number of field points for magnetization
    SUSTempMIN 1.0 # minimum temperature (K) for susceptibility
    SUSTempMAX 300.0 # maximum temperature (K) for susceptibility
    SUSNPoints 300 # number of temperature points for susceptibility
    SUSStatFieldMIN 0.0 # minimum static field (Gauss) for susceptibility
    SUSStatFieldMAX 0.1 # maximum static field (Gauss) for susceptibility
    SUSStatFieldNPoints 2 # number of static fields for susceptibility
    #-----
    gtensor true # Request the G-tensor Calculation
    #-----
    dtensor true # Request the ZFS-tensor Calculation
    #(default if dosoc true)
    #-----
  end
end
!Printbasis
%scf print[p_mos] 1
end

```

10.6 Additional details about the structure Refinement of CoMeBOX

10.6.1 Selected data quality indicators by dataset

10.6.1.1 APEX II/Mo-TXS

Table S24: Quality indicators for different resolution shells from the final integration of the CoMeBOX dataset collected on a Mo-TXS anode with an APEX II detector. Notably, 26 of the inner reflection had to be obtained from fastscans due to severe overexposure.

d [Å]	#Data	#hkl (theory)	%Comp	Redundancy	Rrim	Rpim
Inf - 1.95	440	442	99.55	23.76	0.0168	0.0031
1.95 - 1.29	1028	1028	100.00	28.19	0.0255	0.0050
1.29 - 1.02	1452	1452	100.00	25.10	0.0357	0.0074
1.02 - 0.89	1434	1452	98.76	11.50	0.0355	0.0103
0.89 - 0.80	1602	1603	99.94	12.46	0.0360	0.0107
0.80 - 0.74	1571	1571	100.00	13.21	0.0424	0.0120
0.74 - 0.70	1341	1341	100.00	12.94	0.0468	0.0133
0.70 - 0.67	1246	1246	100.00	12.62	0.0503	0.0143
0.67 - 0.64	1472	1472	100.00	12.16	0.0570	0.0164
0.64 - 0.61	1783	1783	100.00	11.81	0.0662	0.0194
0.61 - 0.59	1374	1374	100.00	11.28	0.0726	0.0215
0.59 - 0.57	1619	1621	99.88	10.97	0.0801	0.0240
0.57 - 0.55	1806	1809	99.83	10.63	0.0934	0.0284
0.55 - 0.54	1037	1039	99.81	10.24	0.1058	0.0325
0.54 - 0.53	1091	1099	99.27	9.90	0.1158	0.0360
0.53 - 0.51	2415	2439	99.02	8.39	0.1239	0.0416
0.51 - 0.50	1371	1398	98.07	7.51	0.1371	0.0483
0.50 - 0.49	1436	1469	97.75	6.81	0.1514	0.0558
0.49 - 0.48	1595	1639	97.32	6.55	0.1613	0.0599
0.48 - 0.47	1787	1968	90.80	5.46	0.1744	0.0675

10.6.1.2 PHOTON III/Ag- μ S

Table S25: Quality indicators for different resolution shells from the final integration of the CoMeBOX dataset collected on a Ag- μ S anode with an PHOTON III detector. Selected scans were collected with the sensitive mode of the new detector. However, this did not improve the quality of the data compared to the ordinary runs.

d [Å]	#Data	#hkl (theory)	%Comp	Redundancy	Rrim	Rpim
Inf - 1.95	437	442	98.87	51.79	0.0261	0.0039
1.95 - 1.29	1026	1026	100.00	52.11	0.0350	0.0048
1.29 - 1.02	1451	1451	100.00	25.71	0.0299	0.0054
1.02 - 0.89	1452	1452	100.00	9.65	0.0269	0.0085
0.89 - 0.80	1605	1605	100.00	9.79	0.0299	0.0094
0.80 - 0.74	1568	1568	100.00	9.41	0.0359	0.0116
0.74 - 0.70	1338	1338	100.00	9.04	0.0394	0.0130
0.70 - 0.66	1692	1692	100.00	8.41	0.0455	0.0155
0.66 - 0.63	1588	1588	100.00	8.22	0.0519	0.0180
0.63 - 0.61	1229	1229	100.00	7.99	0.0595	0.0209
0.61 - 0.59	1365	1365	100.00	7.85	0.0630	0.0223
0.59 - 0.57	1623	1623	100.00	7.53	0.0705	0.0254
0.57 - 0.55	1818	1818	100.00	7.29	0.0869	0.0318
0.55 - 0.54	1035	1035	100.00	6.42	0.1031	0.0402
0.54 - 0.52	2274	2274	100.00	6.64	0.1211	0.0465
0.52 - 0.51	1252	1252	100.00	6.47	0.1326	0.0514
0.51 - 0.50	1402	1402	100.00	6.17	0.1438	0.0571
0.50 - 0.49	1467	1468	99.93	5.56	0.1654	0.0694
0.49 - 0.48	1654	1654	100.00	5.78	0.1774	0.0729
0.48 - 0.47	1785	1830	97.54	5.43	0.1882	0.0784

10.6.1.3 PHOTON III/Mo-TXS

Table S26: Quality indicators for different resolution shells from the final integration of the CoMeBOX dataset collected on a Mo-TXS anode with an PHOTON III detector. Overall, this run yielded the best data quality indicators, as well as the best quality indicators for models refined against it. Therefore, it was chosen as the final dataset for CoMeBOX.

d [Å]	#Data	#hkl (theory)	%Comp	Redundancy	Rrim	Rpim
Inf - 1.95	441	442	99.77	34.19	0.0444	0.0087
1.95 - 1.29	1028	1028	100.00	24.02	0.0411	0.0084
1.29 - 1.02	1451	1451	100.00	20.04	0.0342	0.0079
1.02 - 0.89	1453	1453	100.00	14.95	0.0320	0.0081
0.89 - 0.80	1606	1606	100.00	13.90	0.0351	0.0093
0.80 - 0.74	1572	1572	100.00	13.34	0.0398	0.0107
0.74 - 0.70	1340	1340	100.00	12.81	0.0427	0.0118
0.70 - 0.66	1689	1689	100.00	12.31	0.0463	0.0131
0.66 - 0.63	1590	1590	100.00	11.76	0.0522	0.0151
0.63 - 0.61	1227	1227	100.00	11.13	0.0589	0.0175
0.61 - 0.59	1369	1369	100.00	10.70	0.0614	0.0187
0.59 - 0.57	1620	1620	100.00	10.12	0.0699	0.0218
0.57 - 0.55	1810	1810	100.00	9.65	0.0836	0.0266
0.55 - 0.54	1045	1045	100.00	9.19	0.0918	0.0302
0.54 - 0.52	2279	2279	100.00	8.81	0.1075	0.0358
0.52 - 0.51	1248	1248	100.00	8.37	0.1227	0.0420
0.51 - 0.50	1409	1409	100.00	8.10	0.1286	0.0446
0.50 - 0.49	1467	1467	100.00	7.80	0.1413	0.0499
0.49 - 0.48	1657	1657	100.00	6.72	0.1566	0.0595
0.48 - 0.47	1816	1860	97.63	5.20	0.1691	0.0723

10.6.2 Local coordinate systems, symmetry and chemical constraints

Save for the different metal centre and different dummy positions referred to in Chapter 5.4, local coordinate systems, symmetry and chemical constraints for CoMeBOX were identical to MnMeBOX (see 10.4.3) and FeMeBOX.

10.6.3 Test for overfitting and final refinement strategies

Table S27: Refinement strategy used for cross validation. Steps without tint constitute a usual “standard” MM refinement strategy. Refinement steps tinted green were accepted into the final refinement strategy. Steps tinted red show signs of overfitting or provide no enhancement of model quality and were therefore rejected. Abbreviations: M: monopoles; D: dipoles; Q: quadrupoles; O: octupoles; H: hexadecapoles, U: Uij, k: kappa, U3/4 (atom name): Gram Charlier 3rd/4th order, nosym: no local symmetry constraints, nocon: no chemical constraints, d/p: data to parameter ratio, d1/pm: ratio of low resolution data (up to 1 Å) to multipole parameter.

Step	Parameters	#param	#data	d/p	d ₁ /p _m	R(F ²)
1	SCALE	1	23556	23556	586	0.0625
2	M	14	23556	1682.57	209.29	0.0439
3	MDQOH	170	23556	138.56	31.51	0.0311
4	MDQOHU	428	23556	55.04	31.51	0.0227
5	MDQOHU _{xyz}	557	23556	42.29	31.51	0.0222
6	MDQOHU _{xyz} κ	562	23556	41.91	29.9	0.0216
7	xyz(H)	79	2930	37.09	None	0.0215
8	MDQOHU _{xyz} κ	562	23556	41.91	29.9	0.0215
9	κ'	6	23556	3926	None	0.0213
10	MDQOHU _{xyz} κ	562	23556	41.91	29.9	0.021
11	Sigobs 0	562	27143	48.3	30.03	0.021
12	Nocon N1 N2	592	27143	45.85	25.82	0.021
13	Nosymm N1 N2	612	27143	44.35	23.73	0.021
14	Nocon N3 N4	627	27143	43.29	22.3	0.0209
15	Nosymm N3 N4	647	27143	41.95	20.73	0.0209
16	Nocon methyl groups	668	27143	40.63	19.11	0.0209

17	Nosymm methyl groups	740	27143	36.68	15.49	0.0208
18	Chemcons per molecule	854	27143	31.78	11.68	0.0207
19	Free H-ADPS	1010	27143	26.87	11.68	0.0204
20	H Q0	1012	27143	26.82	11.68	0.0202
21	Nocon	1265	27143	21.46	7.59	0.0202
22	Nosymm	1617	27143	16.79	5.24	0.0203

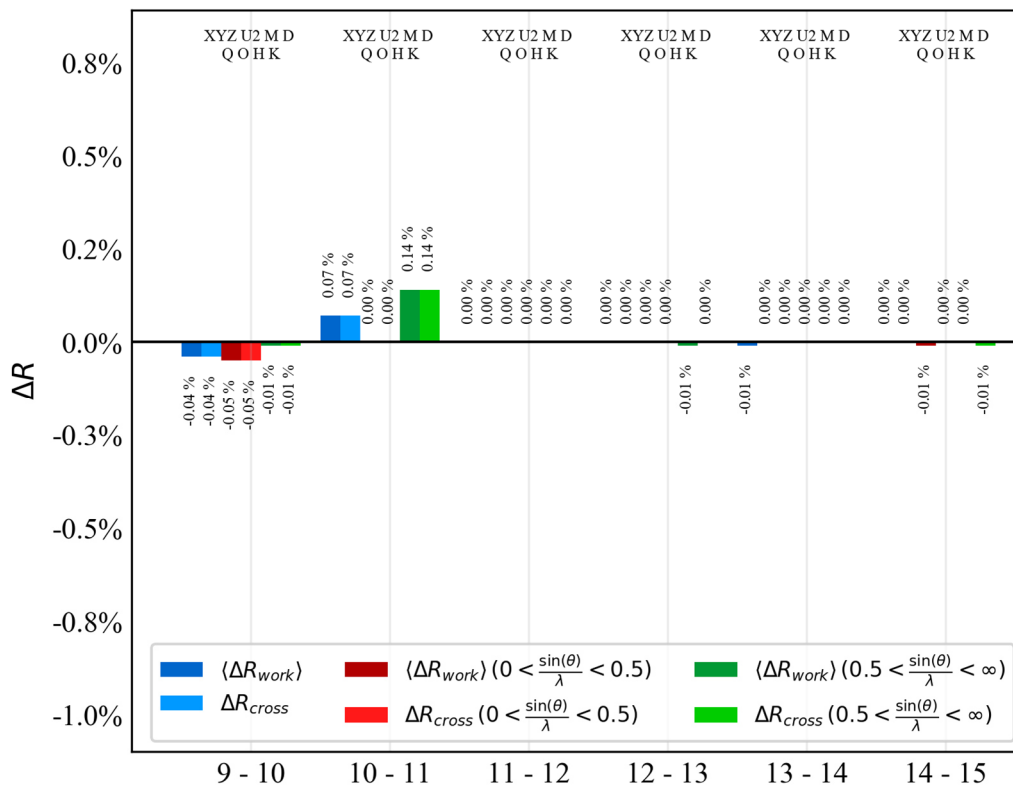
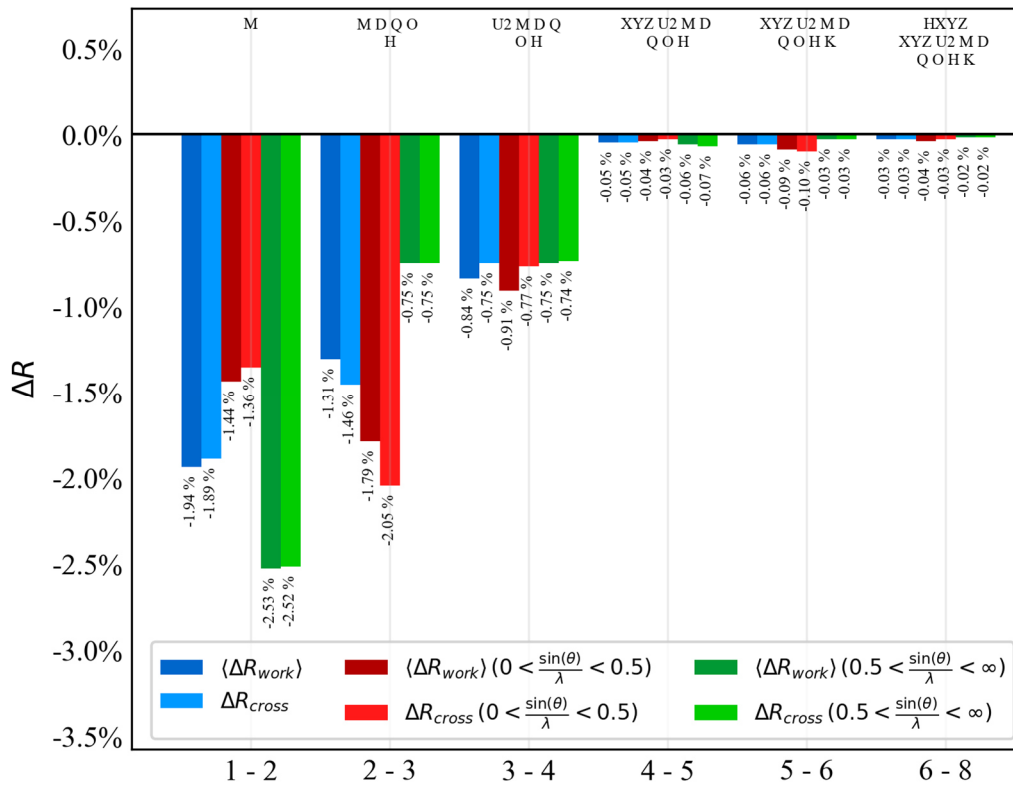
Figure S12: R_{cross} -validation of experimental data.

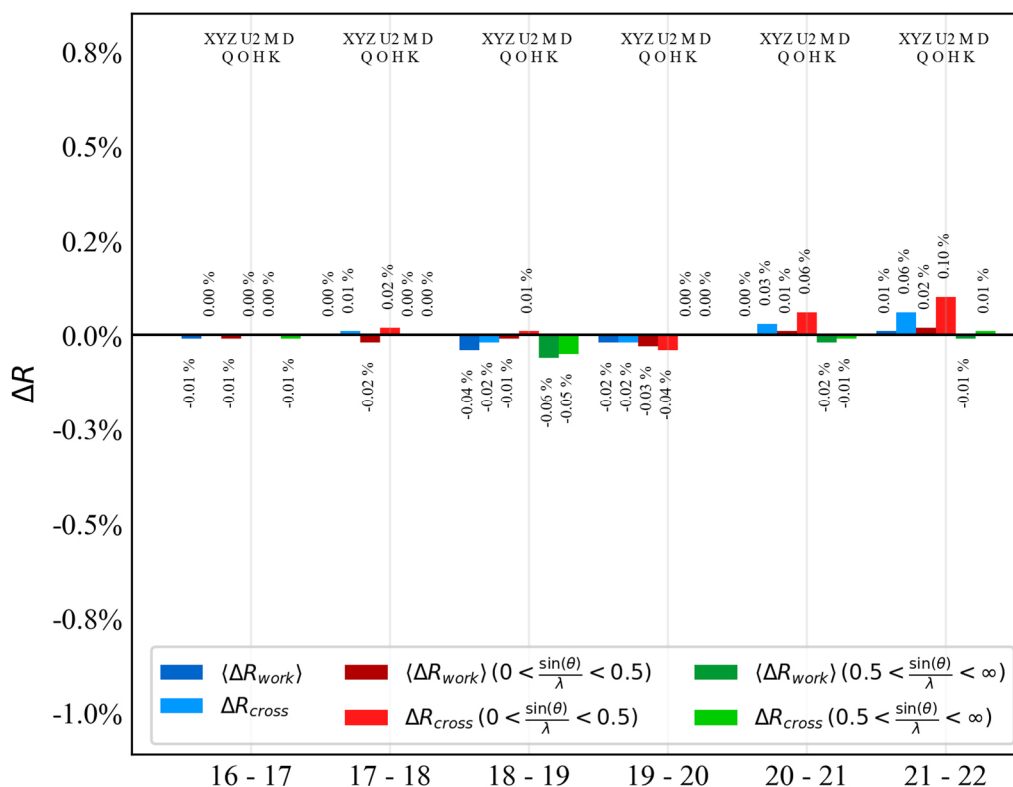
Figure S13: R_{cross} -validation of experimental data, continued.

Table S28: Final refinement strategy for the theoMM model. As the refinement is performed against theoretical data, no positions and vibrational parameters are refined. Abbreviations: d/p: data-to parameter ratio; d_1/p_m : Ratio of low-res data to multipole parameters; SCALE: overall scale factor; M: monopoles; D: dipoles; Q: quadrupoles; O: octupoles; H: hexadecapoles.

Step	Parameters	#param	#data	d/p	d_1/p_m	$R(F^2)$
1	SCALE	1	136393	136393	3465.8	0.02
2	M	14	457608	32686.29	1237.79	0.0201
3	MDQOH	170	457608	2691.81	186.33	0.0072
4	MDQOH κ	175	457608	2614.9	176.83	0.0065
5	κ'	6	457608	76268	None	0.0063
6	MDQOH κ	175	457608	2614.9	176.83	0.0062

Table S29: Final strategy for refinement against experimental data. Abbreviations: d/p : data-to parameter ratio; d_1/p_m : Ratio of low-res data to multipole parameters; SCALE: overall scale factor; M: monopoles; D: dipoles; Q: quadrupoles; O: octupoles; H: hexadecapoles; U: U_{ij} ; xyz(H): free refinement of hydrogen atom positions against the inner data; U3: third-order Gram-Charlier coefficients for anharmonic motion. Until “Sigobs 0”, reflections below 3σ are excluded from the refinement. Residuals are calculated based on the 1Part approach.

Step	Parameters	#param	#data	d/p	d_1/p_m	$R(F^2)$
1	SCALE	1	1	23556	585.6	0.046
2	M	14	14	1682.57	209.14	0.0453
3	MDQOH	170	170	138.56	31.48	0.0243
4	MDQOHU	428	428	55.04	31.48	0.0234
5	MDQOHU _{xyz}	557	557	42.29	31.48	0.023
6	MDQOHU _{xyz} κ	562	562	41.91	29.88	0.0221
7	xyz(H)	79	79	37.06	None	0.0217
8	MDQOHU _{xyz} κ	562	562	41.91	29.88	0.0217
9	κ'	6	6	3926	None	0.0215
10	MDQOHU _{xyz} κ	562	562	41.91	29.88	0.0211
11	Sigobs 0	562	562	48.3	30.01	0.0212
12	Free H-ADPS+Q0	720	720	37.7	30.01	0.0204

10.6.4 DMSDA values of freely refined hydrogen ADPS

Table S30: DMSDA values for the free refinement of hydrogen ADPs against the X-ray data of CoMeBOX.

Bond	Bond length	DMSDA value
C(4) - H(4)	1.0830	200
C(5) - H(5)	1.0830	155
C(6) - H(6)	1.0830	171
C(8) - H(8A)	1.0770	151
C(8) - H(8B)	1.0770	109
C(8) - H(8C)	1.0770	95
C(9) - H(9)	1.0830	132
C(13) - H(13)	1.0830	163
C(14) - H(14)	1.0830	115
C(15) - H(15)	1.0830	153
C(17) - H(17A)	1.0770	99
C(17) - H(17B)	1.0770	100
C(17) - H(17C)	1.0770	120
C(21) - H(21)	1.0830	146
C(22) - H(22)	1.0830	167
C(23) - H(23)	1.0830	120
C(25) - H(25A)	1.0770	45
C(25) - H(25B)	1.0770	123
C(25) - H(25C)	1.0770	63
C(26) - H(26)	1.0830	146
C(30) - H(30)	1.0830	181
C(31) - H(31)	1.0830	175
C(32) - H(32)	1.0830	196
C(34) - H(34A)	1.0770	38
C(34) - H(34B)	1.0770	143
C(34) - H(34C)	1.0770	86

10.6.5 Additional model quality indicator plots

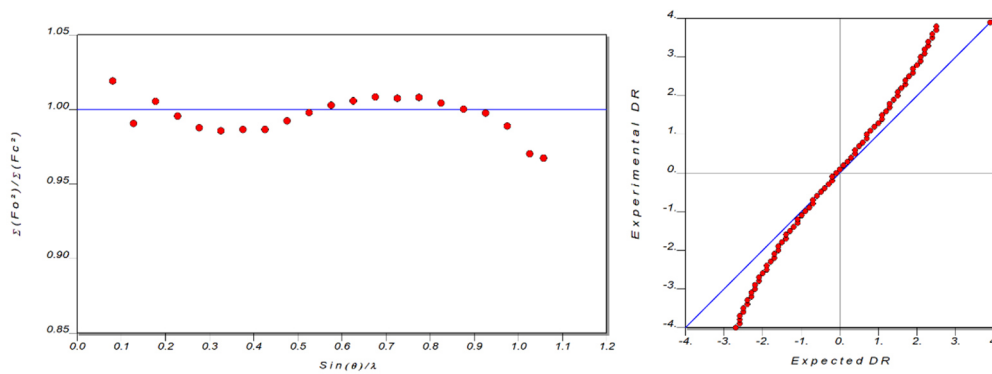


Figure S14: Structure factor plot and normal probability plot for the final refinement of CoMeBOX.

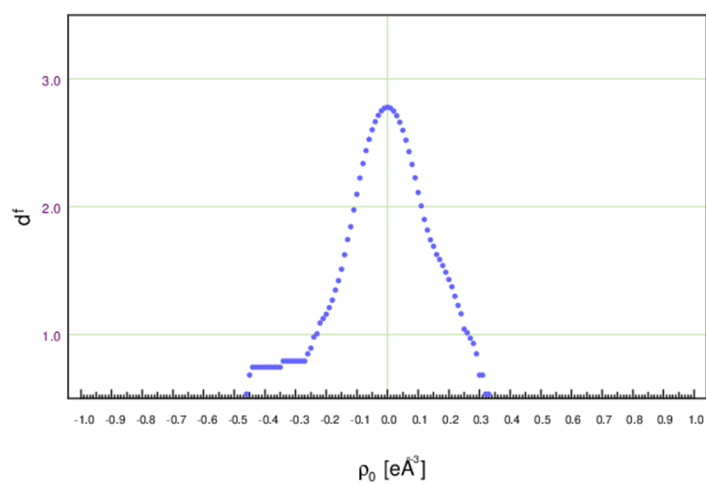


Figure S15: Henn-Meindl plot of the final refinement of CoMeBOX.

10.6.6 Molecular Graph

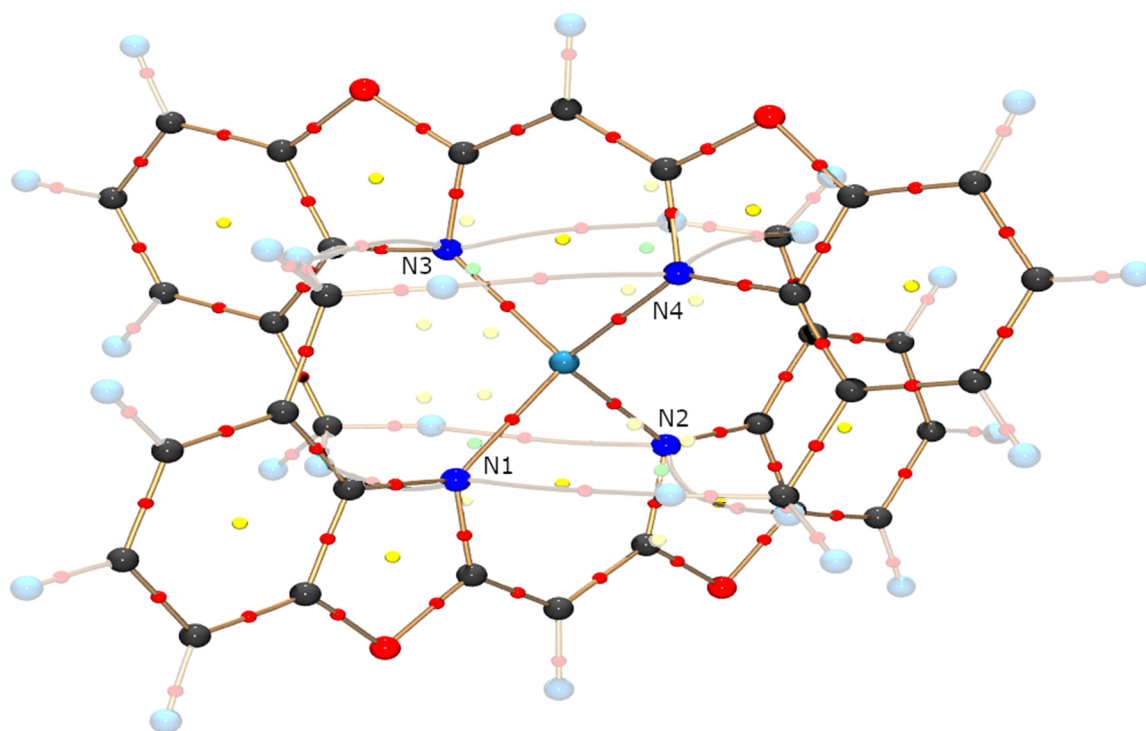


Figure S16: Molecular graph of CoMeBOX. Bond paths are displayed in golden, BCPs are displayed in red, RCPs are displayed in yellow, CCPs are displayed in green. Bond paths originating from/ending at hydrogen atoms are toned down for clarity.

10.6.7 ORCA 5 input for CASSCF/NEVPT2 calculations

! DKH DKH-DEF2-TZVP AUTOAUX NoFrozenscore PAL8 tightscf

```

%rel
picturechange 2
end

%casscf nel 7
  norb 5 #7 electrons in 5 d orbitals
  nroots 10
  mult 4 # 10 quartet states
  actorbs dorbs
  #-----
  printf true
  trafostep rimo
  nevpt2 SC
  #-----
  rel
    nroots 10
    printlevel 3 #Control the amount of printing
    dosoc true #Do the SOC calculation
    #-----
    domagnetization true
    dosusceptibility true
    LebedevPrec 5 # Precision of the grid for different field
                  # directions (meaningful values range from 1
                  # (smallest) to 10 (largest))
    nPointsFStep 5 # number of steps for numerical differentiation
                  # (def: 5, meaningful values are 3, 5 7 and 9)
    MAGFieldStep 100.0 # Size of field step for numerical differentiation
                  # (def: 100 Gauss)
    MAGTemperatureMIN 4.0 # minimum temperature (K) for magnetization
    MAGTemperatureMAX 4.0 # maximum temperature (K) for magnetization
    MAGTemperatureNPoints 1 # number of temperature points for magnetization
    MAGFieldMIN 0.0 # minimum field (Gauss) for magnetization
    MAGFieldMAX 70000.0 # maximum field (Gauss) for magnetization
    MAGNpoints 15 # number of field points for magnetization
    SUSTempMIN 1.0 # minimum temperature (K) for susceptibility
    SUSTempMAX 300.0 # maximum temperature (K) for susceptibility
    SUSNPoints 300 # number of temperature points for susceptibility
    SUSStatFieldMIN 0.0 # minimum static field (Gauss) for susceptibility
    SUSStatFieldMAX 0.1 # maximum static field (Gauss) for susceptibility
    SUSStatFieldNPoints 2 # number of static fields for susceptibility
    #-----
    gtensor true # Request the G-tensor Calculation
    #-----
    dtensor true # Request the ZFS-tensor Calculation
                  #(default if dosoc true)
    #-----
  end
end
!Printbasis PrintMos
%scf print[p_mos] 1
maxcore 30000
end

```

10.7 Additional details about the structure refinement of SPAnH

Information presented here is mostly based on work on my master thesis and is also available in the supporting information of my original publication of this project.^[51] As such, only a slightly shortened list of the full supplementary material will be listed here. Further details about this structure can be found in the publication by Herbst-Irmer *et al.*^[72] mentioned in the main article.

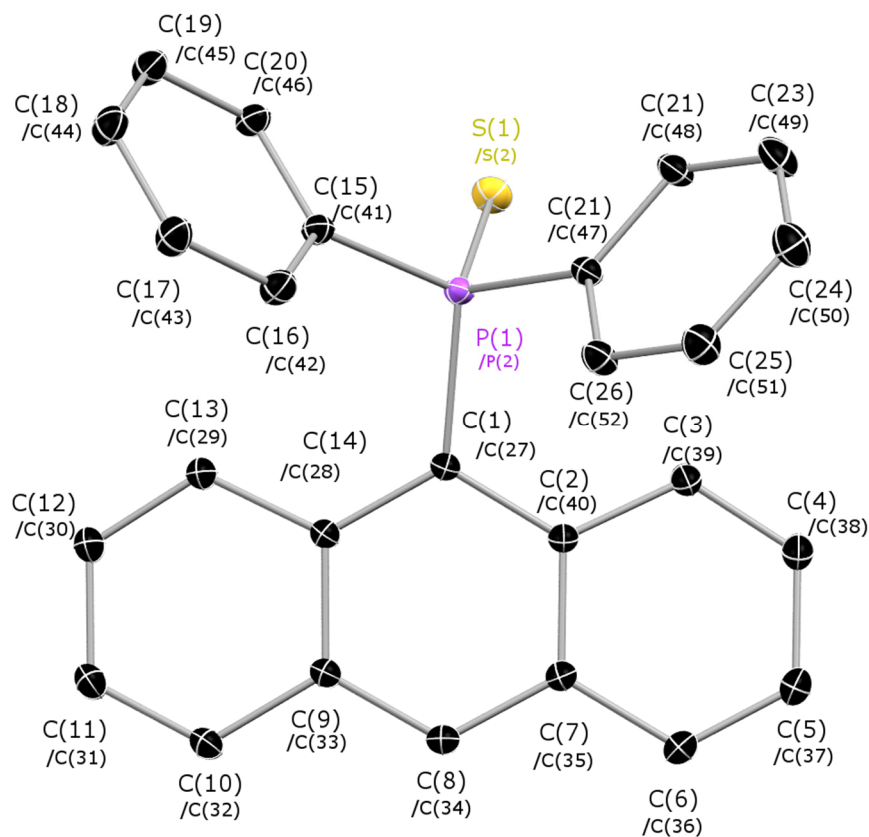


Figure S17: Molecular structure of SPAnH. Only one asymmetric unit is shown. H-Atoms are omitted for visual clarity. ADPs displayed at 50 % probability level.

10.7.1 Local coordinate systems, symmetry and chemical constraints

ATOM	ATOM0	AX1	ATOM1	ATOM2	AX2	R/L	TP	TBL	KAP	LMX	SITESYM	CHEMCON
S1	P1	Z	S1	C2	Y	R	4	1	1	4	_6	
P1	S1	Z	P1	C14	Y	R	4	2	2	4	_6	
C1	C2	X	C1	C3	Y	R	2	3	3	4	_mz	
C2	P1	Z	C2	C3	X	R	2	3	4	4	_mm2	
C3	C2	X	C3	C4	Y	R	2	3	3	4	_mz	C1
C4	C3	X	C4	C5	Y	R	2	3	5	4	_mz	
C5	C4	X	C5	C6	Y	R	3	3	6	4	_mz	

C6	C5	X	C6	C7	Y	R	3	3	6	4	_mz	C5
C7	C6	X	C7	C5	Y	R	2	3	5	4	_mm2	C4
C8	P1	Z	C8	C13	Y	R	2	3	7	4	_mz	
C9	C8	X	C9	C10	Y	R	3	3	8	4	_mz	
C10	DUM0	Z	C10	C11	X	R	3	3	9	4	_mm2	
C11	DUM1	Z	C11	C12	X	R	3	3	9	4	_mm2	C10
C12	DUM2	Z	C12	C13	X	R	3	3	9	4	_mm2	C10
C13	C8	X	C13	C12	Y	R	2	3	8	4	_mz	C9
C14	P1	Z	C14	C19	Y	R	2	3	7	4	_mm2	C8
C15	C14	X	C15	C16	Y	R	2	3	8	4	_mz	C9
C16	DUM3	Z	C16	C17	X	R	3	3	9	4	_mm2	C10
C17	DUM4	Z	C17	C18	X	R	3	3	9	4	_mm2	C10
C18	DUM5	Z	C18	C19	X	R	3	3	9	4	_mm2	C10
C19	C14	X	C19	C18	Y	R	2	3	8	4	_mz	C9
C20	C21	Z	C20	H20C	X	R	3	4	10	4	_3my	
C21	C20	X	C21	C26	Y	R	3	3	11	4	_mz	
C22	C21	X	C22	C23	Y	R	3	3	12	4	_mz	
C23	DUM6	Z	C23	C24	X	R	3	3	13	4	_mm2	
C24	DUM7	Z	C24	C25	X	R	3	3	13	4	_mm2	C23
C25	DUM8	Z	C25	C26	X	R	3	3	13	4	_mm2	C23
C26	C21	X	C26	C25	Y	R	3	3	12	4	_mz	C22
H4	C4	Z	H4	C3	Y	R	2	5	14	2	_6	
H5	C5	Z	H5	C4	Y	R	2	5	14	2	_6	H4
H6	C6	Z	H6	C5	Y	R	2	5	14	2	_6	H4
H7	C7	Z	H7	C6	Y	R	2	5	14	2	_6	H4
H9	C9	Z	H9	C8	Y	R	2	5	14	2	_6	H4
H10	C10	Z	H10	C9	Y	R	2	5	14	2	_6	H4

H11	C11	Z	H11	C10	Y	R	2	5	14	2	_6	H4
H12	C12	Z	H12	C11	Y	R	2	5	14	2	_6	H4
H13	C13	Z	H13	C8	Y	R	2	5	14	2	_6	H4
H15	C15	Z	H15	C14	Y	R	2	5	14	2	_6	H4
H16	C16	Z	H16	C15	Y	R	2	5	14	2	_6	H4
H17	C17	Z	H17	C16	Y	R	2	5	14	2	_6	H4
H18	C18	Z	H18	C17	Y	R	2	5	14	2	_6	H4
H19	C19	Z	H19	C14	Y	R	2	5	14	2	_6	H4
H20A	C20	Z	H20A	H20B	Y	R	2	5	15	2	_6	
H20B	C20	Z	H20B	H20A	Y	R	2	5	15	2	_6	H20A
H20C	C20	Z	H20C	H20A	Y	R	2	5	15	2	_6	H20A
H22	C22	Z	H22	C21	Y	R	2	5	14	2	_6	H4
H23	C23	Z	H23	C22	Y	R	2	5	14	2	_6	H4
H24	C24	Z	H24	C23	Y	R	2	5	14	2	_6	H4
H25	C25	Z	H25	C24	Y	R	2	5	14	2	_6	H4
H26	C26	Z	H26	C21	Y	R	2	5	14	2	_6	H4

10.7.2 Test for overfitting and final refinement strategies

Table S31: Final refinement strategy for SPAnH with isotropic hydrogen atoms. Starting values for multipole and κ - parameters were obtained from the INVARIOM database [91] using the software *InvariomTool*. The scale factor is refined in every step. Red denotes newly added parameters. Green denotes the final refinement step with fixed C-H bond distances. At the beginning of the refinement, only reflections with a significance of at least 3σ are taken into account (“sigobs 3”). This limitation is released in step 8. A test for overfitting was performed using a R_{cross} as validation tool.[78]. Abbreviations: M: monopoles; D: dipoles; Q: quadrupoles; O: octupoles; H: hexadecapoles, U: Uij, κ : kappa, U3/4 (atom name): Gram Charlier 3rd/4th order, nosymm: no local symmetry constraints, nocon: no chemical constraints, d/p : data to parameter ratio, d_1/p_m : ratio of low resolution data (up to 1 Å) to multipole parameter.

Step	Parameters	#param	#data	d/p	d_1/p_m	σ cut-off	$R(F^2)$
1	SCALE	1	37280	37280	None	3	0.0267
2	U	505	37280	73.82	None	3	0.0236
3	MDQOHUxyz κ	641	37280	58.16	50.96	3	0.0202
4	xyz(H)	115	4025	35	None	3	0.0191
5	MDQOHUxyz κ	641	37280	58.16	50.96	3	0.0191
6	κ'	12	37280	3106.67	None	3	0.0189
7	MDQOHUxyz κ	641	37280	58.16	50.96	3	0.0189
8	Sigobs 0	641	41640	64.96	52.16	0	0.0189
9	MDQOHUxyz κ					0	
	U3 (S2, P2)	721	41640	57.75	52.16		0.0166
10	MDQOHUxyz κ					0	
	U3, U4 (S2)	736	41640	56.58	52.16		0.0165
11	MDQOHUxyz κ					0	
	U3 (C5), U4	746	41640	55.82	52.16		0.0164
12	MDQOHUxyz κ					0	
	U3 (C43-46), U4	786	41640	52.98	52.16		0.0163
13	MDQOHUxyz κ					0	
	U3 (C24), U4	796	41640	52.31	52.16		0.0162
14	U3 (C12), U4	806	41640	51.66	52.16	0	0.0162

15	U_{ij} , XYZ, M, D, Q, O, H, κ , U3 (S2), U4	816	41640	51.03	52.16	0	0.0161
16	U_{ij} unconstrained	1044	41640	39.89	52.16	0	0.0149
17	H(xyz) without RESET	1158	41640	35.96	52.16	0	0.0149

Table S32: Subsequent release of constraints for tested for overfitting *via* cross-validation.^[78]

Step	Parameters	#param	#data	d/p	d_1/p_m	σ cut-off	$R(F^2)$
1–17	As before						
18	Nocon Anthracene	1476	41640	28.21	17.84	0	0.0146
19	Nosymm P	1476	41640	28.21	17.84	0	0.0146
20	Nosymm S	1514	41640	27.5	16.48	0	0.0145
21	Nosymm	1882	41640	22.13	9.1	0	0.0141
22	Nocon	3382	41640	12.31	3.45	0	0.0131

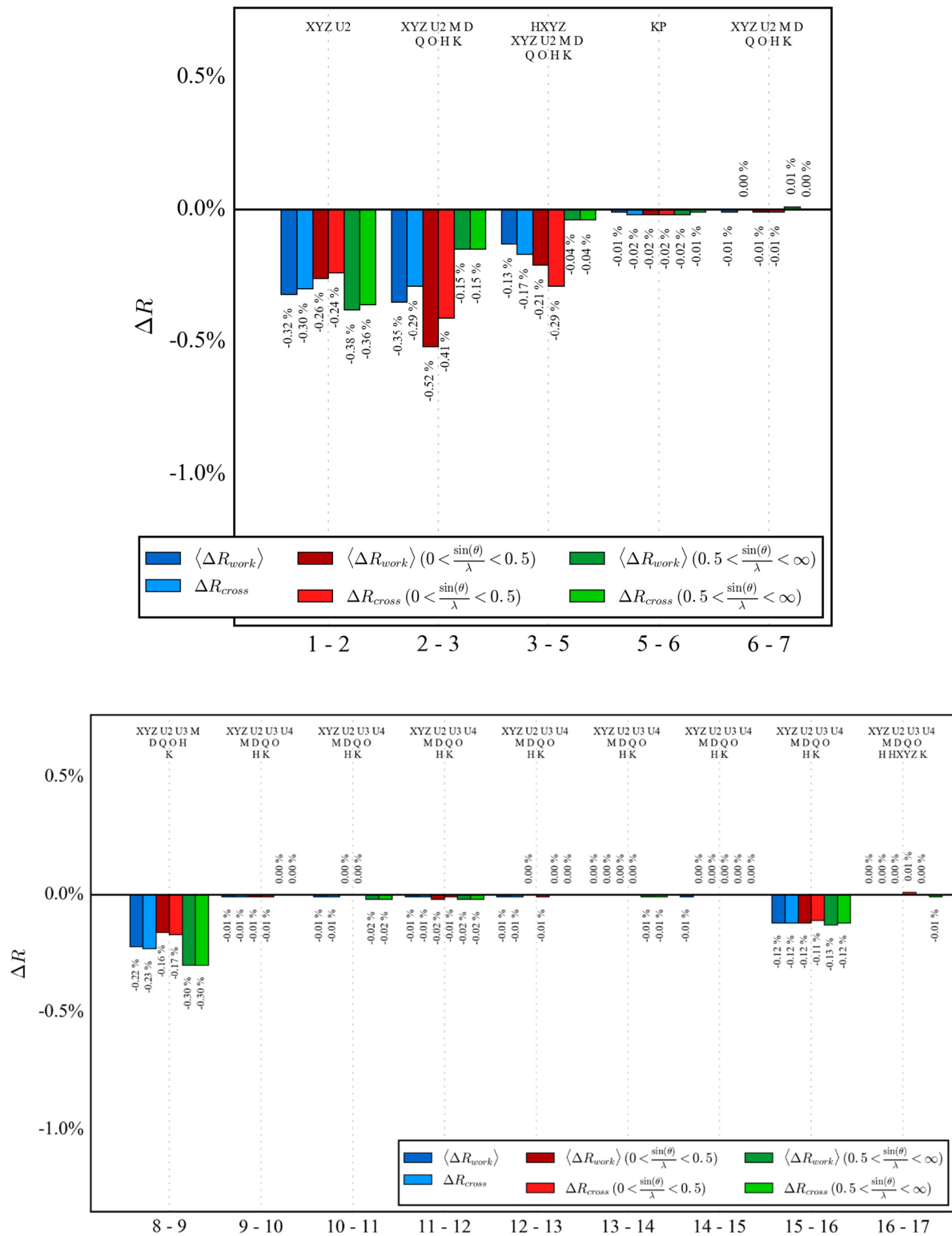


Figure S18: Cross-validation output plot for steps included in the final refinement of SPAnH. The generally joined improvement of both R_{work} and R_{cross} indicates that all introduced parameters are meaningful.

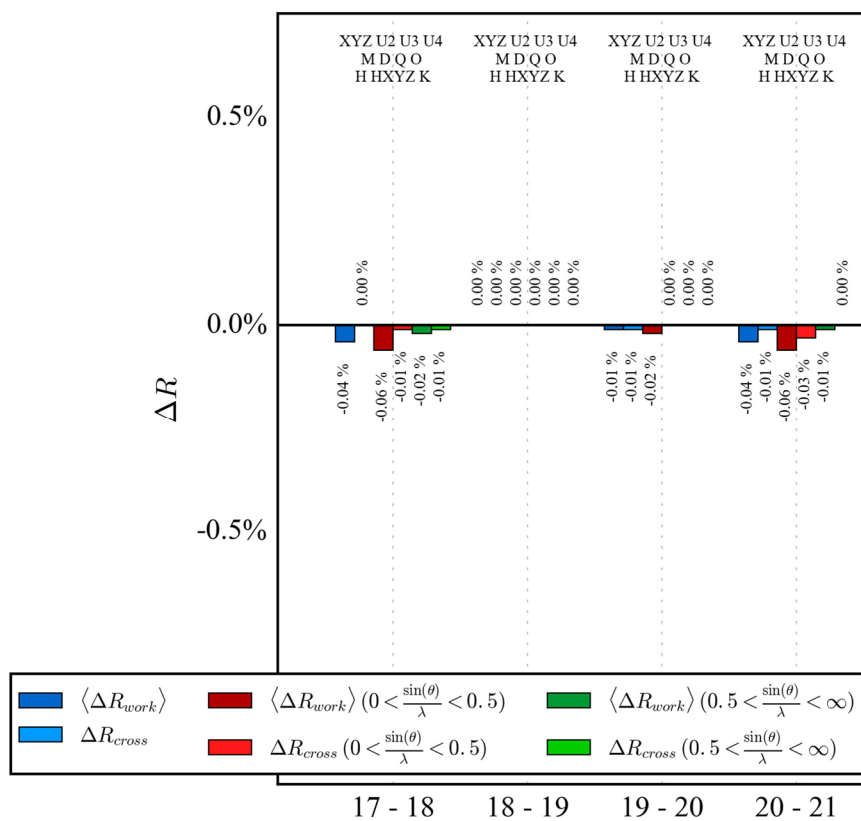


Figure S19 Cross-validation output plot for steps excluded from the final refinement of SPAnH. All steps include a worsening of the R_{cross} while R_{work} stays constant or improves. This is a sign of overfitting.

10.7.3 Residuals after final refinement step against X-ray data with fixed C-H distances

10.7.3.1 Neutron ADPs with Neutron Distances

$R(F)$	=	0.0139	$R_{\text{all}}(F)$	=	0.0155	$R_w(F)$	=	0.0113
$R(F^2)$	=	0.0148	$R_{\text{all}}(F^2)$	=	0.0152	$R_w(F^2)$	=	0.0217
GOF _w	=	1.5616	GOF	=	1.5616	N_{ref}/N_v	=	51.0294

10.7.3.2 SHADE

$R(F)$	=	0.0141	$R_{\text{all}}(F)$	=	0.0157	$R_w(F)$	=	0.0115
$R(F^2)$	=	0.0151	$R_{\text{all}}(F^2)$	=	0.0155	$R_w(F^2)$	=	0.0222
GOF _w	=	1.5918	GOF	=	1.5918	N_{ref}/N_v	=	51.0294

10.7.3.3 APD-Toolkit

$R(F)$	=	0.0140	$R_{\text{all}}(F)$	=	0.0156	$R_w(F)$	=	0.0114
$R(F^2)$	=	0.0149	$R_{\text{all}}(F^2)$	=	0.0153	$R_w(F^2)$	=	0.0218
GOF _w	=	1.5673	GOF	=	1.5673	N_{ref}/N_v	=	51.0294

10.7.3.4 Aniso without H-Q0

$R(F)$	=	0.0140	$R_{\text{all}}(F)$	=	0.0156	$R_w(F)$	=	0.0114
$R(F^2)$	=	0.0151	$R_{\text{all}}(F^2)$	=	0.0155	$R_w(F^2)$	=	0.0219
GOF _w	=	1.5747	GOF	=	1.5747	N_{ref}/N_v	=	39.9233

10.7.3.5 Aniso with H-Q0

$R(F)$	=	0.0138	$R_{\text{all}}(F)$	=	0.0154	$R_w(F)$	=	0.0112
$R(F^2)$	=	0.0145	$R_{\text{all}}(F^2)$	=	0.0149	$R_w(F^2)$	=	0.0214
GOF _w	=	1.5408	GOF	=	1.5408	N_{ref}/N_v	=	39.8851

10.7.4 List of evaluated BCPs between the toluene molecule and the anthracene moiety

The observed electron densities at the investigated intermolecular BCPs are rather small. The standard uncertainties of the BCPs and Laplacian are of the same order of magnitude as the values themselves and should therefore be treated careful regarding their validity.

Table S33: Properties of the BCP between H8 and X2_C30. X2_C30 is generated from the asymmetric unit by applying the symmetry operation $-X, 1-Y, 2-Z$ to the SPAnH molecule.

	ρ	$\nabla^2\rho(\mathbf{r})$	R_{ij}	$d1$	$d2$	<i>Hessian Eigenvalues</i>			ε
<i>Neutron Data</i>	0.05	0.45	2.7512	1.0816	1.6696	-0.16	-0.09	0.71	0.8
<i>Neutron Data (tab. distances)</i>	0.05	0.45	2.7512	1.0816	1.6696	-0.16	-0.09	0.71	0.8
<i>SHADE_H</i>	0.05	0.49	2.7535	1.0752	1.6783	-0.14	-0.08	0.7	0.87
<i>APD-H</i>	0.05	0.467	2.7575	1.0838	1.6737	-0.15	-0.08	0.7	0.83
<i>Aniso-H</i>	0.05	0.46	2.7565	1.0801	1.6763	-0.15	-0.08	0.69	0.84
<i>Aniso-H (no Q0)</i>	0.03	0.51	2.8938	1.0918	1.802	-0.07	-0.02	0.6	2.13

Table S34: Properties of the BCP between H10 and X2_C28. X2_C28 is generated from the asymmetric unit by applying the symmetry operation $-X, 1-Y, 2-Z$ to the SPAnH molecule. The BCP given for Aniso-H (no Q0) was found between H10 and X2_C27 instead. The BCP given for Aniso-H (no Q0) was found between H10 and X2_C40 instead. Both of these atoms are generated from the aforementioned symmetry operation.

	ρ	$\nabla^2\rho(\mathbf{r})$	R_{ij}	$d1$	$d2$	<i>Hessian Eigenvalues</i>			ε
<i>Neutron Data</i>	0.07	0.59	2.7146	1.0316	1.683	-0.2	-0.08	0.86	1.57
<i>Neutron Data (tab. distances)</i>	0.07	0.585	2.7146	1.0316	1.683	-0.2	-0.08	0.86	1.57
<i>SHADE_H</i>	0.06	0.63	2.7122	1.0232	1.689	-0.17	-0.06	0.86	2.1
<i>APD-H</i>	0.07	0.61	2.7148	1.0286	1.6862	-0.19	-0.07	0.86	1.75
<i>Aniso-H</i>	0.07	0.60	2.7067	1.0247	1.682	-0.19	-0.07	0.85	1.71
<i>Aniso-H (no Q0)</i>	0.051	0.633	2.7452	1.1086	1.6365	-0.1	-0.05	0.79	0.91

10.7.5 Calculated interaction energies

For “Neutron Data (tab. distances)”, calculations were performed based on a refined with ADPs from Neutron results and C-H bond distances fixed to values provided by the INVARIOM database (1.08225 Å).

Table S35: Interaction energies between H8 / H10 and the neighbouring anthracene moiety. The given energies are calculated between the H-Atom and the centre of the anthracene moiety. All energies given in kJ/mol.

	E_{ES}	E_{ex-rep}	E_{disp}	E_{tot}	E_{ES}	E_{ex-rep}	E_{disp}	E_{tot}
Neutron Data	-9.3	15.5	-5.6	0.5	-11.4	25.9	-8.4	6.1
Neutron Data (tab. distances)	-9.3	15.5	-5.6	0.5	-11.4	25.9	-8.4	6.1
SHADE	-8.2	15.1	-5.5	1.4	-10.3	25.9	-8.5	7.2
APD	-8.6	15.1	9.6	0.9	-10.7	25.9	-8.5	6.7
Aniso-H	-8.8	15.1	-5.5	0.7	-11.0	25.9	-8.5	6.4
Aniso-H (no Q0)	-5.3	15.1	-5.5	4.3	-6.1	25.9	-8.5	11.4

10.8 Additional details about the structure Refinement of SPAnPS

Information presented here is mostly based on work on my master thesis and is also available in the supporting information of my original publication of this project.^[51] As such, only a slightly shortened list of the full supplementary material will be listed here.

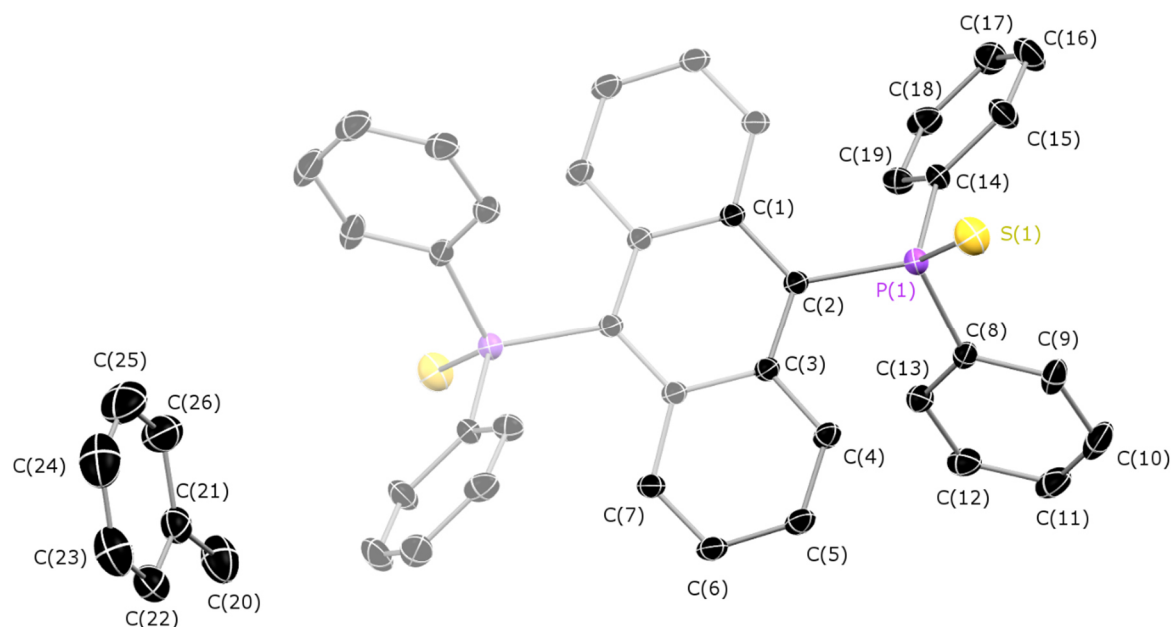


Figure S20: Molecular structure of SPAnPS. Hydrogen atoms are omitted for visual clarity. ADPs are shown at 50 % probability level

10.8.1 Local coordinate systems, symmetry and chemical constraints

ATOM	ATOM0	AX1	ATOM1	ATOM2	AX2	R/L	TP	TBL	KAP	LMX	SITESYM	CHEMCON
S(1)	P(1)	Z	S(1)	C(2)	Y	R	4	1	1	4	_6	
P(1)	S(1)	Z	P(1)	C(14)	Y	R	4	2	2	4	_6	
C(1)	C(2)	X	C(1)	C(3)	Y	R	2	3	3	4	_mz	
C(2)	P(1)	Z	C(2)	C(3)	X	R	2	3	4	4	_mm2	
C(3)	C(2)	X	C(3)	C(4)	Y	R	2	3	3	4	_mz	C(1)
C(4)	C(3)	X	C(4)	C(5)	Y	R	2	3	5	4	_mz	
C(5)	C(4)	X	C(5)	C(6)	Y	R	3	3	6	4	_mz	
C(6)	C(5)	X	C(6)	C(7)	Y	R	3	3	6	4	_mz	C(5)
C(7)	C(6)	X	C(7)	C(5)	Y	R	2	3	5	4	_mm2	C(4)

C(8)	P(1)	Z	C(8)	C(13)	Y	R	2	3	7	4	_mz	
C(9)	C(8)	X	C(9)	C(10)	Y	R	3	3	8	4	_mz	
C(10)	DUM0	Z	C(10)	C(11)	X	R	3	3	9	4	_mm2	
C(11)	DUM1	Z	C(11)	C(12)	X	R	3	3	9	4	_mm2	C(10)
C(12)	DUM2	Z	C(12)	C(13)	X	R	3	3	9	4	_mm2	C(10)
C(13)	C(8)	X	C(13)	C(12)	Y	R	2	3	8	4	_mz	C(9)
C(14)	P(1)	Z	C(14)	C(19)	Y	R	2	3	7	4	_mm2	C(8)
C(15)	C(14)	X	C(15)	C(16)	Y	R	2	3	8	4	_mz	C(9)
C(16)	DUM3	Z	C(16)	C(17)	X	R	3	3	9	4	_mm2	C(10)
C(17)	DUM4	Z	C(17)	C(18)	X	R	3	3	9	4	_mm2	C(10)
C(18)	DUM5	Z	C(18)	C(19)	X	R	3	3	9	4	_mm2	C(10)
C(19)	C(14)	X	C(19)	C(18)	Y	R	2	3	8	4	_mz	C(9)
C(20)	C(21)	Z	C(20)	H(20C)	X	R	3	4	10	4	_3my	
C(21)	C(20)	X	C(21)	C(26)	Y	R	3	3	11	4	_mz	
C(22)	C(21)	X	C(22)	C(23)	Y	R	3	3	12	4	_mz	
C(23)	DUM6	Z	C(23)	C(24)	X	R	3	3	13	4	_mm2	
C(24)	DUM7	Z	C(24)	C(25)	X	R	3	3	13	4	_mm2	C(23)
C(25)	DUM8	Z	C(25)	C(26)	X	R	3	3	13	4	_mm2	C(23)
C(26)	C(21)	X	C(26)	C(25)	Y	R	3	3	12	4	_mz	C(22)
H(4)	C(4)	Z	H(4)	C(3)	Y	R	2	5	14	2	_6	
H(5)	C(5)	Z	H(5)	C(4)	Y	R	2	5	14	2	_6	H(4)
H(6)	C(6)	Z	H(6)	C(5)	Y	R	2	5	14	2	_6	H(4)
H(7)	C(7)	Z	H(7)	C(6)	Y	R	2	5	14	2	_6	H(4)
H(9)	C(9)	Z	H(9)	C(8)	Y	R	2	5	14	2	_6	H(4)
H(10)	C(10)	Z	H(10)	C(9)	Y	R	2	5	14	2	_6	H(4)
H(11)	C(11)	Z	H(11)	C(10)	Y	R	2	5	14	2	_6	H(4)
H(12)	C(12)	Z	H(12)	C(11)	Y	R	2	5	14	2	_6	H(4)
H(13)	C(13)	Z	H(13)	C(8)	Y	R	2	5	14	2	_6	H(4)
H(15)	C(15)	Z	H(15)	C(14)	Y	R	2	5	14	2	_6	H(4)
H(16)	C(16)	Z	H(16)	C(15)	Y	R	2	5	14	2	_6	H(4)

H(17)	C(17)	Z	H(17)	C(16)	Y	R	2	5	14	2	_6	H(4)
H(18)	C(18)	Z	H(18)	C(17)	Y	R	2	5	14	2	_6	H(4)
H(19)	C(19)	Z	H(19)	C(14)	Y	R	2	5	14	2	_6	H(4)
H(20A)	C(20)	Z	H(20A)	H(20B)	Y	R	2	5	15	2	_6	
H(20B)	C(20)	Z	H(20B)	H(20A)	Y	R	2	5	15	2	_6	H(20A)
H(20C)	C(20)	Z	H(20C)	H(20A)	Y	R	2	5	15	2	_6	H(20A)
H(22)	C(22)	Z	H(22)	C(21)	Y	R	2	5	14	2	_6	H(4)
H(23)	C(23)	Z	H(23)	C(22)	Y	R	2	5	14	2	_6	H(4)
H(24)	C(24)	Z	H(24)	C(23)	Y	R	2	5	14	2	_6	H(4)
H(25)	C(25)	Z	H(25)	C(24)	Y	R	2	5	14	2	_6	H(4)
H(26)	C(26)	Z	H(26)	C(21)	Y	R	2	5	14	2	_6	H(4)

10.8.2 Test for overfitting and final refinement strategies

Table S36: Final refinement strategy for SPAnPS with isotropic hydrogen atoms. Starting values for multipole and κ - parameters were obtained from the INVARIOM database^[91] using the software *InvariomTool*.^[150] The ten scale factors are refined in every step. Red denotes newly added parameters. Green denotes the final refinement step with fixed C-H bond distances. Abbreviations: d/p: data-to parameter ratio; d_1/p_m : Ratio of low-res data to multipole parameters; SCALE: overall scale factor; M: monopoles; D: dipoles; Q: quadrupoles; O: octupoles; H: hexadecapoles; U: U_{ij} ; xyz(H): free refinement of hydrogen atom positions against the inner data; U3: third-order Gram-Charlier coefficients for anharmonic motion. Until “Sigobs 0”, reflections below 3σ are excluded from the refinement.

Step	Parameters	#param	#data	d/p	d_1/p_m	$R(F^2)$
1	SCALE	10	16587	1658.7	None	0.0342
2	U	178	16587	93.19	None	0.0327
3	U _{xyz}	262	16587	63.31	None	0.0282
4	MDQOHU _{xyz}	414	16587	40.07	25.06	0.022
5	MDQOHU _{xyz} κ	427	16587	38.85	21.63	0.0211
6	xyz(H)	76	2146	28.24	None	0.0205
7	MDQOHU _{xyz} κ	427	16587	38.85	21.63	0.0205
8	κ'	23	16587	721.17	None	0.0204
9	MDQOHU _{xyz} κ	427	16587	38.85	21.63	0.0202

10	Sigobs 0 MDQOHU _{xyzκ}	427	22130	51.83	22.59	0.0202
11	U3 (S1, P1, C9–12, C20–21, C24–26) MDQOHU _{xyzκ}	537	22130	41.21	22.59	0.0179
12	U3 (C5–6, C22–23, C16–18) MDQOHU _{xyzκ}	607	22130	36.46	22.59	0.0173
13	U3, U4 (S1, P1) MDQOHU _{xyzκ}	622	22130	35.58	22.59	0.0172
14	κ'	23	22130	962.17	None	0.0171
15	MDQOHU _{xyzκ} , U3, U4	637	22130	34.74	22.59	0.0169
16	H-Uij unconstrained	769	22130	28.78	22.59	0.0148
17	Nocon Anthracene	814	22130	27.19	18.5	0.0147
18	H(xyz) without RESET	880	22130	25.15	18.5	0.0142

Table S37: Subsequent release of constraints for tested for overfitting *via* cross-validation.^[78]

Step	Parameters	#param	#data	d/p	d_1/p_m	σ cut-off	$R(F^2)$
1–18	As before						
19	Nosymm P	111	2146	24.7	17.31	0	0.0142
20	Nosymm S	121	2146	24.16	16.01	0	0.0141
21	Nosymm	215	2146	20.17	9.41	0	0.0135
22	Nocon	439	2146	14.32	4.75	0	0.0122

Nocon = release of all chemical constraints for respective atoms. Nosymm: Refinement of all multipole parameters for respective atoms.

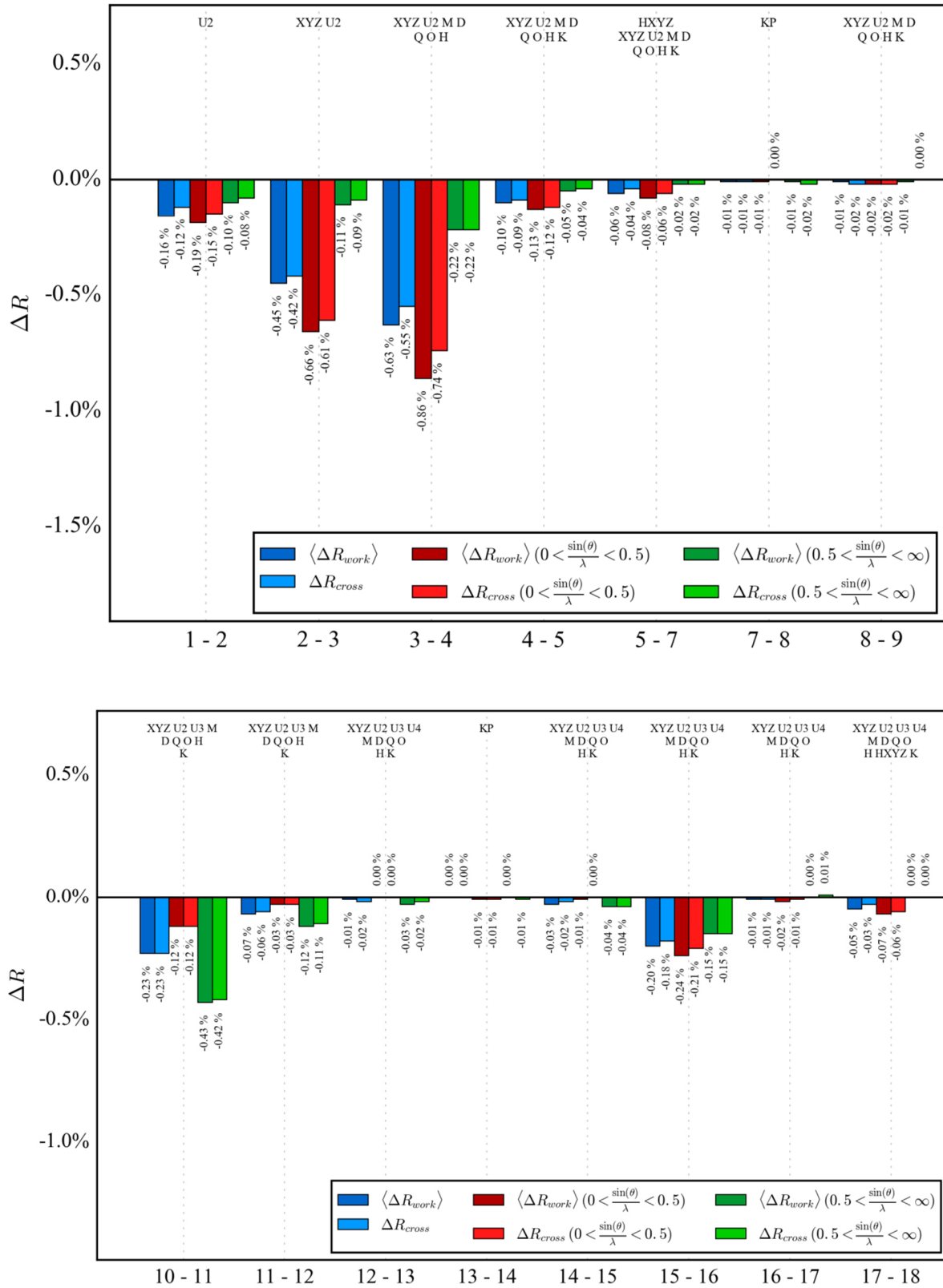


Figure S21: R_{cross} -validation of experimental data.

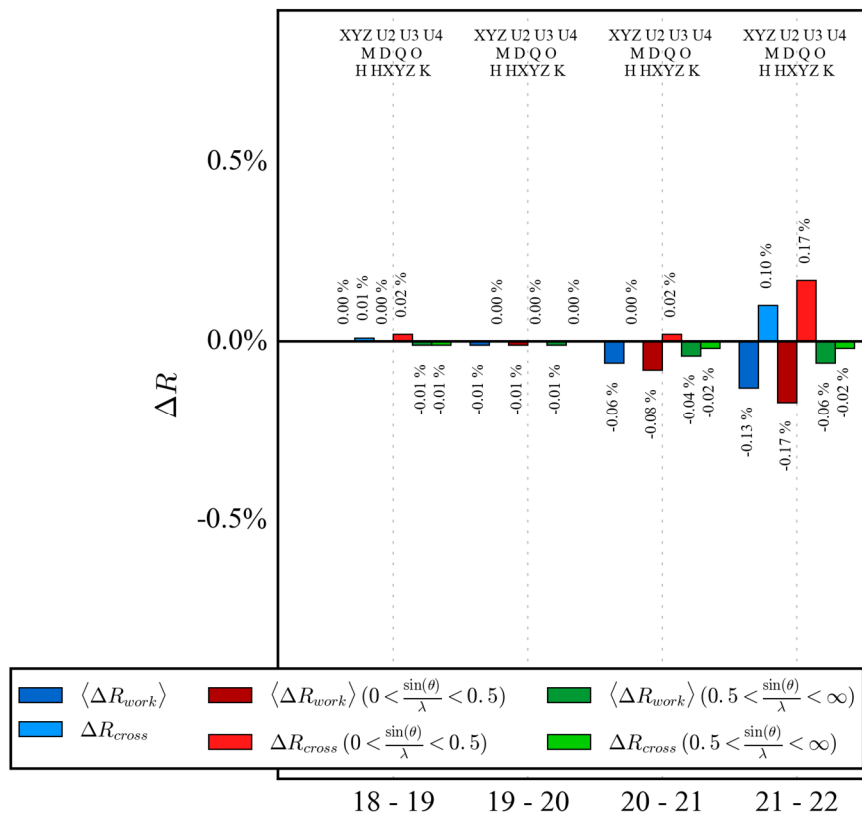


Figure S22: R_{cross} -validation of experimental data, continued.

10.8.3 Residuals after final refinement step against X-ray data with fixed C-H distances**10.8.3.1 Neutron ADPs with Neutron Distances**

$R(F)$	=	0.0258	$R_{\text{all}}(F)$	=	0.0258	$R_w(F)$	=	0.0095
$R(F^2)$	=	0.0155	$R_{\text{all}}(F^2)$	=	0.0155	$R_w(F^2)$	=	0.0184
GOF _w	=	1.2871	GOF	=	1.2871	N_{ref}/N_v	=	32.4487

10.8.3.2 SHADE

$R(F)$	=	0.0263	$R_{\text{all}}(F)$	=	0.0263	$R_w(F)$	=	0.0099
$R(F^2)$	=	0.0164	$R_{\text{all}}(F^2)$	=	0.0164	$R_w(F^2)$	=	0.0193
GOF _w	=	1.3501	GOF	=	1.3501	N_{ref}/N_v	=	32.4487

10.8.3.3 APD-Toolkit

$R(F)$	=	0.0261	$R_{\text{all}}(F)$	=	0.0261	$R_w(F)$	=	0.0097
$R(F^2)$	=	0.0161	$R_{\text{all}}(F^2)$	=	0.0161	$R_w(F^2)$	=	0.0189
GOF _w	=	1.3212	GOF	=	1.3212	N_{ref}/N_v	=	32.4487

10.8.3.4 Aniso without H-Q0

$R(F)$	=	0.0254	$R_{\text{all}}(F)$	=	0.0254	$R_w(F)$	=	0.0090
$R(F^2)$	=	0.0147	$R_{\text{all}}(F^2)$	=	0.0147	$R_w(F^2)$	=	0.0174
GOF _w	=	1.2231	GOF	=	1.2231	N_{ref}/N_v	=	27.2537

10.8.3.5 Aniso with H-Q0

$R(F)$	=	0.0254	$R_{\text{all}}(F)$	=	0.0254	$R_w(F)$	=	0.0090
$R(F^2)$	=	0.0146	$R_{\text{all}}(F^2)$	=	0.0146	$R_w(F^2)$	=	0.0174
GOF _w	=	1.2229	GOF	=	1.2229	N_{ref}/N_v	=	27.1867

10.8.4 List of evaluated BCPs between the toluene molecule and the anthracene moiety

Table S38: Properties at the BCP between X4_H22 and X3_C3 of SPAnPS. X4_H22 is generated from the asymmetric unit by applying the symmetry operation $1/2 + X, 1/2 - Y, 1/2 + Z$ to the toluene molecule. X3_C3 is generated from the asymmetric unit by applying the symmetry operation $-X+1, -Y+1, -Z+2$ to the half of the SPAnPS-molecule present in it.

	ρ	$\nabla^2\rho(\mathbf{r})$	R_{ij}	$d1$	$d2$	Hessian Eigenvalues			ϵ
<i>Neut</i>	0.05	0.39	2.8679	1.1199	1.748	-0.14	-0.08	0.62	0.76
<i>Neutron Data (tab. distances)</i>	0.05	0.393	2.8679	1.1199	1.748	-0.14	-0.08	0.62	0.76
<i>SHADE_H</i>	0.04	0.44	2.8562	1.0911	1.7651	-0.11	-0.06	0.61	0.95
<i>APD-H</i>	0.05	0.43	2.8635	1.1038	1.7597	-0.12	-0.06	0.62	0.89
<i>Aniso-H</i>	0.05	0.41	2.8642	1.1148	1.7493	-0.14	-0.07	0.62	0.85
<i>Aniso-H (no Q0)</i>	0.05	0.42	2.863	1.1095	1.7535	-0.13	-0.07	0.62	0.88

Table S39: Properties at the BCP between H12 and X4_C24 of SPAnPS. X4_C24 is generated from the asymmetric unit by applying the symmetry operation $1/2 + X, 1/2 - Y, 1/2 + Z$ to the toluene molecule.

	ρ	$\nabla^2\rho(\mathbf{r})$	R_{ij}	$d1$	$d2$	Hessian Eigenvalues			ϵ
<i>Neutron Data</i>	0.02	0.23	3.1793	1.2765	1.9028	-0.05	-0.03	0.31	1.04
<i>Neutron Data (tab. distances)</i>	0.02	0.23	3.1793	1.2765	1.9028	-0.05	-0.03	0.31	1.04
<i>SHADE_H</i>	0.02	0.26	3.2171	1.2914	1.9257	-0.05	-0.01	0.32	2.65
<i>APD-H</i>	0.02	0.26	3.242	1.2854	1.9566	-0.05	-0.01	0.33	2.91
<i>Aniso-H</i>	0.02	0.25	3.1861	1.2758	1.9103	-0.05	-0.02	0.32	1.32
<i>Aniso-H (no Q0)</i>	0.02	0.25	3.197	1.2763	1.9207	-0.05	-0.02	0.33	1.56

Table S40: Properties at the BCP between H13 and X4_C22 of SPAnPS. X4_C22 is generated from the asymmetric unit by applying the symmetry operation $1/2 + X, 1/2 - Y, 1/2 + Z$ to the toluene molecule.

	ρ	$\nabla^2 \rho(\mathbf{r})$	R_{ij}	$d1$	$d2$	<i>Hessian Eigenvalues</i>			ε
<i>Neutron Data</i>	0.05	0.43	2.805	1.1052	1.6998	-0.15	-0.07	0.65	1.13
<i>Neutron Data</i> <i>(tab. distances)</i>	0.05	0.43	2.805	1.1052	1.6998	-0.15	-0.07	0.65	1.13
<i>SHADE_H</i>	0.05	0.51	2.8429	1.1016	1.7414	-0.11	-0.02	0.64	4.01
<i>APD-H</i>	0.05	0.48	2.8312	1.0902	1.741	-0.14	-0.05	0.67	1.52
<i>Aniso-H</i>	0.05	0.46	2.8186	1.1117	1.7069	-0.14	-0.05	0.66	1.6
<i>Aniso-H (no Q0)</i>	0.05	0.48	2.8275	1.1075	1.72	-0.14	-0.05	0.66	1.8

10.8.5 Calculated interaction energies

Table S41: Top: Interaction energies between H12 / H13 and the toluene molecule located over the anthracene moiety in the SPAnPS. Bottom: Properties at the intermolecular BCP between H8 - C30 as well as interaction energies between H22 and the anthracene moiety. All energies given in kJ/mol. Due to theoretical limitations, only the electrostatic term of the interaction energy is to be determined reasonably.^[145]

	H(12) ...toluene				H(13) ...toluene			
	E_{ES}	E_{ex-rep}	E_{disp}	E_{tot}	E_{ES}	E_{ex-rep}	E_{disp}	E_{tot}
Neutron Data	-3.3	0.9	-1.6	-2.4	-4.6	10.0	-3.7	1.7
Neutron Data (tab. distances)	-3.6	0.9	-1.6	-2.6	-5.5	6.2	-3.7	0.7
SHADE	-2.0	2.5	-1.6	-1.1	-2.9	9.8	-3.7	3.2
APD	-2.7	2.5	-1.6	-1.8	-3.7	9.9	-3.7	2.4
Aniso-H	-3.5	2.5	-1.6	-2.6	-5.5	9.8	-3.7	0.6
Aniso-H (no Q0)	-3.4	2.5	-1.6	-2.5	-5.3	9.8	-3.7	0.8

	H(22) ...anthracene			
	E_{ES}	E_{ex-rep}	E_{disp}	E_{tot}
Neutron Data	-7.2	11.3	-4.8	-0.8
Neutron Data (tab. distances)	-7.0	11.3	-4.8	-0.5
SHADE	-4.8	11.3	-4.8	1.7
APD	-5.4	11.2	-4.8	0.9
Aniso	-6.4	11.2	-4.8	0.0
Aniso-H (no Q0)	-6.1	11.2	-4.8	0.4

11 References

- [1] a) B. Cornils, W. A. Herrmann, M. Muhler, C.-H. Wong (Eds.) *Catalysis from A to Z. A Concise Encyclopedia*, Wiley-VCH, Weinheim, **2007**; b) B. Cornils, W. A. Herrmann, M. Beller, R. Paciello (Eds.) *Applied homogeneous catalysis with organometallic compounds. A comprehensive handbook in four volumes*, Wiley-VCH Verlag GmbH & Co. KGaA, Weinheim, **2018**]-.
- [2] D. Steinborn, *Fundamentals of organometallic catalysis*, Wiley-VCH, Weinheim, **2012**.
- [3] J. Kretsch, I. Koehne, M. Lökov, I. Leito, D. Stalke, *Eur. J. Inorg. Chem.* **2019**, 2019, 3258.
- [4] D. J. Mindiola, *Angew. Chem. Int. Ed.* **2009**, 48, 6198.
- [5] a) C. Camp, J. Arnold, *Dalton Trans.* **2016**, 45, 14462; b) D. C. H. Do, A. Keyser, A. V. Protchenko, B. Maitland, I. Pernik, H. Niu, E. L. Kolychev, A. Rit, D. Vidovic, A. Stasch et al., *Chem. Eur. J.* **2017**, 23, 5830.
- [6] D.-R. Dauer, D. Stalke, *Dalton Trans.* **2014**, 43, 14432.
- [7] D.-R. Dauer, M. Flügge, R. Herbst-Irmer, D. Stalke, *Dalton Trans.* **2016**, 45, 6149.
- [8] T. Kottke, D. Stalke, *Chem. Ber.* **1997**, 130, 1365.
- [9] H. Gornitzka, D. Stalke, *Eur. J. Inorg. Chem.* **1998**, 3, 311.
- [10] I. Koehne, S. Bachmann, R. Herbst-Irmer, D. Stalke, *Angew. Chem. Int. Ed.* **2017**, 56, 15141.
- [11] Nico Graw, *Dissertation*, Georg-August-Universität, Göttingen, **2022**.
- [12] a) I. Koehne, S. Bachmann, T. Niklas, R. Herbst-Irmer, D. Stalke, *Chem. Eur. J.* **2017**, 23, 13141-13149; b) J. Kretsch, A.-K. Kreyenschmidt, T. Schillmöller, M. Lökov, R. Herbst-Irmer, I. Leito, D. Stalke, *Chem. Eur. J.* **2021**, 27, 9858.
- [13] J. García-Álvarez, E. Hevia, V. Capriati, *Chem. Eur. J.* **2018**, 24, 14854.
- [14] J. Kretsch, A. Kreyenschmidt, T. Schillmöller, C. Sindlinger, R. Herbst-Irmer, D. Stalke, *Inorg. Chem.* **2021**, 60, 7389.
- [15] J. Kretsch, R. Herbst-Irmer, D. Stalke, *Z. Anorg. Allg. Chem.* **2018**, 644, 657.
- [16] J. Kretsch, A. Kreyenschmidt, T. Schillmöller, R. Herbst-Irmer, D. Stalke, *Inorg. Chem.* **2020**, 59, 13690.
- [17] a) F. Schüth, B. Bogdanović, M. Felderhoff, *Chem. Commun.* **2004**, 2249; b) J. Graetz, *Chem. Soc. Rev.* **2009**, 38, 73.
- [18] Z. Yang, M. Zhong, X. Ma, S. De, C. Anusha, P. Parameswaran, H. W. Roesky, *Angew. Chem. Int. Ed.* **2015**, 54, 10225.
- [19] Z. Yang, M. Zhong, X. Ma, K. Nijesh, S. De, P. Parameswaran, H. W. Roesky, *J. Am. Chem. Soc.* **2016**, 138, 2548.
- [20] C. M. Legendre, D. Lüert, R. Herbst-Irmer, D. Stalke, *Dalton Trans* **2021**, 50, 16810.
- [21] D. Lüert, A.-K. Kreyenschmidt, C. M. Legendre, R. Herbst-Irmer, D. Stalke, *Inorg. Chem.* **2022**, 61, 5234.
- [22] I. Koehne, N. Graw, T. Teuteberg, R. Herbst-Irmer, D. Stalke, *Inorg. Chem.* **2017**, 56, 14968.

- [23] a) W. Friedrich, P. Knipping, M. v. Laue, *Interferenz-Erscheinungen bei Röntgenstrahlen, von W. Friedrich, P. Knipping und M. Laue*, Verlag der Königlich-Bayerischen Akademie der Wissenschaften, München, **1912**; b) W. Friedrich, P. Knipping, M. Laue, *Ann. Phys. Chem.* **1913**, 346, 971; c) M. v. Laue in *Nobel Lectures, Physics*, **1914**.
- [24] N. K. Hansen, P. Coppens, *Acta Cryst.* **1978**, A34, 909.
- [25] R. F. W. Bader, *Atoms in Molecules. A Quantum Theory*, Clarendon Press, Oxford, New York, **1990**.
- [26] a) D. Stalke, *Chem. Eur. J.* **2011**, 17, 9264; b) D. Mingos, P. Michael (Eds.) *Structure and Bonding, Vol. 146*, Springer, Berlin, New York, **2016**.
- [27] U. Flierler, D. Stalke, *Struct. Bond.* **2012**, 146, 1.
- [28] C. Gatti in *147, Vol. 147* (Ed.: D. Stalke), Springer Berlin Heidelberg, **2012**.
- [29] J. Hey, D. Leusser, D. Kratzert, H. Fliegl, R. A. Mata, J. M. Dieterich, D. Stalke, *Phys. Chem. Chem. Phys.* **2013**.
- [30] A. Holladay, P. Leung, P. Coppens, *Acta Cryst.* **1983**, A39, 377.
- [31] M. Craven, M. H. Nygaard, J. M. Zadrozny, J. R. Long, J. Overgaard, *Inorg. Chem.* **2018**, 57, 6913.
- [32] E. Damgaard-Møller, L. Krause, K. Tolborg, G. Macetti, A. Genoni, J. Overgaard, *Angew. Chem. Int. Ed.* **2020**, 21203.
- [33] C. Köhler, *Master thesis*, Georg-August-Universität, Göttingen, **2017**.
- [34] D. Schwarzenbach, *Crystallography*, Wiley, Chichester, **1996**.
- [35] W. Massa, *Kristallstrukturbestimmung*, Springer Spektrum, Wiesbaden, **2015**.
- [36] W. Borchardt-Ott, *Kristallographie*, Springer, Berlin, **2002**.
- [37] W. H. Bragg, W. L. Bragg, *Proc. R. Soc. Lond. A* **1913**, 88, 428.
- [38] Bruker AXS Inc., *SAINTE v8.40B*, Madison (WI), USA, **2019**.
- [39] G. M. Sheldrick, *SADABS 2016/2*, Göttingen, **2016**.
- [40] *SADABS User Manual (Area Detector Absorption and Other Corrections) Version 2.03*, Bruker AXS GmbH, Germany, Karlsruhe.
- [41] P. Macchi, H.-B. Bürgi, A. S. Chimpri, J. Hauser, Z. Gal, *J. Appl. Cryst.* **2011**, 44, 763.
- [42] L. Krause, R. Herbst-Irmer, D. Stalke, *J. Appl. Cryst.* **2015**, 48, 1907.
- [43] a) D. W. Bennett, *Understanding Single-Crystal X-Ray Crystallography*, John Wiley & Sons, **2010**;
b) G. M. Sheldrick, *Acta Cryst.* **2014**, A70, C1437; c) A. L. Patterson, *Phys. Rev.* **1934**, 46, 372; d) D. Sayre, *Acta Cryst.* **1953**, A6, 430.
- [44] G. M. Sheldrick, *Acta Cryst.* **2015**, A71, 3.
- [45] L. Midgley, L. J. Bourhis, O. Dolomanov, N. Peyerimhoff, H. Puschmann, *Crystallographic Refinement using Non-Spherical Form Factors in olex2.refine*, **2019**.
- [46] a) M. S. Weiss, *J. Appl. Cryst.* **2001**, 34, 130; b) M. S. Weiss, R. Hilgenfeld, *J. Appl. Cryst.* **1997**, 30, 203; c) K. Diederichs, P. A. Karplus, *Nat. Struct. Biol.* **1997**, 4, 269275.
- [47] G. M. Sheldrick, *XPREF*, Göttingen, **2015**.

- [48] A. Volkov, P. Macchi, L. J. Farrugia, C. Gatti, P. R. Mallinson, T. Richter, T. Koritsanszky, *XD2016- Manual. A Computer Program Package for Multipole Refinement, Topological Analysis of Charge Densities and Evaluation of Intermolecular Energies from Experimental and Theoretical Structure Factors*, **2016**.
- [49] P. Müller, R. Herbst-Irmer, A. L. Spek, T. R. Schneider, M. R. Sawaya, *Crystal structure refinement - A crystallographer's guide to SHELXL*, Oxford University Press, Oxford, **2006**.
- [50] K. Meindl, J. Henn, *Acta Cryst.* **2008**, *A64*, 404.
- [51] C. Köhler, J. Lübben, L. Krause, C. Hoffmann, R. Herbst-Irmer, D. Stalke, *Acta Cryst.* **2019**, *B75*, 434.
- [52] I. N. Bronstein, K. A. Semendjajew, G. Musiol, H. Mühlig, *Taschenbuch der Mathematik*, Harri Deutsch, Frankfurt am Main, **1993**.
- [53] A. Stash, *DRKplot*, Moscow, **2007**.
- [54] V. V. Zhurov, E. A. Zhurova, A. A. Pinkerton, *J. Appl. Cryst.* **2008**, *41*, 340.
- [55] S. C. Abrahams, E. T. Keve, *Acta Cryst.* **1971**, *A27*, 157.
- [56] D. Kratzert, J. J. Holstein, I. Krossing, *J. Appl. Cryst.* **2015**, *48*, 933.
- [57] D. Kratzert, I. Krossing, *J. Appl. Cryst.* **2018**, *51*, 928.
- [58] S. C. Capelli, H.-B. Bürgi, B. Dittrich, S. Grabowsky, D. Jayatilaka, *IUCrJ* **2014**, *1*, 361.
- [59] F. L. Hirshfeld, *Theoret. Chim. Acta* **1977**, *44*, 129.
- [60] M. Wońska, S. Grabowsky, P. M. Dominiak, K. Woźniak, D. Jayatilaka, *Science Advances* **2016**, *2*, e1600192.
- [61] M. Wońska, M. L. Chodkiewicz, K. Woźniak, *Chem. Commun.* **2021**, *57*, 3652.
- [62] M. Fugel, D. Jayatilaka, E. Hupf, J. Overgaard, V. R. Hathwar, P. Macchi, M. J. Turner, J. A. K. Howard, O. V. Dolomanov, H. Puschmann et al., *IUCrJ* **2018**, *5*, 32.
- [63] M. Wońska, D. Jayatilaka, M. A. Spackman, A. J. Edwards, P. M. Dominiak, K. Woźniak, E. Nishibori, K. Sugimoto, S. Grabowsky, *Acta Cryst.* **2014**, *A70*, 483.
- [64] F. Kleemiss, O. V. Dolomanov, M. Bodensteiner, N. Peyerimhoff, L. Midgley, L. J. Bourhis, A. Genoni, L. A. Malaspina, D. Jayatilaka, J. L. Spencer et al., *Chem. Sci.* **2021**, *12*, 1675.
- [65] E. K. Wieduwilt, G. Macetti, A. Genoni, *J. Phys. Chem. Lett.* **2021**, *12*, 463.
- [66] P. N. Ruth, R. Herbst-Irmer, D. Stalke, *IUCrJ* **2022**, *9*, 286.
- [67] S. Pawłędzio, M. Malinska, F. Kleemiss, S. Grabowsky, K. Woźniak, *IUCrJ* **2022**, *9*, 497.
- [68] C. Gatti, P. Macchi, *Modern Charge Density Analysis*, Springer, Heidelberg, London, New York, **2012**.
- [69] A. Volkov, P. Macchi, L. J. Farrugia, C. Gatti, P. R. Mallinson, T. Richter, T. Koritsanszky, *XD2016. A Computer Program Package for Multipole Refinement, Topological Analysis of Charge Densities and Evaluation of Intermolecular Energies from Experimental and Theoretical Structure Factors*, **2016**.
- [70] G. M. Sheldrick, *Acta Cryst.* **2015**, *C71*, 3.

- [71] C. B. Hübschle, G. M. Sheldrick, B. Dittrich, *J. Appl. Cryst.* **2011**, *44*, 1281.
- [72] R. Herbst-Irmer, J. Henn, J. J. Holstein, C. B. Hübschle, B. Dittrich, D. Stern, D. Kratzert, D. Stalke, *J. Phys. Chem. A* **2013**, *117*, 633.
- [73] C. K. Johnson, H. A. Levy, *International Tables for X-Ray Crystallography* **1974**, *IV*.
- [74] W. F. Kuhs, *Acta Cryst* **1992**, *A48*, 80.
- [75] A. Ø. Madsen, *J. Appl. Cryst.* **2006**, *39*, 757.
- [76] J. Lübben, L. J. Bourhis, B. Dittrich, *APD-Toolkit*, **2015**.
- [77] F. Hirshfeld, *Acta Cryst.* **1976**, *A32*, 239.
- [78] L. Krause, B. Niepötter, C. J. Schürmann, D. Stalke, R. Herbst-Irmer, *IUCrJ* **2017**, *4*, 420.
- [79] B. Willis in *International Tables for Crystallography, Reciprocal Space* (Ed.: U. Shmueli), online edition, **2001**, pp. 400–406.
- [80] B. Niepötter, R. Herbst-Irmer, D. Stalke, *J. Appl. Cryst.* **2015**, *48*, 1485.
- [81] a) A. Stash, V. Zavodnik, *Crystallogr. Rep.* **1995**, *41*, 404; b) V. Zavodnik, A. Stash, V. Tsirelson, R. de Vries, D. Feil, *Acta Cryst.* **1999**, *B55*, 45.
- [82] a) E. Espinosa, I. Alkorta, I. Rozas, J. Elguero, E. Molins, *Chem. Phys. Lett.* **2001**, *336*, 457; b) E. Espinosa, I. Alkorta, J. Elguero, E. Molins, *J. Chem. Phys.* **2002**, *117*, 5529.
- [83] D. Cremer, E. Kraka, *Croat. Chem. Acta* **1984**, *57*, 1259.
- [84] Y. A. Abramov, *Acta Cryst.* **1997**, *A53*, 264.
- [85] A. Krawczuk, P. Macchi, *Chemistry Central Journal* **2014**, *8*, 68.
- [86] R. F. W. Bader, T. S. Slee, D. Cremer, E. Kraka, *J. Am. Chem. Soc.* **1983**, *105*, 5061.
- [87] R. F. W. Bader, C. Gatti, *Chem. Phys. Lett.* **1998**, *287*, 233.
- [88] B. Dittrich, C. B. Hübschle, J. J. Holstein, F. P. A. Fabbiani, *J. Appl. Cryst.* **2009**, *42*, 1110.
- [89] O. V. Dolomanov, L. J. Bourhis, R. J. Gildea, J. A. K. Howard, H. Puschmann, *J. Appl. Cryst.* **2009**, *42*, 339.
- [90] C. P. Brock, J. D. Dunitz, F. L. Hirshfeld, *Acta Cryst.* **1991**, *B47*, 789.
- [91] B. Dittrich, C. B. Hübschle, K. Pröpper, F. Dietrich, T. Stolper, J. J. Holstein, *Acta Cryst.* **2013**, *B69*, 91.
- [92] K. N. Jarzembska, P. M. Dominiak, *Acta Cryst.* **2012**, *A68*, 139.
- [93] D. Kratzert, D. Leusser, J. J. Holstein, B. Dittrich, K. Abersfelder, D. Scheschkewitz, D. Stalke, *An Experimental Charge Density Study of Two Isomers of Hexasilabenzene*, **2013**.
- [94] K. Meindl, J. Henn, N. Kocher, D. Leusser, K. A. Zachariasse, G. M. Sheldrick, T. Koritsanzsky, D. Stalke, *Journal of Physical Chemistry A* **2009**, *113*, 9684.
- [95] S. A. Shteingolts, A. F. Saifina, L. F. Saifina, V. E. Semenov, G. K. Fukin, R. R. Fayzullin, *J Mol Struc-Theochem* **2021**, *1228*, 129724.
- [96] C. Jelsch, B. Guillot, A. Lagoutte, C. Lecomte, *J. Appl. Cryst.* **2005**, *38*, 38.
- [97] Bruker AXS Inc., *SAINT*, Madison, **2016**.
- [98] L. Krause, R. Herbst-Irmer, G. M. Sheldrick, D. Stalke, *J. Appl. Cryst.* **2015**, *48*, 3.

- [99] a) A. D. Becke, *J. Chem. Phys.* **1993**, *98*, 5648; b) Lee, Yang, Parr, *Phys. Rev. B* **1988**, *37*, 785; c) P. J. Stephens, F. J. Devlin, C. F. Chabalowski, M. J. Frisch, *J. Phys. Chem.* **1994**, *98*, 11623.
- [100] F. Weigend, R. Ahlrichs, *Phys Chem Chem Phys* **2005**, *7*, 3297.
- [101] F. Neese, *Wiley Interdiscip. Rev. Comput. Mol. Sci.* **2018**, *8*.
- [102] A. Volkov, H. F. King, T. Koritsanszky, *DenProp version 04/01/16*, **2016**.
- [103] A. Zieliński, X. Marset, C. Golz, L. M. Wolf, M. Alcarazo, *Angew. Chem. Int. Ed.* **2020**, *59*, 23299.
- [104] A. Spek, *Acta Cryst.* **2015**, *C71*, 9.
- [105] P. van der Sluis, A. L. Spek, *Acta Cryst.* **1990**, *A46*, 194.
- [106] a) G. Perego, G. Del Piero, M. Corbellini, M. Bruzzone, *J. Organomet. Chem.* **1977**, *136*, 301; b) M. G. Gardiner, G. A. Koutsantonis, S. M. Lawrence, C. L. Raston, *Inorg. Chem.* **1996**, *35*, 5696.
- [107] C. Benelli, D. Gatteschi, *Introduction to molecular magnetism. From transition metals to lanthanides*, Wiley-VCH, Weinheim, Germany, **2015**.
- [108] R. Orbach, *Proc. Phys. Soc.* **1961**, *77*, 821.
- [109] K. N. Shrivastava, *Phys. Stat. Sol. B (physica status solidi (b))* **1983**, *117*, 437.
- [110] a) M. N. Leuenberger, D. Loss, *Nature* **2001**, *410*, 789; b) R. Rabelo, S.-E. Stiriba, D. Cangussu, C. Pereira, N. Moliner, R. Ruiz-García, J. Cano, J. Faus, Y. Journaux, M. Julve, *Magnetochemistry* **2020**, *6*, 69.
- [111] F.-S. Guo, B. M. Day, Y.-C. Chen, M.-L. Tong, A. Mansikkamäki, R. A. Layfield, *Science* **2018**, *362*, 1400.
- [112] C. A. Gould, K. R. McClain, D. Reta, J. G. C. Kragsskow, D. A. Marchiori, E. Lachman, E.-S. Choi, J. G. Analytis, R. D. Britt, N. F. Chilton et al., *Science* **2022**, *375*, 198.
- [113] R. Sessoli, D. Gatteschi, A. Caneschi, M. A. Novak, *Nature* **1993**, *365*, 141.
- [114] a) J. M. Frost, K. L. M. Harriman, M. Murugesu, *Chem. Sci.* **2016**, *7*, 2470; b) C. Rajnák, J. Titiš, J. Moncol, R. Mičová, R. Boča, *Inorg. Chem.* **2019**, *58*, 991; c) C. Rajnák, J. Titiš, O. Fuhr, M. Ruben, R. Boča, *Inorg. Chem.* **2014**, *53*, 8200.
- [115] B. N. Figgis, M. A. Hitchman, *Ligand field theory and its applications*, Wiley-VCH, New York, Chichester, Weinheim, **2000**.
- [116] J. M. Zadrozny, J. Telsler, J. R. Long, *Polyhedron* **2013**, *64*, 209.
- [117] C. M. Legendre, E. Damgaard-Møller, J. Overgaard, D. Stalke, *Eur. J. Inorg. Chem.* **2021**, 3108-3114.
- [118] J. R. Sabino, P. Coppens, *Acta Cryst.* **2003**, *A59*, 127.
- [119] F. Jensen, *Introduction to Computational Chemistry*, John Wiley & Sons Ltd, Chichester, West Sussex, England, **2007**.
- [120] A. Genoni, *Acta Crystallogr A Found Adv* **2020**, *76*, 172.
- [121] a) Z. Su, P. Coppens, *Acta Cryst.* **1998**, *A54*, 646; b) P. Macchi, P. Coppens, *Acta Cryst.* **2001**, *A57*, 656.

- [122] a) B. Dittrich, C. B. Hübschle, M. Messerschmidt, R. Kalinowski, D. Girnt, P. Luger, *Acta Cryst.* **2005**, *A61*, 314; b) B. Dittrich, C. B. Hübschle, P. Luger, M. A. Spackman, *Acta Cryst.* **2006**, *D62*, 1325.
- [123] P. Coppens, *Science* **1967**, *158*, 1577.
- [124] a) B. B. Iversen, F. K. Larsen, B. N. Figgis, P. A. Reynolds, A. J. Schultz, *Acta Cryst.* **1996**, *B52*, 923; b) J. Peters, W. Jauch, *Science Progress* **2002**, *85 (4)*, 297; c) P. Munshi, A. O. Madsen, M. A. Spackman, S. Larsen, R. Destro, *Acta Cryst.* **2008**, *A64*, 465; d) W. Morgenroth, J. Overgaard, H. F. Clausen, H. Svendsen, M. R. V. Jørgensen, F. K. Larsen, B. B. Iversen, *J. Appl. Cryst.* **2008**, *41*, 846; e) M. R. V. Jørgensen, V. R. Hathwar, M. Sist, X. Wang, C. M. Hoffmann, A. L. Briseno, J. Overgaard, B. B. Iversen, *Acta Cryst.* **2014**, *A70*, 679.
- [125] R. H. Blessing, *Acta Cryst.* **1995**, *B51*, 816.
- [126] F. H. Allen, I. J. Bruno, *Acta Cryst.* **2010**, *B66*, 380.
- [127] V. Schomaker, K. N. Trueblood, *Acta Cryst.* **1998**, *B54*, 507.
- [128] a) A. Ø. Madsen, S. Mason, S. Larsen, *Acta Cryst.* **2003**, *B59*, 653; b) A. Ø. Madsen, A. A. Hoser, *J. Appl. Cryst.* **2014**, *47*, 2100.
- [129] J. Lübben, L. J. Bourhis, B. Dittrich, *J. Appl. Cryst.* **2015**, *48*, 1785.
- [130] M. J. Frisch, G. W. Trucks, H. B. Schlegel, G. E. Scuseria, M. A. Robb, J. R. Cheeseman, G. Scamani, V. Barone, B. Mennucci, G. A. Petersson et al., *Gaussian 09, Revision D.01*, Gaussian, Inc., Wallingford CT, **2013**.
- [131] D. Jayatilaka, B. Dittrich, *Acta Cryst.* **2008**, *A64*, 383.
- [132] Z. Fei, N. Kocher, C. J. Mohrschladt, H. Ihmels, D. Stalke, *Angew. Chem. Int. Ed.* **2003**, *42*, 783.
- [133] P. Roversi, R. Destro, *Chem. Phys. Lett.* **2004**, *386*, 472.
- [134] I. Mata, E. Espinosa, E. Molins, S. Veintemillas, W. Maniukiewicz, C. Lecomte, A. Cousson, W. Paulus, *Acta Cryst.* **2006**, *A62*, 365.
- [135] A. E. Whitten, M. A. Spackman, *Acta Cryst.* **2006**, *B62*, 875.
- [136] C. B. Hübschle, B. Dittrich, *J. Appl. Cryst.* **2011**, *44*, 238.
- [137] W. Hummel, J. Hauser, H. B. Bürgi, *J. Mol. Graph.* **1990**, *8*, 214.
- [138] M. N. Burnett, C. K. Johnson, *ORTEP-III. Oak Ridge Thermal Ellipsoid Plot Program for crystal structure illustrations*, **1996**.
- [139] B. Willis, A. W. Pryor, *Thermal Vibrations in Crystallography*, Cambridge University Press, London, **1975**.
- [140] R. E. Rosenfield, JR, K. N. Trueblood, J. D. Dunitz, *Acta Cryst.* **1978**, *A34*, 828.
- [141] J. Lübben, *Dissertation*, Georg-August Universität Göttingen, Göttingen, **2017**.
- [142] J. Zhang, J. Fu, X. Su, X. Wang, S. Song, M. Shi, *Chemistry – An Asian Journal* **2013**, *8*, 552.
- [143] A. Hjorth Larsen, J. Jørgen Mortensen, J. Blomqvist, I. E. Castelli, R. Christensen, M. Dułak, J. Friis, M. N. Groves, B. Hammer, C. Hargus et al., *J. Phys.: Condens. Matter* **2017**, *29*, 273002.

- [144] a) M. Lusi, J. Barbour, *Cryst. Growth Des.* **2011**, *11*, 5515; b) A. Ø. Madsen, *Struct. Bond.* **2012**, *146*, 21; c) L. J. Farrugia, *IUCrJ* **2014**, *1*, 265.
- [145] M. A. Spackman, *J. Chem. Phys.* **1986**, 6579.
- [146] S. P. Thomas, P. R. Spackman, D. Jayatilaka, M. A. Spackman, *J. Chem. Theory. Comput.* **2017**, *14*, 1614.
- [147] M. Das, D. F. O'Shea, *The Journal of organic chemistry* **2014**, *79*, 5595.
- [148] a) J. Paradies, *Synthesis-Stuttgart* **2011**, *2011*, 3749; b) Z. Hassan, E. Spuling, D. M. Knoll, S. Bräse, *Angew. Chem. Int. Ed.* **2020**, *59*, 2156.
- [149] a) H. Wolf, N. Lock, S. F. Parker, D. Stalke, *Chem. Eur. J.* **2015**, *21*, 4556; b) H. Wolf, M. R. V. Jørgensen, Y.-S. Chen, R. Herbst-Irmer, D. Stalke, *Acta Cryst.* **2015**, *B71*, 10.
- [150] P. Luger, C. B. Hübschle, B. Dittrich, *J. Appl. Cryst.* **2007**, *40*, 623.

12 Danksagung

Fast fünf Jahre sind vergangen, seit ich mich entschieden habe, nach dem Master of Education nicht direkt in die Schule zu gehen. Als ich 2018 im Anschluss an meine Masterarbeit den Entschluss zur Promotion gefasst hatte, hat denke ich niemand das Ausmaß an Unsicherheit, Veränderungen und Verzögerungen kommen sehen, die die Corona Pandemie Anfang 2020 mit sich brachte. Nun, wo sich meine Zeit an der Universität Göttingen schließlich dem Ende nähert, möchte ich gerne all jenen danken, die meine Promotion hier möglich gemacht, unterstützt oder in irgendeiner Weise bereichert haben.

Zu allererst sei Prof. Dietmar Stalke gedankt für die Möglichkeit, als Lehramtskandidat in der Chemie zu promovieren. Es hat sich für mich rückblickend als richtige Entscheidung herausgestellt, sowohl die Bachelor-, als auch die Masterarbeit im AK Stalke zu schreiben. Auch in der Promotionszeit habe ich viele spannende Projekte bearbeiten dürfen und konnte auf Tagungen die wissenschaftliche Community kennenlernen. All dies sind Erlebnisse, mit denen ich nie gerechnet hätte, als ich vor nunmehr 10 Jahren mein Lehramtsstudium begonnen habe. Der Plan, mich wie schon andere Lehramtskandidaten zuvor „vor der Schule zu retten“, wird höchst wahrscheinlich von Erfolg gekrönt sein. Ebenso gilt mein Dank Prof. Ricardo Mata, für die Nachsicht mit einigen terminlichen Verzögerungen, die Anregung zu, sowie die Hilfe bei vielen kleinen, aber dennoch ungemein hilfreichen Kurskorrekturen und Zielsetzungen in den letzten zwei Jahren. Den weiteren Mitgliedern der Prüfungskommission danke ich für ihre in die Bewertung dieser Arbeit investierte Zeit. Dr. Christopher Golz insbesondere möchte ich für die großartige Unterstützung bei der Durchführung einiger gemeinsamer Messungen danken.

Ebenfalls bedanken möchte ich mich beim Fonds der Chemischen e.V., für die Finanzierung der ersten zwei Jahre meiner Promotion, meines Arbeitsplatzrechners und meiner Fahrt zur ECM 2019 in Wien.

Ein großer Dank gehört der Arbeitsgruppe Stalke, deren Teil ich in den letzten fünf Jahren sein durfte und immer gerne war. Dr. Regine Herbst-Irmer möchte ich danken für Rat und Tat in vielen kristallographischen Problemen und die langjährige Zusammenarbeit bei der Lehre im Grundpraktikum für Lehramtskandidaten und „Methoden der Chemie III: Röntgenbeugung“. Den anderen über die letzten Jahre leider immer weniger werdenden Mitgliedern des ED-Büros gilt ebenfalls mein Dank. Einige seien hier namentlich erwähnt: Von Dr. Christian Schürmann, Dr. Annika Münch und Dr. Helena Keil konnte ich gerade am Anfang meiner Masterarbeit viel über die Methode der Ladungsdichteuntersuchungen mit QTAIM und den Umgang mit unseren üblichen Computerprogrammen lernen. Niklas, dir möchte ich neben unfassbar viel Hilfe mit Python-Skripten und Eingebungen zu wissenschaftlichem Arbeiten auch dafür danken, dass das Level an schwarzem Humor im Büro in den letzten Jahren nie unter ein kritisches Level gesunken ist! Ganz besonders bedanken möchte ich mich bei Katharina: Für die gute Zusammenarbeit während deiner Bachelorarbeit. Für Rechnungen aus Aarhus, regelmäßiges Mensen und den „Tanz um die Parkbank“ während deiner Masterarbeit. Und für all die gemeinsame Zeit, die wir abseits von Arbeit und Uni zusammen verbracht haben!

Auch dem Rest des Arbeitskreises außerhalb des ED-Büros sei gedankt: Ganz besonders seien hier Dr. Johannes Kretsch und Dr. Daniel Lüert erwähnt, die mich unter eigenem Mehraufwand mit Kristallen für viele meiner Messungen versorgt haben und Dr. Nico Graw hat freundlicherweise toleriert, dass ich eine Ecke seines Labors mit einem Kryostat vollgeräumt habe. Daniel und Helena möchte ich hier außerdem noch mal für viele kleine Gespräche im Büro und in der Küche danken! Als Erweiterung des Arbeitskreises gilt mein Dank außerdem noch den langjährigen Assistenten Oliver und Tina, für die gute Zusammenarbeit bei der Betreuung des Grundpraktikums für Lehramtskandidaten.

Abschließend möchte ich mich noch bei all den wichtigen Menschen in meinem Leben bedanken, die rein gar nichts mit meiner Zeit an der Universität selbst zu tun haben: Guten Freunden wie Boris, Hauke, Ellen und Krischa, dank denen ich es geschafft habe, trotz Corona-Lockdowns einigermaßen bei Verstand zu bleiben. Und natürlich meinen Eltern, die mich immer unterstützt haben, und durch meine Studienzzeit hinweg immer ein offenes Ohr für mich hatten. Danke!